Series Calibration of segmented and multi-layered Micromegas Modules for ATLAS

Maximilian Georg Herrmann

SIGILL. UNIVERSITAT. LUDOVIC. MAXIM.

München 2019

Series Calibration of segmented and multi-layered Micromegas Modules for ATLAS

Maximilian Georg Herrmann

Dissertation
an der Fakultät für Physik
der Ludwig–Maximilians–Universität
München

vorgelegt von
Maximilian Georg Herrmann
aus Aschaffenburg

München, den 19.09.2019

Erstgutachter: Prof. Dr. Otmar Biebel
Zweitgutachter: Prof. Dr. Thomas Kuhr
Tag der mündlichen Prüfung: 31.10.2019

“¿No veis, señor, que no podrá llegar el provecho que cause la cordura de don Quijote a lo que llega el gusto que da con sus desvaríos?”

- Miguel de Cervantes , 1615 , *Segunda parte del ingenioso caballero don Quijote de la Mancha*

Zusammenfassung

Der große Hadronen-Ringbeschleuniger des europäischen Kernforschungszentrum bei Genf wird in den nächsten Jahren stetig verbessert. Dadurch werden mehr Teilchenkollisionen bei den verschiedenen Experimenten am Beschleuniger stattfinden. Diese erhöhte Rate führt zu einer Verschlechterung der Effizienz von bisher genutzten Detektortechnologien. Um weiterhin bei hoher Effizienz die Kollisionen rekonstruieren zu können werden anfällige Detektorsysteme ausgetauscht. Beim größten Experiment, dem ATLAS, ist vorgesehen, die inneren Endkappen des Myon-Spektrometer zu ersetzen. Die Spurdetektoren der neuen Endkappen werden Micromegas-Detektoren bilden. Diese werden als vierlagige Module mit aktiven Flächen von mehr als $2\,\mathrm{m}^2$ gebaut. Micromegas sind Gasdetektoren mit mikrostrukturierten Streifenanoden zur Teilchen-Durchgangsort-Bestimmung. Die Module werden von Gruppen in verschiedenen Ländern und an mehreren Universitäten gebaut. Ein Moduletyp wird an der LMU in Garching bei München fertiggestellt und in Betrieb genommen. Technologiebedingt müssen die Anoden der Module in drei Segmente parallel zu den Streifen aufgeteilt werden.

In dieser Arbeit wird die Vermessung dieser Micromegas-Module mit kosmischen Myonen beschrieben. Die Vermessung soll zur Kalibration der dreigeteilten Anode als auch zur Sicherstellung der Betriebstauglichkeit der Module dienen. Als Referenzsystem werden Driftrohrkammern verwendet, zu deren Drähten die Streifen der Module parallel ausgerichtet werden. Zum Starten der Signalauslese als auch zur Segmentierung entlang der Drähte dienen Szintillator-Blöcke. Dieses Referenzsystem wird zunächst untersucht auf geometrische Abweichungen sowie auf die Fähigkeiten der Spurrekonstruktion.

Als Spurkammern sollen auch die Micromegas-Detektoren bei hoher Effizienz möglichst präzise Spuren rekonstruieren. Daher werden die Einflüsse von elektronischem Rauschen als auch der Signalhöhe auf die Effizienz untersucht. Ein in Garching gebautes Modul besitzt mehr als 12000 Auslesekanäle. Zur Bestimmmung von problematischen Kanälen werden verschiedene Methodiken vorgestellt. Effekte der verwendeten Ausleseelektronik auf das Kanalrauschen und die Signalhöhe werden betrachtet. Durch Produktionstoleranzen variiert die Größe der Signalentstehungszone. Die Auswirkung dieser Schwankung auf die mittlere Signalhöhe wird auf $6\,\%/\mu\mathrm{m}$ bestimmt. Für drei verschiedene Detektor-Gas-Mischungen von Argon und Kohlenstoffdioxid werden die Signalhöhenabhängigkeiten von der angelegten Spannung diskutiert. Es zeigt sich, dass ein höherer Anteil von CO_2 es erlaubt, die Module mit größeren Spannungen und damit größeren Signalen zu betreiben. Dies führt ebenso zu besseren Effizienzen, da größere Signale besser von Rauschen unterschieden werden können. Der nachteilige Effekt von elektronischem Rauschen auf die Effizienz wird diskutiert.

Zur Kalibration der dreigeteilten Anode werden zwei unterschiedliche Ansätze verfolgt. Ein optisches Verfahren rekonstruiert die Positionen des Anodenmaterials an den Rändern. Hierzu wird eine Dreiachsen-Maschine in Kombination mit einer Kamera verwendet. Die Abweichungen der Maschinen-Bewegung vom Soll wird vermessen und ein Vorgehen zur Korrektur beschrieben. Ein Verfahren zur Auswertung der Bilder von Präzisions-Markierungen wird entwickelt. Die Kombination dieser Methoden wird mit Referenz-Messungen verglichen. Der Vergleich liefert Standard-Abweichungen unter $20\,\mu\mathrm{m}$. Der zweite Ansatz rekonstruiert die Abweichungen der Streifengeometrie durch die Abweichungen der Positionsrekonstruktion zu den Spuren im Referenzsystem. Rotationen, Verschiebungen als auch Abweichungen des Streifenabstandes können dadurch bestimmt werden. Zudem wurde bei vielen Segmenten eine U-förmige Verformung der Streifen rekonstruiert. Diese erklärt sich aus der Feuchtigkeitsempfindlichkeit des Anodenträgermaterials. Die Verformung erschwert den Vergleich der beiden Ansätze, da die Geometrie extrapoliert werden muss. Nichts desto weniger konnte auf einem qualitativen Niveau eine Korrelation gefunden werden.

Zur Durchgangsort-Bestimmung und Spurrekonstruktion werden unterschiedliche Methoden für einzelne Lagen untersucht. Ein signalhöhen-gewichtetes Verfahren zeigt passable Ergebnisse von Auflösungen um $100\,\mu\mathrm{m}$ bei senkrechtem Einfall. Die starke Abhängigkeit der Auflösung von der Spursteigung motiviert die Auswertung der Signalzeit. Hierzu werden die Zeiten von drei Evaluationspunkten verglichen. Ebenso werden Effekte durch die Korrektur von kapazitiven Signalkopplungen untersucht. Durch die Breite der Zeitverteilungen ist es möglich die Driftgeschwindigkeit der Elektronen zu bestimmen. Diese Zeiten werden zur Spurrekonstruktion im $5\,\mathrm{mm}$ großen Driftbereich verwendet. Die Positionsrekonstruktion, ähnlich einer Spuren-Drift-Kammer, verbessert die Auflösung für Einfallswinkel größer 15°. Dies geschieht nicht in dem Maße wie durch Teststrahl-Messungen erwartet. Ein drittes Verfahren, welches die Signalhöhen und Zeit kombiniert, zeigt Verbesserungen für alle Winkel.

Zwei der vier Lagen haben gegenläufig um 1.5° gedrehte Streifen innerhalb der aktiven Fläche. Dies ermöglicht die Rekonstruktion der Position des Teilchen-Durchgangs entlang der parallelen Streifen. Die Abhängigkeiten dieser Rekonstruktion von der Spur-Inklination werden untersucht. Dadurch zeigt sich, dass die Skalierung der Position aus den Szintillator-Blöcken um 2% falsch ist. Die Rekonstruktion der Spur durch Verwendung aller vier Lagen wird zuletzt diskutiert.

Abstract

The Large Hadron Collider at the European Organization for Nuclear Research will be upgraded in the next years. Therefore more particle-collisions will happen at the experiments around the accelerator. This higher hit-rate leads to a degradation of the efficiency for some detector technologies used so far. In order to reconstruct the collisions still with high efficiency, susceptible detector-systems will be exchanged. At the largest experiment, ATLAS, it is foreseen to replace the inner-end-caps of the muon-spectrometer. The tracking-detectors of the new end-caps will be Micromegas detectors. Modules of four active layers with active areas of more than $2\,\mathrm{m}^2$ are currently being assembled. Micromegas are gas detectors with a micro-structured strip-anode for the reconstruction of the position of particle-incidents.

The modules are built in several countries and at several universities. One type of module is completed and commissioned at the LMU in Garching near Munich. Production-related the anodes of these detectors are segmented into three parts parallel to the strips. In this thesis, the surveying of these modules with cosmic muons is described. The measurements should be used for the calibration of the threefold anode and ensure the operational reliability. As reference system drift-tube-chambers are used. During measurements the strips are oriented parallel to the wires of the chambers. Scintillator blocks are used for triggering the signal-readout and as coarse segmentation along the wires. In a first step systematics and capabilities of this system are discussed. As tracking-detectors the efficiency and resolution of the Micromegas should be excellent. Therefore effects on the efficiency of electrical noise and variation of the signal-height are discussed. A module built in Garching has more than 12000 readout-channels. Multiple approaches for the determination of problematic channels are discussed. Due to production-tolerances the size of the signal-formation-region varies. The effect of these variations on the mean signal-height is determined to be in the order of $6\,\%/\mu\mathrm{m}$. For three mixtures of argon and carbon dioxide the signal-height-dependencies on the applied voltage are discussed. It is shown that a higher fraction of CO_2 enables the usage of higher voltages and therefore higher signals are produced. Accordingly this leads to better efficiencies, due to the better distinguishability with respect to noise. The disadvantageous effects of electronic noise on the efficiency are also discussed.

For the calibration of the threefold anode, two approaches are followed. An optical surveying is used for the reconstruction of positions on the anode-material at the edges. A coordinate measuring machine combined with a camera is used for this. The deviations of the machine-movement are measured and a procedure for correction is given. For the evaluation of the camera-images, software for the detection and fit of precision markers is developed. The combination of these methods are compared to reference-measurements. The standard deviations of differences between these two measurements are below $20\,\mu\mathrm{m}$. In a second approach the deviations of the strip-pattern to the nominal-design is reconstructed using tracks of the reference system. Rotations, shifts and also deviations to the nominal strip-distances can be reconstructed. Additionally an U-like shape of the strips is reconstructed for many anode-segments. This can be explained by the deformations of the anode-support-material due to humidity. The deformations aggravates the comparison of the two approaches, as the reconstruction has to be extrapolated. None the less on a qualitative-level a good correlation is found.

For incident-position and track reconstruction several methods for single layers are investigated. A signal-height-weighted approach achieves reasonable results of about $100\,\mu\mathrm{m}$ for normal incident. The strong dependence on the track-inclination motivates the evaluation of the signal-time. Therefore the times of three signal-evaluation-points are compared. Also effects due to the correction of capacitive-coupled signals are investigated. Using the width of the time-distributions the drift-velocity of the electrons is reconstructed. Also the track of the incident particle is reconstructed using these times. The position-reconstruction similar to a Time-Projection-Chamber improves the resolution for incident-angles of more than 15°. The improvement is not as large as expected from test-beam-measurements. A third approach, which combines the signal-height and time, reconstructs better resolutions for all angles.

Two of the four layers have strips oppositely rotated by 1.5° within the active plane. This enables the reconstruction of the incident-position along the parallel strip-layers. The dependencies of the reconstruction on the track-inclination is investigated. A wrong scaling of the position reconstructed by the scintillator-blocks is determined to be about 2%. At last the track reconstruction using all four layers is discussed.

Für meine Oma Nadi.

Contents

"But that's not the way of it with the tales that really mattered, or the ones that stay in the mind. Folk seem to have been just landed in them, usually - their paths were laid that way, as you put it... I wonder what sort of a tale we've fallen into?"

- John Ronald Reuel Tolkien , 1954 , *The Lord of the Rings*

1. Motivation

The fundamental interactions of matter and particles can today be probed in large experiments. This is needed due to the high energy which is required to bring the particles close enough and due to the huge amount of collisions produced thereby. With these large experiments not only established theories can be tested, but also new theories can be targeted which might solve some not yet understood questions to nature. To further increase the capabilities and understand nature a bit better, ongoing upgrades are foreseen to the setups of the experiments around the Large Hadron Collider. One of those upgrades is the New Small Wheels project for the ATLAS experiment [ATLAS Collaboration, 2008]. The aim of this thesis is to give insights into the calibration of one new detector technology used for this upgrade. This technology are the Micromegas detectors for track reconstruction of minimal ionizing particles in high flux environments. The following chapter outlines the context of the SM2 Micromegas modules in the New Small Wheel upgrade.

1.1. LHC and ATLAS

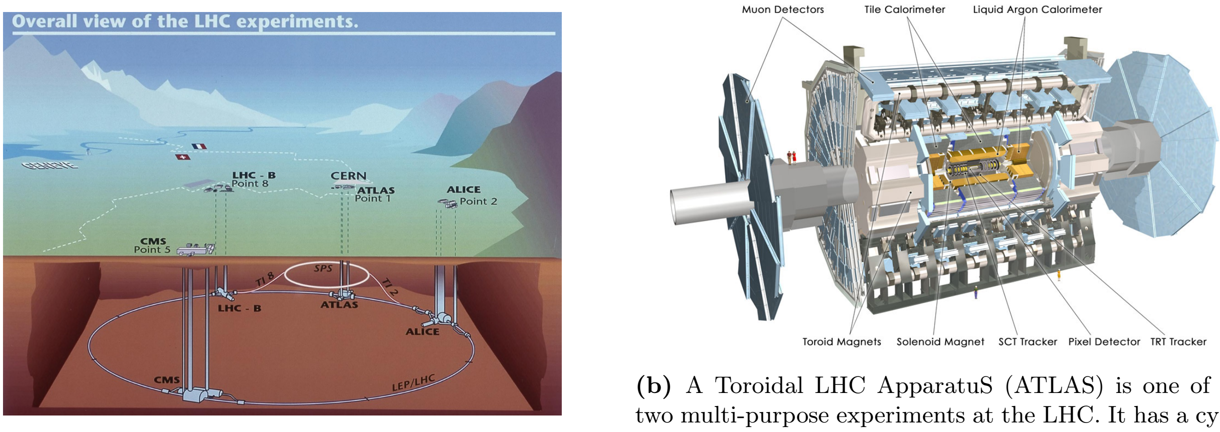

(a) Sketch of the Large Hadron Collider (LHC) located near Geneva at the European Organization for Nuclear Research (CERN). Indicated are the four main experiments ALICE, ATLAS, CMS and LHCb. The LHC accelerates protons up to energies of 6.5 TeV. At the sites of the experiments the two counter propagating beams are collided. Taken from [Caron, 1998].

(b) A Toroidal LHC ApparatuS (ATLAS) is one of the two multi-purpose experiments at the LHC. It has a cylindrical layout around the interaction point of the colliding beams along their axis. At the flat ends of the cylinder a disk-like end-cap-system is installed. Several layers of detectors are for the reconstruction of the tracks and energies of particles emerging the collisions. The outermost detector system, indicated here in light blue, is the muon-spectrometer. Taken from [Pequenao, 2008].

Figure 1.1.: Sketches of the Large Hadron Collider and A Toroidal LHC ApparatuS.

The Large Hadron Collider (LHC) at the European Organization for Nuclear Research (CERN) is a circular accelerator for protons and ions [Brüning et al., 2004]. Through several smaller accelerators the protons reach an energy of 450 GeV before they enter the main ring. In the more than 26 km long LHC ring the particles are further accelerated up to energies of 6.5 TeV. The protons are kept on circular track by super-conductive magnets, which produce magnetic fields of more than 8 T. This is done for two in opposite direction circulating beams with bunches of protons of more than 10^{11} particles. The bunches are 25 ns apart and have during operation at a collision point a size of about 7.55 cm along and 16.7 µm perpendicular to the beam axis. At four intersection points the two beams are colliding (see 1.1a). Around these points specific experiments are placed. A Toroidal LHC ApparatuS (ATLAS) is a multi-purpose experiment for the investigation of the collisions produced at one of these intersection points. It consists of multiple layers of detectors for track and energy reconstruction of particles emerging the collision processes. The design of ATLAS is cylindrical along the beam axis around the intersection point (see 1.1b). At the flat ends of the cylinder detector-wheels are installed for reconstruction of particles which fly along the beam axis. The outermost system of detectors is the muon-spectrometer. In the field of a toroidal magnet the bent track of muons can be measured to reconstruct their momentum. This is achieved currently with Monitored Drift Tube (MDT) chambers. These are gas detectors with multiple layers of 3 cm diameter aluminium tubes. Wires are stretched inside and set to a voltage of about 3 kV. The high field near the wires leads to an amplification of electrons caused by the ionisation of the gas along the path of the muons. The distance to the wire of the muon passage can be reconstructed measuring the time distribution of these electron avalanches. Combining the information of several layers of tubes enables the reconstruction of the muons path.

1.2. New Small Wheel Project

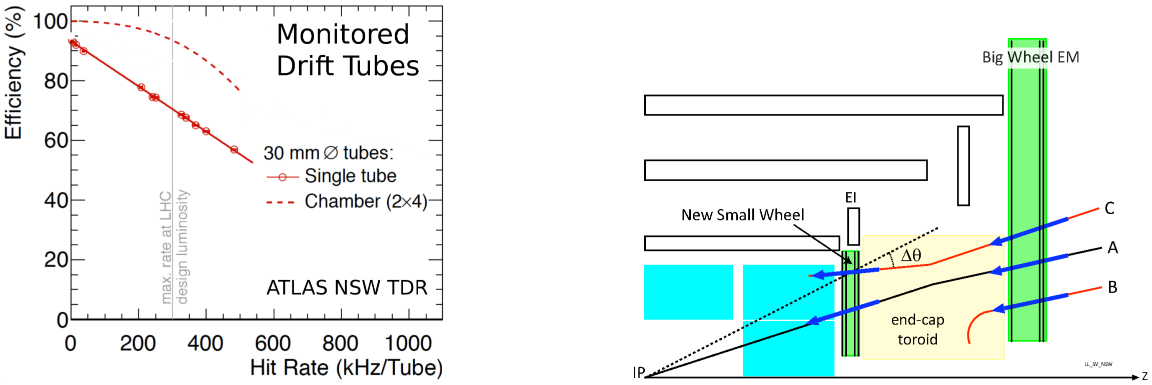

(a) Efficiencies of single Monitored Drift Tubes (MDT, measurements circles, linear fit solid line) and MDT chambers (calculated, dashed line) as function of the single tube hit rate. At design luminosity of the LHC a hit rate per tube of 300 kHz is expected (indicated in grey). Higher luminosities will lead to higher hit rates and therefore to a further degradation of the efficiency of the MDT chambers.

(b) Sketch of tracks going through one quarter of the ATLAS experiment. All tracks A, B and C would be accepted using only the information of the Big Wheel (blue arrows), as they are all pointing to the interaction point (IP). Track B and C can be excluded using additionally the information of the New Small Wheel. Thus the New Small Wheel will reduce the rate of fake triggers due to particles not coming from the interaction point.

Figure 1.2.: Impact of High Luminosity LHC on the performance of the MDTs and reduction of the fake trigger rate using the tracking information of the New Small Wheel. Taken from [ATLAS Collaboration, 2013].

The upgrades of the LHC in the next years will increase its luminosity above ten times the design value (High Luminosity LHC) [ATLAS Collaboration, 2013]. Therefore not only the interactions of interest will be enhanced, but also the background hit rate will increase. Especially the regions along the beam axis next to the intersection points will be exposed to high rates. For the MDTs of ATLAS in this region the background will lead to a loss of efficiency (see 1.2a). In order to cope with the aggravated conditions these detectors at the innermost forward region will be exchanged. Therefore the so called small wheels, as part of the muon-spectrometer, will be replaced by New Small Wheels (NSW, see 1.3a). The new detectors which will be installed should not only maintain the performance at higher rates. Also a rejection of false triggers with additional track-points should be achieved (see 1.2b). For the exchange two redundant detector technologies were chosen with trigger and tracking capabilities at high rates. Small-strip Thin Gap Chambers (sTGC) will be used primarily as trigger. The focus of this thesis is on the Micromegas, which will be used as precision tracker. Both technologies will be constructed as modules of four active layers with sizes of more than $1\,\mathrm{m}^2$. In order to cover a wheel with these modules their shape is trapezoidal (see 1.3b). The effort for the construction is distributed among several national and international collaborations.

The Large Micromegas Modules 1 (LM1) are built by a French Collaboration situated at the center of the commissariat l'énergie atomique et aux énergies alternatives (C.E.A) in Sacaly near Paris. The Large Micromegas Modules 2 (LM2) are built by a Greek-Russian Collaboration in Thessaloniki and in Dubna. The Small Micromegas Modules 1 (SM1) are built by an Italian Collaboration of the Istituto Nazionale di Fisica Nucleare (INFN). The German collaboration builds the small outer Micromegas modules, so called SM2.

This collaboration consists of groups at the several universities. The group at the Johannes Gutenberg Universität (JGU) in Mainz built the cathode-structures. The group at the Julius-Maximilians-Universität in Würzburg perpare the micro-mesh. At the Albert-Ludwigs-Universität in Freiburg several mechanical parts are built for the whole NSW-collaboration. A large part of the construction and the final assembly, as well as performance tests of the SM2 are done at the Ludwig-Maximilians Universität (LMU) in Garching near Munich. After a short description of the main local production steps, the focus of this thesis will lie on measurements performed in Garching to characterize these detector modules.

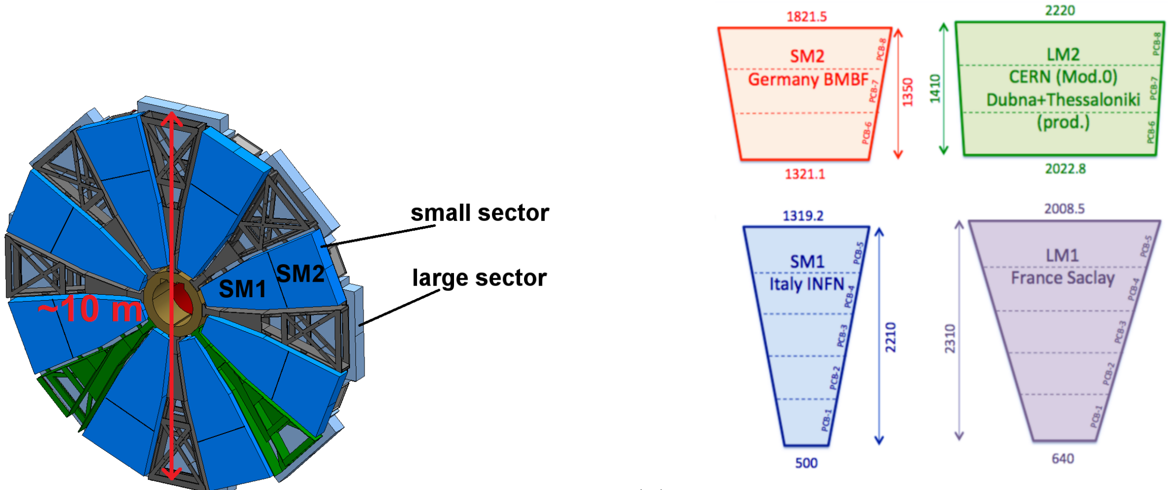

(a) Layout of the New Small Wheels (NSW) for the Micromegas modules. Small and large sectors are overlapping to avoid insensitive areas. The sector wedges consist of inner and outer Micromegas modules.

(b) Sketches of the Micromegas module types for the New Small Wheels. The active areas are for the small modules (SM-type) around 2 m^2, while for the large modules (LM-type) around 3 m^2. This thesis focuses on the SM2 modules.

Figure 1.3.: Sketches of the Micromegas module layout for the NSW. This thesis focuses on the SM2 modules. Taken from [ATLAS Collaboration, 2013].

“Well, I’m pleased to meet you both”, Ben said.
It came out sounding prissy and a little lame.
A silence fell amid the three of them.
It was not an entirely uncomfortable silence.
In it they became friends.

- Stephan King , 1986 , *It*

2. Resistive Strip Micromegas

MICRO-Mesh-GAseous Structure (Micromegas) detectors are gas detectors for track reconstruction of minimum ionizing particles (MIPs) [Giomataris et al., 1996]. They have been developed to overcome resolution-difficulties of multiwire proportional chambers at high particle fluxes. Therefore wires are replaced with micro-strips printed on electrical-insulating materials and the regions of initial ionization is separated from the region of charge-amplification. For the separation the eponymous micro-mesh is required. The working principle of the Micromegas detector is based on the interaction of the through-going particle with the detector gas. Also the movement of the electrons and ions created by these processes are fundamental for the understanding of the detector characteristics. Therefore this chapter first describes these physical processes. Afterwards the working principle of the detector is discussed.

2.1. Energy Loss of Minimum Ionizing Particles

Muons and other charged particles lose energy while they traverse matter. This is caused by the electromagnetic interaction of the particle with the electrons of the medium. The energy is creating mainly electron-ion-pairs, but also causes atomic excitation or radiation. The amount of deposited energy is depending not only on the type of particle, but also on its initial energy, as well as the type of material. To describe this energy loss the Bethe equation can be used (see formula 2.1).

$$-\left\langle \frac{\mathrm{d}E}{\mathrm{d}x} \right\rangle = 4\pi r_e^2 m_e c^2 N_0 \cdot \frac{Zz^2}{A\beta^2} \cdot \left[\ln\left(\frac{2m_e c^2 \beta^2}{I \cdot (1-\beta^2)} \right) - \beta^2 \right] \tag{2.1}$$

variable	value	unit	description
r_e	2.8179403227(19)	m	classical electron radius
m_e	$9.10938356(11) \cdot 10^{-31}$	kg	electron mass
c	299792458	m/s	speed of light
N_0	$6.02214076 \cdot 10^{23}$	mol^{-1}	Avogadro's number
Z			material atomic number
z			particle charge in unit-charges
A			material mass number
β	v / c		velocity of the traversing particle
I	$Z \cdot 10\,\mathrm{eV}$	eV	effective ionization potential of the material

Table 2.1.: Constants and variables needed for the calculation of the mean energy loss according to [Bethe, 1930].

It has to be noted that this description excludes explicitly electrons, as they are quantum-mechanically indistinguishable of the electrons in the medium. The equation describes the mean energy loss rate per traveled distance. This holds for charged particles with $\beta\gamma$ in the range of 0.1 to 1000. For higher energies corrections due to radiative losses by *bremsstrahlung* have to considered. It is convenient to rewrite the equation using the density ρ of the penetrated material by $\frac{1}{\rho}\left\langle \frac{\mathrm{d}E}{\mathrm{d}x} \right\rangle = \left\langle \frac{\mathrm{d}E}{\mathrm{d}\chi} \right\rangle$. The stopping power on the y-axis of figure 2.1 can be interpreted as the mean energy loss per distance [Olive et al., 2014]. The graph describes the energy loss for positive muons penetrating copper, but the general shape of the curve is the same for all charged particles heavier than electrons and all materials. Around $\beta\gamma = 0.1$ the stopping power is decreasing as particles with higher energy lose less energy during interaction with the material. For energies around $300\,\mathrm{MeV/c^2}$ the stopping power reaches a minimum, as afterwards radiative and relativistic effects are increasing. Particles around this minimum are called minimum ionizing particels (MIP). Cosmic muons belong to the group of MIPs. The expected energy deposition of MIPs is Landau-distributed with a differing mean and most probable value. This is due to rare high energy transfers causing long tails in the distributions [Olive et al., 2014].

Another effect due to the electromagnetic interaction of charged particles with matter is multiple scattering. The traversing particle accumulates during material-passage small changes to its initial direction of flight by multiple coulomb-interaction. The accumulation leads to a statistical spread with respect to the initial direction-distribution. The angular width σ_θ of this spread can be described after [Olive et al., 2014] by

$$\sigma_\theta = 13.6\,\mathrm{MeV/c}\frac{z}{\beta p}\sqrt{x/X_0}\left[1 + 0.038\ln\left(\frac{xz^2}{X_0\beta^2}\right)\right]. \tag{2.2}$$

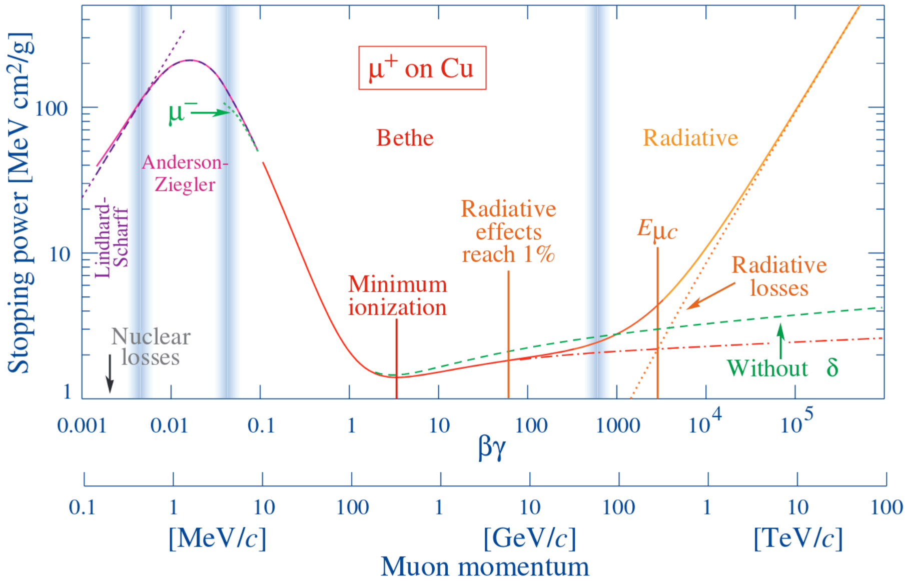

Figure 2.1.: Stopping power as function of muon momentum [Olive et al., 2014], [Groom et al., 2001].

Here x denotes the traversed distance in the material of radiation length X_0. The velocity, momentum and charge of the incident particle is given by β, p and z, respectively. This description is only accurate to about 11%. A more accurate formula is given by [Lynch and Dahl, 1991]. Both of these approaches describe the angular-spread Gaussian-like. The actual distributions features long tails due to nuclear interactions, which are not taken into account.

2.2. Electron and Ion Interaction in Gases

The freed electrons and ions in the gas commonly recombine or diffuse. In order to detect the charges, electric fields are applied to separate negative from positive charge-carriers. This leads to the question of the interactions of these charge-carriers with the gas-atoms or molecules in the presence of electric fields. For the ions, which are orders of magnitude heavier than the electrons, the fields in the ranges considered for a Micromegas lead to a constant drift. The velocity for this drift is depending on the gas, its pressure and is linear with the applied field. The dependence on the gas is described by the ion-mobility μ, which is for argon-ions in argon-gas $1.54\,\mathrm{cm}^2/(\mathrm{Vs})$ at a nominal pressure of 1013 mbar. For the electrons their low mass and their indistinguishability to the bound-electrons in the gas leads to a more complicated behaviour. Depending on the electric field, the gas-mixture and pressure, several regimes have to be distinguished. For Micromegas two regions are considerable. Low fields, in the range up to about 1 kV/cm, lead to a constant electron-drift. The collisions with the gas-atoms randomize the movement, while the field leads to an average drift along the field-lines. As the main interaction with the gas happens with the shell-electrons the drift is depending on the actual gas-mixture. This is seen in figure 2.2.

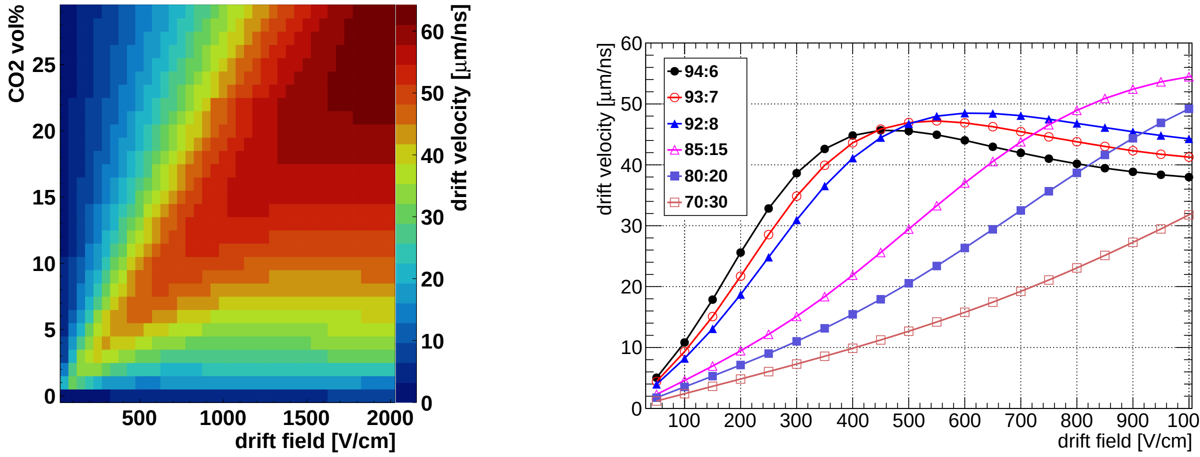

(a) Drift velocities color encoded as function of the drift-field and the CO_2 addition to argon.

(b) Drift velocities as function of the drift-field for several mixtures of Ar:CO_2.

Figure 2.2.: The drift-velocity of electrons is depending on the applied electric field as well as the actual mixture of Ar:CO_2. Simulated using MAGBOLTZ [Biagi, 1995] for a temperature of 20 °C and 960 mbar.

Here the dependence of the drift-velocity on the mixture of argon-CO_2 is shown as function of the electric-field.

The randomization of the electron-movement leads to a diffusion of the electrons along their average path due to the field. This can be expressed by diffusion coefficients transverse and longitudinal to this path (see figure 2.3).

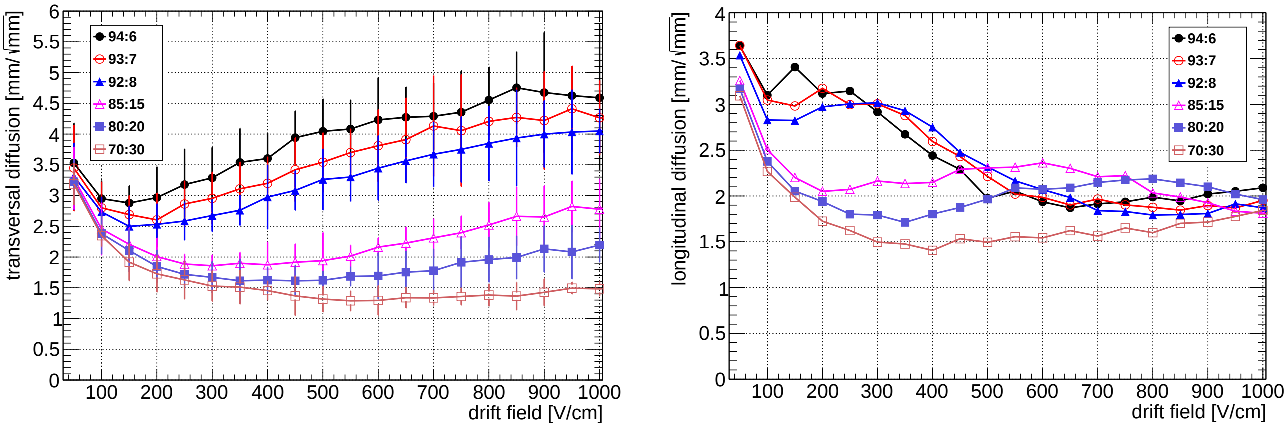

(a) Transverse diffusion as function of the drift-field for several mixtures of Ar:CO_2.

(b) Longitudinal diffusion as function of the drift-field for several mixtures of Ar:CO_2.

Figure 2.3.: Due to the statistical interaction with the gas atoms the drift of electrons is not straight, but the electron distribution is spread. This spread is called diffusion and is transverse and longitudinal to the drift direction. It is depending on the gas-mixture and the drift-field mainly. Simulated using MAGBOLTZ [Biagi, 1995] for a temperature of 20 °C and 960 mbar.

In the second regime starting around 30 kV/cm the strong acceleration of the electrons enables gas-amplification. For this the electrons have to ionize the gas-atoms during their collisions. Further they have to collect enough energy between the collisions for the next ionization. If these criteria are fulfilled the electron-number is increased after each collision and therefore an avalanche of electrons is created. This is described by [Townsend, 1910]. As important gas-parameter the Townsend-coefficient α is the inverse of the mean free path of the electrons between the collisions. It therefore describes the increase of the electron-number per length if the field is high enough.

2.3. Working Principle

The Micromegas-technology is since its invention under steady development [Bortfeldt, 2014], [Klitzner, 2019]. As for this thesis solely the Micromegas used for the NSW-upgrade are discussed, the concepts are described explicitly for this case.

The electron-ion-pairs created in the gas volume by MIPs get separated in an electrical field of about 0.6 kV/cm. This field is generated between a planar cathode at negative voltages and a grounded stainless steel micromesh. These structures are about 5 mm apart from each other, therefore a negative voltage of about 300 V has to be applied to the cathode.

For NSW Micromegas the nominal gas-mixture is 93 volume % argon and 7 volume % carbon dioxide. Therefore the electric field of 600 $\frac{\mathrm{V}}{\mathrm{cm}}$ leads to a plateau of the drift-velocity of 47 µm/ns for the electrons. In order to be able to detect these electrons created by the MIPs in the primary ionization they have to be amplified. This is achieved in a high electric field of about 47.5 kV/cm beneath the micromesh. To generate this field the anode, a micropattern resistive strip layer, is set to a voltage of 570 V. The high field is produced by the very small distance of about 0.12 mm between the mesh and the resistive strips.

This distance is guaranteed by insulating pillars made of soldering mask material with 0.12 mm height attached to the anode. The mesh is attracted due to electrostatic force to the anode and held therefore at design distance by these pillars. The electrons are guided by field-lines through the micromesh caused by the high ratio of the electric fields beneath and above. Below the micromesh the high electric field leads to Townsend-avalanches, which increase the number of electrons reaching the anode by a factor of about 40000.

For the reconstruction of the intersection position and track of the MIPs a layer of copper readout strips is located beneath the resistive strip layer. These strips receive a charge-signal by capacitive-coupling to the charges on the resistive layer. Also a slower signal by the ions created in the avalanche is induced by the ion drift movement towards the micromesh. These signals are only created on readout strips directly below the electron avalanches. Therefore the intersection position of the MIP can be reconstructed using these signals on the strip structure below the anode. Straight copper strips with a pitch of 425 µm are used for the NSW Micromegas. This enables a resolution of better than 100 µm in test beams with tracks being perpendicular to the anode plane [Flierl, 2018]. The resolution is only concerned on the anode plane in the direction perpendicular to the readout strips. For tracks inclined to the electrode planes also the time-information of the signals has to be used for the reconstruction. Electrons created near the cathode drift a longer time than electrons created near the micromesh. Therefore the time when the electrons lead to an avalanche, hence the signal-time, scales linearly with the position of the primary ionization between the cathode and the mesh.

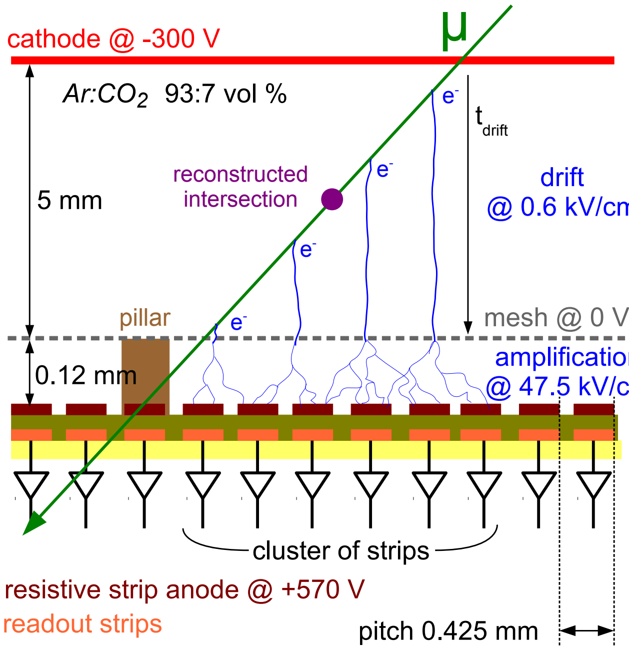

Figure 2.4.: Sketch of the working principle of a resistive strip Micromegas. The three planar and parallel electrodes are the cathode at −300 V, the grounded stainless steel micromesh and the resistive strip-anode at +570 V. Minimum ionizing particles like muons create electron-ion pairs in the gas-mixture of argon and carbon dioxide between cathode and micromesh. The electrons follow the field-lines through the micromesh due to the high ratio between the amplification and the drift-field. Between the mesh and the resistive strip-anode the electrons get amplified. The evaluation of the signals on the copper readout strips enables the position and track reconstruction.

The main reason for their development and use of the Micromegas are their high-rate-capability. This is achieved by the small region of amplification. While the electrons from the drift-region trespass the micromesh, the high field-ratio ensures also the neutralization of the ions from the amplification-region at the micromesh.
Another important aspect is the protection from discharges. Discharges can occur due to defects or inhomogeneities in the amplification-region, but also due to strongly ionizing particles present for example as background particles in the ATLAS experiment. Discharges are created if the number of free electrons is exceeding the Raether-limit [Raether, 1964]. Then a conducting plasma, called streamer, between anode and mesh leads to an equalization of the potentials.
These discharges can be problematic in two ways. First the field configuration is distorted due to the huge amount of charges created. Also the anode and the mesh can be drawn on the same voltage. Therefore the common principle of detection does not work and the detector is ineffective as long as the streamer exists. The second problem is the amount of energy released on the anode-structure during charge-flow between anode and mesh. The charge-flow can cause heat dissipation and by this destroy the anode-surface. In order to protect the detector from these effects and increase its high-rate-capability by reducing the dead-time a resistive layer is used as anode. The high resistivity ensures a fast breakdown of the streamer as the charges can not flow fast enough from the other parts of the anode to keep the potential locally high. This effect should be limited only to the part of the detector where the discharge occurs, as only here the charges flow into the streamer [Burnens et al., 2011].

> *"But the Solar System!" I protested.*
> *"What the deuce is it to me?" he interrupted impatiently:*
> *"you say that we go round the sun. If we went round the moon it would not make pennyworth of difference to me or to my work."*
>
> - Arthur Conan Doyle , 1887 , *A Study in Scarlett*

3. Layout and Construction of SM2 Micromegas Modules

Besides the performance of the detectors, the modules have to fulfill technical requirements to fit in the ATLAS experiment. Therefore the Micromegas modules built in Germany for the NSW project have to satisfy mechanical and electrical tolerances. The design of the modules is specified and with that the production process as well as the quality control. In the following chapter the layout of the SM2 modules is described and the most important production steps are explained.

3.1. Micromegas Quadruplet

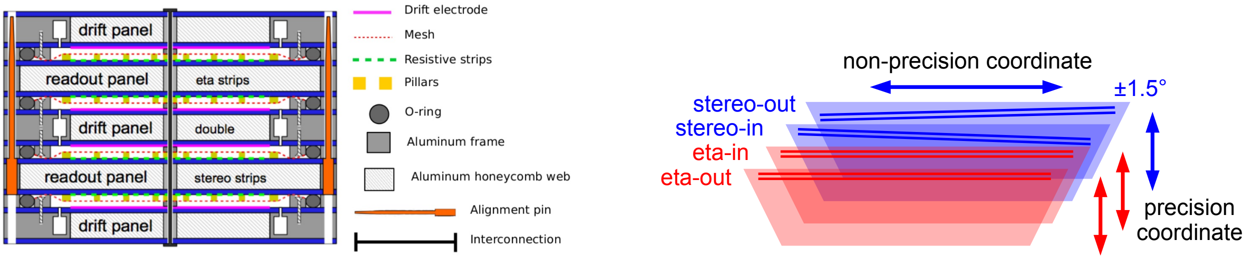

(a) Micromegas quadruplet consisting of five panels. Taken from [Sidiropoulou, 2018].

(b) Orientation of the strips in the four layers.

Figure 3.1.: The Micromegas quadruplets consist of five panels which enclose four gas volumes (see 3.1a). The signals generated in these volumes will be collected on four readout anodes with specific strip layout (see 3.1b).

One quadruplet consists of four active Micromegas volumes. They are stacked in a way that the electrode planes (cathode, mesh and anode) are parallel. Therefore two inner layers will be sandwiched by two outer ones. The orientation of the drift and amplification-gaps are alternating (see figure 3.1a). By this arrangement the anode of two layers, one outer and one inner, can be built on the same structure. These structures are called readout panels. Similar structures are used for the cathodes, which are called drift panel. One of these drift panels is sandwiched by the two readout panels and holds therefore the two cathodes of the inner Micromegas volumes. It is called the central drift panel. The cathodes for the outer Micromegas will be on separate panels with only one side facing an active volume. They are the outer drift panels.

For the mechanical requirements of the panels several aspects have to be considered. First the supporting structures of the wheels in the ATLAS cavern should not be deformed by too much weight. Therefore the panels have to be lightweight. Second the deformation of one module in itself should be minimized. Therefore the panels have to be stiff. These two requirements can be met by a honeycomb sandwich structure. To achieve the stiffness honeycomb is glued between anode and the cathode-sheets.

These sheets are produced in industry as Printed Circuit Boards (PCB). Due to the technical limitations in this industry the PCBs for the electrodes are limited in size [ATLAS Collaboration, 2013, p.50]. Perpendicular to the readout strips, in precision-direction, the limitation is about 600 mm. Along the copper readout strips the size is not limited in the range needed for the NSW Micromegas of about 2 m. Due to the restriction in precision-direction the electrodes are segmented and built by aligning three or five PCBs next to each other. For the SM2 Micromegas three PCBs, with 1024 strips each, are used for one anode (see figure 3.2a).

For the panel production the main quality criteria are planarity and alignment. The planarity is needed to ensure the homogeneity of detector properties over the whole active area. Variations in planarity not only lead to minor deviations in the drift-gap and therefore in the drift-time-measurements. Also these deviations would lead to variations of the amplification-gap and by this to different a gain over the active area. The alignment criteria is of huge importance for the track reconstruction of the muons in the ATLAS experiment. Therefore a good alignment during the production of the anodes is critical. A full set of quality criteria, with in detail specifications, can be found in [Bini et al., 2014].

The modules have a trapezoidal shape in order to form the wheels out of wedges (see figure 1.3). The strips are oriented parallel to the parallel sides of the trapezoid. This enables the position-reconstruction along the height of the trapezoid or in radial direction of the wheel. The segmentations of the anode due to the PCB size-limitation also has to be in this direction (see figure 3.2a). A slight overpressure is created by the gas-flow during operation. To avoid a blow up of the outer panels due to this, six interconnections are used. They are distributed over the active area to minimize the deformation following ANSYS simulations [ANSYS, Inc., 2013]. In the following a naming-convention for the four active layers is used, as seen in table 3.1. This convention is given not only for the finished detector-module, but is also used during assembly of the individual parts.

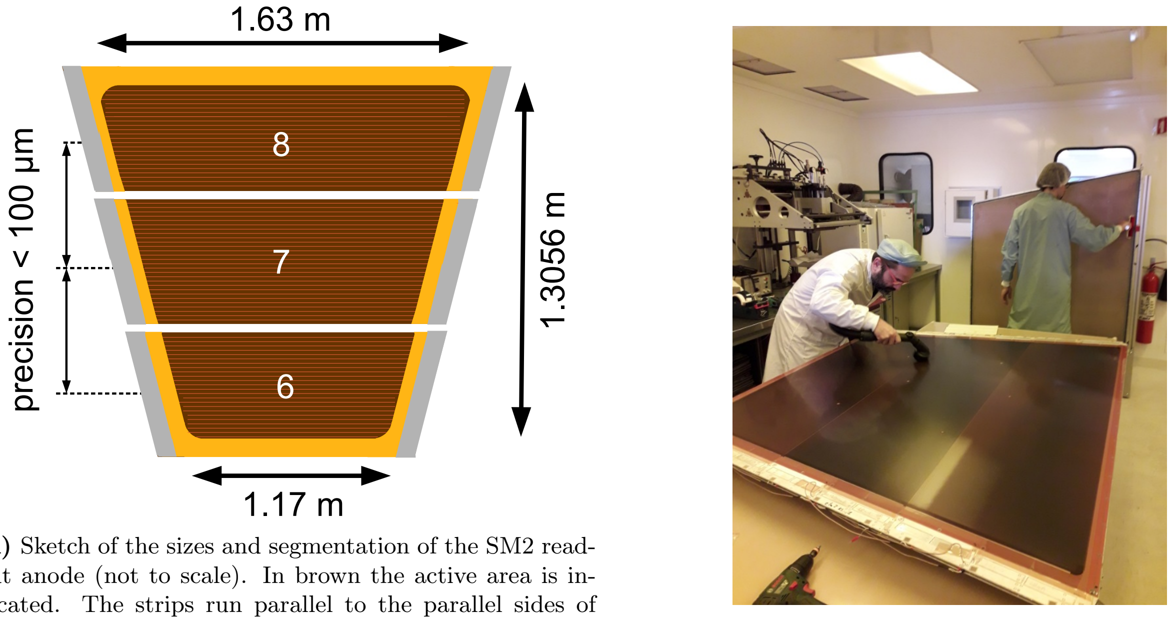

(a) Sketch of the sizes and segmentation of the SM2 readout anode (not to scale). In brown the active area is indicated. The strips run parallel to the parallel sides of the trapezoid. The inactive border region is indicated in bright orange. The connection to the electronics and cooling is achieved within the gray area. The alignment of the readout-PCB should be better than 100 µm.

(b) Readout anode panel (front) and drift panel with micromesh and cathode (back) during assembly. To prevent dirt and dust in the amplification-region, which would cause discharges and sparks, good cleaning is necessary.

Figure 3.2.: The Micromegas for the NSW have a trapezoidal shape. The readout anode is segmented into three adjacent Printed Circuit Boards (PCB). All electrode structures next to the amplification (anode, mesh) have to be inspected and cleaned very carefully.

A different naming-scheme is used at CERN. The stereo and the eta-layers are built respectively on the same structures as will be described in the next chapter 3.2. For the investigation of the layer-properties the order during the construction is given as gluing side. The last column concerns the arrangement of the module in the Cosmic Ray Facility (CRF).

Munich	CERN	gluing side	CRF arrangement
stereo-out	L4	1	top
stereo-in	L3	2	
eta-in	L2	1	
eta-out	L1	2	bottom

Table 3.1.: Naming convention for the four active layer of a SM2 Micromegas module, see figures 1.3b and 3.1a.

As the active area is partitioned into three readout-PCBs these segments will be called small board (6), central board (7) and large board (8). The numbering corresponds to the fact that the module will build a wedge in combination with the SM1 module. The readout-PCBs of this module are numbered 1 to 5 due to its five-fold segmentation (see figure 1.3b).

3.2. Panel Construction

The panels for the electrode planes are built in a two step gluing process [Lösel and Müller, 2015] , [Müller, 2017]. The PCBs which are on the surfaces of the panels hold the electrodes. They sandwich the aliminium honeycomb and additional aluminium bars for stiffness and cooling. Each PCB layer will be glued separately to the honeycomb, therefore two steps are needed.

Three main tools are required during gluing to ensure the two major quality criteria for the panels. A granite table with a planarity better 6 µm is used to transfer the intended flatness. This table is equipped with holes connected to a vacuum pump to enable vacuum suction on the surface.

A similar flat and also with holes for suction equipped structure called stiffback will be used for the flatness of the other side. This stiffback is light and can also be connected to a vacuum pump for suction on the flat surface. The active areas of the PCBs will face these structures to mirror their flatness after curing of the glue.

The third tool, a precision aluminium frame, is dedicated to the alignment. Two rings are glued on the back of each board, before the PCBs are placed on the granite. The rings are glued opposite to specific alignment marker via a dedicated positioning process. The two alignment marker are opposite to each other at the tapered borders of the PCB (see figure 3.3a). They were produced during the same step as the copper readout strips at

the position of the central strip of the readout board. Therefore they enable the alignment of the center of the readout PCB.
To align the rings of the PCBs with respect to each other and absolutely on the table the aliminium frame is used (see figure 3.3b). It has holes at the nominal positions of the alignment markers. The PCBs are placed on the table facing the granite with the active area. The frame is placed on top of the PCBs movable via Teflon stands on the granite outside of the PCB area. The holes and the rings are then coarsely aligned. By threading pins through the holes to grab the rings on the PCBs underneath the position of the PCBs is fixed by the frame. The frame can then be aligned via distance pieces to dedicated aluminium cylinders glued on the table. Therefore the PCBs are at a very precise reproducible position on the table.

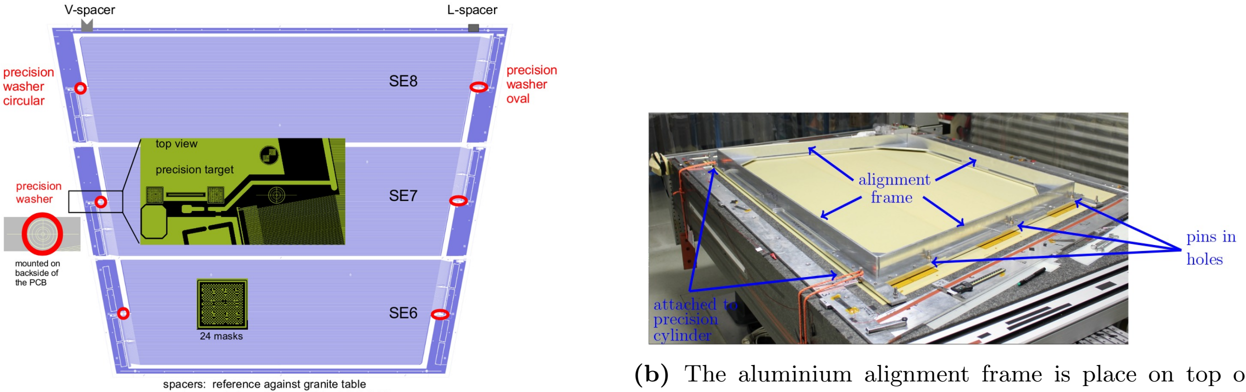

(a) Active area of a SM2 Micromegas layer. Indicated are the positions of markers and masks for alignment. Rings are glued for alignment, beneath six markers, indicated in red. Using the V-shaped and flat distance pieces the active area can be aligned absolutely with respect to reference pins.

(b) The aluminium alignment frame is place on top of the three PCBs. Pins, thread through holes in the frame, grab rings glued on the PCBs. Therefore the position of the PCBs is defined with respect to the frame. Cylinders, which are permanently fixated on the table, enable a repetitive alignment of the frame on the table. Therefore the position of the PCBs on the table can be aligned with high accuracy.

Figure 3.3.: Dedicated alignment procedures are required due to the threefold segmentation of the SM2 Micromegas active area. Taken from [Hertenberger, 2016].

At this position they are temporarily glued via tape to the table. Kapton tape is used to seal the common border between the PCBs. By engaging the vacuum-pump connected to the table the PCBs are finally fixated on the table and the frame can be removed. Similar distance pieces as at the alignment frame for positioning on the table are glued on the PCBs. This enables during the second gluing step, the alignment of this side to the pins on the table. Glue is distributed on the surface and the honeycomb and the bars are placed within. To ensure the right height the stiffback is placed on the dry side of the honeycomb and the bars on top. The stiffback is held at correct distance from the granite surface by metal pieces at the borders outside of the panel. The flat surface of the stiffback guarantees that the honeycomb is pressed well into the glue that it is not sticking out of the envelope defining the gluing height. The glue has to cure one night.
On the next day the half-panel is removed from the table. The second side is aligned with the frame the same way as the first side. The first half panel is sucked to the stiffback with the active area. Again glue is distributed on the non-active surface of the PCBs on the granite, after sealing, vacuum suction and removal of the frame. The stiffback with the sucked half-panel is placed preliminary aligned above the glue. The distance is assured by screws with Teflon stands.
The half-panel is aligned with the distance pieces to the cylinders on the table by moving the stiffback. By lowering the screws at the stiffback the half panel is placed into the glue on the second side. The thickness is maintained by distance pieces and the gravitational sag is compensated. The bare panel is finished for further processing after curing of the glue over night.

3.3. Module Assembly

Before the final closure of a Micromegas quadruplet the panels have to be drilled. Holes for assembly the panels are needed, as well as holes for grounding and the readout electronic. The drift panels get additionally equipped with frames on which the mesh is glued in another step. The height of these frames define the drift-region between mesh and cathode of 5 mm. After the mesh is glued the cathode is no longer directly accessible. Therefore the high voltage connection and cleanness of the cathode surface has to be ensured before. In order to remove remnants from the production the anode and drift panels with the mesh are cleaned wet some days before assembly. This is done in several steps.
First tap-water and an industrial soap is used to remove oils and lipids. This is applied with brushes on the active surfaces and the mesh for several minutes. Then a low pressure tap-water-spurt is used to remove the soap. The last step of wet cleaning is the treatment with a high pressure deionized water-jet. Afterwards the panels are dried and stored in a clean and heated room at about 40 °C.

Directly before the closure a dry cleaning is performed. This is done first with a vacuum cleaner on the anode and the mesh. During this step the brushes on the nozzle of the vacuum cleaner should remove remnants around the pillar. Dust is removed from the anode and the mesh using cleaning-hand-rollers.

The assembly is performed vertically. During the closing the alignment between the panels is achieved via the distance pieces. The panels slide with these distance pieces on rails. Therefore one layer can be closed by sliding the two corresponding panels, one readout and one drift panel, together. This is done successively for all layers. After all panels are moved together fifty screws are used to close the module at the borders and to press the gas-tightening O-ring. Across the active area the six interconnections are screwed in at last.

“Remember: Your focus determines your reality.” - Qui-Gon Jinn

- 1999 , *Star Wars: Episode I - The Phantom Menace*

4. Setup for Module Validation

In order to ensure that a module is fully operational it has to show that it can reconstruct muons over its whole area. Therefore measurements have to be performed with equipped readout electronics, as well as applied high voltage and flushing gas. These measurements can either be performed in a testbeam or with cosmic muons. In the following these two approaches are described, but the focus is placed on the cosmic-measurements. The reason for this is that for series calibration the huge effort for a testbeam is not feasible. Also only the part of the module which can be covered by the beam can be tested at once. The beam size is typically about $10\,\mathrm{cm} \times 10\,\mathrm{cm}$ for muon beams due to the reference detector system. Therefore a lot of measurements would be necessary for a $2\,\mathrm{m}^2$ sized module. Measurements with cosmic rays can be performed over a period of several days and cover the whole area at once. To classify the cosmic results, the first SM2 prototype module was tested using high energy muons and pions as well.

4.1. Testbeam Setup

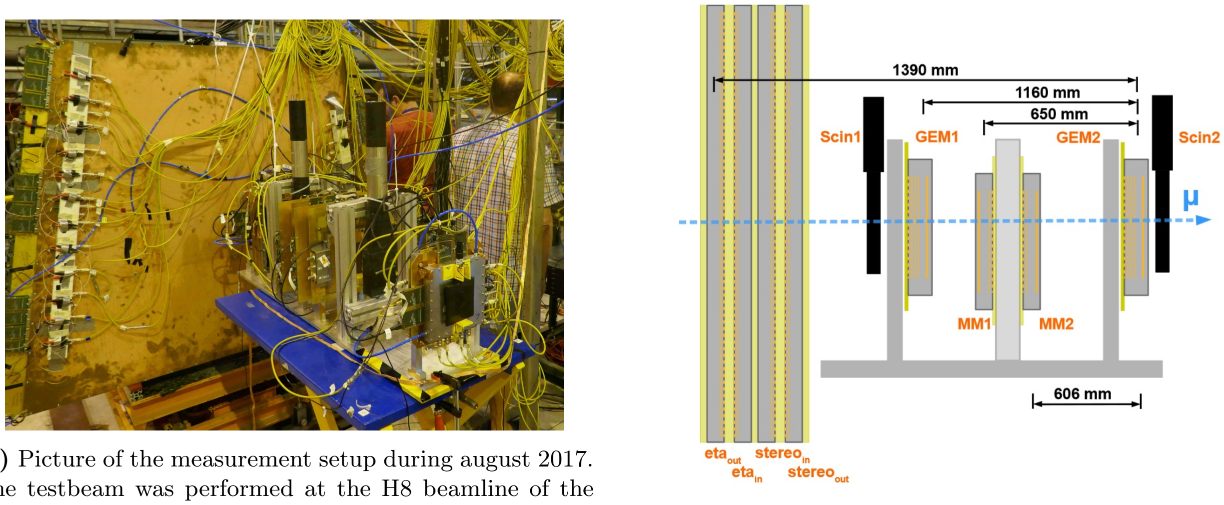

(a) Picture of the measurement setup during august 2017. The testbeam was performed at the H8 beamline of the SPS at CERN. The large copper area is the outer surface of the SM2 prototype, named Module Zero. On the blue table the reference tracking telescope is situated. Also the trigger scintillators are visible. The green APV25 frontend ASICs can be seen attached on the left side of the module. Yellow cables are for the high voltage supply, black for the readout of the electronics.

(b) Sketch of the measurement setup during a testbeam. Behind the Micromegas quadruplet a reference tracking telescope of several micro pattern gaseous detectors with two dimensional readout is placed. Also the trigger scintillators are shown. The blue muon track goes through all detectors and enables the comparison of the performance of the module with the reference.

Figure 4.1.: Setup of the H8 testbeam during august 2017 shown in a photograph and as sketch. Taken from [Flierl, 2018].

During the testbeam the module was placed in the beam of the H8 beamline of the Super Proton Synchrotron (SPS). A reference tracker system was situated after the module (see figure 4.1b). The anode planes of the module and the reference detectors are perpendicular to the beam axis. The comparison is made by extrapolating the reconstructed track in the reference system to the module. With this the difference of the position estimation by the two systems, the residual, can be calculated. The reference was set up with small micro-pattern-gaseous-detectors of known performance. In august 2017 this setup was used for the investigation of the first SM2 prototype, called module zero (see 4.1a), using 120 GeV pion and muon beams. Four two-dimensional resistive strip bulk Micromegas and two two-dimensional GEM detectors were used as reference tracker. The trigger for the readout is acquired by two plastic scintillators at both ends of the telescope. This enabled the study of about $9\,\mathrm{cm} \times 9\,\mathrm{cm}$ of the active area within a single run. For the investigation of perpendicular and inclined incident the module was tilted with respect to beam and reference chambers. Measurements were performed at 0°, 20° and 30°.

4.2. Cosmic Ray Facility

The measurements for the calibration of the SM2 modules are performed in the Cosmic Ray Facility (CRF) in Garching near Munich. The main work of this thesis is based on the usage of this facility as reference for the characterization of the modules. The reference system itself was prepared and built already during the commissioning of the original muon track detectors for ATLAS [Biebel et al., 2003], [Kortner, 2002], [Rauscher, 2005]. An important aspect of this work includes that the measurements for one module should not take too much time. This means in about one week a Micromegas module should be installed, measured and removed from the facility. During the measurement-period an amplification scan has to be performed to calculate the turn on curve for each high voltage sector. Also the measurements should acquire enough statistics to enable the reconstruction of the board and layer alignment [Lösel, 2017].

4.2.1. Reference Detector System

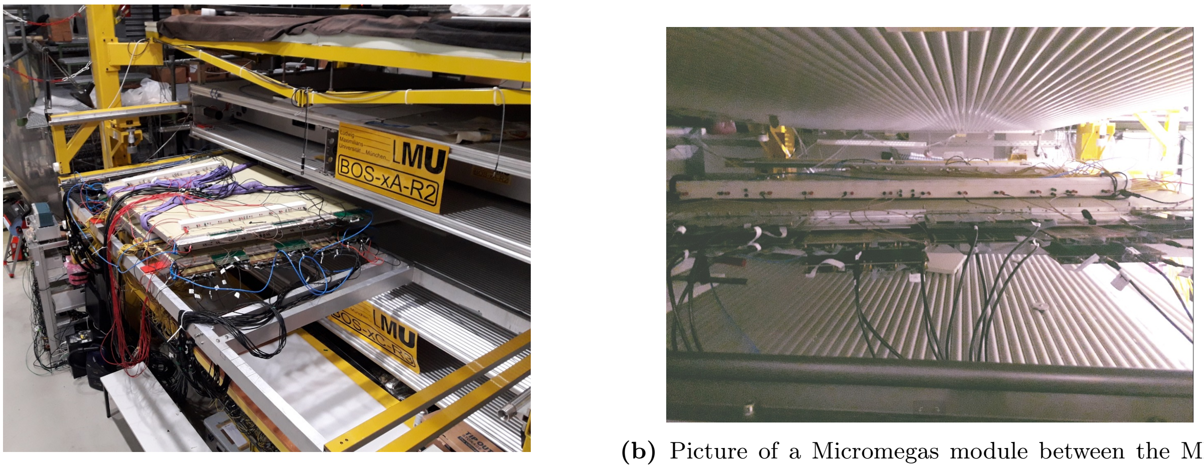

(a) Picture of the Cosmic Ray Facility in Garching near Munich. A Micromegas module is prepared for data-taking with black HDMI-cables and red high-voltage cables. The modules are placed on a support structure, which can be moved between the MDT chambers.

(b) Picture of a Micromegas module between the MDT chambers. The strips of the module are oriented parallel to the tubes of the reference chambers. On top of the module high voltage distribution boxes are situated. The readout electronics are attached at both tapered sides of the module.

Figure 4.2.: Pictures of the CRF setup for the characterization measurements of Micromegas modules.

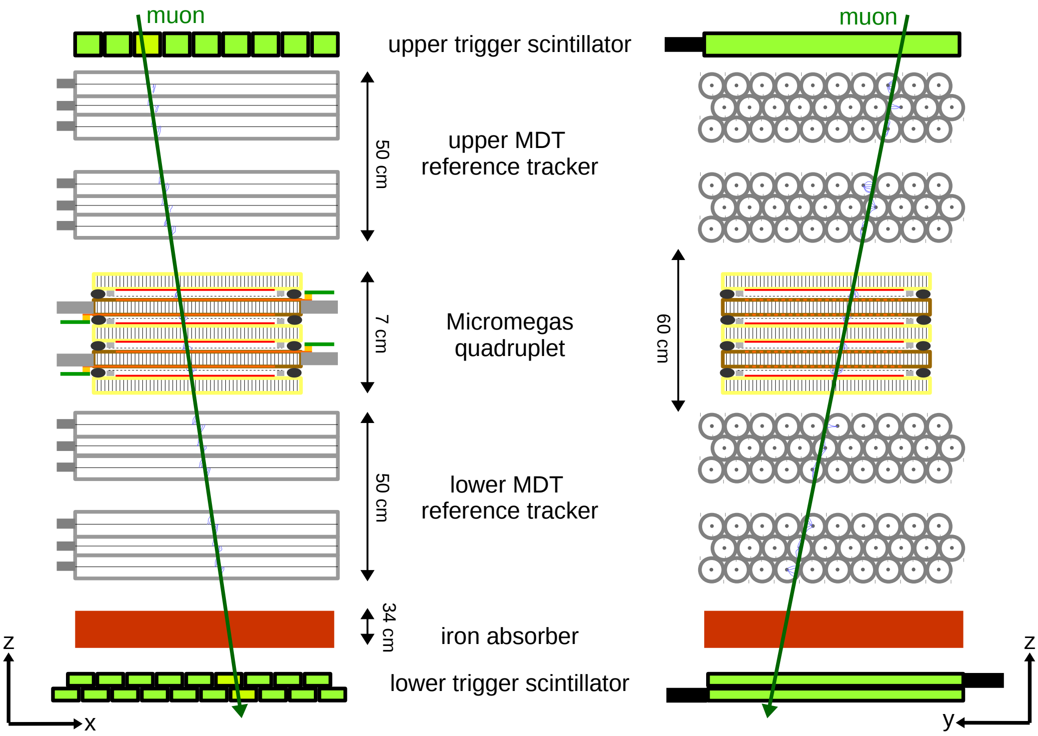

Figure 4.3.: Sketch of the measurement setup for the CRF. The x-y-plane is parallel to the surface. The non-precision coordinate x is positive from south to north. The precision coordinate y is positive from east to west. The z axis is directed upwards along the zenith. The MDT reference trackers (grey bars and circles) sandwich the Micromegas quadruplet (mainly yellow and red) and reconstruct the track in the y-z plane. For triggering segmented scintillator layers (green) are on top and on the bottom of the setup. This segmentation enables a coarse resolution in the x direction. For a hardware cut of the muon energy below $E_\mu = 600\,\mathrm{MeV}$ an iron absorber (brown) of 34 cm is above the lower hodoscope. Drawing not to scale.

The Cosmic Ray Facility consists of two Monitored Drift Tube (MDT) chambers for precision tracking in the y-z-plane (see picture and sketches in figure 4.2 and 4.3). The wires of the chambers are oriented parallel to and reconstruct the track perpendicular to the y-z-plane. The z-axis is pointing along the zenith. Each reference chamber consists of two multilayers with three layers of tubes. The chambers are placed one above the other with about 60 cm space in between. This enables the interpolation of the tracks into the test detector. For triggering three layers of 2 m long plastic scintillator are used in coincidence. One layer is above the upper MDT chamber and the others below the lower chamber. These layers consist of 10 cm broad scintillators connected to photomultiplier tubes. The orientation of the long axis of the scintillators is perpendicular to the wires of the MDT. A coarse position information along the wires of the MDT can be achieved using the knowledge which scintillators are hit. Therefore these scintillator layers act as hodoscopes and a rough track in the x-z-plane can be reconstructed. To reject muons with low energy a 34 cm thick iron absorber is installed between the lower MDT and the lower scintillator layer. These low energy muons would degrade the resolution of the reconstruction by multiple scattering. This hardware cut of the muon energy is estimated to be around 600 MeV [Rauscher, 2005].

4.2.2. Systematics

In order to be able to reconstruct geometrical deviations of the Micromegas modules the reference system of the CRF has to be understood. The tracks reconstructed by the two MDT chambers as well as coarsely by the scintillator-hodoscopes will be used to investigate the modules. Therefore the systematic uncertainties of this system will be studied in the following. For this the measured track properties have to be evaluated. A track is defined by its intersection of the central plane between the MDT and its slope in x and y direction. The z coordinate is for this definition just a parameter[1]. The slopes can be interpreted as the tangent of the angle between the track and the axis to the zenith projected to the specific direction. The bare distribution of the track variables can be seen in figure 4.4a and 4.4b for measurements during January and February 2019.

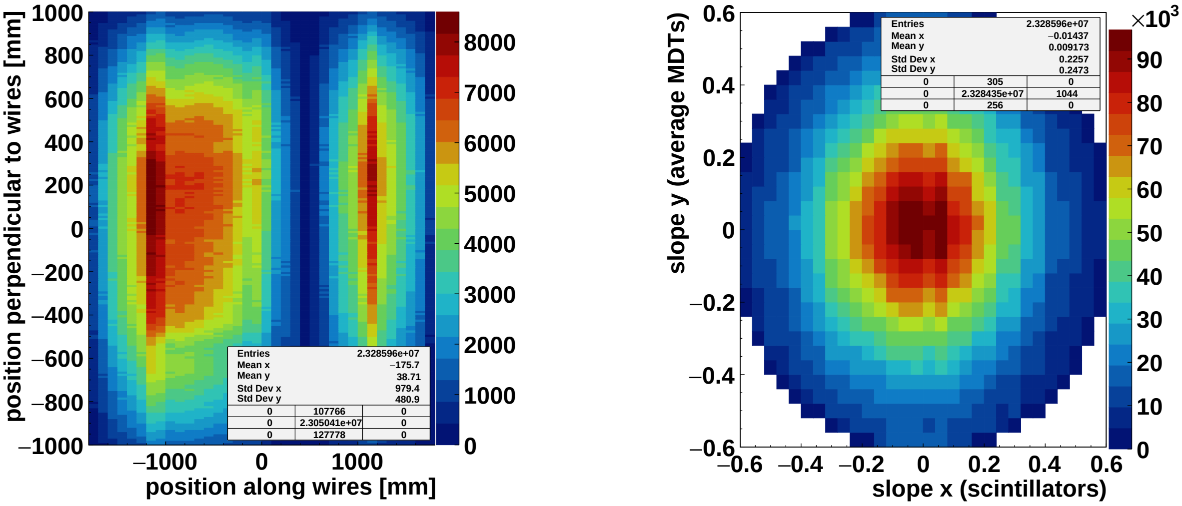

(a) Reconstructed hit distribution in the central plane between the MDTs. The inhomogeneous illumination is given due to trigger segmentation and angular acceptance.

(b) Distribution of reconstructed track slopes. Precision reconstruction is done in y direction using the MDT chambers. In x direction a 10 cm coarse track information is given by the scintillator-hodoscopes.

Figure 4.4.: Distributions of the track parameter for measurements in the CRF between 26.01.19 and 13.02.19. Tracks are defined by their intersection with the central plane between the MDT and their slopes in x and y direction. With this a track can be evaluated at a given position in z.

The inhomogeneities in 4.4a have to be explained, while noting the different scale of the axes. In y direction (perpendicular to the wires) a decreased number of entries towards the borders can be seen due to the limited angular acceptance. Along the wires, in x direction, two regions of interest are created due to a combination of the scintillators into trigger groups. Also an excess of entries between -1200 and -1000 mm in x can be seen, which is probably due to noisy photo multiplier tubes. The region of x between -1400 and 300 mm and y between -800 and 300 is chosen for testing of the Micromegas modules. The modules will be installed at this position, because the space is well accessible and yields a high illumination. None the less the effects due to the inhomogeneous hit distribution have to be taken into account. The absolute range of track slopes in figure 4.4b goes up to 0.6 for both axis, which corresponds to a maximal inclination angle of about 31°. Large angles have for this setup only very low statistics. Therefore the analysis will mostly be limited to tracks with slopes up to 0.5 or angles up to 25°.

For the precision reconstruction perpendicular to the wires, the tracks of the two MDTs are averaged. The errors of the track reconstruction done by the MDTs can be investigated using the difference between the track

---

[1] The track is described in the c-z-plane by $c = t_c + m_c \cdot z$, with $c \in \{x, y\}$.

parameters of each chamber. This is shown in figure 4.5. While the sharp and therefore good comparability of the two chambers can be seen, also effects due to mis-reconstruction have to be noted. On diagonals in figure 4.5a the track-fit for one chamber obviously fails, which introduces the linear dependence of the slope and intercept differences. Satellites in the intercept difference (see figure 4.5b) can be observed at ± 90 mm which arise for tracks with ± 30° inclination. Here the MDT track reconstruction fails, due to indistinguishable cases when the track passes on the left or the right side of the wires. The distribution of slope differences (figure 4.5c) is not as peaked as the intercept differences. This can be explained by multiple scattering of the cosmic muons, which will be discussed in the next chapter 4.2.3. The mis-reconstruction are suppressed by three orders of magnitude and are therefore no problem for the measurements.

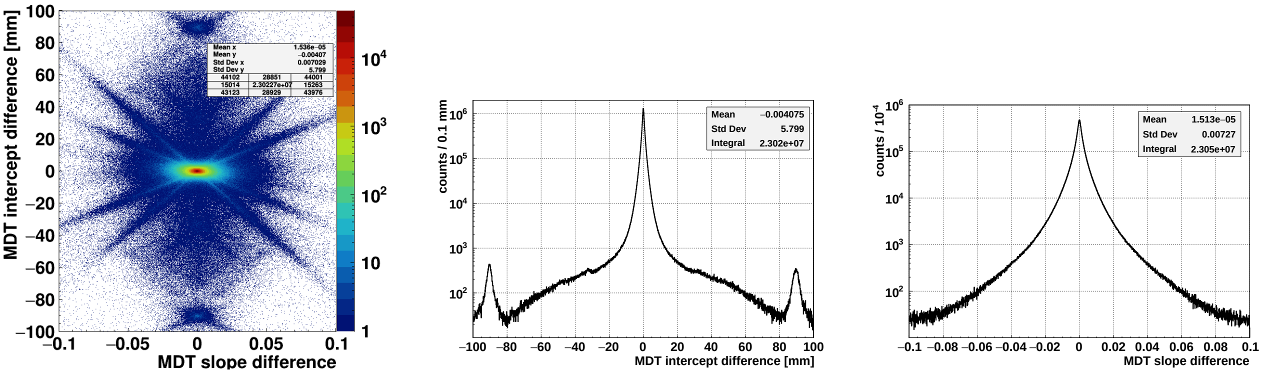

(a) MDT Intercept difference as function of the slope difference.

(b) MDT intercept difference.

(c) MDT slope difference.

Figure 4.5.: Difference of the tracks from the two MDT evaluated by their slope difference and intercept difference.

One important aspect of measurements using a tracking reference system is the ability to reconstruct geometrical deviations. Therefore the geometrical imperfections and systematics of the reference have to be known. These can be studied for the CRF using the track-difference of the MDTs as function of the position. The mean intercept-differences between the two chambers are shown in figure 4.6 as function of the position along and perpendicular to the wires. Most mean deviations stay below ±10 µm. Structures in this range are due to minor deviations between the chambers and are thus are negligible.

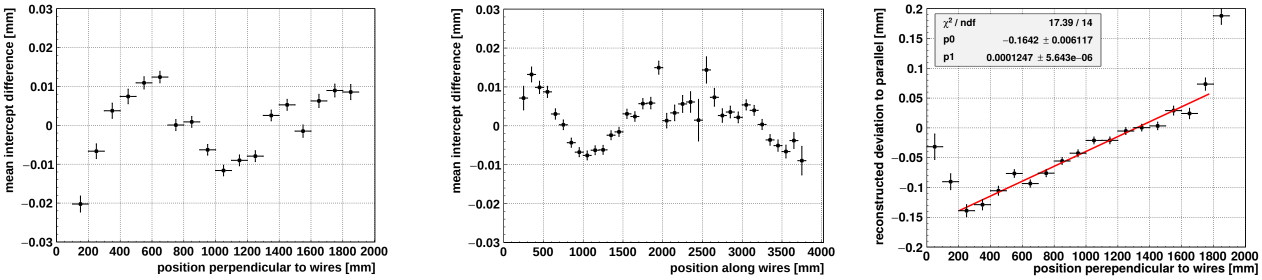

(a) Mean intercept difference perpendicular to the wires.

(b) Mean intercept difference along the wires.

(c) Reconstructed deviation of the nominal distance between the MDTs, perpendicular to the wires.

Figure 4.6.: Reconstructed differences of the two MDTs position resolved. The intercept of the tracks is in the plane between the MDT chambers. At this position the Micromegas modules are installed.

Also the vertical alignment of the two chambers can be investigated. This is done similar to the approach for detector alignment described by [Lösel, 2013]. The difference of the tracks is evaluated as function of the track-inclination. This has to be done position dependent. The slope of these distributions corresponds to the deviation of the central plane from zero between the two chambers. For the position along the wires no dependence was found and the maximum deviations were less than 50 µm. The deviations perpendicular to the wires are shown in figure 4.6c. The linear dependence suggests a rotation of one chamber with respect to the other. The slope of the fit corresponds to an angle of about $(7.2 \pm 0.6) \times 10^{-3\circ}$. The outer points not fitted are due to biased reconstructions caused by the limited angular acceptance at the edges.

For the resolution determination of the Micromegas the difference to the MDT-predictions will be used. As the MDT prediction has also a finite resolution it is important to investigate this. Here the same approach is chosen as will be described in detail for the Micromegas in chapter 7.1.1. The distribution of differences between the two MDT-track-predictions extrapolated to the central plane is investigated for different track-inclinations. These distributions are fitted with double-Gaussian-functions to determine the width using the standard deviations σ. An exemplaric fit, the σ's and the ratios of the two Gaussians are shown in figure 4.7. These distributions show that the MDT-resolution is almost independent of the track-inclination. The slight degradation to higher

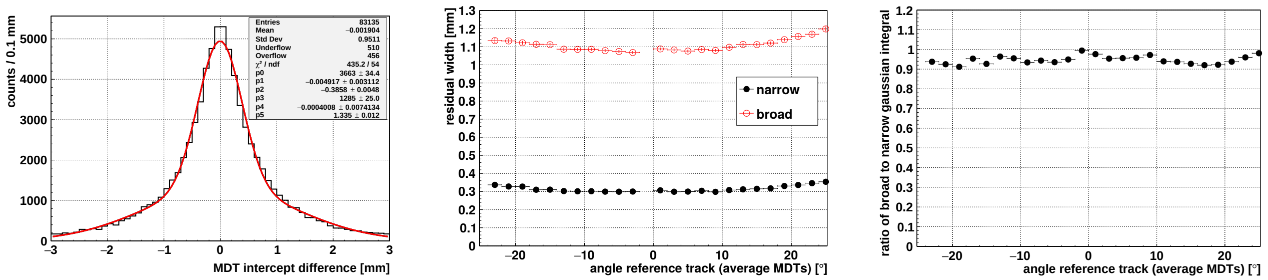

(a) Intercept difference of the two MDT tracks.

(b) Width of the two fitted Gaussians.

(c) Ratio of the two fitted Gaussians.

Figure 4.7.: The MDT intercept difference distribution can be fitted with a double Gaussian. This is as function of the average track slope. The ratio as well as the width of the distributions stays almost constant over all considered slopes.

track-slopes could be explained due to the larger amount of material which the muons have to cross. More material leads to more multiple scattering, which increases the track difference between the two chambers.

4.2.3. Muon Tomography

The effect of multiple scattering, as discussed in chapter 2.1, can be used to reconstruct the material distribution in the CRF. A first approach of this was discussed in [Lösel, 2017]. The intersection of tracks from the MDTs was investigated if their inclination differs more than 3°. Therefore measurement-periods of several months were required to accumulate enough statistics. This duration-requirement can be understood by the low fraction of events with such large slope-differences (seen in figure 4.5c). A suppression of about three orders of magnitude can be seen for events with track-slope-differences larger than 0.05. Since the measurements with the SM2 Micromegas only allowed short periods, due to ongoing exchange of the modules, a different approach is investigated.

The following evaluation is based on data collected during measurements with module seven end of January and beginning of February 2019. About 23 million events are used. First the track-differences are investigated for tracks going through the module or without passage. This can be seen in figure 4.8, for a single day measurement. In figure 4.8a the difference between the two MDT-tracks is evaluated in precision-direction (y) for various positions between the chambers (z). For figure 4.8b the width of this difference is evaluated for the distribution without and with module. For the central plane ($z = 0$), at which the module is located, the increase in width of the distribution due to the module is about 20 µm. Extrapolating the tracks from the central planes to different z-positions increases the difference between the two references. This increase is enhanced for tracks going through the module.

Hence two conclusions can be made. First, the best comparison between the MDT-chambers can be made in the central plane. This is expected due to the longer extrapolation for one of the MDT-chambers if going further away from the center. The second insight is that the resolution in this central region is not much affected by the multiple scattering. Another interesting feature of this distribution is the change of width-difference-increase around ±300 mm. This can be explained due to the position of the MDT-chambers, which are located around 300 mm to 800 mm apart from the center.

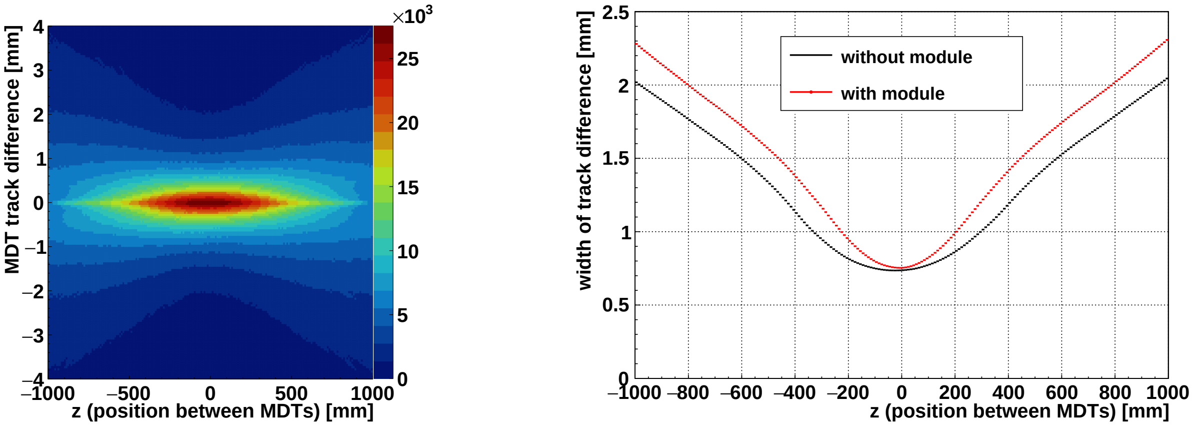

(a) Difference of the two MDT tracks evaluated over a large z-range.

(b) Width of the MDT track difference distribution as function of the z-position.

Figure 4.8.: The MDT tracks are extrapolated to reconstruct the path of the muon at various locations. To estimate the quality of this extrapolation, the difference between two tracks has to be considered. The width of the difference-distribution enables this quality-check.

Since the intersection-point-reconstruction is not much affected in the central-region the increasing track-difference has to be caused mainly by the slope-differences. Therefore the distributions of slope-differences without and with module is investigated in figure 4.9. In figure 4.9a the two distributions are overlaid after normalization. The differences are seen only very faintly. For a better distinguishability the ratio of the two distributions is shown in figure 4.9b. Here the differences become more obvious. Tracks passing through the detector have a higher contribution to slope-differences above 0.005. Hence the selection as suggested by [Lösel, 2017] can be increased by an order of magnitude.

The slight asymmetry is probably caused by the placement of the module in the CRF. The module was situated at the outer border of the measurement volume. Due to this the inclination-angles are not symmetrical. The feature of pronounced slope-differences at around ±0.019 could be a characteristic scattering-angle. More likely this is due to the starting loss of statistics for higher slope-differences.

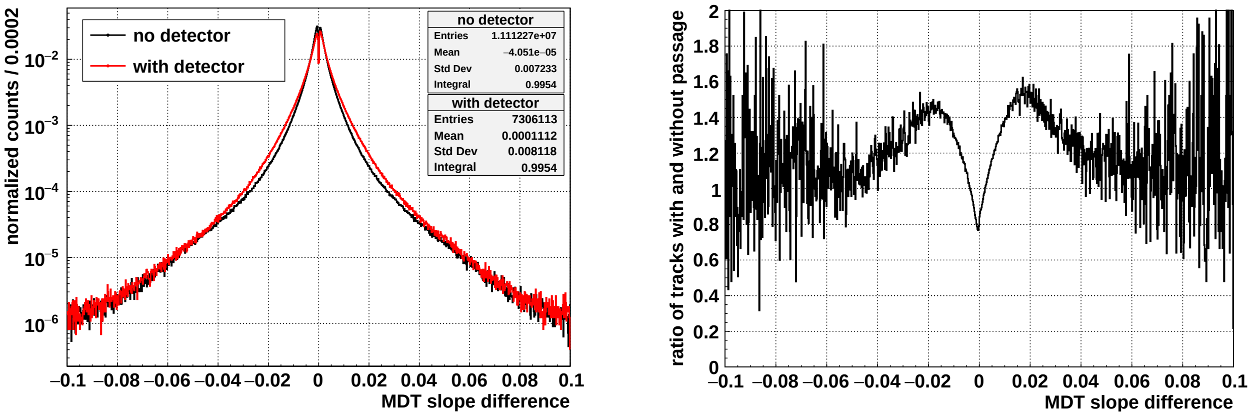

(a) Normalized distribution of differences between the slope of the two reference tracks by the MDT. Tracks without passage through the detector are shown in black. In the red distribution tracks went through the detector.

(b) Ratio of tracks as function of the slope difference for the distributions of tracks going through the detector and not going through.

Figure 4.9.: Influence of the detector material on the slope-difference of the two MDT tracks. Due to multiple scattering larger slope differences are seen for tracks with passage through the detector.

To investigate the position-reconstruction-capabilities the track-differences have to be evaluated position dependent. This is done in figure 4.10. Here the width of the two distributions is evaluated using the standard deviations. This is done for partitions of the active area with a size of 10 cm × 10 cm. For both track-parameter-distributions an increase of the width in the region of the module ($x \in [-1200\,\text{mm}, 200\,\text{mm}]$ and $y \in [-1000\,\text{mm}, 400\,\text{mm}]$) is observed. The trapezoidal-shape of the module is clearly visible due to the dense material at the edges. Also the internal bars, glued between the honeycomb-sheets, can be seen around y equals to −50 mm and −550 mm. Structures seen at y equal ±600 mm and x equal 0 mm are probably support structures of the MDT-chambers.

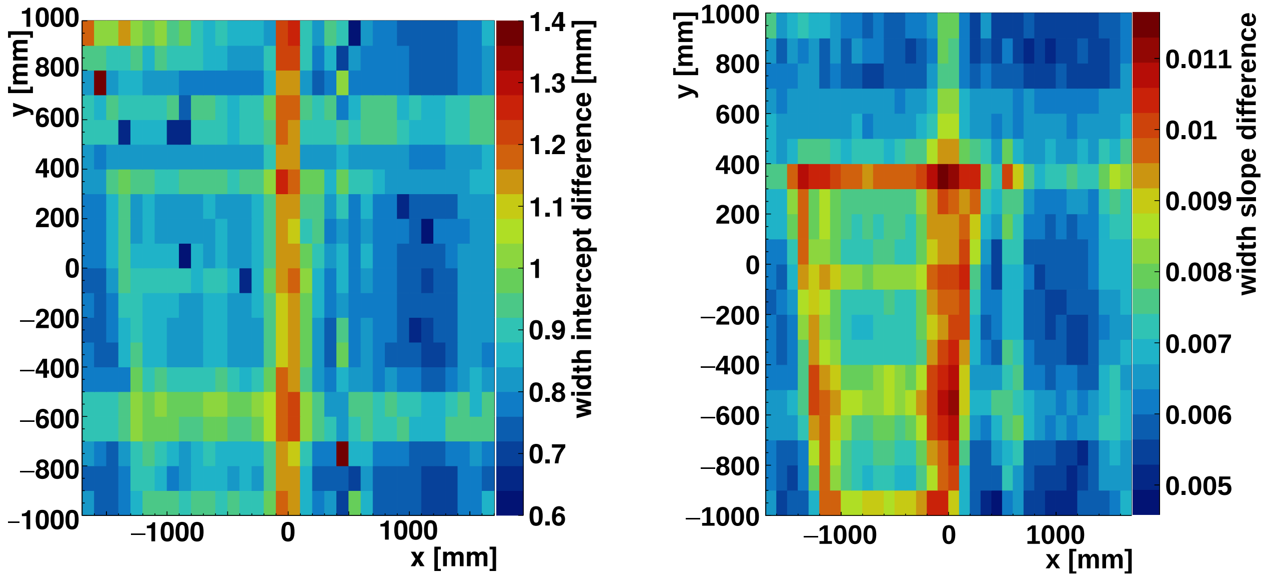

(a) Width of the distribution for the intercept differences between the MDT tracks.

(b) Width of the distribution for the slope-differences between the MDT tracks.

Figure 4.10.: The effect of multiple scattering can be seen in both track parameter distributions.

For a better resolution of these structures the approach of [Lösel, 2017] is followed to reconstruct the intersection of the two tracks given by the MDTs. This reconstruction gives for each event a point in the y-z-plane. The region of x between -1000 mm and -100 mm along the wires is chosen to reconstruct the structures of the module. The resulting distribution for all tracks without a selection for high track-slope-differences can be seen in figure 4.11a. In this distribution about eight million of the total 23 million events are reconstructed in the given range. For the other tracks the intersections are reconstructed outside of this window and are therefore not considered. The plot has a bin-width of 10 mm in both directions.

Already for this approach features of the material-distribution are reconstructed. The aluminium bars at around y equal -950 mm, -550 mm, -100 mm and 350 mm are visible. Despite this, the distribution is mainly described by a bulk around the center. Instead of selecting only large slope-differences the intersection-points can be weighted by their slope-difference. This is done for the other distributions of figure 4.11.

For figure 4.11b the investigation of the resolution of the reconstructed structures is made by comparing the width measured to width expected from the structure. The projection onto the z-axis required the width-determination via the Full-Width-Half-Maximum (FWHM) approach. Using this the width of the bars is determined to be in the order of 300 mm. In a Micromegas module five 10 mm hollow bars are assembled. Therefore the resolution in this direction is only very coarse. For the precision-direction (y) the resolution is much better and the width of the bars of about 30 mm is well reconstructable using the FWHM.

The track-intersections can also be projected onto the other two coordinate-planes seen in figures 4.11c and 4.11d. This enables the three-dimensional reconstruction of the material distribution.

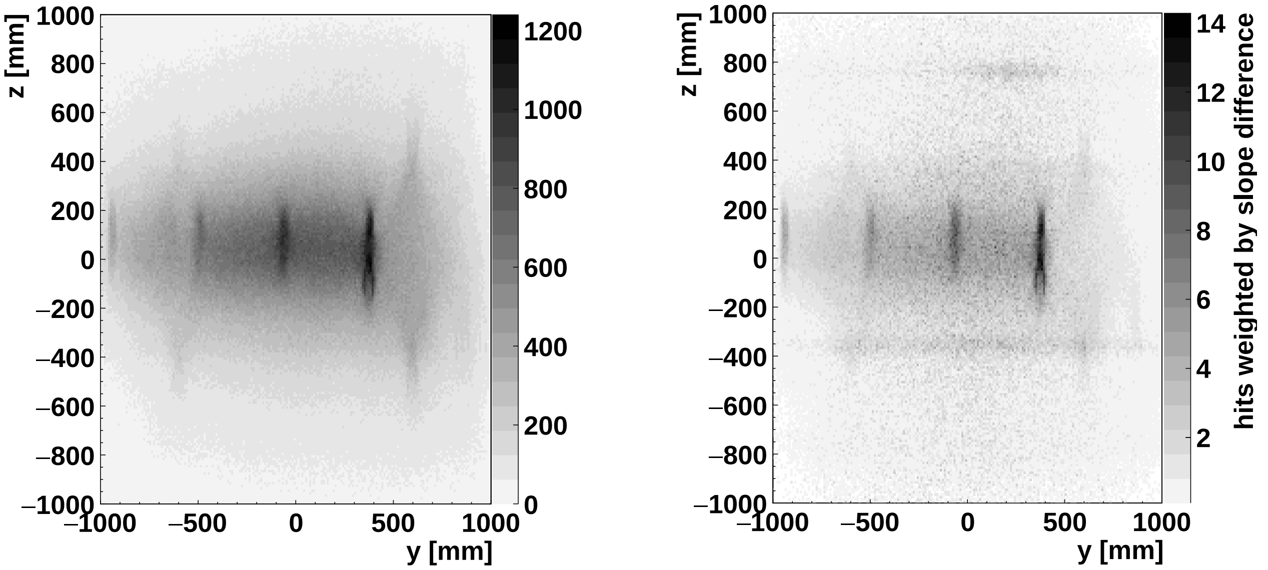

(a) Unweighted intersections in the y-z-plane.

(b) Intersections in the y-z-plane weighted by the slope-difference.

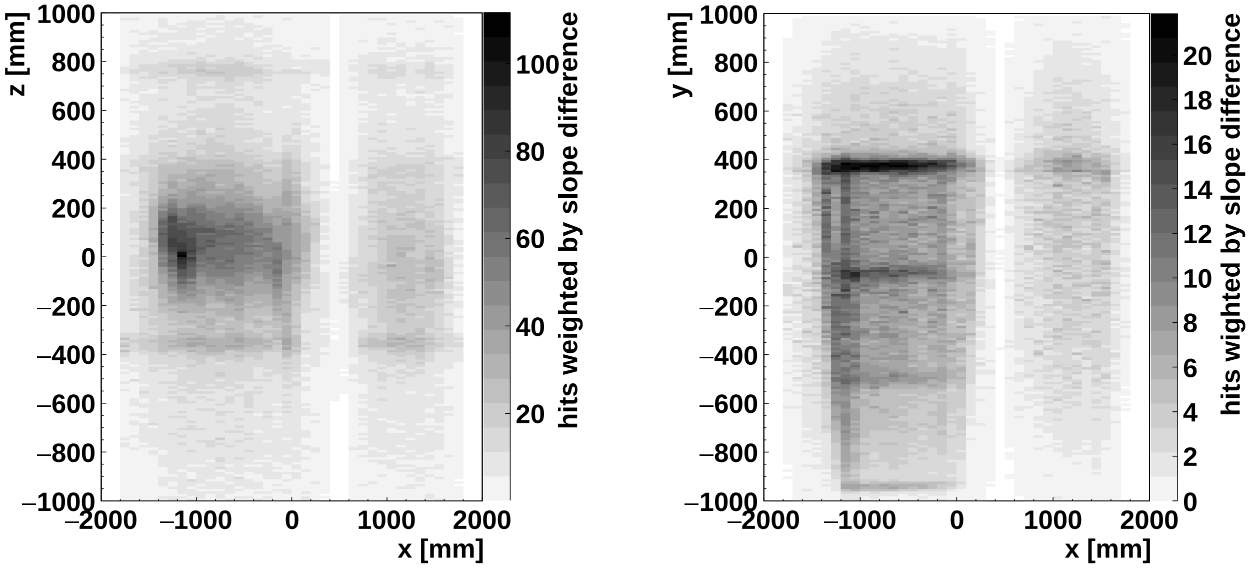

(c) Intersections in the x-z-plane weighted by the slope-difference.

(d) Intersections in the x-y-plane weighted by the slope-difference.

Figure 4.11.: Reconstructed track intersection of upper and lower MDT. The weighting of the intersection by the slope-difference increases the resolution. Different projections of the intersections enable a detailed reconstruction.

4.3. Micromegas Readout

For the reconstruction of muon tracks with the Micromegas modules the signals on the copper readout strips have to be recorded and evaluated. The following chapter describes the electronics, data acquisition system and the software for the measurements in the testbeam and the CRF.

4.3.1. Signal Digitization with APV25 Frontend Electronics

For the sTGC and the Micromegas of the NSW specific readout electronics is developed [De Geronimo et al., 2012]. Due to the ongoing development and the production of the technology no measurements with the final electronics were possible during the course of this thesis. Therefore an alternative electronic setup was used. The signals of the copper readout strips are recorded with so called APV25 [Jones, 2001] front-end electronics. The APV25[2] is an Application Specific Integrated Circuit (ASIC). It consists of 128 channels connected individually to charge-sensitive preamplifiers, shapers and a analogue pipeline memory. The signal of each channel can be inverted and sampled with a rate of 40 MHz. For the measurements a hybrid board is used, which houses the chip connected to a Panasonic and an HDMI connector (see figure 4.12a).

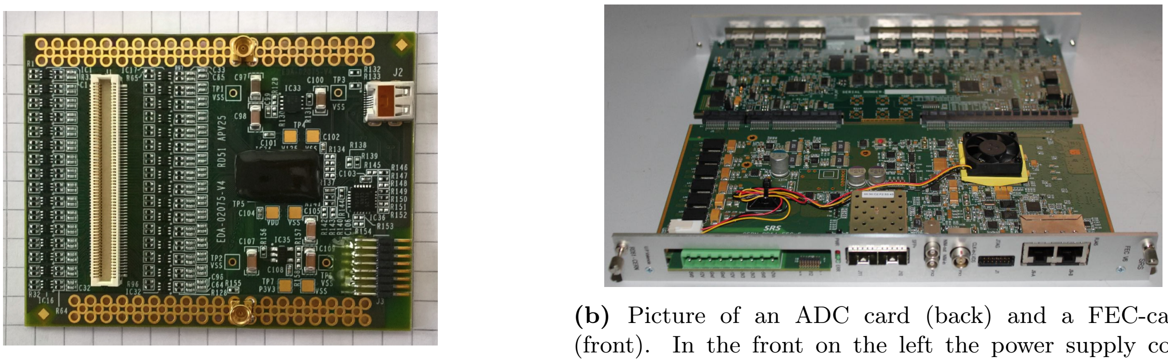

(a) Picture of an APV25 hybrid board. The actual chip is hidden under the black protection cover. Also visible is the Panasonic connector on the left and the HDMI connector on the upper right. The lower right connector is for usage as master-slave pair with a ribbon cable.

(b) Picture of an ADC card (back) and a FEC-card (front). In the front on the left the power supply connector in light green can be seen. At the center are special connectors for the ethernet communication. The two Lemo connections for trigger in- and output can be seen right to the center. At the back end the eight HDMI connectors are visible.

Figure 4.12.: Picture of parts for the scalable readout electronics [Martoiu et al., 2013].

Each channel is connected via adapter cards over the Panasonic connector to one copper strip of the module. Therefore each strip-signal can be evaluated individually. To record these sampled signals the APV is connected via HDMI-cables to an Analog-to-Digital-Converter card (ADC). This card is connected to a so called Front End Concentrator card (FEC, see figure 4.12b). The FEC collects the signals and enables a further processing, as well as data-transmission to the data-acquisition (DAQ) computer. The combination of these two cards is in the following referred to as FEC. Over the HDMI-connection a common clock is distributed to all APVs of one FEC. A FEC has eight HDMI connections for APV input.

Additionally APVs can be connected via ribbon cables as master-slave pairs in order to share the HDMI connection. Therefore one FEC-card can readout sixteen APVs and with this 2048 strips individually. The FEC-card sends the data via ethernet to a PC if a trigger signal is received in a specific input channel. In addition, from the FEC a signal is sent via a similar output channel which enables the correction of the jitter. The jitter is the difference in time of the rise of the 40 MHz-clock and the arrival of a trigger-signal. This difference is random but should lie equally distributed in a 25 ns broad window due to the clock-rate.

For the readout of a full SM2 quadruplet 96 APVs and 6 FEC-cards are needed. A systematic connection of this readout system to a module can be achieved using four APVs of one FEC for one sixth of each layer. These four APVs per layer are connected on the same adapter-board to the detector (see figure 4.13a). The adapter-board itself is in touch with the copper readout strips via elastomeric connectors touching the ends of the strips. On the adapter-board the elastomeric connector touches a mirrored set of strip-ends which are rooted to the channels of the Panasonic connector.

The measurements are performed using 24 time-samples of the 40 MHz-clock for each channel. To reduce the data-rate zero-suppression is essential. This means to discard signals which are not associated with a muon-passage. The discrimination between hit and no-hit of a channel is achieved by comparing the signals of all channels of one APV. For each channel the standard deviation of the 24 measured charges is calculated. With these the mean standard deviation across the APV is determined. A channel is considered as hit if its standard deviation is twice as high as the mean. This approach is chosen to maximize the selection of useful hits, while keeping the contribution due to noise low enough. Noise in this sense is considered as signal, which is identified as hit, while no actual muon-passage is the cause for the signal-generation. So this can be large baseline fluctuations of specific channels or signals generated by electronic-signal-coupling from the environment. For events which

---

[2] In the following the chip is referred to as APV.

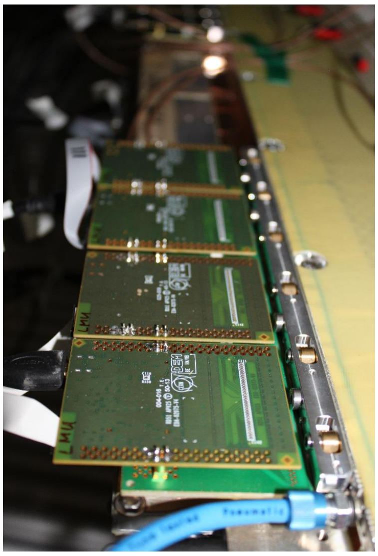

(a) APV on hybrid boards in master-slave pair-configuration connected to a module via an adapter card.

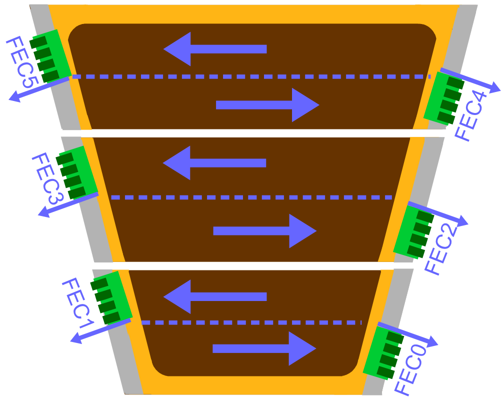

(b) Sketch of the mapping for the SM2 readout. The segmentation due to the readout with six Front End Concentrator cards (FECs) is indicated in blue. Also the direction in which the readout is placed with respect to the strips is indicated as blue arrows. In dark green the APV25 hybrids are indicated sitting on the adapter-boards seen in light green.

Figure 4.13.: One layer of a SM2 Micromegas module is readout by 24 APV connected to six FEC-cards.

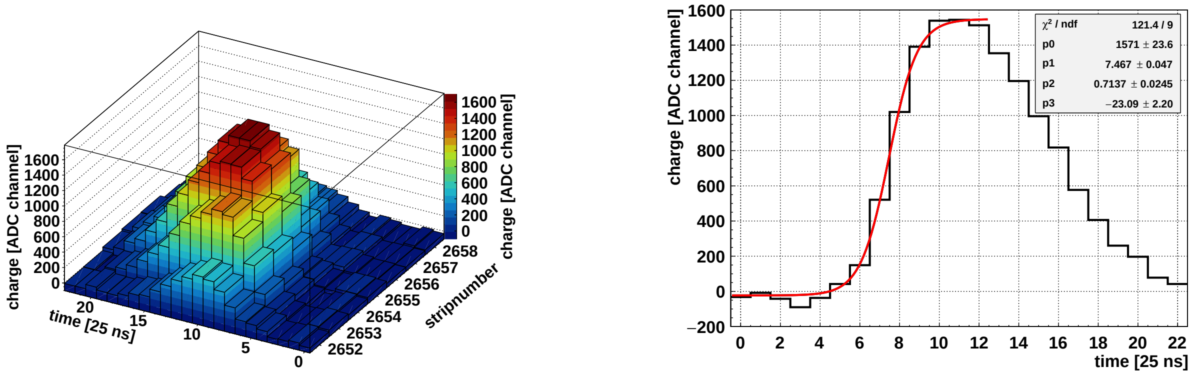

(a) Event display of a muon track. For each strip the signal is sampled in 25 ns steps, 24 times. The sampled charge is indicated in height and color on the z axis. The typical shape of the signal can be seen on each of the channels with the highest values in the center (red).

(b) Inverse Fermi fit of a single-strip-signal. After minor variations of the base-line a sharp rise can be seen. In the last timebins the signal is slowly declining. The fit is performed to extract a better time-resolution than the 25 ns sampling.

Figure 4.14.: Signal from the APV25 readout electronics.

are connected to the energy deposition of a particle in the detector typical signals can be seen in figure 4.14a. Commonly several neighboring strips measure a charge-evolution over several time-bins. As seen in figure 4.14b for a single channel, this means a sharp rise of charges above the baseline. At a certain time and charge the signal saturates and falls off much slower.

Using these signals the charge and the time-information of the MIP energy-deposition has to be extracted. The signals should correspond to the ion-drift caused by the electron avalanches created after the initial energy-deposition [Klitzner, 2019]. Therefore the height of these signals is associated to the number of charges created during the amplification. For this association the maximum measured charge of the 24 time-bins is used.

The initial energy-depositions occur across the drift-gap. The drift-velocity of the electrons causes a different timing of signals which are produced at different positions in the drift-gap. To reconstruct this timing the signals are evaluated with an inverse-Fermi-function given by

$$q(t) = \frac{p_0}{1 + \exp\left(\frac{p_1 - t}{p_2}\right)} + p_3 \tag{4.1}$$

The function describes the rising edge of the signal and is used to determine the timing using parameters p_1 and p_2. A summary of the fit-parameter and their interpretation can be found in table 4.1. In chapter 7.2.1 a discussion about the time-evaluation of the signal with this function will be given. Here it should be noted that the slope of the rising edge, which is parameterized by p_2, can be used to distinguish between signal and noise. As noise leads to fluctuations of the charge around the baseline, the fit of noise receives small values of p_2. The discrimination can be achieved by discarding signals with fit-parameters smaller than 0.1, which corresponds to 2.5 ns [Lösel, 2013].

parameter number	variable	unit	typical range	description
0	q_{max}	ADC channel	100 - 1600	maximum of signal-height
1	t_0	25 ns	5 - 15	inflection of Fermi fit ⇒ 50% of signal-height
2	t_{rise}	25 ns	0.1 - 2	proportional to rise time of signal
3	q_0	ADC channel	-100 - 100	charge baseline

Table 4.1.: Overview of the single-strip-signal fit-parameter. The observed charge $q(t)$ is described with the time-parameter t given in 25 ns, defined by the 40 MHz-clock.

4.3.2. Trigger and Datastream Merging

The muon-passage creates a signal in scintillators of the upper and the lower hodoscopes. These signals are discriminated and sent to a coincidence-unit. The trigger coming from the coincidence of the scintillators is distributed equally to each FEC-card (see figure 4.15a). Upon trigger they send the data from the APVs via the User Data Protocol (UDP) to the PC.

During the same time a trigger is sent to the PC. While the PC is receiving data it blocks further trigger with a veto-signal send to the coincidence. Besides sending the data to the PC the FECs also send a signal to a Time to Digital Converter (TDC). This TDC records the time difference between initial trigger and FEC-signal. As the FEC-signal is synchronous to the internal clock of the FEC, the measured time of the TDC can be used to correct the jitter (see figure 4.15c). The UDP-data sent to the PC by the FECs is combined into a single event-package. For this a program waits until all FECs have sent successfully the data and stops afterwards the veto-signal. The event-package is stored in a FIFO-file.

From this a script distributes the event-packages to multiple processes of the zero-suppression-software. This parallelization is required to enable a higher readout-rate. The zero-suppression-software stores the data, after processing, in root-tree format [Brun and Rademakers, 1997]. For each instance of this software an individual file is created. During the measurements of the SM2 modules six instances of this program are used.

A description of the MDT-data-taking can be found in [Biebel et al., 2003] and [Rauscher, 2005]. The setup enabled a readout-rate of 100 Hz for the full Micromegas modules with 12288 channels. During tests with three additional FEC-cards connected to a second Micromegas detector, a doublet[3], a readout-rate of 70 Hz is achieved for 18432 channels.

The data of the two systems (MDT and Micromegas) have to be combined after the measurement. This is achieved using an event-id and the unixtime-stamp. For this, the six root-files from the zero-suppression-software have to be combined. Here, the important aspect is the correct ordering of the events for the further combination with the MDT-data. The data of the MDTs have to be evaluated before combination, after this the format is also a root-tree. The raw TDC-data are stored in the same files as the MDT-data, from which the times are extracted and stored also as root-tree. These three root-tree-files, from the Micromegas, the MDT and the TDC are combined in a final step to files with 5000 events.

The combination of the three files reduces the amount of usable events by about a half. This is very unpleasant and is caused probably by events which receive problematic event-ids. Therefore a typical half-day-measurement with about four million trigger produces about 400 combined files. The results in the following will be based mainly on the evaluation of these files. A similar data-stream-setup was used for the Micromegas of the testbeam in 2017 at the H8 beamline, as described by [Flierl, 2018].

---

[3] The design of the four-layered Micromegas modules enables also the construction of modules with just two active layers. These are called doublets and were built and used during the early phase of the series production for testing.

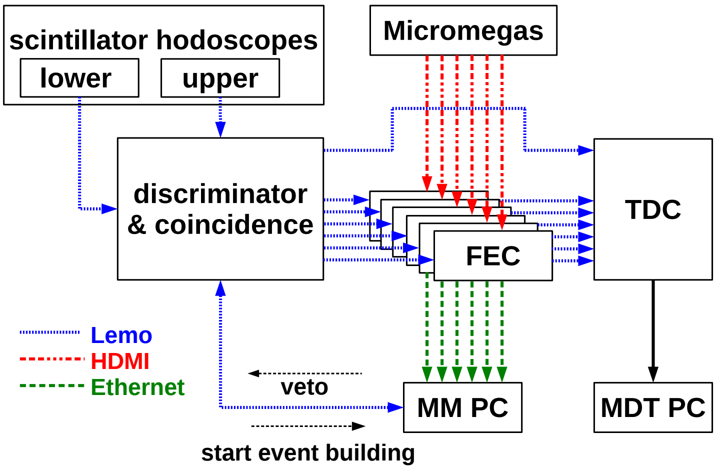

(a) Scheme of the trigger distribution in the CRF. Coming from the scintillators the trigger is distributed to enable the full readout of the Micromegas module.

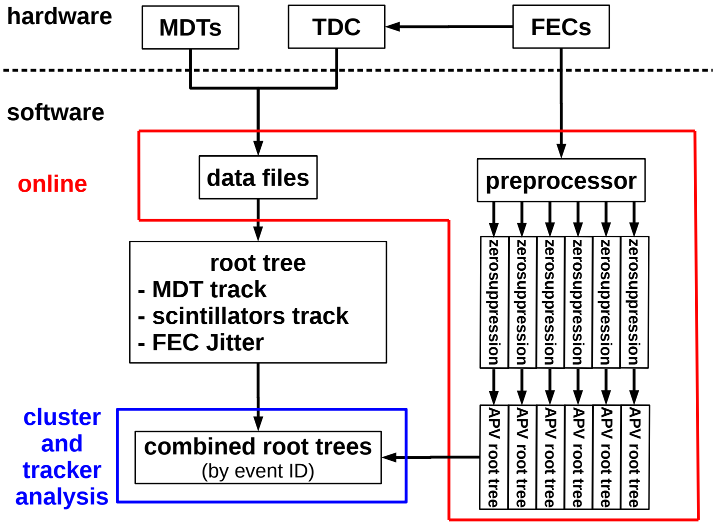

(b) Scheme of the data-streams and their processing during and after the measurements. On software-side the online-processes are parallelized to increase the data-recording rate. The cluster and tracker analysis is performed offline, after the measurements are finished

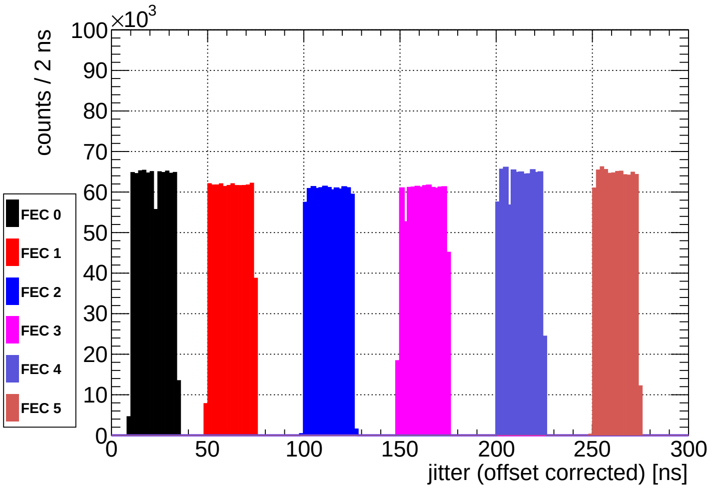

(c) Recorded jitter of six FEC-cards. The jitter is shifted for offsets to show the distributions next to each other. The jitter-distributions have the expected 25 ns width due to the 40 MHz-sampling-rate.

Figure 4.15.: The CRF trigger and the data-streams in the CRF are distributed over several parallel channels to enable a high readout-rate. The recording of the jitter via TDC enables an unbiased time-evaluation.

5. Module Characterization

The characterization of a Micromegas module describes its performance. A module should measure the tracks of the through-going muons. Therefore the performance is considered as the efficiency and the resolution to reconstruct the muons passage. Efficiency and resolution can vary with the operational parameter, so with the applied voltages and the used gas-mixture. Also the homogeneity of the efficiency and the resolution are important aspects. Systematic effects due to the readout electronics and the reconstruction techniques have to be excluded. In the following chapter the focus will lie on the efficiency.

The next two chapters will be dedicated to the resolution. This separation is done because for the resolution two things have to be disentangled. Failures during the construction of the modules can lead to inhomogeneities of the position-reconstruction. Therefore the deviations coming from these failures have to be understood and calibrated. The other point is the algorithm for the track reconstruction. These algorithms have to be tested and compared.

The efficiency can be defined by the ratio of well reconstructed muon tracks divided by all triggered muons going through the detector. The detection and with this the reconstruction is influenced by the quality of the readout anode. The micro-pattern anode can have inhomogeneities and failures, which should be detected and understood. As the reconstruction is done using the signals on the copper readout strips, their connectivity has to be tested. The gap for the gas-amplification is defined by the distance pieces called pillars. Therefore the effects coming from the deviations in this volume are also investigated.

5.1. Dead and Noisy Channel

The quality of the copper strips influences directly the efficiency. The strips can be accidentally cut during the manufacturing process or be badly connected. A cut would lead to the loss of this readout channel and therefore to a part of the active area which is not responsive. Bad connection could be due to insufficient compression of the elastomeric connector between the copper strips on the detector and the adapter-board for the APV25 electronics. A reduction of signal-height or increased noise would be the consequence. Noise in this case means the disturbance of the signal on a strip. This can be seen in signals coming from muons or from the variation around the baseline without a particle passage. Noisy channels show larger variations around the baseline than other channels. Vice versa dead or unconnected channels should have a lower variation, as the capacitance of the channel is reduced. The APV25 chips, as the main tool for the signal processing, influence heavily the variation of the measured charges. Effects caused by the detector itself, so cut or noisy strips, have to be disentangled from effects introduced by the electronics. Therefore the noise behavior of different modules has to be compared. If the same channels are identified as noisy or dead for different modules either the electronics can be the cause or systematic problems during the manufacturing. To determine the noise of readout channels two approaches are investigated. The first attempt is to evaluate the baseline-variation of the channels, while the second is to search for problematic channels in cosmic data.

5.1.1. Noise Estimation using the Charge Baseline-Variation

For the determination of the baseline-variation σ_c the signal of each channel is recorded about 10000 times in so called pedestal runs. Each record contains 24 charge samples for each channel separated by 25 ns, same as for a measurement run. The charge variation of these samples is calculated for each channel and the mean of the variation over all records is considered. The calculation for one channel c which measured charges $q_{r,s}$ over records r and samples s is given by:

$$\sigma_\mathrm{c} = \frac{1}{\#\,\mathrm{records}} \sum_{r\,\in\,\mathrm{records}} \sqrt{\frac{1}{\#\,\mathrm{samples}-1} \sum_{s\,\in\,\mathrm{samples}} \left(q_{r,s}-\overline{q_r}\right)^2} \quad . \tag{5.1}$$

Here $\overline{q_r}$ denotes the averaged sampled charge over all samples of one record r. The baseline-variations are shown exemplaric for two layers in figure 5.1. On the y-axis σ_c is measured in ADC channels. In black for each of the 3072 strips of one layer the values are drawn. For the larger red points the values of the 128 readout channels for one APV25 chip are averaged and their variation is shown as error bar. The distribution of variations is quite different for the two layers. In figure 5.1b the sigmas stay almost all below 40 ADC channels. On the contrary in 5.1a the sigmas spread widely even for a single APV-chip. The distributions are influenced by the grounding quality. The grounding quality is given by the conductivity between the ground of the readout electronics and the common ground of the detector. Hereby it is essential to avoid grounding loops. One of the main problems for the noise behavior is the close connection of the high voltage supply to the readout electronics. The high voltage is generated in a CAEN mainframe [CAEN, 2019] connected to the local power network at 230 V AC at 50 Hz. The connection of the high voltage supply to the detector is achieved via SHV cables which distribute also the ground of the mainframe to the detector. This introduces a lot of noise as can be seen if the mainframe is shutdown. Then the whole distribution is shifted down by about 1 to 10 ADC channels. Before a measurement several of these pedestal runs are taken in order to improve the noise behavior. In between the grounding for problematic chips is redone guided by the quality of the distributions.

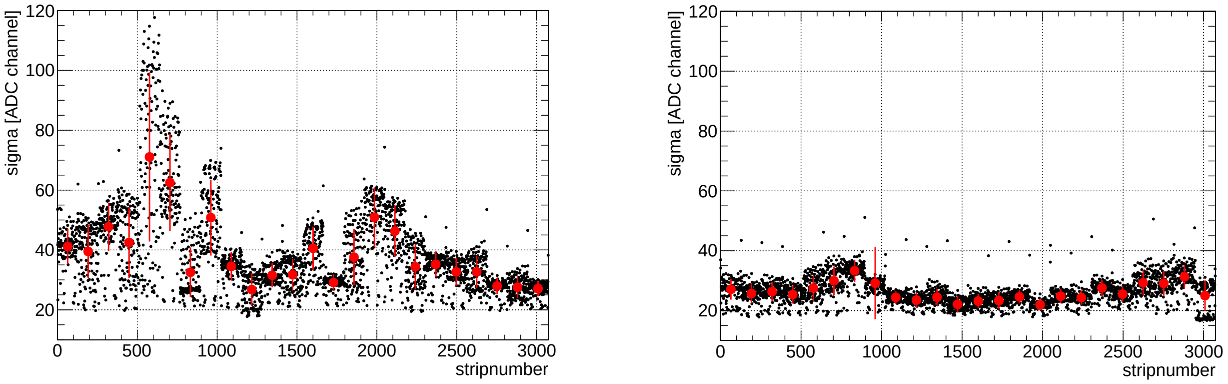

(a) Noisy layer with problematic readout chips.

(b) Layer with good noise characteristic.

Figure 5.1.: Variation of the baseline for each strip of one layer (black) and the averaged value for one readout chip with the standard deviation as error bar (red). Examples shown are for a noisy and a quiet layer. The inhomogeneities of the readout channels influence the homogeneity of the module for the reconstruction of muons.

To disentangle the effects of the detector from the effects of the readout electronics the channel variations have to be normalized. This is done by subtracting from the channel value the mean of the corresponding chip. Dividing this difference by the variation over the chip, the values for the channels should be independent of the chip quality. The values are shown in color ordered for each APV channel in 5.2a. Here each rectangle or bin is representing an individual strip of one layer of a Micromegas module. The horizontal lines of same color correspond to the same channels in different APVs with similar characteristic. This is a systematic electronic effect which has to be taken into account. Most of the channels are within -1 to 1 standard deviations to the mean (green to yellow). A group of channels is at about -2 standard deviations difference (light blue). Also channels can be seen which do not fit into this pattern and have 3 or more normalized variations. Noisy channels can be determined by searching for these outliers. For the identification of outliers the average normalized variation over all 96 APV-chips of one module for each channel is calculated. The result can be seen in figure 5.2b.

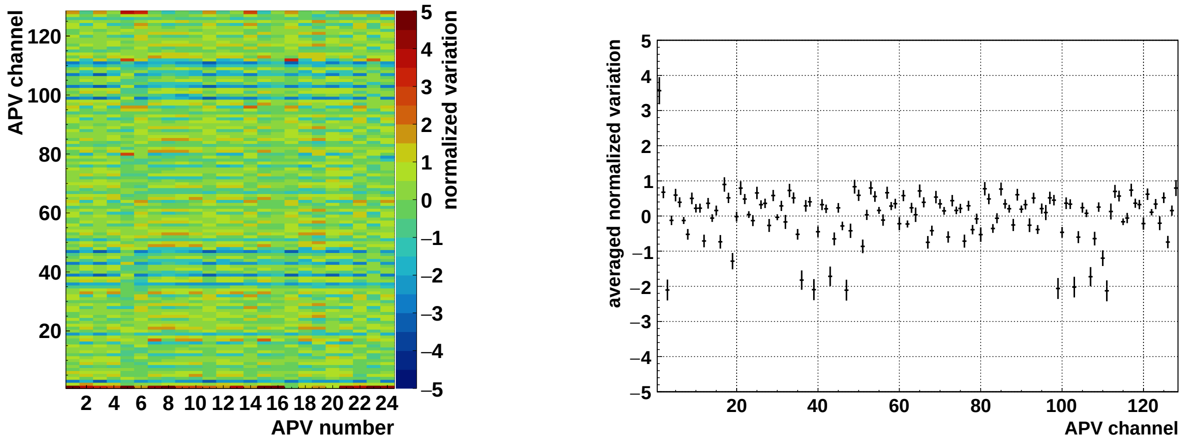

(a) The charge baseline-variation of the 128 channels for each of the 24 APVs connected to one layer of a Micromegas module. The variation is normalized by averaging over all channels of one chip and calculating the difference to this mean. The difference is then divided by the standard variation of the baseline-variations over the chip.

(b) For each of the 128 channels of an APV an averaged normalized variation is shown. The averaging is performed over 96 APVs of one module.

Figure 5.2.: Each APV has similar noisy or quiet channels as seen in the left plot by the horizontal lines with a similar color. This becomes more clear in the average over all chips of a module in the right plot.

The values in figure 5.2b can be seen as calibration for the baseline-variations measured with the APV25. Here the channels with different variations can be distinguished. Channels 3, 36, 39, 43, 47, 99, 103, 107, 111 are around -2 standard deviations to the mean. Therefore they show systematically a lower baseline-variation than the other channels. It has to be noted that the common APV channel numbering starts at 0, while in this case the numbering starts at 1. This distribution can be distorted by large outliers. Especially for the first and the last channel very different values are recorded as seen in figure 5.2a. Because of this, these channels are evaluated separately.

To test this approach for the four modules five, six, seven and eight pedestal-measurements were taken. The normalized variations are calculated and the difference to the APV baseline-variation calibration is considered. If this difference is larger than 2.4 the channel is assigned as noisy. The channel is counted as dead for differences below -2.4. The value 2.4 is chosen as the distributions of differences showed standard deviations in the order of 0.8. Therefore strips with less than three standard deviations of difference are considered as good. The channels identified as bad by this method, so with differences larger than three standard deviations, are shown in figure 5.3 for the four modules. In blue strips are indicated which are either connected to the first or the last channel of an APV. As can be seen by the large amount of dead strips found by this method the APV baseline-variation calibration overestimates the variation of the first and the last channel. This is probably due to some large outliers which were used for the calibration and therefore distorted the mean. For noisy channels two points can be observed. First, layer eta-out and stereo-in feature several strips which are noisy for each module. Second, the other noisy channels are found in groups close to each other. This could be explained by problematic APV-chips. Besides the large amount of strips connected to the first and last channel of an APV, which are found as dead (blue lines) only few strips are identified as unresponsive. The largest fraction of dead strips, which are not connected to the first or the last APV channel, are found at high strip-numbers for the two eta-layers. Actually the last thirty strips in the eta-layer should be detected by this method as dead, because they are not connected due to design reasons of this layer. As this did not work the conclusion is that this method is unsuitable for detection of dead strips. The found noisy strips in each module should be removable by exchanging the APV at the corresponding positions. The method is probably affected by the large average noise value. As can be seen in figure 5.1a even for a layer with good noise characteristic the mean variations over an APV are above 20 ADC channels. Therefore the effect of dead or noisy channels caused by the detector is probably washed out completely. Another approach is necessary.

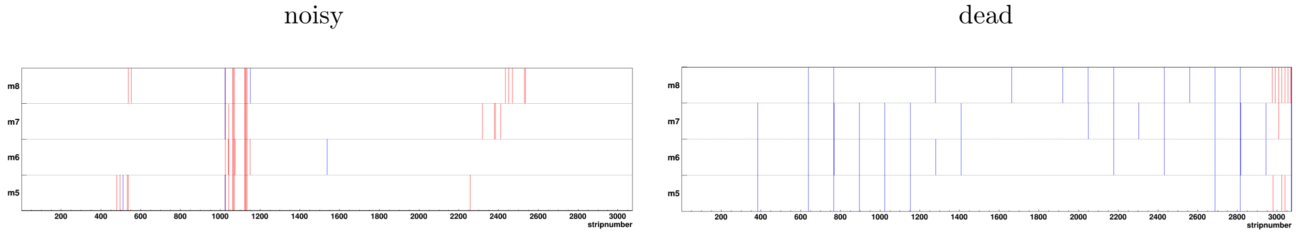

(a) eta-out

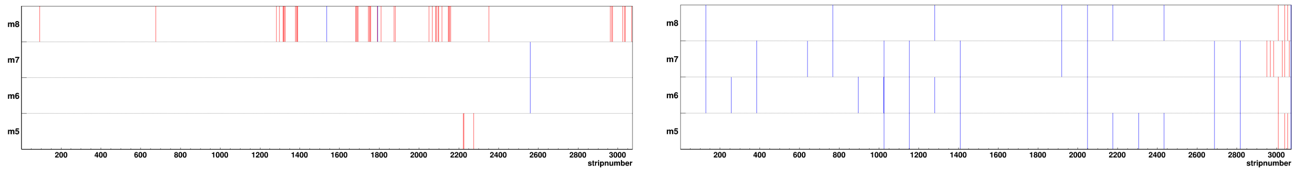

(b) eta-in

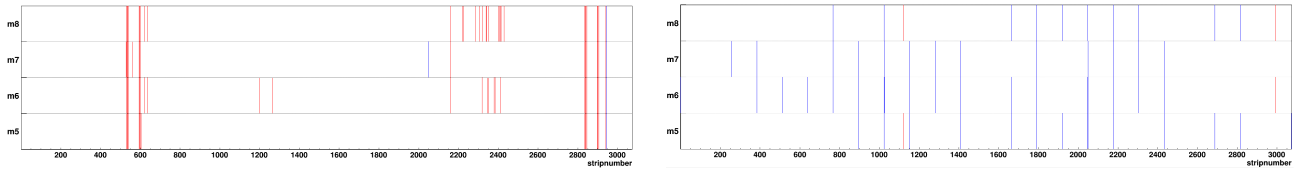

(c) stereo-in

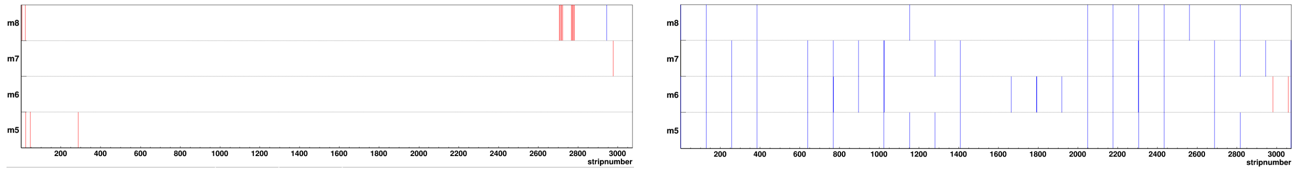

(d) stereo-out

Figure 5.3.: Noisy and dead channels identified by the evaluation of the charge baseline-variation. The channels above the threshold are shown separately for the four layers of four modules (5,6,7,8). In blue strips exceeding threshold connected to the first or the last channel of an APV are shown, while other strips are indicated red.

5.1.2. Search for Problematic Channels in Cosmic Data

Noisy and dead strips can be identified using their response behavior during cosmic-measurements. For this the bare distribution of strips passing the zero-suppression can be considered. An exemplaric distribution for one layer can be seen in figure 5.4a. In an ideal case one would expect a linear increase of counts to higher strip-numbers due to the trapezoidal shape[1] of the module. This is washed out and superimposed by the inhomogeneous illumination of the CRF. Therefore the increase in hits for strips at larger strip-numbers is less steep than expected. Not all muon tracks pass through the active area of the layer therefore also events are recorded with only noise in the detector. Noise hits are also present for tracks going through the detector. As the noise should be almost homogeneously distributed over the channels it adds only a global offset. Noisy channels can be seen at several spots with higher counts than those for the average distribution. For figure 5.4a the second gluing side of eta-panel three is chosen which features dead strips due to a PCB-production mistake in the early stage. Therefore this module will not be installed in ATLAS, but can be used for investigations. The unconnected strips are near the PCB-borders between the readout-boards around 1000 and above 2000. In addition the 30 not connected strips at the last PCB can be seen. For the validation of the modules the implementation of an automatic search for these channels is required. Therefore in the following multiple approaches for this are discussed.

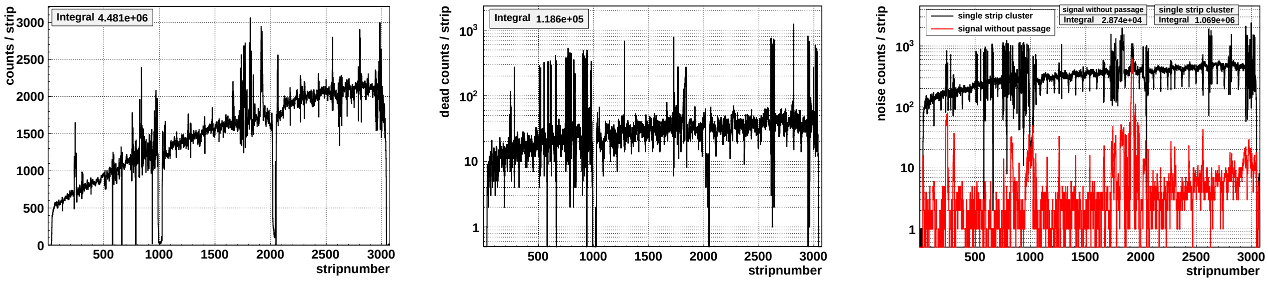

(a) Distribution of hits passing the zero-suppression.

(b) Distribution of hits missing in a cluster.

(c) Distribution of hits for two different selections of noisy channels.

Figure 5.4.: The signal of the strips can be affected by noise or the connection quality to the electronics. Therefore the distributions of strips passing certain signal quality criteria have to be evaluated in order to reconstruct problematic channels. Four strip distributions are shown for one layer of a module. In 5.4a the whole sample is used after the zero-suppression. In 5.4b strips are counted as dead, if they are missing in a cluster. Noisy strips are selected in two ways (see figure 5.4c). They can appear as single one-strip-cluster (black). Also strips in a multi-strip-cluster are counted as noise if the track did not pass the detector (red).

Dead channels should be identifiable by searching for holes in strip-clusters of muon tracks. Holes can occur due to the inhomogeneous ionization along the path of the muon. This is statistical and therefore each strip should be affected in the same way[2]. The distribution of strips which are missing in a cluster can be seen in figure 5.4b. High counts should correspond in this case to dead channels, as they do not contribute in a cluster as often as other strips. Frequently channels with high counts in the overall distribution show also high counts in the distribution as missing in a cluster. This can be explained by the deformed pulse shape of noisy channels. These signals are discarded during cluster-building and therefore counted as missing. Another problem which arises for the identification of dead channels with this approach can be seen for the unconnected regions around strip-numbers 1000 and 2000. As several neighboring channels are not connected in those regions, no clusters at all are found and therefore the strips can not be counted this way as missing. Therefore the approach to just search for high counts in this distribution is not promising.

Noisy channels can be searched for using the strip-clustering. A muon-passage is expected to create signals on multiple strips due to transverse diffusion and the inclination. With this assumption hits in isolated strips could be identified as noise. The black distribution of figure 5.4c shows the reconstructed single hits. As this distribution shows similar characteristics as the first distribution no real advantage is achieved. Of this distribution the main contribution is produced due to insufficient zero-suppression.

The tracking capabilities of the CRF can be used to search for clusters, when the muon is not passing through the module. A large contribution of these clusters in a localized region corresponds to neighboring strips, which are simultaneously noisy. This could be due to electronic problems or scratches of the copper-strips, which connect these strips. For the chosen data-set the red-distribution of figure 5.4c is reconstructed as simultaneously noisy. By comparing this distribution to figure 5.4a, two peaks around strip-numbers 245 and 1890 are found in both. These peaks correspond to about 20 problematic strips. The fluctuations of this distribution suggests a problematic investigation using this method.

The distribution of all hit strips can roughly be fitted with a polynomial of second degree (see figure 5.5a). Dead and noisy strips can then be identified using the difference of measured counts to the expected counts by the

---

[1] The long baseline (1.63 m) is about 27% longer than the short baseline (1.17 m).

[2] Here the same argument as for the overall hit distribution holds, therefore a similar increase to higher strip-numbers should be observed

fit. This difference is normalized to the expected counts to account for the inhomogeneous illumination. In the scaled distribution (see figure 5.5b) dead strips are seen for values below -0.4. This value is not statistically motivated, but empirically observed to be suitable in the most cases. The identification of noisy strips is more problematic as no consistent value for the identification could be found. Another problem for the automation of this method is the distortion of the fit by regions with more or less counts. This can occur if APV-chips or even whole adapter-boards, which are connected to problematic FECs, reconstruct too many hits. The reconstruction of too few hits is mostly caused by high-voltage-sectors, which are not on the nominal voltage during these measurements.

To account for all these cases a systematically biased but more robust method is implemented. For each APV separately the mean and the standard deviation of counts is calculated. With this the channels are selected, which reconstruct more hits than three standard deviations above the mean of their respective chip. In a similar fashion dead strips are identified by searching for strips with counts less than three standard deviations below the mean. The bias of this method is made due to the inhomogeneous illumination. The hit distribution over one APV-chip is not constant, therefore the standard deviation of hits is systematically larger. This leads to an underestimation of noisy and dead strips. Also the mean is distorted if a lot of problematic channels are connected to the same chip. None the less, this method is chosen as the most robust of the tested implementations.

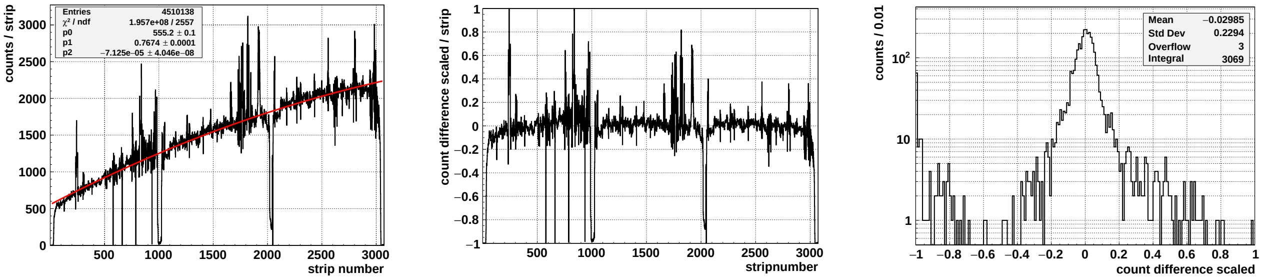

(a) Distribution of strips passing the zero-suppression fitted with a second degree polynomial.

(b) Difference of the counts to the expected value by the fit divided by the expectation.

(c) Distribution of differences to the fit divided by the expected value.

Figure 5.5.: For the identification of dead and noisy strips the overall distribution of hit strips is fit and outliers are found by the deviation to this fit.

5.2. Pulse-Height

The energy deposition of the muons in the gas volume is determined from a charge pulse on the copper readout strips. This is achieved by the amplification of the primary electrons after passing the mesh and the following ion movement. The charge pulse is shaped and preprocessed by the APV25 chips and the processed signal is then investigated. The muon energy deposition is statistical and thus the creation of primary electrons is spread along the path. The drift of the electrons in the gas leads to a broadening of the charge distribution due to transverse diffusion. Finally the amplification-process spreads the charges further. Therefore the charge-signals are present on several readout strips. For the reconstruction of the deposited energy the signals of the readout strips are evaluated at their maximum. This charge value is assigned to the corresponding strip. Neighboring strips are combined to so called clusters and their sum of charges is proportional to the deposited energy.

The evaluation of the strip charge-signals can be biased due to the response behavior of the APV25 chips. For a single APV-chip the measured maximum charges of all channels can be seen in figure 5.6a. A small peak below 100 ADC channel can be identified as noise due to the insufficient zero suppression for charges in this range. The dynamic range of the APV for charge reconstruction is limited. Therefore the chip saturates for higher charges, which can be seen at the peak around ADC channel 1350. The distribution of charges between ADC channel 100 and ADC channel 1200 is Landau-like. This can be explained by the statistical energy deposition of the muons in the thin gaseous detector. The deviations to the expected Landau-distribution have to be explained. First, the start of the distribution is cut off due to the zero suppression, which discards too low charge-signals. These signals can be furthermore suppressed by their deformed shape due to high baseline-variations, which leads to a rejection. Second, the amplification of the electrons can vary along the strips due to the size of the pillars. The pillar-height can vary due to the manufacturing of the readout-PCB. Therefore the same amount of energy deposited at different sites in the detector can lead to different pules-heights. Third, the tracks of the muons can be of any inclination to the readout anode[3]. This can lead to an overlap of signals originating from electrons created in different regions between the cathode and the mesh. The overlap can distort the signal, which influences the charge measurement.

Another problematic effect is caused by the varying quality of the APV-chips and their systematics. This can be seen in figure 5.6b. Here the measured charges are shown for each strip individually. All channels show the Landau-like distributions. Groups of 128 channel, belonging to one APV-chip, show a similar characteristic

---

[3] Due to the angular acceptance of the CRF only inclination angles within ±30° are expected.

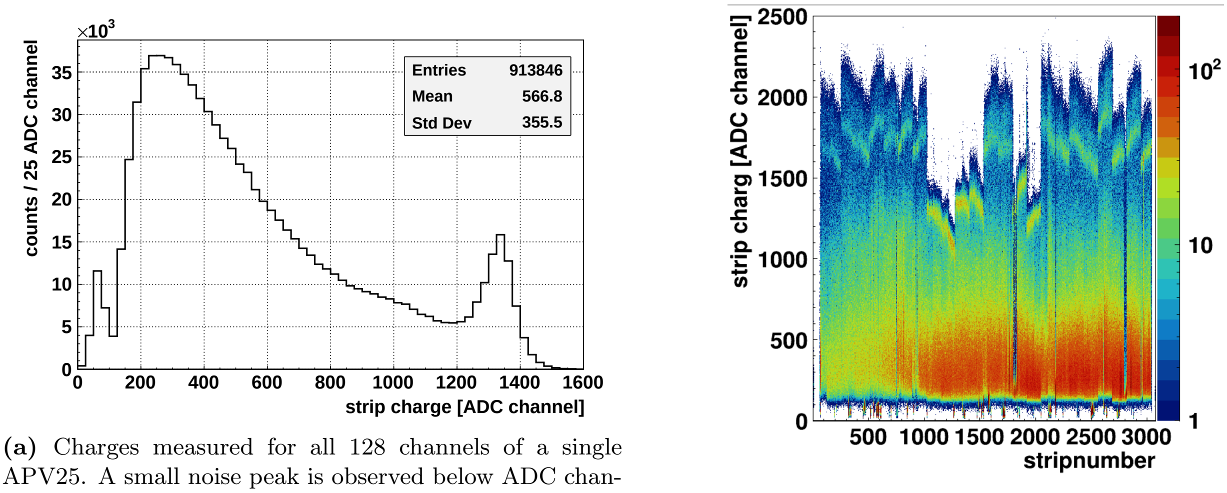

(a) Charges measured for all 128 channels of a single APV25. A small noise peak is observed below ADC channel 100. The main peak is due to instantaneous ionization along the muons path with an exponential decay. The saturation peak around ADC channel 1350 is due to limited dynamic range of the APV25.

(b) Measured charges for each strip. An APV25 chip reads out 128 neighboring strips. Each chip can have a different dynamic range. This is seen by the different sets of maximum measured charges.

Figure 5.6.: The charge measurement is distorted and limited by the APV25 readout. This is seen for a long term measurement of module 3 at 560 V anode voltage with the nominal gas-mixture of Ar:CO$_2$ 93:7 vol%. The drift-voltage was at 300 V for the outer eta-layer.

of the saturation peak. The position of the saturation peak varies within a single APV by about 200 ADC channels. Despite the distortion for high charge values the most probable value of all strips is almost identical and around ADC channel 300. Therefore the charge measurement should only in extreme cases be influenced by this electronic problem.

To evaluate the reconstruction performance of the detector the sum of strip charges in a cluster is investigated. This rejects the systematics due to the inhomogeneous ionization and electronic problems. Another important property of these clusters are the number of strips which a cluster contains, this is called the multiplicity. The sum of charges and the number of strips are related as seen in figure 5.7a. This arises by the fact that both values are related to the deposited energy. For these figures hits for tracks with different inclination angles are averaged. Therefore the multiplicity varies according to the projection of the track length on to the readout-area. Also the cluster-charge varies with the inclination as a longer path length increases the probability for more energy deposition. The correlation of strip multiplicity and mean cluster-charge can be evaluated for several voltages and with different gases. It shows that for almost all cases in the range between 2 and 8 strips including the increase of mean cluster-charge is about 800±100 ADCchannel/strip.

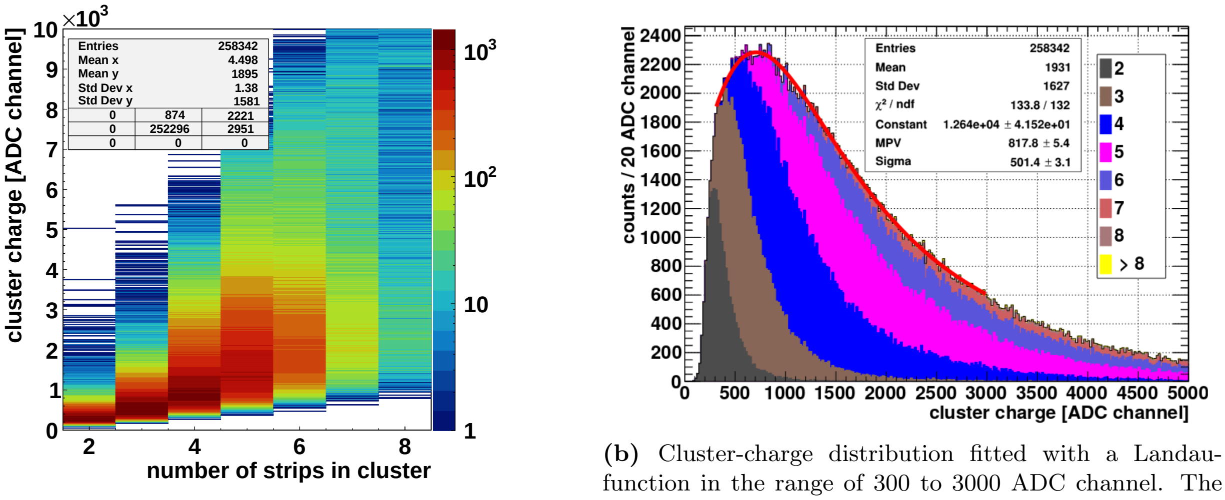

(a) Cluster-charge as function of number of strips in the cluster.

(b) Cluster-charge distribution fitted with a Landau-function in the range of 300 to 3000 ADC channel. The contributions of the different strip multiplicities are colored separately.

Figure 5.7.: The energy deposition of the muons is spread along their path. Therefore the created charges are distributed over several strips. A cluster of neighboring strips can be associated with a particle passage. The sum of charges in a cluster is proportional to the deposited energy. Examplaric distributions of cluster-charges for module 8 eta-out board 8 at 570 V amplification-voltage and 300 V drift-voltage with the nominal gas-mixture of Ar:CO$_2$ 93:7 vol%.

For the characterization of the modules it is important to investigate the cluster-parameter, charge and strip-multiplicity, with varying operational parameters. This was done by taking several measurements with three mixtures of Ar:CO$_2$. As mixtures 93:7, the nominal mixture foreseen for the operation in the NSW, 85:15 and 80:20 volume percent were chosen. For each mixture measurements of different sets of amplification-voltages were used. The measurement for a single amplification-voltage took about half a day and yielded in this setup about 3 million triggers. Module eight and a doublet built from eta-panel three were chosen as test-chambers for these measurements. First the investigation will focus on results concerning only one readout board. This is done to disentangle effects coming from differences between the quality and properties of these anode structures. Also differences due to the electronics can be discarded by this. The chosen PCB is the large board (8) of layer eta-out.

mean multiplicity normalized cluster-charge distribution

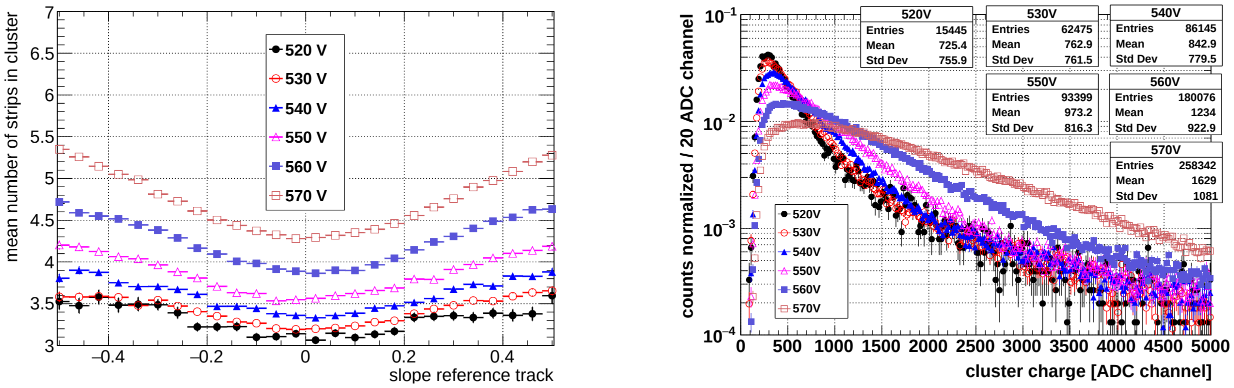

(a) Ar:CO$_2$ 93:7 vol% , $U_{\mathrm{drift}} = 300\,\mathrm{V}$

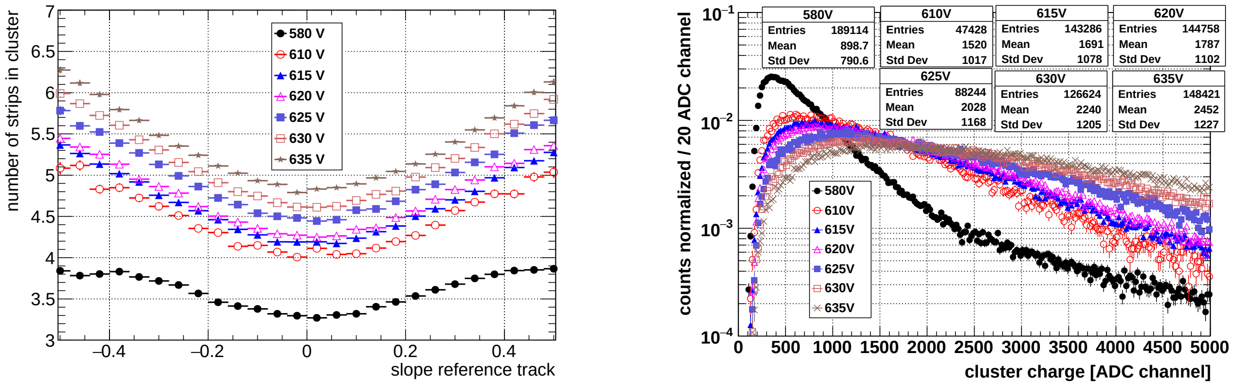

(b) Ar:CO$_2$ 85:15 vol% , $U_{\mathrm{drift}} = 300\,\mathrm{V}$

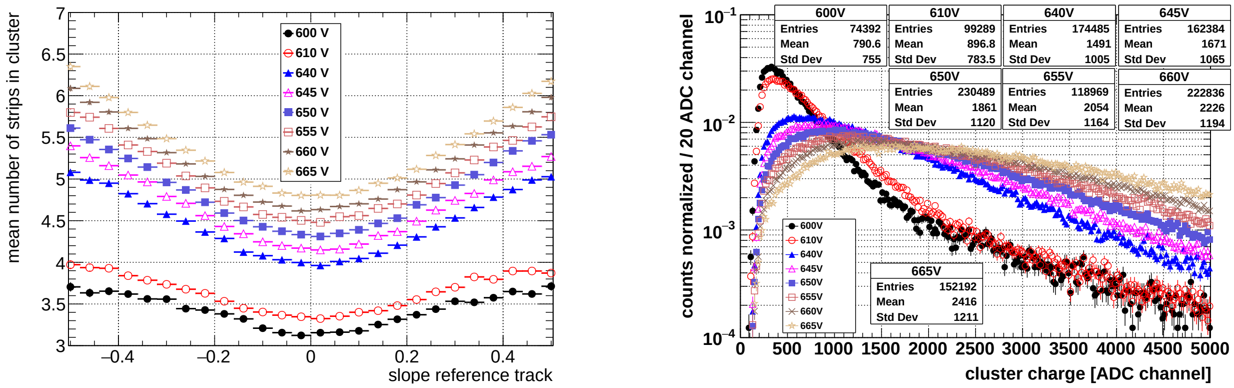

(c) Ar:CO$_2$ 80:20 vol% , $U_{\mathrm{drift}} = 475\,\mathrm{V}$

Figure 5.8.: Mean number of strips as function of the reference track slope and the normalized cluster-charge distributions. Shown are the distributions for three gas-mixtures and various amplification-voltages.

The normalized cluster-charge distributions can be seen on the right-hand-side of figure 5.8. For each gas-mixture the distribution gets broader for increasing amplification-voltage. Also the most probable value is shifting to higher values. This is expected, as larger amplification-voltages lead to a higher field in the amplification-gap and therefore to a larger gain during the electron avalanches. It can also be noted that for the nominal mixture (93:7) the maximal measured voltage of 570 V is not as broad and as highly peaked, as for the other two gas-mixtures. This observation can be compared to the left-hand-side of figure 5.8. Here the mean number of strips in the clusters, i.e. the multiplicity, is shown as function of the slope of the reference track. As expected the number of strips increases for larger track-inclinations. Also the overall distribution increases for increasing amplification-voltages. This can be explained by two effects. First, a higher field in the amplification-gap leads to higher transparency of the mesh for the electrons created in the drift-region. Therefore more electrons reach the amplification-stage and less are lost before they can be detected. Second, a higher amplification-field leads to more charges created during the avalanches. This produces higher signals, which are therefore better detectable, because the distinction from noise or baseline fluctuations is simplified. The comparison of the different gas-mixtures shows that the highest reachable voltage for the nominal mixture reconstruct a distribution with lower values than the other two mixtures. It has to be stated that the detector could not be operated with voltages higher than 570 V for Ar:CO_2 93:7 volume percent. Higher voltages would lead to an increased discharge-rate due to manufacturing impurities. As these discharges lead to localized currents in the order of several mA, the active surface could be damaged. For the other two gas-mixtures the volume fraction of CO_2 is higher. This quencher-gas leads to a suppression of additional charge-creation by capturing UV-photons created during the avalanches. As the detector can be ramped-up to higher voltages safely the cluster-charge and strip multiplicity increases accordingly.

To investigate the properties of the clusters quantitatively these distributions have to be evaluated. For the multiplicity the mean and the standard deviation are plotted as function of the amplification-voltage for the three gas-mixtures in figure 5.9a. In addition the difference of mean number of strips for almost normal incident and more inclined incident is shown. For normal tracks, slopes between ±0.04 were chosen, while for an inclined incident the tracks should have an absolute slope larger than 0.44. This corresponds to angles of about ±2.3° and 24° respectively. The increase of the mean multiplicity with larger amplification-voltages is clearly visible. Comparing this to the left-hand-side of figure 5.8 one observes that the mean of the overall distribution is dominated by the contribution from almost normal tracks. This is due to the track slope distribution in the CRF (see figure 4.4b). The standard deviation stays around 1.2 strips almost constant over all amplification-voltages for the three gases. Therefore the width of the distributions is primarily caused by statistical effects coming from the integration over many track angles and the inhomogeneous ionization of the muons. The increasing difference in mean multiplicity of inclined to normal tracks for larger amplification-voltages suggests that more strips are passing the zero-suppression. An explanation is the higher charge per strip which increases the probability for a single strip to pass the threshold. A higher charge per strip can be deduced by comparing left and right-hand-side of figure 5.9, as done in figure 5.10a.

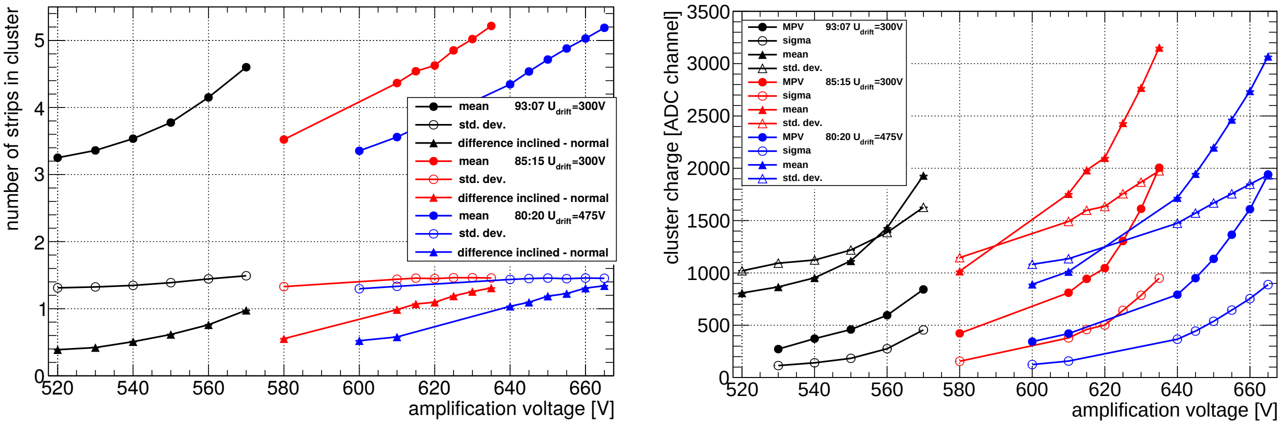

(a) Properties of the multiplicity, ie. the number of strips in a cluster, as function of the amplification-voltage for three gas-mixtures. The mean, the standard deviation (std. dev.) and the difference of the mean for inclined and normal tracks are shown. Normal tracks are considered between ±2.3° inclination, while inclined tracks are more than 24° tilted.

(b) Properties of the cluster-charge distribution as function of the amplification-voltage for three gas-mixtures. The most probable value (MPV) and the sigma are parameters extracted by a Landau-fit of the distributions. Also shown are the mean and the standard deviation. An exponential rise expected due to the increase of charge-amplification in the Townsend avalanches is seen for the mean and the MPV.

Figure 5.9.: The number of strips in a cluster, called multiplicity and the cluster-charge are the most prominent characteristics, which influence the efficiency. They are depending on the operational parameter, namely the gas-mixture and the amplification-voltage. The dependencies are exemplarily shown for module 8 eta-out board 8. The actual trend depends also on the pillar-height and the environmental situation, e.g. temperature and pressure.

In figure 5.9b the statistical properties of the cluster-charge distributions are shown. The mean and the standard deviation are calculated for the distribution limited to 5000 ADC channels. The Most Probable Value (MPV) and the sigma are extracted by fitting Landau-functions to the distributions. The fits have a lower limit of 300 ADC channels. As already seen in figure 5.8 not only the parameters describing the position of the cluster-charge distributions, but also the widths are increasing with amplification-voltage[4]. This can be explained by the inhomogeneous ionization of the muons. As their energy-loss fluctuates also the cluster-charge gets a broad distribution. By increasing the amplification-voltage the differences between the signal strength of the muons is further enhanced. Therefore the width of the cluster-charge distribution gets larger. An estimation of the energy resolution of the Micromegas can be made by the ratio of width to position of the cluster-charge distribution. The ratios are shown separately for the standard deviation and the sigma from the Landau-fit in figure 5.10b, divided by mean and MPV respectively. While for the sigma-ratios some sort of saturation around 0.5 is observed, the standard deviation ratios decrease almost linearly with the amplification-voltage. The two gas-mixtures with a higher fraction of CO_2 seem to reach a better energy resolution, than the nominal mixture.

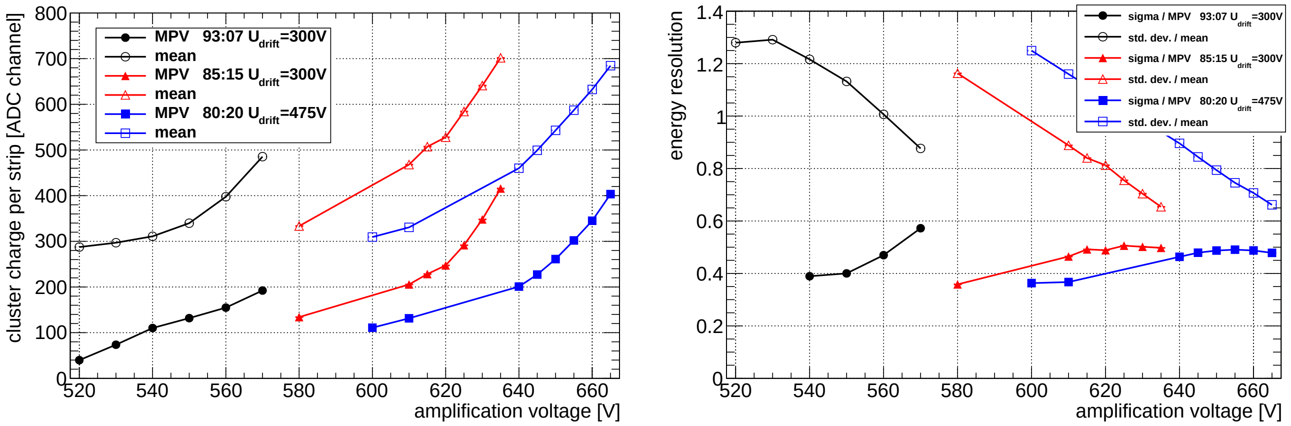

(a) The most probable value (MPV) and the mean of the cluster-charge distribution divided by mean number of strips as function of the amplification-voltage. An exponential rise is expected due to the increasing number of charges created during the Townsend-avalanches. This ratio is an estimation for the charge seen on a single strip.

(b) The ratio of the cluster-charge distribution width by the position of the distribution. For the filled symbols the sigma of the Landau-fit is used as width estimation and for the position the MPV. For the empty symbols the standard deviation is used as estimation of the width and the mean for the position. This ratio is an estimation for the energy resolution.

Figure 5.10.: The distributions of cluster-properties, i.e. multiplicity and charge, enables the estimation of single channel pules-height and energy resolution. The single channel pulse-height is related to efficiency due to the need for zero-suppression and noise reduction. Energy resolution is commonly not concerned in a Micromegas, as these detectors are used for triggering and tracking.

Until now the pulse-height was investigated just for one readout-board. In the following the discussion will be extended to investigate the differences between the PCBs. The main difference between the boards should originate from the pillar-height, as this determines the amplification-field and so the gain. The amplification-curves like in 5.9b of all boards have to be described in a way to make them comparable between each other. This can be achieved with two approaches. One can either compare the pulse-heights only for one set of amplification-voltages or try to describe the developments.

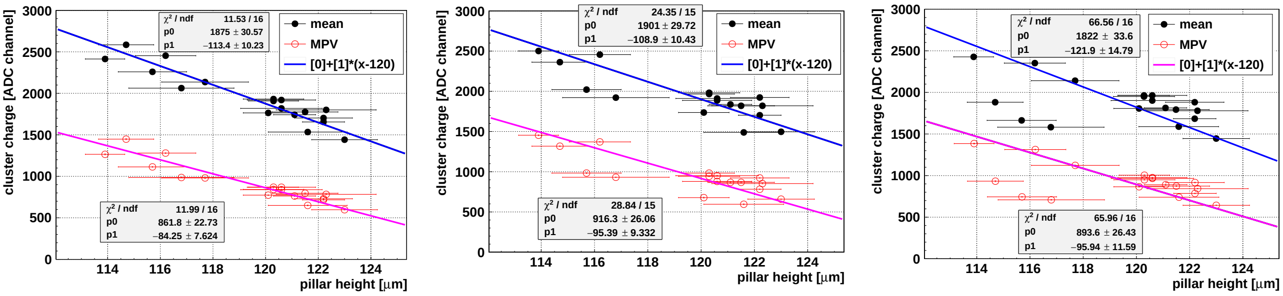

(a) Ar:CO_2 93:7 vol%
$U_{\mathrm{amp}} = 570\,\mathrm{V}$
$U_{\mathrm{drift}} = 300\,\mathrm{V}$

(b) Ar:CO_2 85:15 vol%
$U_{\mathrm{amp}} = 615\,\mathrm{V}$
$U_{\mathrm{drift}} = 300\,\mathrm{V}$

(c) Ar:CO_2 80:20 vol%
$U_{\mathrm{amp}} = 645\,\mathrm{V}$
$U_{\mathrm{drift}} = 475\,\mathrm{V}$

Figure 5.11.: The mean and the most probable (MPV) cluster-charge as function of the pillar-height, for three gas-mixtures at the given voltages. Each dot correspond to the measurements for a single readout-board. The correlation confirms the Townsend-amplification character, as the pillar-height determines the amplification-field and therefore the gain.

For the first approach amplification-voltages have been selected at which the gases show almost similar efficiency (discussed in the next chapter 5.3). A suitable choice is 570 V for 93:7, 615 V for 85:15 and 645 V for 80:20.

---

[4] The position is described by the mean and the Most Probable Value (MPV). The width is described by the standard deviation and the sigma.

For these values the mean and most probable (MPV) pulse-height can be correlated to the pillar-height as seen in 5.11. The pillar-height is measured during the quality control at CERN, before the PCBs are send to the production-sites. This is done with tactile-probes at several positions, all over the active area. Therefore the mean of these measurements is used for the correlation, while the standard deviation is assigned as error-bar. The distributions are fit with a modified linear function to make the intercepts (p_0) comparable. This parameter corresponds to the mean or most probable pules-height at a pillar-height of 120 µm. The χ^2/ndf reveals the best correlation for the 93:7 gas-mixture. For all gas-mixtures the fitted slopes are compatible within the errors. The deviation between the intercepts can be explained by the coarse selection of voltages with similar pulse-height. The decrease in reconstructed charge per pillar-height can be scaled by the intercepts to make a more general statement. This is calculated in table 5.1. The values are comparable within the errors and suggest an overall fluctuation of pulse-heights of more than 60% according to the observed pillar-heights.

Ar:CO$_2$ vol%	mean %/µm	MPV %/µm
93:7	-(6.0±0.6)	-(9.8±1.0)
85:15	-(5.7±0.6)	-(10.4±1.1)
80:20	-(6.7±0.8)	-(10.7±1.1)

Table 5.1.: Pulse-height change per increased pillar-height.

For the second approach one has to remind the dependencies of the gain G and the first Townsend coefficient α. [Rose and Korff, 1941] give a good parametrization of α. Using this and the ideal-gas-law, [Adloff et al., 2009] arrives at a description of the gain

$$G = \exp\left(d \cdot \alpha\right) \tag{5.2}$$

$$= \exp\left[\ \frac{Apd}{T} \cdot \exp\left(-\frac{Bpd}{TU} \right)\ \right] . \tag{5.3}$$

Here p and T are the pressure and the temperature of the gas, respectively. A and B are gas-parameters, which have to be determined experimentally for individual gas-mixtures. The distance d traveled by the electrons in the electric field is assumed to be the same as the distance between the electrode plates. The voltage difference between the plates is described by U. This is not an ideal description of the situation in a Micromegas. The actual amplification-field is not homogeneous, but is distorted due to the mesh-structure and the anode-surface[5]. Using this parametrization one could fit the dependence of the charge-evolution as function of the amplification-voltage. The fit can be parametrized by $f(x) = \exp(p_0 \exp(-p_1/x))$, where x is the amplification-voltage and $f(x)$ describes the measured pulse-height. In the parameters p_0 and p_1 the dependencies on the pressure, temperature and the pillar-height as distance between the plates are incorporated. Several problems are encountered for this fit. The measurements for single voltage-points had a duration of several hours up to a day. During this time the temperature, but especially the pressure varied. In the CRF the temperature is controlled in the range of ±2°. Whereas the pressure was observed to change up to 15 hPa related to the atmospheric pressure. For the average measured values[6] this corresponds to absolute changes of about 2%. The unstable environmental conditions actually prohibits the direct comparison of different voltage-measurements in this case. Another problem is the double-exponential dependence, which aggravates the fit. Especially the measurements at lower voltages do not match for this description. In order to account for these problems, equation 5.3 is linearized. The first order Taylor-expansion around the nominal pillar-height of d_0 =120 µm is given by

$$\begin{aligned} G(d) = {} & \exp\left(a \cdot d_0 \cdot e^{-b \cdot d_0}\right) \\ & + a \cdot (1 - b \cdot d_0) \cdot \exp\left(-b \cdot d_0 + a \cdot d_0 \cdot e^{-b \cdot d_0}\right) \cdot (d - d_0) \\ & + \mathcal{O}\left((d - d_0)^2\right) \quad , \end{aligned} \tag{5.4}$$

where

$$a = \frac{A \cdot p}{T} \quad \text{and} \quad b = \frac{B \cdot p}{T \cdot U} \quad . \tag{5.5}$$

Therefore the pulse-height as function of the pillar-height is fit linearly. This is done for all amplification-voltages separately, similar to figure 5.11. The gas-parameters A and B can be determined by the fit-parameters p_0 and p_1 according to

---

[5] This is seen for example in field-simulations shown in [Kuger, 2017].

[6] The CRF is controlled to about 21 °C. The local pressure for Garching was observed to be around 955 hPa.

$$A = \frac{T}{p} \cdot \frac{\ln(p_0)}{d_0} \cdot \exp\left(1 - \frac{d_0 \cdot p_1}{p_0 \cdot \ln(p_0)}\right) \tag{5.6}$$

$$B = \frac{T \cdot U}{p} \cdot \left(\frac{1}{d_0} - \frac{p_1}{p_0 \cdot \ln(p_0)}\right) \quad . \tag{5.7}$$

Dependencies on the other parameters are expected, due to this approximation. Therefore the reconstructed gas-parameters are shown as function of the amplification-voltage in figure 5.12. This is done separately for the mean and MPV of the cluster-charge distributions.

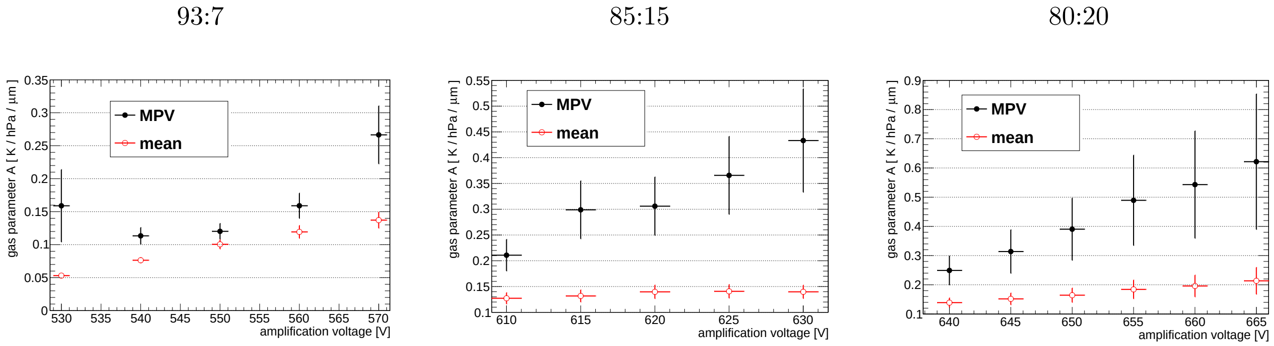

(a) Reconstructed gas-parameter A.

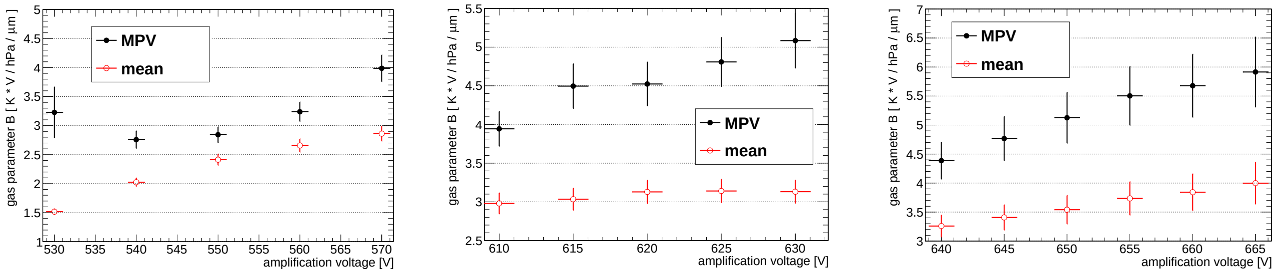

(b) Reconstructed gas-parameter B.

Figure 5.12.: Using a linear approximation of formula 5.3 the gas-parameters A and B are reconstructed. Therefore the cluster-charge-dependence on the pillar-height is fitted linearly. This is done for three gas-mixtures of argon and CO_2 as function of the amplification-voltage.

For the two mixtures with a higher fraction of CO_2 almost linear dependencies on the amplification-voltage are reconstructed for the gas-parameter. While the 93:7 mixture shows an approach of the reconstructed values by the mean and the MPV around 550 V. This difference could originate due to the higher observed gain for the two alternative mixtures at the shown voltages. In order to approximate definite values, the intersections of the linear dependencies are calculated. For the nominal mixture the mean value around the closest approach is used for this approximation. The calculated values are seen in table 5.2. Due to the extrapolation large errors have to be given on these values, in the order of the reconstructed value itself. Therefore this is just a very coarse reconstruction. The deviating value for 85:15 could be explained by a wrong chosen cathode-voltage. None the less the values for 80:20 are in a same order as reference-measurements in a more controlled environment. [Lippert, 2012] reports values of $A = (0.1112 \pm 0.0006)\,\frac{\text{K V µm}}{\text{Pa}}$ and $B = (2.197 \pm 0.007)\,\frac{\text{K V µm}}{\text{Pa}}$ for this mixture.

Ar:CO_2 vol%	A [$\frac{\text{K V µm}}{\text{Pa}}$]	B [$\frac{\text{K V µm}}{\text{Pa}}$]	voltage [V]
93:7	0.11	2.6	550
85:15	0.14	3.2	607
80:20	0.11	2.6	624

Table 5.2.: Reconstructed gas-parameter from the intersection of the curves in figure 5.12. The voltage of the intersection is also stated. The uncertainties on these values are in the same magnitude as the first digit, therefore this is only a very coarse description.

During this investigation only a limited set of boards and therefore of pillar-heights are used. The effect of pulse-height variation with pillar-height is also seen for a larger sample of modules. In figure 5.13 the results for modules one, three, six and seven are summarized. For this comparison the distinction between eta and stereo-boards is made, to illustrate the differences caused by the two different manufacturing companies of stereo and eta PCBs. The average pulse-height-change per increased pillar-height is reconstructed for this investigation in the range of 4 %/µm. This could indicate a slight systematic bias in the preceding investigation.

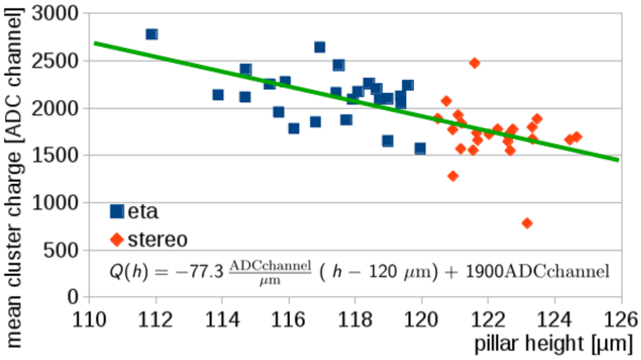

Figure 5.13.: Mean cluster-charge per board as function of pillar-height. Measured for boards in module one, three, six and seven at an amplification-voltage of 570 V.

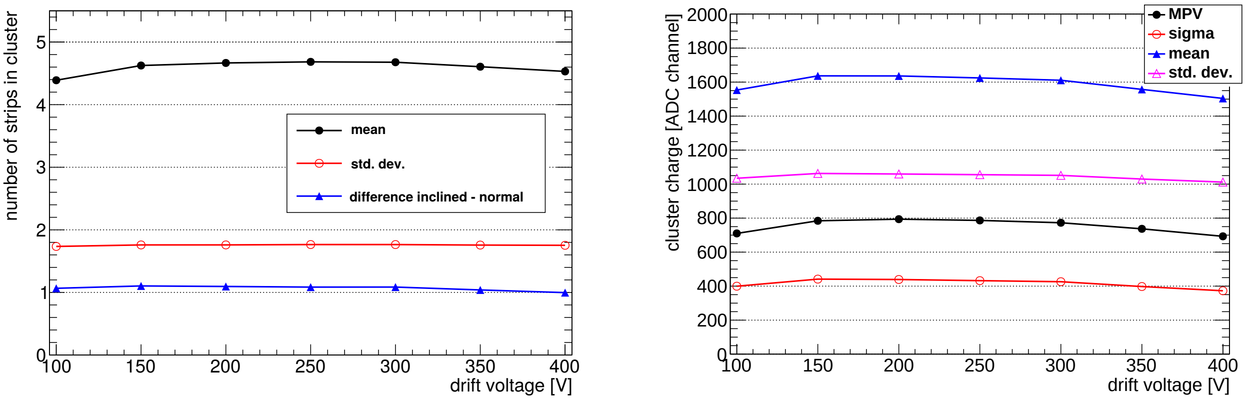

(a) Properties of the multiplicity, i.e. the number of strips in a cluster, as function of the drift-voltage. The mean, the standard deviation (std. dev.) and the difference of the mean for inclined and normal tracks are shown. Normal tracks are considered between ±2.3° inclination, while inclined tracks are more than 24° tilted.

(b) Properties of the cluster-charge distribution as function of the drift-voltage. The most probable value (MPV) and the sigma are parameters extracted by a Landau-fit of the distributions. Also shown are the mean and the standard deviation.

Figure 5.14.: The distributions of cluster-properties, i.e. multiplicity and charge are in certain ranges independent of the drift-voltage. Therefore this operational parameter should only slightly influence the efficiency of the detector. Shown are exemplaric the properties for module 3 eta-in board 7 with the nominal gas-mixture of Ar:CO_2 93:7 volume percent at an amplification-voltage of 560 V.

The dependence of cluster-properties on the drift-voltage can be seen in figure 5.14. The drift-field influences only indirectly the amplification-process by guiding the electrons to the mesh. The ratio of amplification to drift-field determines in combination with the gas-mixture and the mesh-type the transparency of the mesh to the electrons. The transparency is higher for higher ratios of amplification to drift-fields. This can be explained by the field-lines, which are guiding the electrons through the mesh-windows. Therefore a decrease of pulse-height with rising drift-voltage is expected as the higher drift-field leads to a lower ratio. This effect is slightly seen for the increasing drift-voltages. At lower drift-voltages also a decrease of pulse-height can be seen. This is due to the finite charge-integration-time of APV-electronics. The low drift-field leads to a long drift-time of the electrons. This causes a loss of charges outside of the APV-time-window. Therefore the cluster-charge drops for too low drift-fields.

Cluster-charge-maps are used for the homogeneity-investigation of the pulse-height over the active-area [Lösel, 2017]. The active-area is therefore subdivided into partitions. In precision-direction the width of these partitions corresponds to the width readout by one APV[7]. Therefore the effects of different chips can be disentangled. In non-precision-direction a width of 10 cm is used due to the coarse resolution of the scintillator-hodoscope. Exemplaric distributions are shown in figure 5.15. Here the cluster-charge distributions are fit with a Landau-function for each partition separately. The most probable value is shown color-encoded in these maps for the corresponding partition. Differences between the boards and the high-voltage-sectors can be seen. Also local hot-spots are found. These are probably due to variations of the pillar-height.

---

[7] One APV readout 128 strips. The strips have a pitch of 0.425 mm. For the partitions a width of 54.4 mm is used.

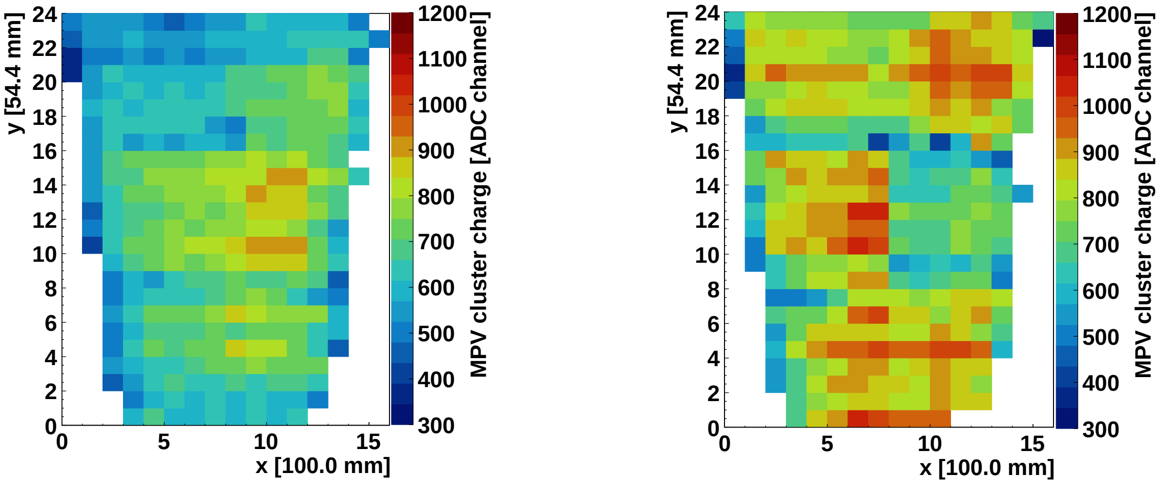

(a) Stereo-in. **(b)** Stereo-out.

Figure 5.15.: Maps of the most probable value (MPV) of the cluster-charge distribution determined by a Landau-fit. The cluster-charge influences directly the efficiency as too low charged signals are suppressed by noise-cuts. Exemplaric plots for module twelve at 570 V amplification-voltage.

5.3. Efficiency

The efficiency of a tracking detector is calculated using the comparison of reference tracks and the detector response. Not only a signal should be produced, but also a good track should be reconstructible. As each layer of the Micromegas modules for the NSW should work like a independent detector, these layers are investigated separately. For the tracks of the CRF the comparison with the module can be achieved by requiring the passage through the active area. A good detector response can then be defined if the hit in one layer is within a certain range to the track intersection prediction. For this purpose the hit reconstruction can be achieved by calculating the position of the leading cluster within one layer in the CRF coordinate-system. The efficiency is then calculated by dividing the number of good responses by the total number of tracks passing through the detector. This quantity is dependent not only on the operational parameter but can also vary over the active area of the layer. Therefore the efficiency has to be calculated separately for each partition of the active area. Using this also effects coming from the coarse resolution of the scintillator-hodoscope can be disentangled.

Exemplaric efficiency-maps can be seen in figure 5.16. For these distributions a hit is considered as efficient, if the difference of measured and reference position is between ±5 mm. The value of 5 mm is motivated by two considerations. First the drift-gap has a width of 5 mm. Therefore the inhomogeneous ionization of the muons can lead to reconstruction-differences up to 2.9 mm[8]. The range in which a good hit can be reconstructed is further broadened by multiple scattering. So the large range accounts for the accumulation of these two effects. The second aspect is more pragmatic. The evaluation of the modules using the implemented software has to be performed over the whole series production. Different effects like the mechanical positioning of the module in the CRF could broaden the difference-distribution of measured and reconstructed position. This is shown in chapter 7.1.1. In order to ensure still a reliable efficiency reconstruction a broad range has been chosen.

As can be seen by the comparison of the two efficiency-maps in figure 5.16, several features have to be understood for their interpretation. Starting with 5.16b the trapezoidal shape can be recognized immediately. The orientation of the strips is from left to right, therefore the precision coordinate is on the y-axis. Horizontal lines correspond to single APV-chips and therefore to 128 strips. The lines with lower efficiency at the bottom and the top can be explained by the not-connected strips in the design. This was a design-choice to overlap exactly with the active area of the rotated stereo-strips. Therefore a loss of efficiency is expected. The missing partitions for the lower APV can be explained by the low statistics, which leads to an exclusion of these bins. Another effect which can be seen at the left border is a rise of efficiency upwards. Here the trapezoid covers more area for partitions with higher y-value. These edge effects have to be neglected therefore the analysis focuses on partitions in the central areas. The inner APVs which have a lower efficiency can either have a collection of dead strips or the electronics could be problematic.

The effect of bad electronics can be seen especially in figure 5.16a. Here also the differences between the three readout-PCBs[9] are visible. For the central board (7) two effects are adding up. The high-voltage-sectors divide the readout-boards into two halves. The central board (7) has the left sector not on the nominal, but on a lower voltage[10]. A lower voltage leads to less amplification, which reduces the efficiency due to the loss of low-charged

---

[8] For the CRF the maximum track angle is 30°. Therefore the projection of the path onto the readout-area can be of this size.

[9] The small board (6) is ranging from y-partition 0 to 8. The central board (7) is ranging from y-partition 8 to 16. The large board (8) is ranging from y-partition 16 to 24.

[10] The voltage on some sectors have to be reduced due to large currents. Currents occur due to discharges which create conductive plasma-channels. These channels could harm the anode-surface. The discharges can be created by not well prepared anode-surfaces.

signals. Therefore the left side of this board has lower values. The second effect is problematic electronics. Four APVs per layer are read out by one FEC-card. These chips are connected to the module on the same adapter-board, reading out one sixth of a module. The FEC reading out the lower part of the central board (7), this means y from partition 8 to 12, was problematic during this measurement. Therefore the efficiency is systematically spoiled in this region. The same effect can be seen for the large board (8). Here the FEC-card reading out the upper part of the board is also spoiling the efficiency reconstruction. To prevent these effects worsening the performance two things have to be done. During the final assembly of the module it has to be ensured that each high-voltage-sector reaches the required voltages. This is achieved over several days of testing and reassembling in order to bring the sectors into operational voltage-range. Also the electronics have to be tested during pedestal-measurements.

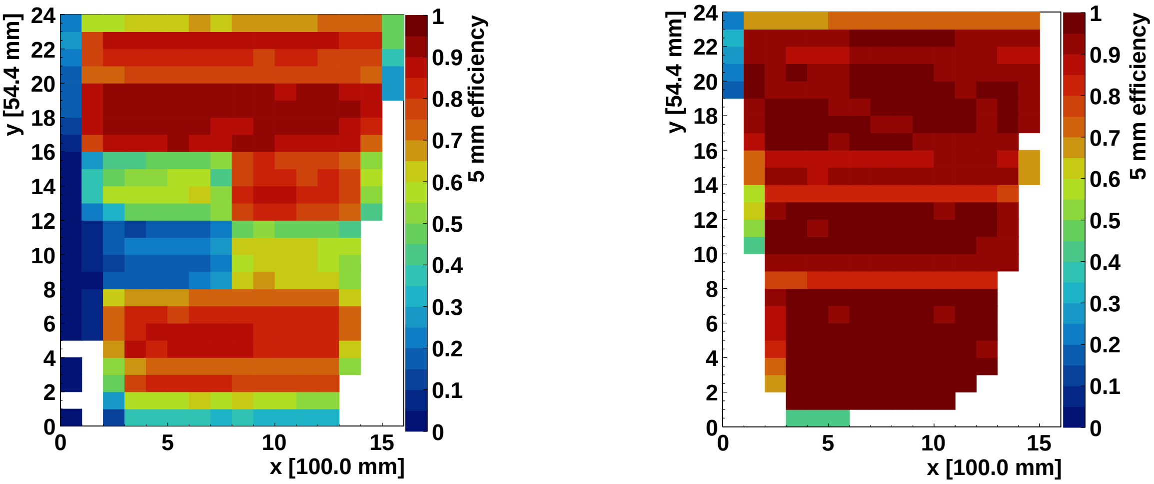

(a) Module 6 eta-in at 570 V amplification-voltage and 300 V drift-voltage with the nominal gas-mixture of Ar:CO_2 93:7 vol%. The left high-voltage sector of the central board (7) could run only at 540 V. This degrades the efficiency locally.

(b) Module 8 eta-out at 665 V amplification-voltage and 475 V drift-voltage with an alternative gas-mixture of Ar:CO_2 80:20 vol%.

Figure 5.16.: 5 mm efficiency for a very problematic layer (left) and a very good layer (right).

The effect of bad electronics is not detector-related, because the used APVs are only for series testing before shipping of the modules to CERN. To investigate the magnitude of impact on the efficiency, the pedestal-measurements of module seven is investigated. The baseline-fluctuations of the stereo-layers, shown in figure 5.17c, reconstruct for some APVs large fluctuations. This corresponds to a problematic behavior. Some chips have less fluctuations and low sigma values are promising good signal-responses. For the same two layers the efficiency-maps are shown in figure 5.17a. Here several lines[11] of low efficiency are observed next to lines with high efficiency. In order to compare these two measurements the efficiencies are averaged over the central length of the strips for each APV individually. The efficiency per APV can be seen in figure 5.17b. The sigma behavior can be compared directly to the efficiencies[12] in this plots. For the stereo-in layer the three APVs with the largest fluctuations show also the lowest efficiency. An almost linear dependence can be seen for APVs on the large board (8) of stereo-out, both in the efficiency and in the sigma behavior for six APVs on the right-hand side.

The similarities between the two measurements suggest a correlation between the efficiency and the baseline-fluctuations. This is expected as noise of the electronics aggravates the discriminability of the signals. To quantify this effect the efficiency is plotted as function of the baseline-variation per APV in figure 5.18a. Here the correlation can be seen for each layer individually. The green fit suggests a mean loss of efficiency of about 0.5% per ADC channel of variation. The threshold-level of the electronics and the software are influencing this correlation. Also the pulse-height biases this dependence as larger signals can be discriminated better from noise. This can be noticed by comparing the eta and the stereo-layers. Typically the stereo-layers have higher pillars than the eta-layers[13]. Due to this the pulse-height of the stereo-layers is lower than for the eta-layers (see figure 5.11). Therefore the efficiency of the stereo-layer is systematically lower at the same voltage than for the eta-layers.

During the validation-measurements of the modules for the NSW a turn-on-curve for the individual high-voltage-sectors[14] is reconstructed. These curves determine at which amplification-voltages the sector reaches certain

---

[11] The orientation of the plots in figure 5.17a is rotated with respect to figure 5.16. This is done to make the plots better comparable to the pedestal-measurements.

[12] The APVs at the border have to be neglected due to the un-rooted strips.

[13] This is a production issue of the PCBs. The eta and stereo-PCBs are produced by different companies for the SM2 modules.

[14] In the investigation only the inner area of the high-voltage-sectors is concerned. This is done to avoid border effects like the trapezoidal-shape or the overlap due to insufficient alignment. Therefore the sectors consider an effective area of 320 mm × 186.5 mm size.

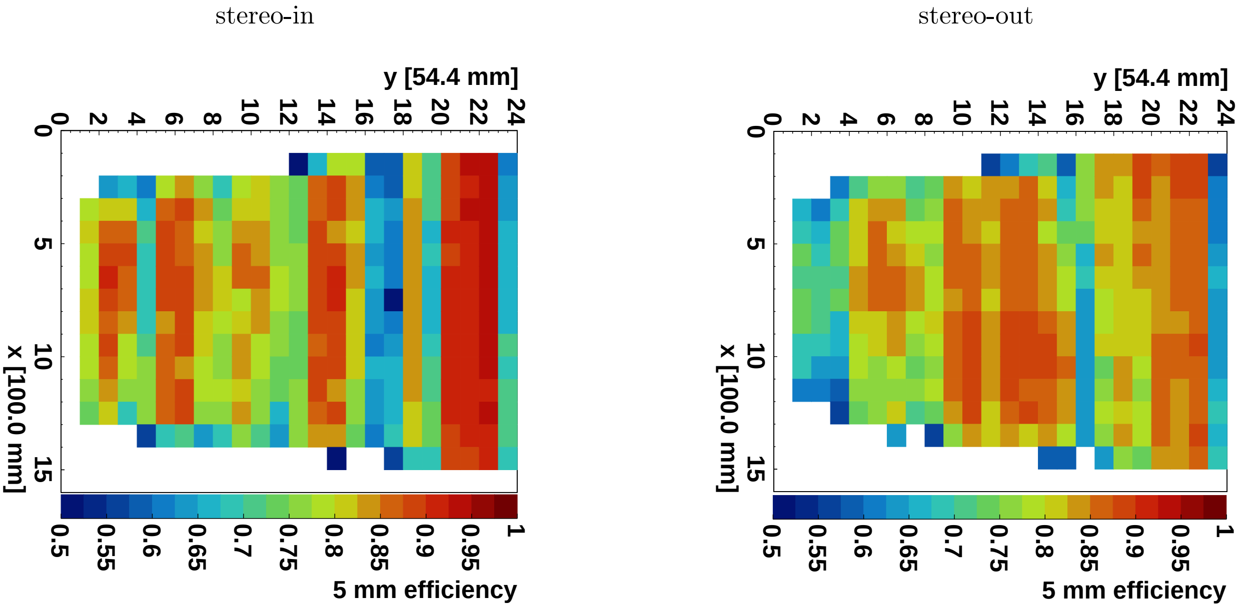

(a) 5 mm efficiency-map.

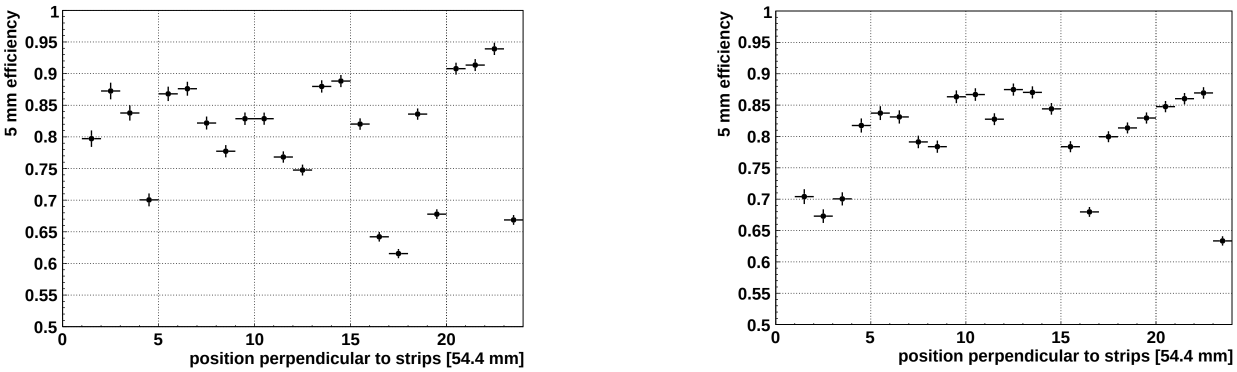

(b) 5 mm efficiency for the central area of each APV individual.

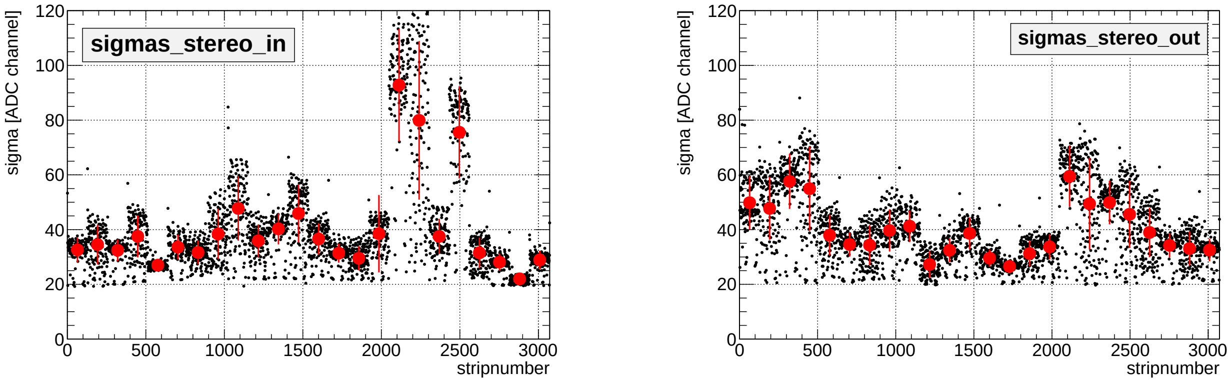

(c) Baseline-fluctuation for each channel (black) and averaged over one APV (red).

Figure 5.17.: The efficiency-maps show bands with lower efficiencies. These bands corresponds to single APV-chips. For some of these chips higher baseline fluctuations are measured.

reconstruction-efficiencies. At low voltages the efficiency is zero due to the missing gas-amplification. Beginning from a certain voltage, at which sufficient avalanches occur, the efficiency rises to a maximum. In an ideal case the rise of this curve would be very step, until a plateau is reached. This plateau describes the maximum reachable efficiency, which can be limited due to several effects. Unconnected strips, noisy electronics or inhomogeneous gas-amplification can limit the efficiency. A long extension of the plateau is desirable, before the maximum-voltage is reached. The maximum-voltage is the highest voltage, which can be reached before continuous discharging between mesh and anode starts. For most of the SM2 modules tested at Munich with the nominal gas-mixture this voltage was around 570 V. Unfortunately the modules reach at this voltage hardly the efficiency-plateau as can be seen in figure 5.19. In these plots the comparison between different reconstruction techniques is made. The described 5 mm-efficiency is seen for one high-voltage sector of the eta-in layer of module twelve in the black

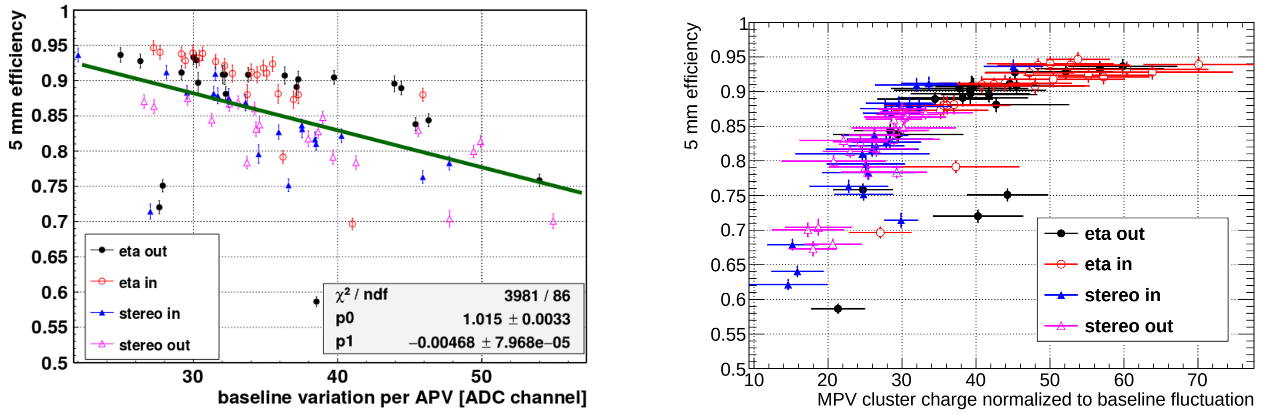

(a) The 5 mm-efficiency as function of baseline-variation per APV.

(b) The 5 mm-efficiency as function of the most probable cluster-charge normalized to the baseline-variation.

Figure 5.18.: The efficiency is affected by electronic noise and the signal-height seen as cluster-charge. The efficiency-measurement was performed with module seven at the nominal amplification-voltage of 570 V.

curve of figure 5.19a. For the red curve not all tracks are considered, but an additional hit in the eta-out layer within 5 mm to the track is requested. This subset of tracks is then considered for the efficiency-calculation. As can be seen a systematically slightly higher turn-on-curve is reconstructed. An explanation for this could be mis-reconstruction of the MDTs, which would be discarded by this selection. Also large noise, which is spread over the whole module could be excluded using only the subset. Another point is the selection of only high energy muons. The MDT-chambers have much larger active volumes compared to one Micromegas-layer. Therefore the detection-probability for minimum-ionizing-particles should be higher in the larger volume. The request for a hit in another layer can then mainly select particles with a larger energy-deposition. Even shower of cosmic particles could cause the degradation of the efficiency for a single layer. In figure 5.19b another effect of the MDT-tracks on the efficiency is investigated. Here the comparison between normal and inclined tracks is made. The tracks are distinguished at 10° inclination. The efficiency for normal tracks is increased. One would assume higher efficiencies for inclined tracks due to the longer path in the drift-gap and therefore an higher energy-deposition. This effect gets lost due to the spread of charges over several readout strips. The spread leads to a decreased charge per strip. Therefore the efficiency is limited due to the electronics threshold and the zero-suppression.
The undesired low efficiencies for the maximum-voltage lead to several investigations during the early phase of the series production. One investigation concerned the usage of a different kind of micro-mesh for two layers of module twelve. Meshes differ in their transparency of electrons and also affect the amplification and drift-field [Kuger, 2017]. In figure 5.19c turn-on-curves are compared for module twelve. Shown are the curves for individual high-voltage-sectors of each layer. The outer two layers were assembled with a mesh of 45 µm aperture and a wire-thickness of 18 µm. The inner two layers were assembled with the nominal mesh of 71 µm aperture and a wire-thickness of 30 µm. For all amplification-voltages a higher efficiency is reconstructed for the layers with the alternative mesh. This can be explained by the higher cluster-charge for these layers. An explanation for the higher pulse-height is the larger expected amplification-field for meshes with smaller wire-thickness [Kuger, 2017].
Another observation is the lower efficiency of the stereo-in layer compared to the eta-in layer. As mentioned in the last chapter 5.2 the pillar-height varies between the readout-boards. Therefore the pulse-height differs between eta and stereo-layers.

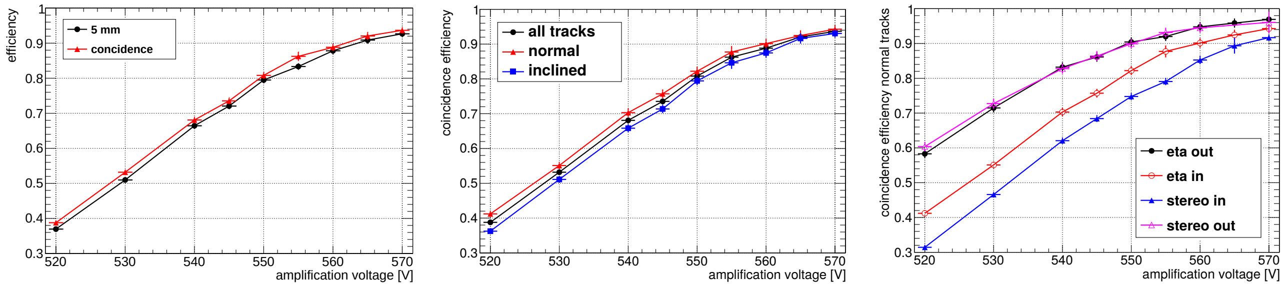

(a) For the 5 mm-efficiency the hits in the eponymous range are considered. The coincidence-efficiency requires for the tracks a hit in the other layer on the same readout-panel of the module.

(b) Coincidence efficiency for all, normal and inclined tracks. The separation for normal and inclined tracks is made for this plot at 10°.

(c) For the layers eta-out and stereo-out of module 12 different meshes were used. A positive effect on the turn-on-curve is reconstructed.

Figure 5.19.: Efficiencies of single high-voltage-sectors as function of the amplification-voltage. The detector-quality, but also the reconstruction method influence the turn-on-curves. Exemplaric plots for module twelve. The eta-in layer is considered for the first two plots. The central area of the high-voltage sectors are considered, with a size of about 320 mm × 186.5 mm.

The effect of varying pulse-height across the active surface can be seen very drastically for the eta-in layer of module twelve, shown in figure 5.20a. A strange observation is the similar development of the cluster-charge along the strips, so in x-direction, for the three different boards. The boards were produced separately and should therefore have no common distribution of the pillar-heights. This development suggests also other effects besides the pillar-height, which influence the pulse-height. One possible explanation for this layer could be a clogged gas-supply at the upper left corner. The gas is distributed from pipes placed at the parallel borders of the trapezoid. For the measurements in the CRF the inlet is on the long side and the outlet on the short side. A clogged inlet leads to an inhomogeneous gas-flow. Combined with leakages this can produce regions with a larger fraction of gas contaminated by air, which reduces the gain. As seen in figure 5.20b also the efficiency follows the same behavior. This observation affirms the strong correlation between pulse-height and efficiency.

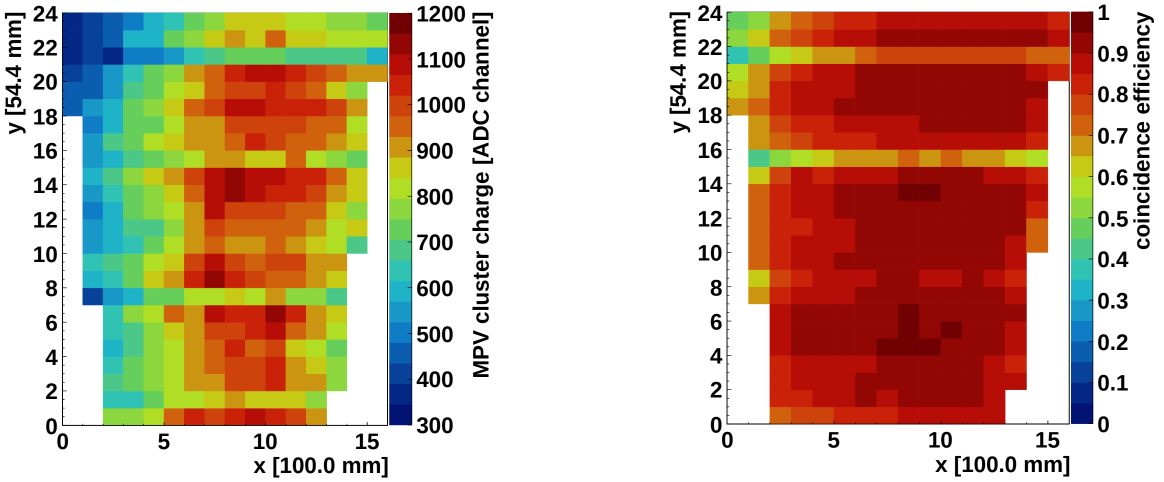

(a) Map of the most probable value (MPV) of the cluster-charge distribution determined by a Landau-fit.

(b) Map of the coincidence-efficiency. Here only tracks are considered, which generated a signal also in the other eta-layer.

Figure 5.20.: The cluster-charge influences directly the efficiency as too low charged signals are suppressed by noise-cuts. Maps of the pulse-height and the efficiency over the active-area suggest a strong correlation. Exemplaric plot of module twelve eta-in at 570 V amplification-voltage.

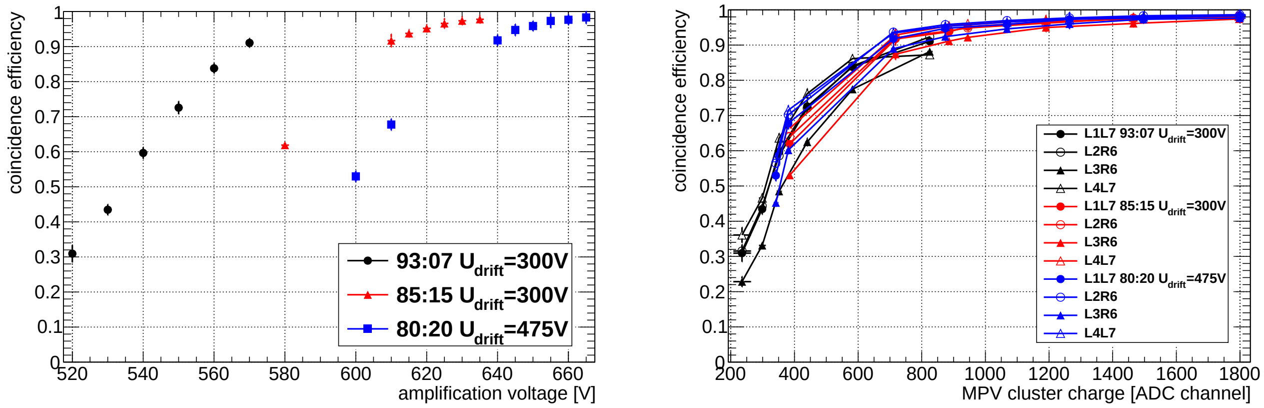

(a) Coincidence efficiency as function of the amplification-voltage. Shown are exemplaric curves for a high voltage sector of the eta-out layer of module 8.

(b) Coincidence efficiency as function of the most probable value (MPV) of a fit to the cluster-charge distribution. Shown are the curves for single HV-sectors of all layers of module 8.

Figure 5.21.: The efficiency is directly influenced by the pulse-height. The three colors in the two plots indicate three different mixtures of Ar:CO_2.

The efficiency is also investigated for the Ar:CO_2 gas-studies performed with module eight. The results are shown in figure 5.21. The higher reachable pulse-heights for the two gas-mixtures with a larger fraction of CO_2 leads accordingly to higher efficiencies. In comparison to figure 5.9b one observes similar efficiencies for similar pules-heights in figure 5.21a. The efficiencies for 93:7 at 570 V, 85:15 at 615 V and 80:20 at 640 V are almost identical. This can be explained by the fixed electronic threshold and zero-suppression. The amplification has to reach a certain value to generate signals to overcome the threshold. Therefore the correlation of pulse-height and efficiency in figure 5.21b can be understood as the electronic sensitivity. The correlation reconstructs the transition to efficiencies above 90% somewhere between 600 and 800 ADC channel. The large spread of efficiencies for lower amplification-voltages can be understood due to problems of noisy electronics. The upper limit of this curve converges to the true limitation for this electronics without problems or connectivity issues.

The same behavior is observed for single APVs as seen in figure 5.18b. Here the cluster-charge is normalized to the baseline-variation of the corresponding chip. Therefore it can be concluded that the cluster-charge has to be about 40 times as large as the baseline-variation in order to achieve 90% efficiency with this setup. Vice versa this corresponds to the requirement that the baseline-variation has to be about 2% of the cluster-charge for 90% efficiency.

The measurements with module zero allow for a direct comparison of testbeam and cosmic-reconstructions. This is shown in figure 5.22. Due to a different anode production, the prototype module was operated at slightly higher amplification-voltages. A first observation is the much lower efficiency for low voltages reconstructed in the CRF than in the testbeam. This can directly be explained by the lower cluster-charges. During both measurements the eta-layers show a higher pulse-height. Therefore their higher efficiency as seen in the CRF-measurement is expected. For the testbeam measurement this is not observed due to unconnected strips for the eta-out layer in the measurement region. The differences of the cluster-charge evolutions for these two measurements could be explained by several effects. The energy spectra of the muons during the testbeam is certainly different to the spectrum of the cosmic particles. Due to the averaging over all incident-angles, the cluster-charge distribution for the CRF is deformed compared to the testbeam. Next to this the investigated area is much larger for the cosmic-measurement. Another reason for the differences could be the different noise-environment of the two setups. As seen during pedestal-measurements the overall noise-level is increased after installation between the MDT chambers in the CRF. This higher noise-level probably leads to the loss of low charged signals and therefore to the decrease of the cluster-charge. But also here the direct correspondence between cluster-charge and efficiency is observed. The eta-in layer reaches during testbeam 90% efficiency at a voltage of about 570 V with a cluster-charge of about 1100 ADCchannel. A slightly higher cluster-charge of about 1200 ADCchannel at 90% efficiency is observed in the CRF for an amplification-voltage of 580 V. A strong correlation between pulse-height and efficiency of module zero can also be found in [Herrmann, 2019], shown as maps for eta-in. Further differences between testbeam and cosmic-measurement could be slightly different gas-mixtures, humidity in the gas, the temperature as well as absolute pressure.

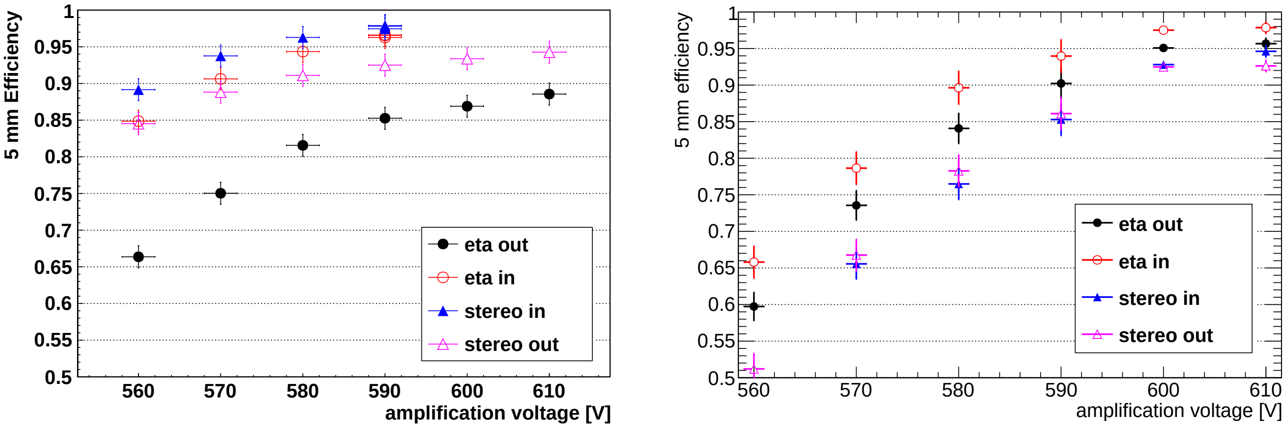

(a) Efficiency at testbeam. **(b)** Efficiency in the CRF.

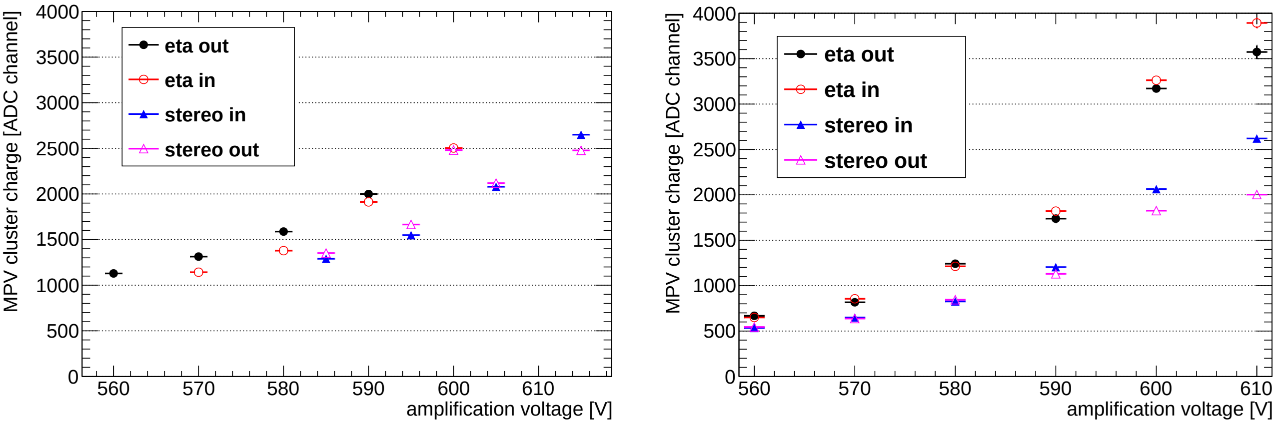

(c) MPV cluster-charge at testbeam. **(d)** MPV cluster-charge in the CRF.

Figure 5.22.: Module zero is investigated both during a testbeam at the H8-beamline of the SPS at CERN, as well as in the CRF. The direct comparison reveals lower reconstructed efficiencies at low voltages during the CRF measurements. This can be explained by the also lower cluster-charges. Results for the testbeam are taken from [Flierl, 2018]. For the CRF-measurements one HV-sector per layer is considered.

Concluding, the efficiency-reconstruction in the CRF is limited due to the noise-level, as well as the effects of the cosmic particle distributions. None the less the measurements can be used to investigate the differences between the modules and layers. Also effects coming from the inhomogeneities of the production-processes can be disentangled.

6. Reconstruction of Readout-Board Alignment

For a precise track reconstruction the exact knowledge of the readout pattern is fundamental. The pattern could be distorted from the nominal design by several effects. On a single PCB the pitch and the shape of the copper strips can deviate due to the manufacturing process. Also the further treatment during production of the readout panels can lead to irregularities. The main effect of deviations to the nominal pattern is expected to come from the segmentation of the readout anode.

Each segment, in this case a PCB, can have an individual shift and rotation within the readout plane. Perpendicular to the readout plane deviations are kept small by the dedicated planar construction. The following chapter outlines the approaches to reconstruct and calibrate the shifts and rotations within the readout plane. First, an optical inspection of the bare readout panel will be described, which enables a fast quality control during production. Second, a more time consuming, but more complete and application-related reconstruction with cosmic-measurements will be discussed.

6.1. Optical Surveying using a Coordinate Measuring Machine

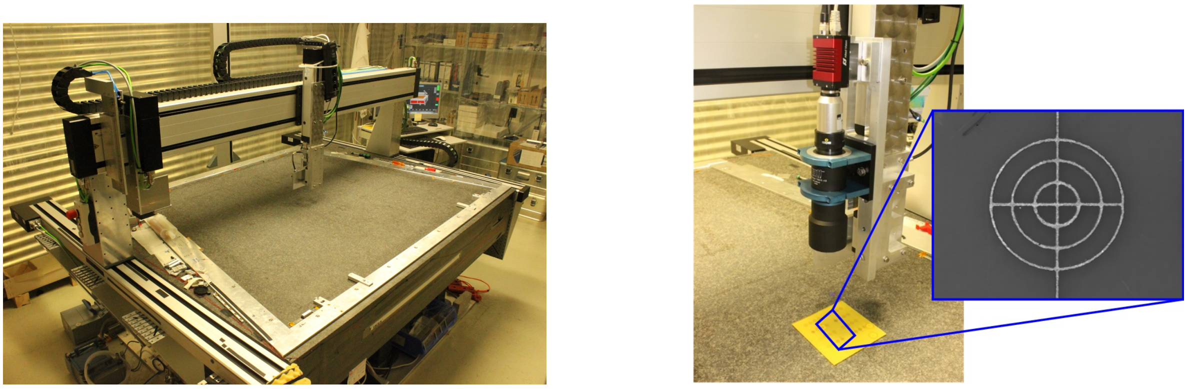

(a) Picture of the Coordinate Measuring Machine at the LMU. The bridge can be moved on the two rails along the sides of the table. In the other direction the arm can be moved along a rail in the bridge.

(b) Picture of the telecentric camera attached to the measurement-arm above a test-PCB with a marker. The arm is moved on constant height above the table to take pictures with the camera at multiple marker positions. A detail of the marker-image is superimposed.

Figure 6.1.: The Coordinate Measuring Machine (CMM) at LMU consists of three ball-type-linear-drives (behind the black sealing) which define the three axis. These drives are attached to the granite table at the borders where the tapered sides of the panels are located. Therefore this axis (y) defines the precision coordinate perpendicular to the strips. The drive in the bridge holding the telecentric camera enables the movement along the strips in non-precision-direction (x). The measurment-arm can also be moved vertically (in z) but is kept at constant height during measurements.

To reconstruct the alignment of the PCBs the position of specific markers have to be measured relative to each other. The alignment of the boards can be deduced using the nominal positions and comparing the measured positions to these. At the LMU the position-measurement is performed using a Coordinate Measuring Machine (CMM) combined with a telecentric camera.

The CMM is attached to the granite-table on which the panel is glued before. Two rails are screwed at the sides of the table, where the tapered borders of the panel are placed. The axis defined by these rails is perpendicular to the readout strips and therefore in precision-direction. On these rails a bridge can be moved with another rail giving the non-precision-axis along the strips. At this bridge a measurement-arm is attached, which can be moved up and down, so perpendicular to the surface. The position of the measurement-arm is controlled and measured by the linear-bearing-units, which move the machine on the rails. Each unit has a nominal resolution of 10 µm.

The camera is mounted at the measurement-arm facing the granite surface. It features a telecentric optic in order to ensure a straight positioning and to enable the measurement at various heights [Beyerer et al., 2016], [Opto Engineering, 2019]. A telecentric optic makes an orthographic projection of an object onto the camera. This is achieved by an aperture at the focal point of the lens-system. Pictures of the markers on a panel surface are taken in order to measure their position. The position of the marker in the CMM coordinate-system can be reconstructed by combining the position of the CMM during the picture taking and the position reconstructed in the picture.

This approach has two drawbacks. First, one has to be sure about the position information given by the CMM. Therefore the deviations of these values have to be investigated. The calibration of these deviations will be discussed in the following chapter 6.1.1. The second drawback is that the pictures of the markers have to be evaluated in order to reconstruct the position of the marker. This detection and fit of the marker position will be discussed in chapter 6.1.2. Both of these issues were investigated by two supervised and dedicated bachelor theses [Feil, 2017], [Neubert, 2018].

6.1.1. Calibration of the CMM

The deviations of the CMM movement from ideality can be measured using an external reference system. For this a laser-interferometer is chosen. A common industrial laser-interferometer can measure distances with a sub-micro-meter precision in one direction. By aligning the beam along one of the CMM-axes the deviations can be calculated by the difference of the nominally moved distances and the measured distances by the laser-interferometer.

In order to calibrate the CMM deviations this measurement has to be performed for both axes and at several positions. The deviations of the machine should then be calculable at each position in the measurement-volume by interpolating these measurements. As the camera for the picture taking is attached to the measurement-arm of the CMM, the deviations of this arm have to be calibrated. The measurement-arm can tilt with respect to the surface, therefore not only errors in the plane of measurement have to be considered. The tilt can be measured by either determination with an angular optic of the laser-interferometer or by combining measurements at several heights.

The laser-interferometer consists of a laser-head, a reference-element and a moving-element (see figure 6.2). The laser-head emits the laser-light with vertical and horizontal polarizations for the interference. For the detection of the reflected beams in the laser-head, a CCD is integrated. The reference-element acts as beam-splitter of the two polarizations and as reflector for one of the two components. The second component is emitted to the moving-element, which just reflects this component on a parallel path. The distance between two points can be measured by counting the interference maxima of the two laser-light-components.

One laser-light-component travels to the reference-element and back, therefore its path-length stays constant. The second component traverses the reference-element, reaches the moving-element and is reversed. While the moving-element is moved the path-length of the second component changes and therefore the interference between the two components is changing. The moved distance is given by the number of counted maxima times the wavelength of the laser-light. Systematic errors arise due to the dependence of the wavelength on the environment, i.e. temperature, humidity and pressure. Therefore these quantities are measured simultaneously and the wavelength is corrected.

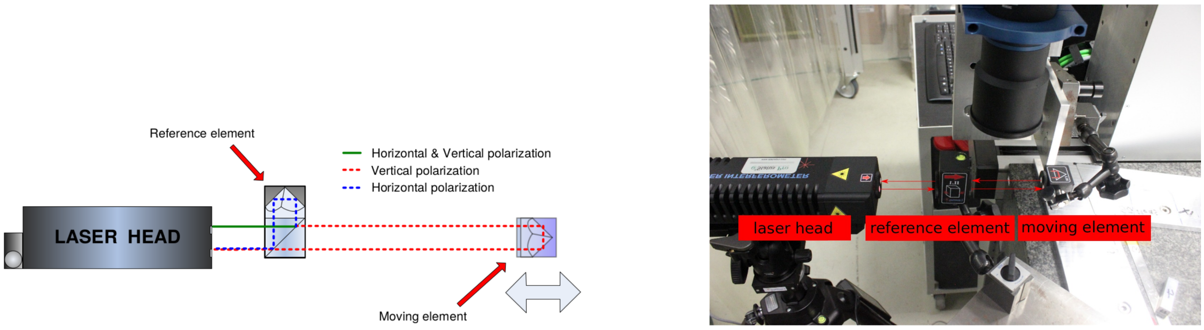

(a) Sketch of the measurement setup for the laser-interferometer. The diagonally polarized beam is split in the reference-element. Horizontal polarization is reflected back directly. Vertical polarization reaches the moving-element, before reflection. The reflected beam is superimposed to the reference beam on a CCD in the laser-head. Taken from [Lasertex, 2015].

(b) Picture of the measurement setup with the laser-interferometer. The moving-element acting as reflector is attached to the measurement-arm. The reference-element is fixed to the table. The laser-head emits a diagonally polarized beam and collects the reflected light on a CCD. Taken from [Feil, 2017].

Figure 6.2.: For the measurement of the CMM-movement-deviations a laser-interferometer is used. The movement of the CMM-measurement-arm is measured using the attached moving-element. The interference of the two beam-components is measured on the CCD integrated in the laser-head. The deviation is reconstructed using the counts of interference-maxima.

For a deviation measurement first the laser and the optics have to be prepared. The path of the laser is coarsely aligned by eye with the measurement axis by adjusting the laser-head, which is mounted on a tripod. A good attachment of the moving-element is necessary to ensure the same movement as the measured object. This is crucial as an uncommon movement between moving-element and measurement object would distort the measurement significantly. The laser-path is aligned precisely with the machine movement by repeating the following steps:

1. Locating the moving-element with the machine to the point farthest away from the laser-head in the measurement-direction.
2. Adjusting the laser-head so that the laser-spot hits the moving-element at the right position.
3. Relocating the moving-element with the machine to a close point near the laser-head.
4. Adjusting the moving-element to collect the laser and reflect it back onto the CCD in the laser-head.

The typical number of iterations is between 5 and fifteen. For this procedure the reference-element is not present. When the laser-path is aligned, the reference-element has to be positioned between laser-head and moving-element. Here the optic has to be aligned simultaneously to the outgoing and the reverted beam. As last step it has to be checked if the spot of the laser-beam is hitting the CCD, while the machine is moving the moving-element on the whole measurement path.

During the measurement the machine is moved in steps. After each step the machine waits for the measurement of the laser-head, as the beam has to stabilize. This takes about ten seconds. Then the difference between nominal distance and measured distance is calculated and the machine is moved to the next position. For the right choice of the step-length several measurements were taken over different total lengths and with different step-sizes. As seen in figure 6.3 a step-length of 2 mm is sufficient to reconstruct the structure of deviations.

The first undesired observation are the large overall fluctuations of the deviations with more than ±100 µm. Thus, uncalibrated measurements with this machine are expected to have large systematic errors. Second, a twofold periodic structure is observed as seen in the detailed view in figure 6.3b. To evaluate this structure the discrete Fourier-transform is calculated, which reveals the frequencies and amplitudes of the signal (see 6.3c). The oscillation with a larger amplitude of about 50 µm has a frequency of $0.01\,\mathrm{mm}^{-1}$. This can be explained by the screwing of the rails for the machine movement at distances of 10 cm. The faster oscillation with a frequency of $0.05\,\mathrm{mm}^{-1}$ has an amplitude of about 25 µm. The ball-type-linear-drives are using threads with a periodicity of 2 cm, which leads probably to this deviation behavior.

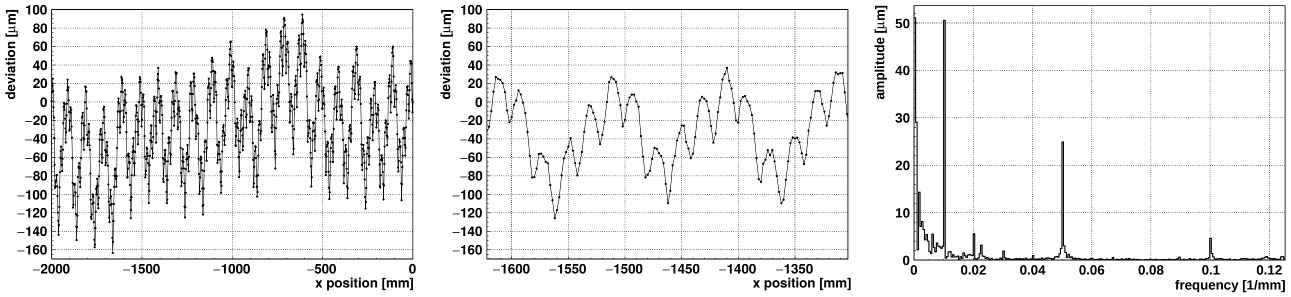

(a) Deviation of the CMM movement to the nominal position measured by the laser-interferometer along the non-precision position of the bridge (along the strips). Undesired large fluctuations of more than ±100 µm are a superposition of several imperfections of the machine movement.

(b) Detail of the deviation measurement along the non-precision-direction from 6.3a. A periodic structure is visible with two kinds of oscillations. The smaller has a height of about 50 µm and a peak distance of about 20 mm. The larger oscillation has a height of about 140 µm with a periodicity of about 100 mm.

(c) Discrete Fourier-transform of the signal from 6.3a. Two main oscillations are observed with frequencies of $0.01\,\mathrm{mm}^{-1}$ and $0.05\,\mathrm{mm}^{-1}$. Their amplitudes are about 50 µm and 25 µm. The other peaks are higher orders of these two main contributions.

Figure 6.3.: The deviations of the coordinate measuring machine (CMM) are a convolution of an overall structure with two kind of oscillations. The overall structure comes from the mechanical imperfections, while the oscillations are due to the periodic screwing and the ball-type-linear-drives. Taken from [Feil, 2017].

The inner structure of these two oscillations enables the reduction of measurement points. For this the Whittaker-Kotelnikov-Shannon-sampling-theorem [Kotelnikov, 1933] is used. It states that any signal is reconstructible if the sampling-frequency is higher than two times the maximal frequency of the signal. As the maximum observed frequency is $0.05\,\mathrm{mm}^{-1}$ the step-length of 2 mm is increased to 8 mm. This corresponds to a reduction of the sampling-frequency from $0.5\,\mathrm{mm}^{-1}$ to $0.125\,\mathrm{mm}^{-1}$. Therefore the sampling is well within the limit to apply the theorem. With this the measurement-time of about 5 h is reduced to only a quarter of that time. The time-reduction enabled the variety of measurements explained in the following. Using the Whittaker-Kotelnikov-Shannon-sampling-theorem the signal $f(x)$ can be reconstructed at the position x using the formula

$$f(x) = \sum_{n=1}^{N} f_n \cdot \frac{\sin\left[\pi \cdot \left(\frac{x}{d} - n\right)\right]}{\pi \cdot \left(\frac{x}{d} - n\right)} \quad . \tag{6.1}$$

Here the sum goes over the N sampling-points. Therefore f_n corresponds to the value measured for the n-th sampling-point. The distance between the samplings is given by d. The latter part of the formula can be rewritten as the sinc-function.

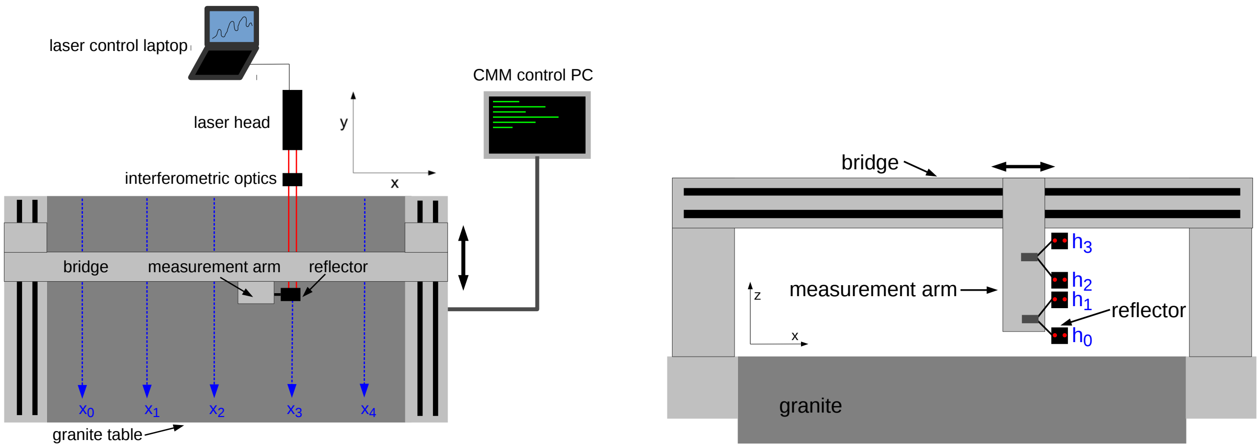

(a) Top view of the measurement setups for the calibration of the precision-axis of the coordinate measuring machine (CMM). At five positions in x direction measurements were performed along the linear drives in y direction.

(b) Front view of the measurement setups for the calibration of the tilt of the measurement-arm of the CMM. For each position in x direction measurements at four heights above the granite were performed.

Figure 6.4.: Several measurements have to be performed for the calibration of the CMM. The positions and directions were chosen as seen in the sketches to interpolate the errors of the machine. Taken from [Neubert, 2018].

The systematics of the machine are investigated using deviation-measurements along several lines at different positions, also repetitive and from opposite directions. The measurements from opposite directions reconstruct the same deviations. Therefore it can be concluded that no systematic errors due to the choice of direction occurs. The difference between measurements from the same side of the machine going forth or back showed an influence of the backlash. Backlash occurs due to the change of the movement direction, which causes mechanical parts to lose temporary grip. For the non-precision-axis along the bridge a backlash of about 5 µm and for the precision-axis of about 40 µm is measured. This is very unfortunate, but can be explained by the bridge-weight, which has to be moved along the precision-axis. To account for this effect during the alignment-measurements of the panels, the movement along the precision-coordinate is only made in one direction. Repetitive measurements of the same axis reconstruct a repeat-accuracy of about 7 µm. The deviations along the bridge, so in non-precision-direction, showed no dependence of the position perpendicular.

The most problematic obstacle for measurements with this setup are the dependencies of the measurement-arm-movement along the precision-axis. The movement along this axis shows a dependence on the position of the arm along the bridge, so along the orthogonal axis. This can be seen in figure 6.5a. Here, the measurements at five positions equally distributed along the bridge are compared (see figure 6.4a). Using the measured deviations the deviations at any point should be reconstructible by an interpolation. [Feil, 2017] showed that an interpolation in general works (see figure F.1 in the appendix).

Comparing figure 6.5a with figure 6.3a, one recognizes much larger deviations. An explanation for this is the measurement height. As indicated in figure 6.4b the reflector can be attached at different heights above the granite to the measurement-arm. The measurements for four heights (see figure 6.5b) showed a systematic increase in the deviations for larger heights. This suggests a tilting of the measurement-arm. The changing tilt leads to an increasing deviation for measurements not close to the rotation-center of the tilt. It can be concluded that the rotation center is close to the surface of the granite as the measurements at lower heights show less large deviations. Therefore the rotation is caused by a tilt of the whole bridge. The bridge could tilt due to uneven movement on the rails at the borders of the table.

Also the dependence of the deviations along the precision-axis on the position along the bridge can be explained by the movement on the rails. If one side of the bridge moves differently than the other side this introduces an angle between the two axis, which is not 90°. This angle can be reconstructed by measuring the length of the sides of a triangle defined by the two axis and a diagonal. With a diagonal length of about 2.5 m the deviation to 90° is determined to be $(36.5 \pm 0.1) \times 10^{-3}$°. The measurement was repeated for a second triangle with a different orientation and slightly different position on the table. For this second measurement the same angular deviation up to the last digit of accuracy is reconstructed.

The calibration of the non-equal movement of the bridge on the two rails, as well as the tilt of the measurement-arm is faced, using the interpolation of several measurements. Therefore measurements were done systematically distributed. The already mentioned five positions along the bridge and the four heights above the granite-surface are used for this. The approach reconstructs the tilt of the arm along the precision-axis using the four height measurements. This is done for each position along the bridge separately. With these reconstructed tilts the measurement deviations at any given height could be interpolated. Choosing one common height for the five positions along the bridge the deviation of the movement between these positions is interpolated. The scheme for this method is sketched in figure 6.6a.

During the application of this approach, it is observed that the four measurements at different heights for the tilt-reconstruction are well described with a linear fit. This is especially remarkable as the measurements for

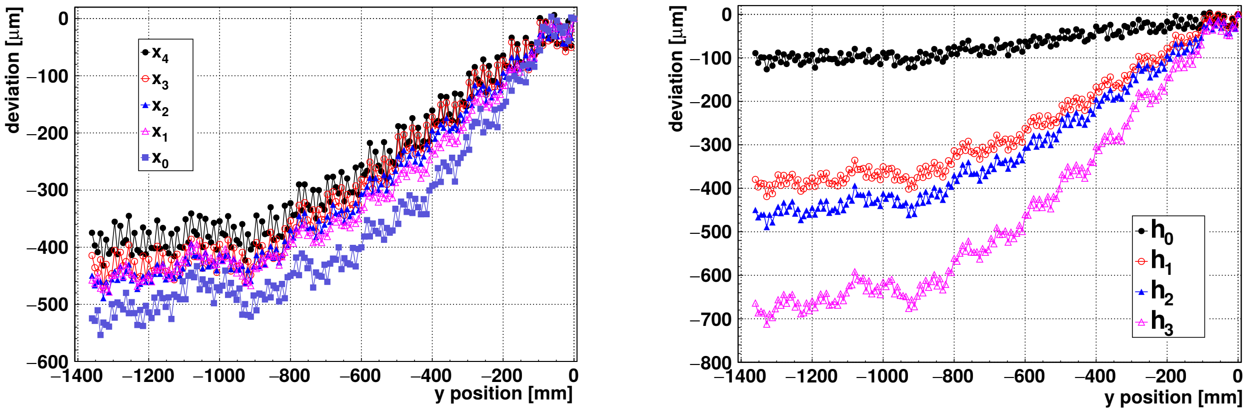

(a) Deviations to the nominal position along the precision-direction in y for measurements at five positions in x direction. The height of the reflector above the granite is kept almost constant.

(b) Deviations to the nominal position along the precision-direction in y for measurements at four heights above the granite. The position along the bridge, so in x direction, stayed unchanged at position x_2 in figure 6.4a.

Figure 6.5.: The deviation measurements are performed by starting at zero and moving to negative values. Therefore the plots have to be interpreted from right to left. First the deviations absolutely increase, until at around −900 mm the deviations settle and fluctuate around some constant. By comparing the different measurements it can be seen that the deviation is depending on the position of the measurement-arm along all axis. This can be explained by the difference between the movement of the two linear drives in y direction. Also the height at which the reflector is attached to the arm influences heavily the deviation behavior. By this an inclination of the measurement-arm can be inferred. Taken from [Neubert, 2018].

the two middle heights were taken with the reflector attached to different positions. Despite this, the heights of these two measurements are almost the same. The observed deviations of measurements at these two heights differ only slightly. Therefore it can be concluded that the tilt of the arm is followed well by the moving-element. The position of the marker should be reconstructed within the plane of the active area on the panel. Therefore the evaluation-height for the tilt-deviation-fit should be set to the height of the panel surface[1] above the granite. At this height the differences to the interpolation-fit of the extrapolated deviations are up to ±100 μm large. This indicates that the extrapolated deviations are not on a straight line.

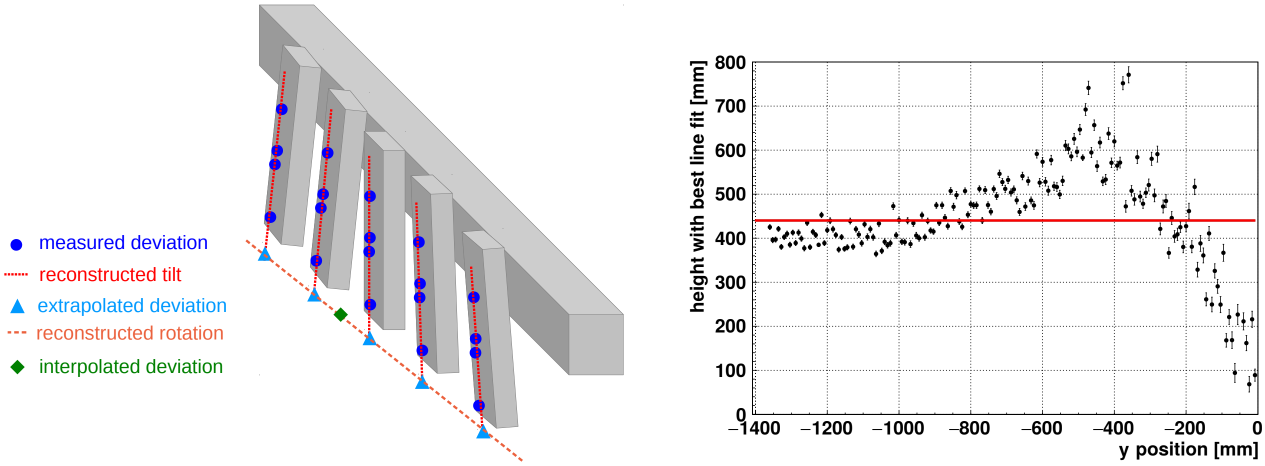

(a) Sketch of the reconstruction-approach for the deviations at any given position. The deviations are measured perpendicular to the shown reconstructed lines at the blue spots. Using these values the extrapolations and interpolations are done using linear fits. Not to scale.

(b) For the position along the precision-axis the height is determined at which the reconstructed deviations receive the best interpolation-fit. The deviations reconstructed at the five positions along the bridge are described best with linear functions at these heights. The red line indicates the height of the lower edge of the bridge.

Figure 6.6.: The reconstruction of the deviations at any given point requires the interpolation of several measurements. These interpolations are not ideal as the best conformity is achieved at varying heights.

The reason for the deviation from a line of the extrapolated deviations could be a torsion of the bridge-beam. A torsion would lead to different inclinations of the measurement-arm along the bridge. The axis of the torsion should be at the height with the best linear fit to the extrapolated deviations. This height is determined for figure 6.6b, by minimizing the accumulated differences to the linear fit as function of the evaluation-height. For the heights with the best line-fit, the differences to the fit are only in the range up to ±20 μm. Unexpectedly

---

[1] The thickness of a readout-panel is about 11.5 mm. Therefore the height above the granite correspond to this thickness.

this height varies as function of the position in precision-direction (y).
Comparing this evolution with the single measurements from figure 6.5, one recognizes in both a unsystematic behavior starting around −900 mm. This is caused by a bad screwing of the rails to the table, as already observed by [Müller, 2017].
The red line in figure 6.6b indicates the height of the lower edge of the bridge. Therefore the first part of the distribution reconstructs this as torsion axis. Until now the torsion effect could not be calibrated, as more measurements along the bridge would be needed. Therefore the calibration-approach, without considering the torsion, has to be compared to reference-measurements. A comparison could indicate whether the interpolated deviations are in the right order of magnitude. This will be discussed in chapter 6.1.4.

6.1.2. Detection and Fit of Precision Marker

There are two kinds of markers suitable for position measurements. They are located at the tapered borders of the boards. The first kind is used also during the gluing of the alignment rings. Therefore their position is of special interest for the evaluation of the alignment procedure. These markers are placed in the same position along the precision coordinate as the central strip of each board. The marker itself consists of a cross-hair with three concentric rings. The second kind are masks with a chessboard-like pattern, called Rasmasks (see figure 6.10a). This chessboard-like pattern is coded at each ninth column and row to enable an identification and fit of the marker in a global system. For these masks a specific software developed at Nikhef exists to evaluate the pictures [Dekker et al., 1993]. Therefore only for the first kind of markers an evaluation software has to be implemented. The approach for this is explained in the following. For the setup of the evaluation software the OpenCV library for C++ has been used [Bradski, 2000].

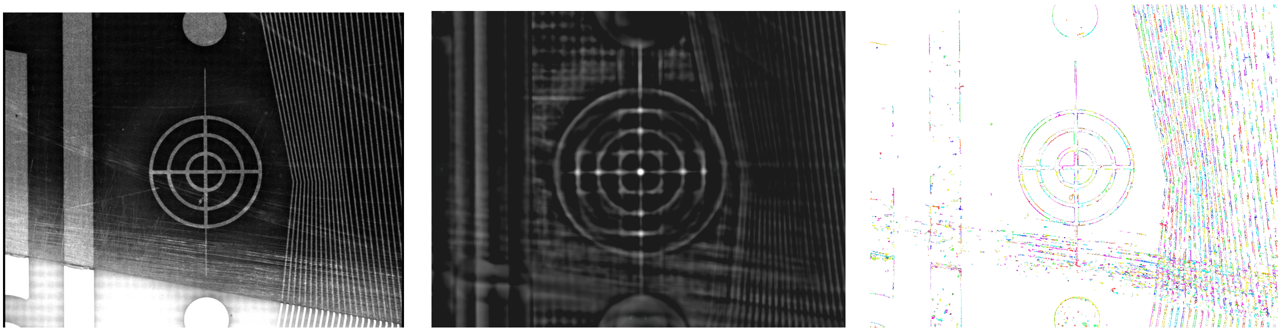

(a) Image of a precision marker for position-reconstruction after rescaling to improve the contrast. On the left the high voltage connection line can be seen. The rooting of the readout strips is visible on the right-hand-side. These structures have to be neglected for the position-reconstruction.

(b) Result of the template matching algorithm by comparing the image of a marker with a template of the innermost circle. Bright pixels correspond to a high convolution value, which describes good agreement between template and image. The center of the marker yields the highest convolution value, therefore it is brightest.

(c) Found contours in the marker-image by the Canny Edge detector [Canny, 1986] and the algorithm for border following by [Suzuki and Abe, 1985]. Pixels which were identified belonging to a common contour are colored the same.

Figure 6.7.: The evaluation of the marker-images involve several steps of processing. First, the image contrast has to be improved by scaling and adjusting the brightness. Second, a rough estimate of the marker center in the image is reconstructed by a template matching approach. For the reconstruction of the marker center, the contour of the outermost circle is used. Taken from [Neubert, 2018].

An image taken with the system at the LMU contains for each pixel an eight-bit brightness-information. An exposure time of 15 ms is chosen to stay with the pixel values well within this range without saturation. If too many pixels are in saturation the relative information between the pixels is lost. Also a too low brightness can cause information-loss due to indistinguishable features. The images of the precision marker are first linearly scaled to increase the contrast. Scaling in this case means that the single pixel brightness is multiplied with a factor and then an overall brightness value is added. Contrast describes the brightness difference between objects and features in the image with respect to the background. A scaled picture of a marker can be seen in figure 6.7a.
Problematic for the algorithms and therefore for the position-reconstruction are other features in the image which have to be filtered. This is achieved in two steps. First, a template matching method searches for the coarse center of the marker. This is done by comparing the image with a smaller image, the template, which contains only the inner ring of a marker. The comparison is achieved by searching in the convolution of the template and the image for an extremum.
In the second step, the approaches of [Feil, 2017] and [Neubert, 2018] differ. During the investigations of [Feil, 2017] only the pictures of a test-marker were evaluated. For this marker a suitable method was the conversion of the image into a bit-map. This is achieved by setting all pixels with brightness above a certain threshold to one and all other pixels to zero. From the pixels set to one, only those with a certain distance to

the estimated center by the template matching are used (see figure 6.8a). A circle-fit to these selected pixel positions is used to reconstruct the center. This approach is not applicable to the images of the marker from the series-production of the SM2 Micromegas. The reason for this is the problematic brightness distribution in comparison to the test-marker. The PCB for the test-marker is very smooth without scratches and without a coverlay. On the contrary the marker-images of the series-production are very inhomogeneous and the marker itself is not very bright. This is mainly caused by the coverlay.

Therefore [Neubert, 2018] developed a different approach. The contours in the images can be reconstructed using the Canny Edge Detector from [Canny, 1986] and an algorithm for contour-detection by [Suzuki and Abe, 1985]. From the found contours, those are selected which are at a certain distance to the estimated center of the marker. The distance is chosen to select contours corresponding to the outer border of the rings. In this approach four fits are made to these contours in order to reconstruct the center. Each fit describes one semi-circle of the ring. Using the upper and the lower-half-fit the horizontal position is reconstructed. Vice versa using the left and the right-half-fit the vertical position is determined. This approach is chosen as the semi-circle-fit is most sensitive to the opposite borders of the half-circle.

Several drawbacks of these approaches were observed. The scaling has to be performed carefully, as too high contrast can lead to artefacts due to the inhomogeneous surface of the PCB. These artefacts together with other features close to the marker, like scratches, can lead to undesired reconstructed contours. Contours are detected if the brightness change between pixels exceeds a threshold-value. Therefore this threshold had to be adjusted for different light situations and features in the picture. The additional contours can distort the fit of the circle if they are too close or even on the marker.

Multiple measurement-series were made for the investigation of this method. First, the optimal distance to the measurement surface is determined. This is achieved by the evaluation of pictures taken at several heights above the granite. The optimum is found using the Laplacian-transform of these images. The determined optimal-distance of 19 cm corresponds to the focal-distance of the telecentric optics. A scaling of the image-pixel-size to the mm-scale is reconstructed using the known diameter of the marker. The measured scaling-factor of 8 µm/pixel is in good agreement with the known image ratio of 0.46 and the pixel-size of 3.69 µm.

To test the position-reconstruction capabilities, the camera was moved using the CMM in a triangle above the marker. Two sides of the triangle were parallel to the CMM x and y-axis with a length of 5 mm. The movement was stopped each 0.1 mm for the picture-taking with the camera. The reconstructed centers of these pictures are shown in figure 6.8b. For a comparison not only the center of the outer ring is reconstructed, but also the centers of the two inner ones. Therefore this plot shows that in general the three fits can separately reconstruct this movement. A detailed view of the upper line of the reconstructed triangle is shown in figure 6.8c. Here the differences between the three reconstructions are visible. The constant offset between the reconstructions suggests an error of the test-marker. Larger imperfections of this marker could be explained by the limitations in the production-setup at the local workshop.

Despite this offset, the movement is reconstructed identically for the three circles. Therefore the irregularities to a straight line have to be features of the machine-movement. The almost discrete jumps could be due to the finite resolution of the decoder for the movement of the linear-bearing-units. If the decoder is fluctuating between two values during movement along the other axis, such jumps could be seen. In the following the outer ring is used for the position-reconstruction. This is done because here the most contours can be reconstructed and therefore the fit is the most stable. An improvement of the method could be the averaging over fits for all ring-contours. To save PC-resources and keep the reconstruction as simple as possible this is not implemented.

Measurements with several series panels were performed. For this, one panel at a time is aligned on the table with respect to the precision pins. The camera is moved with the CMM above each of the six precision markers and a picture is taken of each. The positions for picture-taking were the same for each panel. In the following the pictures are evaluated. A first observation are the differences between eta and stereo panels. The quality of the marker-images differs between these two panel types. The pictures of eta-markers have a better contrast and can be evaluated therefore easier. The problem of the markers on stereo-panels is that the brightness of the marker itself is very similar to the brightness of the surroundings. This is caused by a different etching-procedure used for these panels.

In order to account for this effect, the parameters for scaling and the threshold for edge detection were optimized separately for the two kind of panels. For the markers on the eta-panels optimal values for the pixel-multiplication are 5 and for the pixel-offset are -50. A threshold of 65 is used. The stereo-markers are evaluated with a pixel-multiplication of 6 and a pixel-offset of -300. The increased pixel-multiplication required a higher threshold of 85. These values are found iteratively and can vary depending on the light-situation and the image-quality. The latter is influenced and mostly given by the surface-structure of the panel at the marker. The reconstructed radius of the circles can be used to estimate the stability of the fits. For 96 measured markers on 16 eta-panels a mean radius of 481.6 pixels with a standard deviation of 1.2 pixels is reconstructed. A mean radius of 481.7 pixels and standard deviation of 2.0 pixels is reconstructed for 78 stereo-markers on 13 panels.

Despite the good agreement of the mean values the large standard deviations are unsatisfactory. A larger spread for the stereo-markers is expected due to the aggravated fits. The standard deviation has to be interpreted using the known pixel to length conversion-factor of 8 µm/pixel. Therefore this variation corresponds to uncertainties in the range of ten to twenty µm. These large fluctuations can be caused besides bad fits also due to features of the markers themselves. The size of the markers could fluctuate due to humidity or temperature. Also the

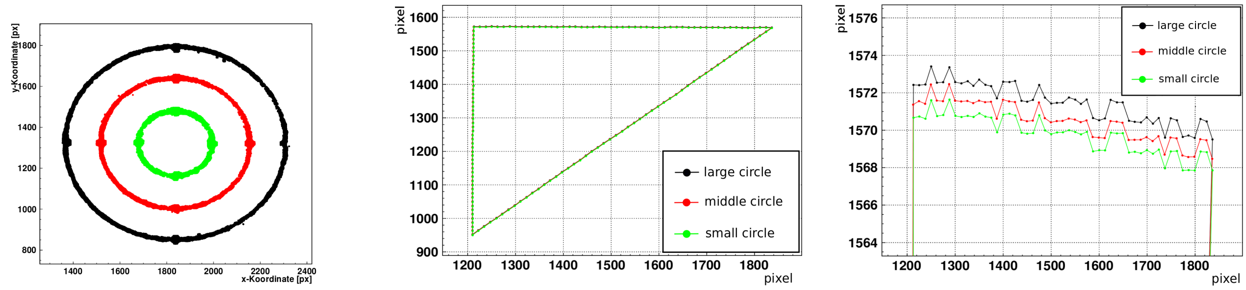

(a) Pixels in image coordinates identified belonging to the three rings of the marker. For the test-marker-evaluation it is sufficient to use the pixel distributions for the circular-fit. Due to features on the PCB this evaluation does not work for the series-marker.

(b) Reconstructed positions on images, which were taken at positions distributed in a triangle. The positions are reached by moving the measurement-arm of the CMM at which the camera is mounted. Overlaid are the positions reconstructed by the separate fits to the three rings of the marker.

(c) Upper line of the reconstructed triangle. The constant shift between the reconstruction of the three circles can be interpreted as an error of the test-marker.

Figure 6.8.: For the investigation of the position-reconstruction using a contour-fit, the movement of the CMM is reconstructed. This is done for the outer borders of the three markers separately. Taken from [Feil, 2017] and [Neubert, 2018].

edges at which the fit is performed can be more or less undefined due to the manufacturing process.

For the position-reconstruction only the reconstructed center is important. To evaluate this, one side of the first eta-panel was measured seven times within an hour. For three measurements the suggested light-setting was used, while for the other four a higher exposure-time was chosen. This required a slight adjustment of the evaluation-parameters. Despite this, no systematic effects of the exposure-time is reconstructed for these pictures. The positions of the markers in the images are reconstructed and the standard deviation between the measurements is calculated. A difference between the reconstruction in precision and in non-precision-direction[2] is observed. For the precision-direction the standard deviation is between 0.2 to 0.6 pixel for the six markers. In non-precision-direction larger standard deviations of about 0.6 to 1.2 pixels are reconstructed. This means for the position-reconstruction a limit on the accuracy with this setup of about 5 µm in precision-direction and of about 10 µm in non-precision-direction.

6.1.3. Combination of CMM and Fit Position

The position of the marker within the CMM coordinate-system is reconstructed by adding the evaluated center in the image to the position of the CMM during picture-taking. A trivial, but important consideration has to be made for the right combination of CMM-direction and picture-axis. If this is done wrongly, it leads to deviations in the order of several mm are observed. Therefore effort was made to ensure that this combination is done correctly.

In order to evaluate these values the difference to design-pattern is calculated. Sketches of the dimensions of the design-pattern can be found in appendix D. For the calculation a global fit is performed, which minimizes the difference of each point within the area to the nominal position. The fit has three free parameters, the shift in precision (y) and non-precision (x) direction, as well as the rotation (ϕ). The coordinates of the nominal positions are chosen such that these shifts represent the center of the readout-panel[3]. The fit is performed by minimizing

$$\chi^2 = \sum_{i=1}^{N} \delta_i^2 \quad , \tag{6.2}$$

where δ_i can be

$$\text{(a)} \quad \delta_i^2 = \triangle y_i^2 \qquad \text{or} \tag{6.3}$$

$$\text{(b)} \quad \delta_i^2 = \triangle y_i^2 + \triangle x_i^2 \quad . \tag{6.4}$$

---

[2] Precision-direction is perpendicular to the strips, which means in y direction of the CMM and along the width of the images. Non-precision-direction is along the strips. This corresponds to the x direction along the bridge of the CMM and along the height of the images.

[3] In the following plots the center of the coordinate-system is not representing this position. An arbitrary coordinate-system is shown, which should just indicate the length scales and positions of the marker.

Here the difference of the i-th of N reconstructed points (x_i, y_i) to the reference points (X_i, Y_i) is considered following

$$\tag{6.5}$$

$$\triangle x_i = \cos(\phi) \cdot (x_i - x) - \sin(\phi) \cdot (y_i - y) - X_i \tag{6.6}$$

$$\triangle y_i = \sin(\phi) \cdot (x_i - x) + \cos(\phi) \cdot (y_i - y) - Y_i \quad . \tag{6.7}$$

For case (a) the fit parameter x is fixed to the mean reconstructed x_i of all points. During minimization only the other two parameters are varied. Vice versa for case (b) the other two parameters are fixed to the rotation and mean values reconstructed on the central board (7). This distinction follows two motivations. Case (a) reconstructs the average position of all markers on the panel, while in case (b) the central board (7) is considered as reference axis. Exemplarily reconstructed deviations to the nominal design with these two approaches are shown in figure 6.9. These values are calculated for the already mentioned measurements of the first series eta-panel. Here no calibration of the CMM-positions is used. Therefore these results are very unexpected as the deviations in precision-direction[4] are within an acceptable range of ±50 µm.

The larger deviations in non-precision-direction are expected due to the elongation and shrinkage of the PCB-material for the readout-boards. The deviations in precision-direction can almost be translated from one approach to the other by the addition of the value on the central board (7). This can be understood due to the minimal rotation of the panel with respect to the CMM coordinate-system. Typical values for the rotation are in the range of $0.1\,\frac{\mathrm{mm}}{\mathrm{m}}$. For the seven measurements of the first eta-panel the standard deviations between the fit-parameters are calculated to investigate the stability of the two approaches.

Both showed almost the same results of a standard variation in precision-direction of about 2 µm and of about 5 µm in non-precision-direction. As expected, approach (b) reconstructs the rotations with a standard deviation of about $1\,\frac{\mu\mathrm{m}}{\mathrm{m}}$ more stably compared to approach (a) with a standard deviation of $3\,\frac{\mu\mathrm{m}}{\mathrm{m}}$. For the single point position-reconstruction the standard deviations are ranging from 3 µm to 11 µm in non-precision-direction and 2 µm to 3 µm in precision-direction. These measurements demonstrate the good repetitive accuracy of the CMM.

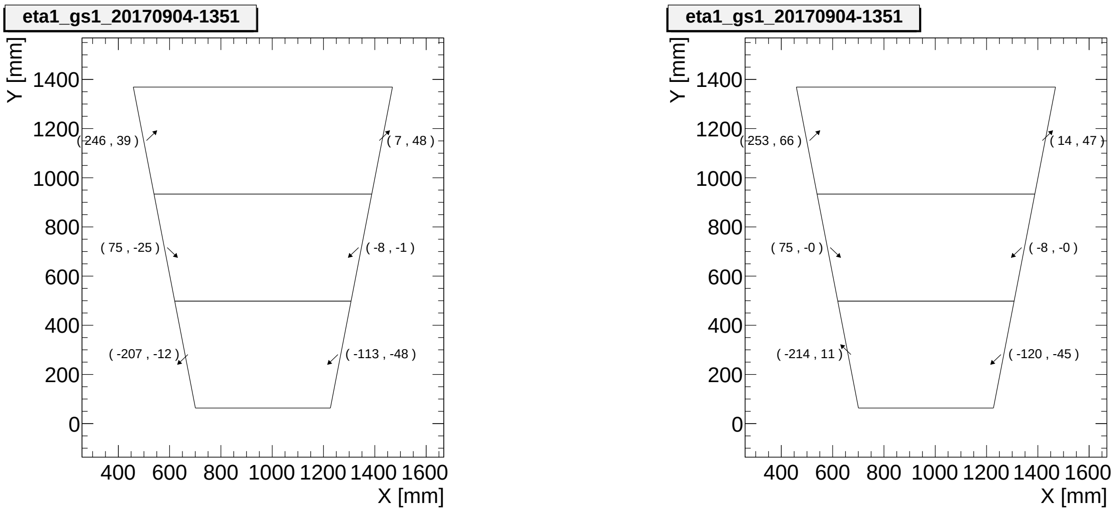

(a) Minimization using the rotation and the shift in precision-direction (y) as free parameter. The shift in non-precision-direction is set to the average of all measured points.

(b) Minimization using the shift in non-precision-direction (x) as free parameter. The rotation and the shift in precision-direction is fixed by the points on the central board (7).

Figure 6.9.: Reconstructed deviations of the precision marker positions to the nominal design for two fit-approaches. The tuples are given in µm and represent the values $\triangle x_i$ and $\triangle y_i$ after minimization. The arrows just represent the general direction of displacement, without scale or exact orientation. No calibration of the CMM-positions is applied yet.

Before a measurement is performed the SM2 panels are aligned on the granite-table with respect to the precision pins. This is done to guarantee constant placement with respect to the positions of picture-taking. As the images cover a larger area than the marker slight mis-alignments can also be detected. To test how such mis-alignments influence the deviation-reconstructions, using the global-fit, the second gluing-side of eta-panel ten was measured several times. Four times three measurements where performed, each three featuring a common setup. First, the panel was aligned as usual to the pins. Second, the movement of the measurement-arm with the camera was alternated to reach each marker from the same direction. This was done to test the effect of the backlash on the reconstruction. For the third sample a distance piece of 250 µm was placed between the panel and the pin on one side. Therefore a rotation is simulated. Similarly a distance piece of 500 µm was placed for the fourth set between panel and pin on the other side.

---

[4] The deviations in precision-direction corresponds to the second values in the brackets of figure 6.9.

Using the global fit it is possible to reconstruct these displacements and rotations with an accuracy of about 10 µm. The reconstructed deviations are varying between these measurements with standard deviations between 2 µm to 5 µm in precision-direction. Therefore it can be concluded that the global-fit works and that it describes the deviations. Also the described slight mis-alignments on the table do not cause mis-reconstructions.

6.1.4. Comparison with Rasmask Measurements

In order to check the calibration of the CMM, the deviation-reconstructions have to be compared to reference-measurements. Therefore two measurement-campaigns were performed at the French Micromegas construction-side near Saclay. The French group is building the LM1-type Micromegas modules. They have set up a similar, but more precise CMM for about ten times the budget spent on the CMM in Munich. During the first measurement campaign, in November 2017, tests with the laser-interferometer reconstruct an accuracy of this machine of better than 10 $\frac{\mu m}{m}$ [Giraud, 2018]. Their deviation-reconstruction also uses a camera attached to the measurement-arm of the machine. Instead of the marker, the French colleagues use the Rasmasks (see figure 6.10a) to reconstruct the mis-alignments of the panel. Three large and one small of these masks are printed in the same step as the copper strips on each of the tapered sides of the PCBs. Therefore 24 masks in total are on one side of a readout-panel. Their placement can be seen in the appended figure D.2. The small masks are placed close to the markers, 29 mm further to the edge of the PCB. In the first measurement-campaign eta-panel two and stereo-panels one and two were measured on both gluing sides. During the second campaign, in December 2018, eta-panel eight, nine and ten, as also stereo-panels nine, ten and eleven were measured.

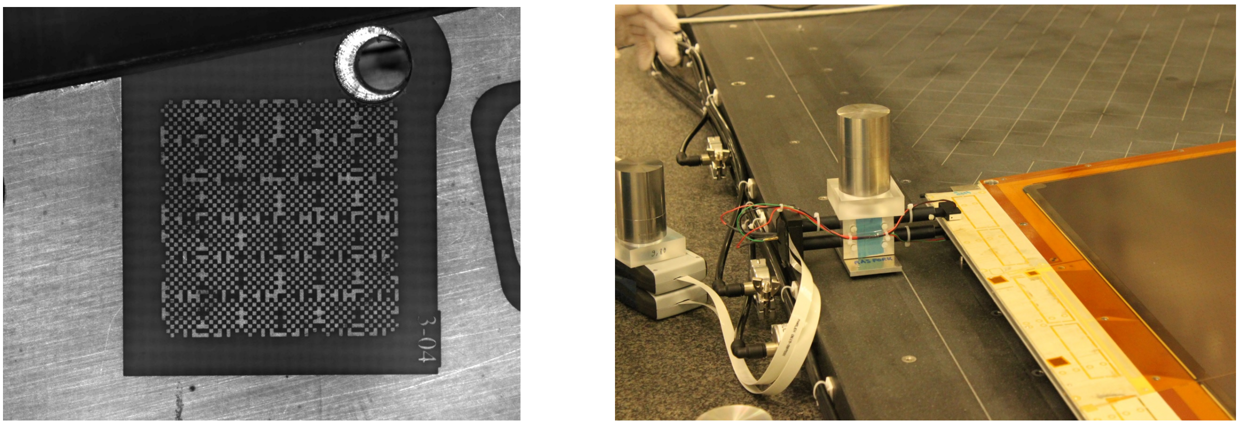

(a) Picture of a rasmask taken with the position-measurement-setup at the LMU. Six of these masks are present on each readout-board for position-reconstruction. Two additional smaller ones are located near the high-voltage-power-line.

(b) Picture of the two-fold rasfork developed at Saclay for the layer-to-layer alignment-reconstruction-measurement. The tool is attached during measurements to the readout-panel at the position of the rasmasks. By comparing the top and the bottom mask the alignment of the two surfaces should be reconstructable. Developed by [Giraud, 2016].

Figure 6.10.: In total 24 masks on each panel-surface enable the reconstruction of the board-alignment.

Besides the in-plane alignment, which reconstructs the positions of the boards on one gluing-side of a panel, also the layer-to-layer-alignment can be reconstructed. For this the French team developed the so called Rasfork (see figure 6.10b) [Giraud, 2016]. The tool compares the positions of the masks on both sides of a panel. The comparison is achieved by pictures taken simultaneously from opposite masks. The tool has to be initially calibrated for the offsets and rotations of the picture-coordinates. All collaboration-sites received these tools for alignment-measurements during production. By a comparison of measurements done at Saclay and Munich, a good agreement was confirmed of about 10 µm in precision-direction.

The main objective of Rasfork-measurements is to reconstruct large shifts or rotations between the layers. Exemplaric results for both kinds of measurements, which will be discussed together with cosmic-reconstructions in chapter 6.2.5, can be seen in figures E.1 and E.2.

After the measurements in Saclay, the panels were remeasured in Munich as described in chapter 6.1.3, for the in-plane alignment. Unfortunately the setup in Munich had to be changed between the campaigns. An additional arm was connected to the machine for the glue-distribution during panel-construction. Therefore the camera attachment at the measurement-arm had to be changed, to avoid collisions. This introduced the reversion of the image-coordinates with respect to the CMM-axes. Also the measurement position of the arm changed, as the camera is displaced. Despite these obstacles for both measurement-campaigns the reconstructions between Saclay and Munich could be compared. The results are shown in figure 6.11.

For this comparison the deviation differences between the Munich and the Saclay measurements are calculated. Only the differences in precision-direction are considered as these are most-important for the track reconstruction using the strip-pattern. The measurements in Saclay were evaluated at the small masks, as these are closest to the marker, which are measured in Munich. The first value in the brackets of figure 6.11 corresponds to the mean difference, while the second represents the standard deviation of differences. The differences for the first

Measurements of eta-panel two and stereo-panels one and two performed 2017.

Measurements of eta-panels eight and ten and stereo-panels nine, ten and eleven performed 2018.

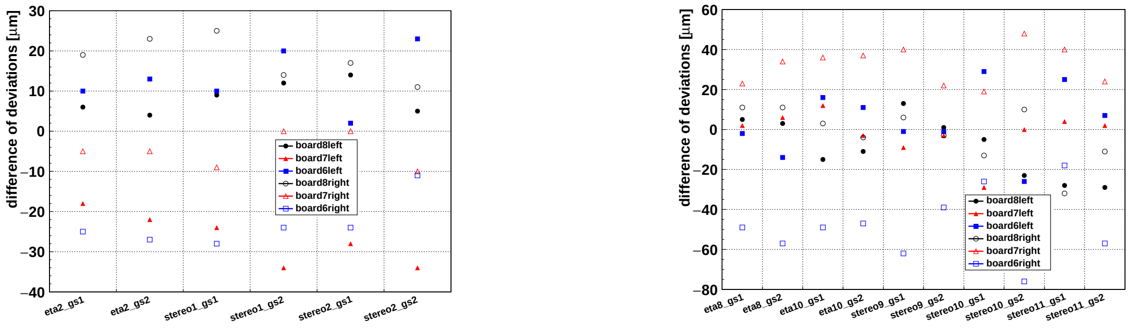

(a) **(b)**

Differences between the two-deviation-measurements for the six positions.

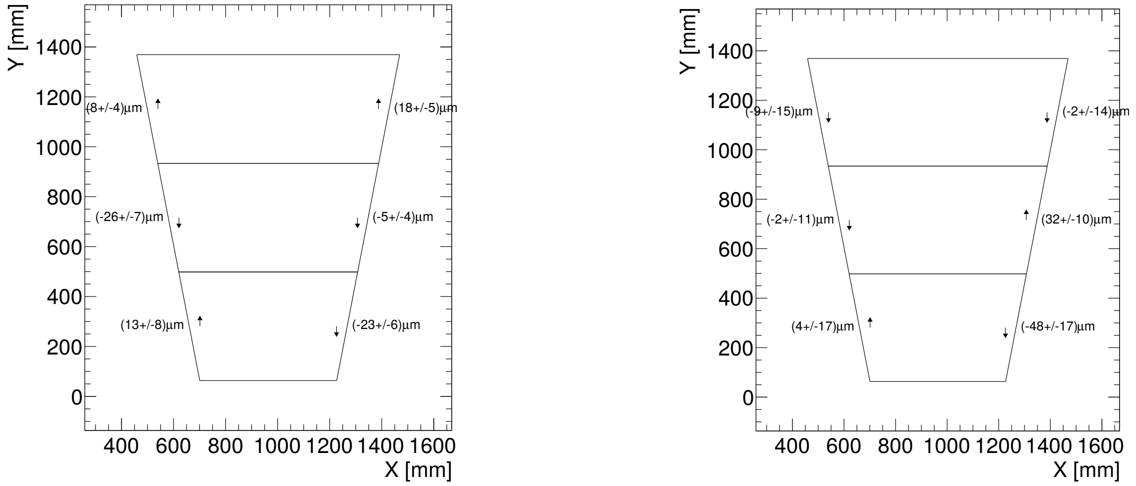

(c) **(d)**

Mean and standard deviation of the measurements at the six positions.

Figure 6.11.: Differences between the measurements performed at the CMM in Munich and the CMM in Scaley. In figures 6.11c and 6.11d the mean values and standard deviations are shown. The mean values differ due to an alternated setup at the CMM in Munich. Additional attachments at the CMM in Munich increase the standard deviations for the second measurement campaign. No calibration of the CMM-positions is applied yet.

campaign show only standard deviations up to 8 µm. The standard deviations of the second campaign fluctuate in the range of 10 µm to 17 µm. These large values show a worse comparison for the second campaign.

Several explanations can be found for this worsening with respect to the first campaign. As the additional arm introduces more weight on the bridge, the accompanying deformations could worsen the repetitive accuracy of the machine. Another point is that more readout-panels are investigated for the second campaign. This could introduce larger fluctuations due to statistical effects on the boards. The largest problem is the time-elapse between the measurement in Saclay and Munich. For the first campaign the measurements were performed within two weeks. After the measurements in Saclay for the second campaign, twenty days elapsed for the measurement in Munich. Also the weather during this time-period could have caused deformations of the panels during transport and storage. Despite this, the mean differences and the single differences between the measurements show not as large values as expected from the calibration-measurements of the CMM.

The mean values in figure 6.11 can be interpreted as constant offsets. Therefore they should be comparable to the interpolated deviations of the machine-movement (see chapter 6.1.1). To do this comparison the deviations are interpolated at the measurement positions. The interpolated values are shown in figure 6.12 for the measurement positions of both campaigns. Comparing the mean deviations in figure 6.11 and the interpolated deviations in precision-direction in figure 6.12, no correlation can be found.

The discrepancy between the observed mean differences of the alignment-measurements and the calculated CMM deviations can have multiple reasons. The machine is modeled not in full detail with the presented calibration. So the interpolations showed not always linear behaviors. Also rotations of the measurements arm around the z-axis could not be taken into account. A strong restriction is also the missing description of the behavior for the line-of-sight for the camera. Furthermore the comparison between the measurements in Saclay and Munich can be biased due to the different positions of the markers and the masks. None the less using the CMM in Munich large mis-alignments should still be detectable.

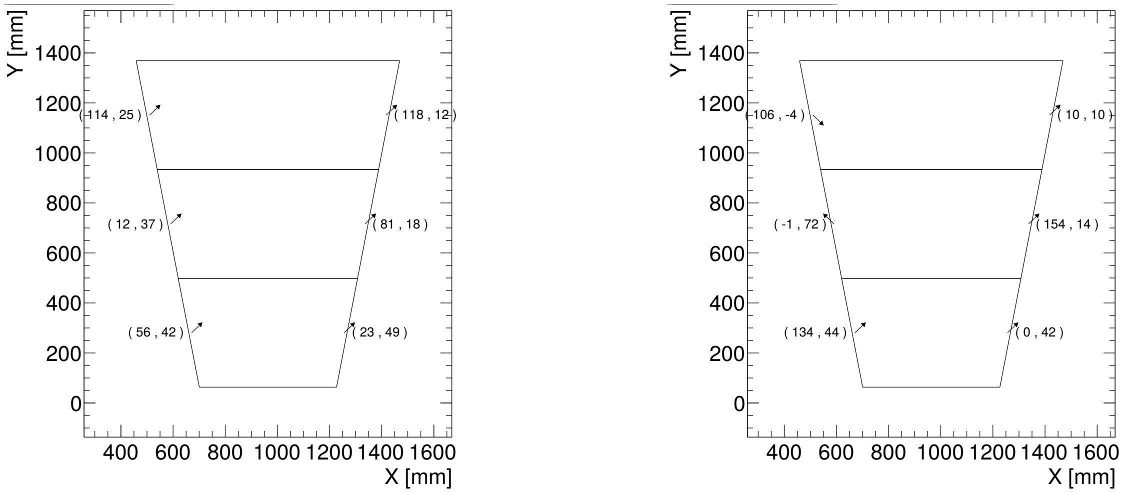

(a) Positions measured 2017.

(b) Positions measured 2018.

Figure 6.12.: Reconstructed deviations of the CMM-positions for the positions of the two measurement-campaigns. The reconstruction is performed according to chapter 6.1.1 using the approaches of [Feil, 2017] and [Neubert, 2018]. The tilt-deviation-fits are evaluated at the height of the panel-surface above the granite.

6.2. Strip Alignment Reconstruction using Cosmic Muon Tracks

The alignment of the readout-PCBs as well as deviations of the strip pattern from the nominal design can be reconstructed using cosmic muons referenced by precision track-detectors. For this the position of particles measured in one layer of the module has to be compared to the reference track extrapolated into this layer. The difference of measurement and reference, calculated for each traversing particle individually, is called residual. The alignment reconstruction is achieved using the dependence of the mean residual on the position in the detector. The systematics which arise due to the averaging for this mean have to be considered as well. In the following the approaches to reconstruct the deviations to the nominal pitch, the strip-shape and the rotations and shifts of the readout-PCBs will be discussed.

In a Micromegas the position of a through-going muon is measured using the strip-signal. The strips are numbered to identify their position on the readout anode. A cluster is built of neighboring strips, which are exceeding a certain threshold and satisfy certain signal requirements during a muon passage. For these clusters an average strip-number is calculated by taking the sum of the charge weighted strip-numbers which are contained in the cluster. This strip-number can then be scaled to an actual position on the readout anode by multiplying with the distance between the strips. The position is given perpendicular to the strips beginning from the edge of the active area with the first strips. In order to compare the reconstructed position with a reference system like other similar detectors this position has to be transformed into the global coordinate-system. Therefore first the procedure to align the Micromegas data in the CRF coordinate-system is explained.

6.2.1. Micromegas Alignment

The alignment of the Micromegas is achieved using a coordinate transformation into the CRF-system. A coordinate transformation for this case is performed with six parameters (see appendix C). These parameters have to be calculated from the residual-distributions. The parameters describe the shift along the three axes and the rotations around the axes. The determination of these parameters is achieved in several iterative steps. As the four planes act as individual detectors, each layer could be aligned separately. To reduce redundant steps the alignment-parameters are first determined only for one layer. After this, the alignment of the other layers is performed starting from the nominal design.

A first coarse alignment is achieved by just considering the mean difference between MDT track and the position in the Micromegas. This difference $\triangle y$ corresponds to a first estimation for the shift in precision-direction, so along the y-coordinate. Also the position of the Micromegas between the MDT chambers, so in z-direction, is determined in this first step. This is done according to the prescription of [Lösel, 2017]. Therefore the residual is plotted as a function of the slope of the reference track as seen in figure 6.13a. The slope of this distribution corresponds to the shift $\triangle z$ perpendicular to the active area.

Crucial for the reconstruction of the detector-performance is the parallelism of the Micromegas-strips and MDT-wires. A dependence of the residual on the coarse position given by the scintillator-hodoscope is interpreted as rotation around the z-axis. This rotation α_z corresponds to strips and wires being not parallel. Typical values for the yet measured modules lie between $\pm 3\,\frac{\mathrm{mm}}{\mathrm{m}}$, which correspond to angles of $\pm 0.17°$. Some modules had larger rotations, which aggravate their investigation. These three parameters, $\triangle y$, $\triangle z$ and α_z are the most important variables for the alignment in the CRF-system. After each following step these parameters have to be checked. The position in non-precision-direction $\triangle x$, so along the wires, is estimated using the stereo reconstruction. This will be discussed in chapter 7.4.1. The last two parameters describe the rotation of the readout-plane in the CRF-system. Their determination is achieved by considering the vertical shift, perpendicular to the readout-plane, as function of the position. For this the residual dependence on the reference-track-slope is calculated for each partition of the active area separately. An exemplaric map of reconstructed shifts $\triangle z$ can be seen in figure 6.13b. A linear dependence on the position along the y-axis describes a rotation around the x-axis and vice versa. The fit of these dependencies determines the alignment-parameter α_x and α_y. After alignment of one layer, its overall residual is centered around zero and the mean value shows almost no dependence on the reference-track-slope.

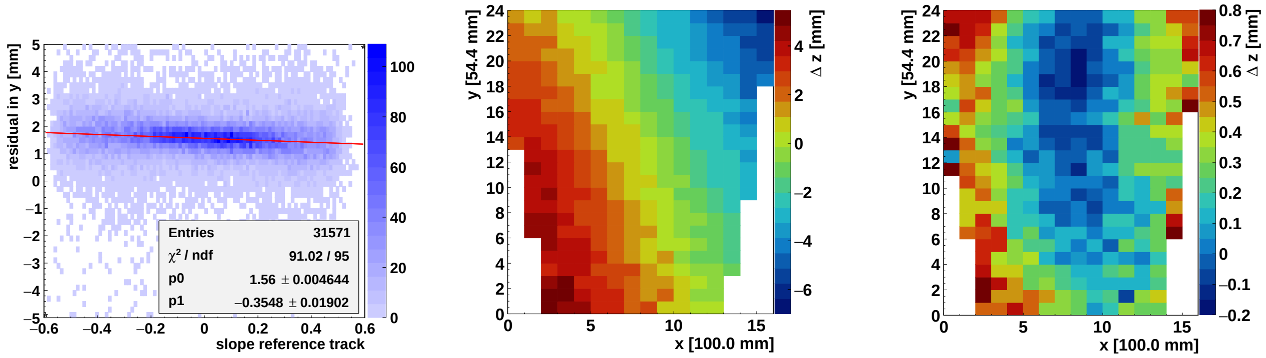

(a) Residual as function of the reference-track-slope. The shift in precision-direction corresponds to the first fit-parameter. A shift perpendicular to the active area is seen as slope of the distribution given by the second fit-parameter. Taken from [Herrmann et al., 2017].

(b) Deviation of the active area from the central area between the MDT. The rotations seen by the linear dependencies of $\triangle z$ have to be corrected during alignment. Exemplaric plot before alignment of module three eta-out.

(c) Deviation of the active area from a flat plane. A gravitational sag due to insufficient support can be seen along the center. Exemplaric plot after alignment of module one eta-out.

Figure 6.13.: For each partition of the active area the residual-distribution has to be evaluated. The dependence on the slope of the reference track is determined using a linear fit. With this the rotations around the x and y-axis can be measured and corrected. After this alignment deformations due to gravitation can be reconstructed.

For the alignment of the other layers almost the same parameters can be used. The stereo-layers are built with a dedicated rotation of 1.5°. This has to be taken into account for their rotation around the z-axis, so in the parameter α_z. All layers have to be adjusted in z-direction individually, this means $\triangle z$ differs between them. In one layer the position is reconstructed in the center of the drift-gap, as here the average cluster-centroid is determined. The distance between the drift-gap-centers of neighboring layers can be calculated using the design-values.

For layers on the same readout-panel a slightly different distance is estimated than for the central layers, which are separated by the double-drift-panel. In the first case two times each half of the drift-gap, the amplification-gaps and the mesh-thicknesses have to be taken into account. Also the readout-panel-thickness has to be considered. In the second case also two times half of the drift-gap contributes, but here only the thickness of the double-drift-panel has to be added. This sums up to a distance of 16.9 mm for an outer to an inner layer[5] and to 16.35 mm for the distance of the inner layers[6]. Whether these design-values are reached can be reconstructed by determining for each layer the z-position individually. As average distance between the eta-layers a value of 16.58 mm with a standard deviation of 0.08 mm is reconstructed. For the stereo-layers a mean distance of 16.98 mm and a standard deviation of 0.25 mm is observed. The inner layers show distances of 16.44 mm with a standard deviation of 0.20 mm. The larger fluctuations for the later two values are probably caused by the worse resolution of the stereo-layers due to the additional rotation. These values could be systematically biased by the rotations of the readout-plane with respect to the CRF-system. Despite this no correlations between the alignment-parameters are observed yet.

Another mechanical-alignment-effect is seen exemplarily in figure 6.13c. This is the deviation to a flat plane reconstructed for one layer using the alignment procedure from [Lösel, 2017]. The same structure and magnitude is reconstructed for the other three layers of the same module. The deviation corresponds to a gravitational sag due to insufficient support in the center of the module. This effect is unproblematic for the use-case in the NSW as the modules will be assembled vertically, but has to be considered in the CRF. During measurements with a slightly different setup the module was supported only in the center. Therefore a sag of the edges is reconstructed using this method.

---

[5] $d_\mathrm{outer} = 2 \cdot \left(\frac{1}{2} \cdot d_\mathrm{driftgap} + d_\mathrm{amplificationgap} + d_\mathrm{mesh}\right) + d_\mathrm{readoutpanel} = 2 \cdot \left(\frac{1}{2} \cdot 5\,\mathrm{mm} + 0.12\,\mathrm{mm} + 0.08\,\mathrm{mm}\right) + 11.5\,\mathrm{mm} = 16.9\,\mathrm{mm}$

[6] $d_\mathrm{inner} = 2 \cdot \frac{1}{2} \cdot d_\mathrm{driftgap} + d_\mathrm{driftpanel} = 2 \cdot \frac{1}{2} \cdot 5\,\mathrm{mm} + 11.35\,\mathrm{mm} = 16.35\,\mathrm{mm}$

6.2.2. Pitch-Deviation

The distance between the center of adjacent copper readout strips, called pitch, can deviate to the nominal value. This can be due to production failures or more probable due to deformations of the PCB. The FR4 material used for the PCBs of the NSW Micromegas is highly affected by humidity. This is seen by the shrinkage or enlarging of the PCB with falling or increasing humidity [Bortfeldt et al., 2016]. Therefore the deviation to the nominal pitch value has to be investigated. To reconstruct this deviation the residual as function of the position perpendicular to the readout strips has to be considered. A linear dependence of the two values suggests a scale-error, which can be interpreted as a deviation of the pitch. This can be explained with figure 6.14a.
For a normal track going centrally through a readout-board the mean reconstructed position is for boards with nominal, shrinked or enlarged width the same. For tracks displaced from the center of a readout-board the mean residual is displaced if the nominal pitch is assumed and the board has not the nominal size. This can be seen indicated by the arrows. The position in the shrinked case is reconstructed too far to the right. Vice versa in the enlarged case the position is reconstructed closer to the center, which means in the example more to the left. As the residual is the difference of the centroid-position times the pitch to the reference, the pitch scales the centroid to the reference.

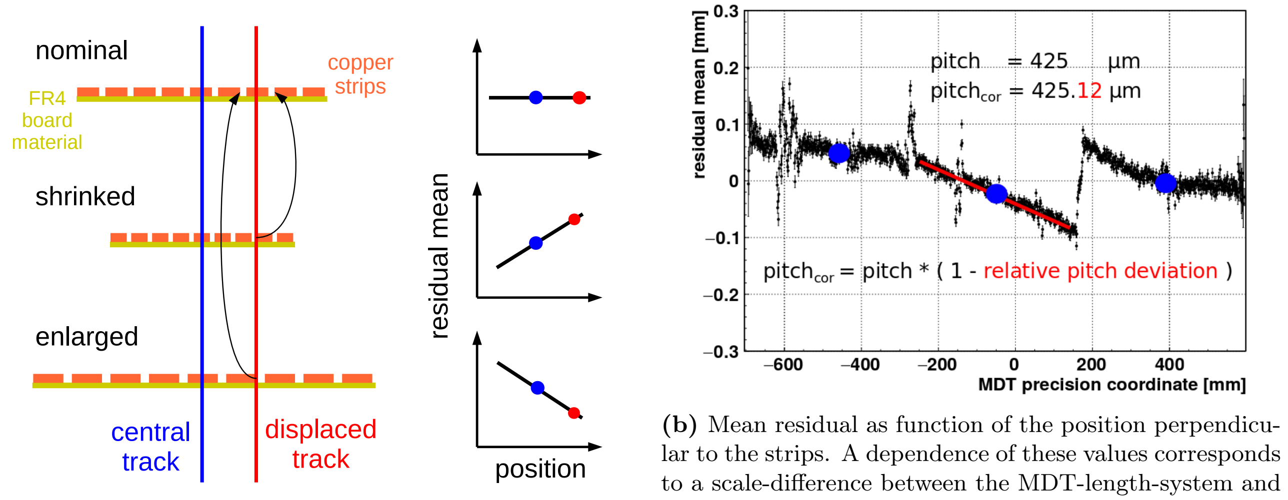

(a) Scheme of the influence of the pitch-deviations on the position-reconstruction. For boards with a nominal pitch a constant mean residual is reconstructed for central and displaced tracks. A positive dependence indicates a shrinked board, while a negative dependence is reconstructed for enlarged boards. Not to scale.

(b) Mean residual as function of the position perpendicular to the strips. A dependence of these values corresponds to a scale-difference between the MDT-length-system and the Micromegas-length-system. Each board can be assigned a different scale, if individual slopes are observed. Therefore this corresponds to a deviation from the nominal pitch between the strips. Also the shifts between the readout-PCBs are visible and can be used for the calibration. Reconstruction for the eta-in layer of module zero.

Figure 6.14.: Model and measurement of the pitch-deviations.

The effect has to be corrected for each readout-board of a layer individually [Herrmann, 2019]. Therefore the calculation of the hit position has to be adjusted. This is done using

$$y = c \cdot p_{\mathrm{cor},b} + N \cdot \frac{(b+0.5)}{B} \cdot (p_{\mathrm{nom}} - p_{\mathrm{cor},b}) - 0.5 \cdot N \cdot p_{\mathrm{nom}} \quad , \tag{6.8}$$

by accounting for the different centers of the boards. The assumption for the formula is that the centers of the readout-boards should be aligned due to the dedicated construction with the alignment-frame. With this the elongation or shrinkage of the board is originating from the center.

variable	value (nominal for SM2)	unit	description
y		mm	reconstructed position in the Micromegas system
N	3072	number	total number of strips in the Micromegas layer
c		strip-number	centroid, charge weighted average strip-number of cluster
B	3	number	total number of boards in the Micromegas layer
b		index	board number counted from zero to B-1
p_{nom}	0.425	mm	eta - nominal pitch
	0.42485	mm	stereo - nominal pitch
$p_{\mathrm{cor},b}$	p_{nom}	mm	corrected pitch for board with index b

Table 6.1.: Parameter for formula 6.8.

Several problematic effects were encountered investigating the modules with this method. As seen in figure 6.14b some spots along the active area show a large fluctuation of the mean residual. These fluctuations arise due to non-responsive and therefore inefficient areas, which can either be due to electronic problems or disconnected-strips. The reasons for this were discussed in 5.1. The mean residual is deformed by this as the actual distribution at these spots is filled with noise hits from other regions of the layer (see figure 6.15a). As noise hits are random the distribution shows a linear dependence of -1 between residual and position. This is only seen for large residuals.

Another effect are systematic shifts due to wrongly attached readout electronics. The adapter-boards have to be placed well aligned at the footprints. If the boards are displaced by one strip this is seen in the mean residual behavior by a shift of one pitch, so about 425 µm. It is well understood how this can happen for a whole adapter-board. During the mounting the alignment of the footprints and the zebra-connector can be distorted. Therefore a shift of one strip can occur if this is not done properly.

Such shifts are also seen for single APV-chips, so groups of 128 strips. A shift by one pitch of a single chip could not be explained by an alignment failure between the footprints and the zebra-connector. This would be seen also by the other chips of the same adapter-board. There are several other explanations, which could not be disentangled. The Panasonic connector for this chip could be wrongly mounted or the rooting of the adapter-board could have a failure. Also the APV-chip itself can be problematic when the channels are not rooted in the proper order. Another reason could be the wrong channel-number-assignment in the FEC-card. For the reconstruction of the pitch-deviation these shifts have to be corrected.

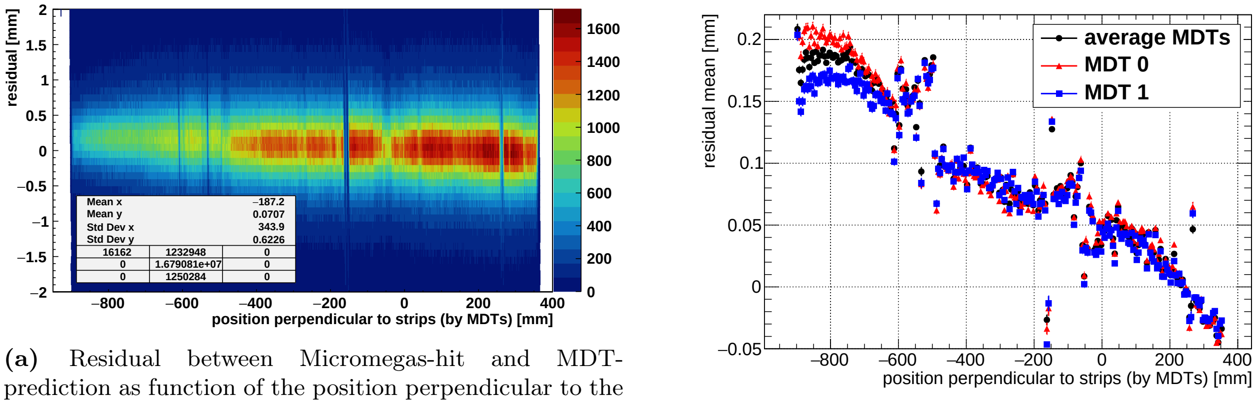

(a) Residual between Micromegas-hit and MDT-prediction as function of the position perpendicular to the strips. Shown for module 3 eta-out. Due to badly connected electronics several regions show fewer hits than expected

(b) Mean residual as function of the position perpendicular to the strips. Shown for module 3 eta-out. The inefficient regions seen in 6.15a distort the mean-calculation.

Figure 6.15.: The residual dependence on the position perpendicular to the strips enables the reconstruction of pitch-deviations. The evaluation of the residual-distributions can be distorted due to inefficient regions, which lead to undesired and non-physical correlations. Also the effects coming from the reference have to be considered. Discrepancies between the reconstruction of the two MDT-chambers are observed.

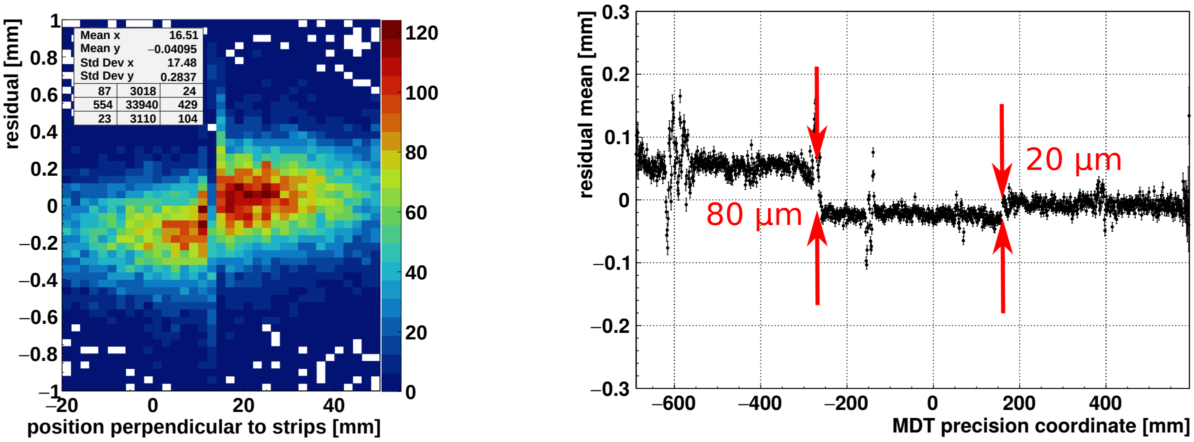

(a) Residual reconstructed during the H8 testbeam of module zero, at the junction between the central board (7) and the large board (8). A jump is observed.

(b) Mean residual as function of the position perpendicular to the strips, after correction of the pitch-deviation.

Figure 6.16.: For module zero both testbeam and cosmic-measurement show a jump between the central board (7) and the large board (8). The cosmic-measurement reconstructs the reason for the jump as a deviation of the nominal pitch (seen in figure 6.14b). After correction for this effect using formula 6.8, much smaller shifts between the boards are reconstructed.

A useful application of this investigation is the reconstruction of the center-to-center alignment between the readout-boards. The fit for the determination of the pitch-deviation can be rewritten from the common first-degree-polynomial-form. By using $f(x) = p_0 + p_1 \cdot (x - c_b)$, where c_b denotes the board-center perpendicular to the strips, one receives the shift of the board-center in the parameter p_0. Here p_1 corresponds to the pitch-deviation. To investigate systematic effects of the reference system the residual can be calculated for the two MDT chambers separately. This is done in figure 6.15b. As seen for the largest part of the module the three residuals are in good agreement, with the largest differences of about 10 µm. At the left border of the plot larger discrepancies can be observed, which are systematic shifts between the two MDTs of about 40 µm. The difference of the two reconstructions arises probably at this position, due to the limited angular acceptance. Here the active area of the MDTs ends, which is also seen in the hit distribution in 6.15a. Therefore the residual-distribution can be biased due to the inhomogeneous illumination.

In order to compare this reconstruction to another measurement, the data of the module zero testbeam are investigated. A jump between the central board (7) and the large board (8) is reconstructed using the track of the telescope in the testbeam seen in figure 6.16a. The jump could not be explained by the testbeam measurement besides a shift of the whole PCB. Figure 6.14b shows for the eta-in layer of module zero also large differences around position 150 mm during cosmic-measurements. The cosmic-measurement reconstructs a pitch-deviation as the true reason for the jump between the boards. Correcting this effect the shifts between the centers of boards can be seen in figure 6.16b. The correction is performed using formula 6.8.

6.2.3. Strip-Shape and Board Rotation

In the nominal design the copper readout strips are straight for precise reconstruction perpendicular to them. Their parallelism should only be distorted if the readout-boards are misplaced during panel production. But the readout-boards themselves can be deformed as seen in chapter 6.2.2. Therefore it is advisable to investigate the shape of the strips. This can be done by considering the residual between hit in the Micromegas-layer and MDT-track for each board individually. The shape of the strips can be deduced by calculating the mean-residual as function of the position along the strips. The position along the strips is given by the coarse resolution of the scintillator-hodoscope. An exemplaric distribution is shown in figure 6.17a. To exclude systematics and to reconstruct the alignment between the boards the reconstructed strip-shapes of different boards have to be compared. This is done for one layer in figure 6.17b.

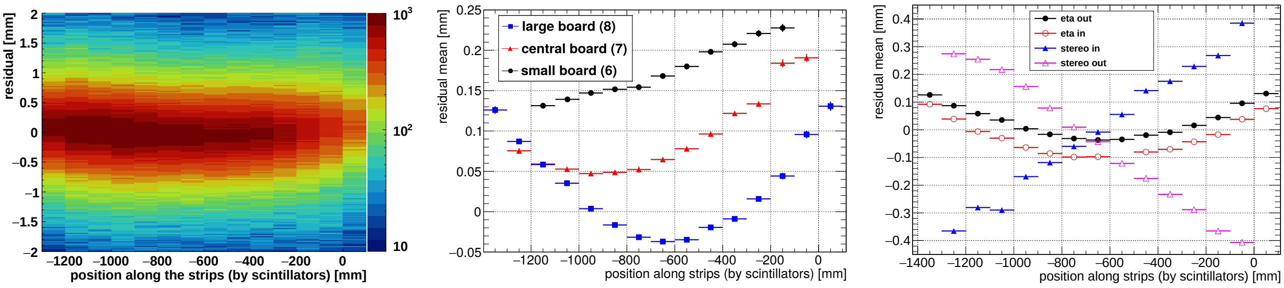

(a) Residual as function of the position along the strips for the large board (8) of the eta-out layer of module 3.

(b) Mean residual as function of the position along the strips for all boards of layer eta-out for module 3.

(c) Mean residual as function of the position along the strips for the large boards (8) of all layers of module 3.

Figure 6.17.: The strip-shape can be reconstructed using the dependence of the residual as function of the position along the strips. The position along the strips is given by the scintillator-hodoscope.

The first thing to notice is the different shape of the three boards in figure 6.17b. While the large board (8) shows a U-like behavior of the residual mean, the other two boards have more a linear dependence. In this case a linear dependence corresponds to a rotation of the board with respect to the CRF-system. During Micromegas alignment the whole detector-plane is aligned to the CRF-system. Therefore the individual rotation of the boards shows that the alignment is not perfect. Also for the central board (7) a small U-like behavior can be recognized. This is suppressed by the overall rotation of this board. To investigate the deformation of the strips on a single board these rotations have to be corrected. This can be done by assigning to each readout-board an individual rotation in the precision-plane. By comparing the strip-shape of the same board-type of different layers, the alignment between the layers can be estimated. This is shown in figure 6.17c. Here for the large board (8) of module three the strip-shapes of the four layers are shown.

It has to be mentioned that the two stereo-layers are treated separately as individual detector-layers. This is done in order to reconstruct their alignment, as well as to investigate their individual properties. During alignment the nominal inclination of ±1.5° is assumed[7] for these layers with respect to the eta-layers. The linear dependence of the residuals by the stereo-layers on the position along the strips corresponds to an additional rotation. It is observed for all stereo-layers of all yet built modules. For the inner layer a mean value of the additional rotation of $0.66\,\frac{\text{mm}}{\text{m}}$ with a standard deviation of $0.16\,\frac{\text{mm}}{\text{m}}$ is observed. The outer layer shows a mean of $-0.59\,\frac{\text{mm}}{\text{m}}$ with a standard deviation of $0.10\,\frac{\text{mm}}{\text{m}}$. The sign of the two rotations indicates that the stereo-layers are not as much rotated as they should be. Module twelve was investigated up-side-down, to exclude systematic

---

[7] This angle corresponds to a rotation of $26.186\,\frac{\text{mm}}{\text{m}}$, which would be otherwise seen as slope in the strip-shape plot.

effects due to the order of the readout-layer. It showed values[8] which are in agreement with the measurements of the previous modules.

Several possible explanations can be given for the additional rotations. An alignment-failure during construction of the readout-panels is excluded. The alignment between the layers should be achieved by the positioning with respect to the pins on the granite-table. If the PCBs for one layer have different distances to the left and the right pin this introduces a rotation of the layers with respect to each other. Such a rotation would also be seen for the eta-layers as they are constructed with the same procedure. Therefore this kind of failure should not be the reason for the observed rotation as the eta-layers are much more parallel (see black and red curves in figure 6.17c). Also the size of mis-alignment which would be in the order of half a millimeter would have been noticed.

A real source for alignment-errors could be an unexpected deviation of the nominal design of the PCBs. As many people work together in this project a lot of critical steps are performed by different persons. For example a failure during the design of the readout-PCBs could be translated to a wrong alignment. A wrong design could introduce shifts and rotations by a wrong placement of the marker, which are used for positioning on the table. This kind of error can not be excluded. All systematic effects of the CRF-system can also not be ruled out. The position-information by the scintillator-hodoscope is very rough and can be biased due to scale-errors. A scale-error could arise due to a wrongly assumed distance between the scintillator-blocks. Even with a wrong scale a rotation for one layer can be corrected. The residual-dependence is minimized by the position given from the scintillator-hodoscope. But the rotation-factor which is used for this correction is not in agreement with the actual rotation. Therefore this rotation-factor could not be compared in the case of a wrong scale between different layers. This would explain the additional rotation of the stereo-layers, as the nominal rotation from the design is assumed.

None the less a comparison of the rotation between readout-boards of the same layer can be made. For this the rotation of the central board (7) is used as reference. The rotation is subtracted from the rotations of the other two boards in order to make them comparable. For the most PCBs of all layers of all yet measured modules this difference is below $0.1\,\frac{\text{mm}}{\text{m}}$. The rotation can be extrapolated to the positions of the alignment-masks. Therefore the position of the borders of the PCBs is during panel-construction under control in the order of $100\,\mu\text{m}$.

The boards which are outlying with larger deviations to the rotation of the central board are among others the stereo-boards of module zero. For this module an old alignment-system was used, which got exchanged for series-production. The investigation of module zero at the H8 testbeam was done across several positions along the strips of each board. Therefore the rotation of the stereo-layers can be reconstructed by the residual with respect to the eta-out layer. Using the dependence of the mean-residual on the position along the strips the rotation is calculated. Only a coarse position information along the strips is available for these measurements as the module was moved mechanically. The values for the rotations of the boards are about $(26.2 \pm 0.9)\,\frac{\text{mm}}{\text{m}}$ and are therefore in good agreement with the expectation of $26.186\,\frac{\text{mm}}{\text{m}}$. But due to the large error the observed mis-rotation reconstructed by the CRF can not be excluded.

A test of the stability of the rotation-reconstruction is made with the eta-panel of module three. This module was disassembled for tests during the early phase of series production. Using the eta-panel a working doublet was built, consisting only of two active Micromegas layers. This doublet was remeasured in the CRF during the measurements of several other modules. The comparison of the reconstructed rotations between the boards showed almost the same values during all measurements. The maximum difference of reconstructed rotations between individual measurements of the eta-three-doublet are $0.03\,\frac{\text{mm}}{\text{m}}$. As the alignment-parameter, so the absolute rotations and positions, varied between these measurements the method seems to be reliable.

6.2.4. Calibration Impact on Alignment Homogeneity

The inhomogeneities of the readout-pattern due to pitch-deviations and the individual shifts and rotations of single PCBs can be corrected. The reconstructed shifts, rotations and pitch-deviations of the first measured modules can be found in the appendix G. The effect of the corrections on the homogeneity is shown in figure 6.18. For one layer the distributions of deviations to the nominal pattern are shown before and after calibration. This kind of plots are called in the following mean-residual-maps. For each partition the dependence of the residual on the track-slope is fitted linearly. The intercept of this fit corresponds to the residual for perpendicular incident and should reconstruct the deviation to the nominal pattern.

One can see clearly the much more homogeneous distribution after calibration (see figure 6.18b), as more partitions show similar colors. Despite this, still systematic deviations due to the strip-shape are observed after the calibration. For all modules the standard deviation over the surfaces is calculated, in order to quantify the effect of the correction on the overall distributions. This is done before and after calibration. The correlation of these standard deviations is shown in figure 6.18c. An improvement of the homogeneity for almost all layers of modules is observed.

The improvement for the stereo-layers is much larger, seen by the high values before correction and almost similar values to the eta-layers after correction for the blue triangles in figure 6.18c. This can be explained by the initial assumption of the nominal rotation of the stereo-layers. The observation is a measured rotation smaller than expected, which leads to the larger inhomogeneities before calibration. As this effect could also be

---

[8] For module 12 the inner-stereo-layer had a rotation of $-69 \pm 2\,\frac{\text{mm}}{\text{m}}$ w.r.t the eta-layers, the outer-stereo-layer $61 \pm 3\,\frac{\text{mm}}{\text{m}}$. The signs are changed with respect to the other modules as expected due to the flip of the readout-planes.

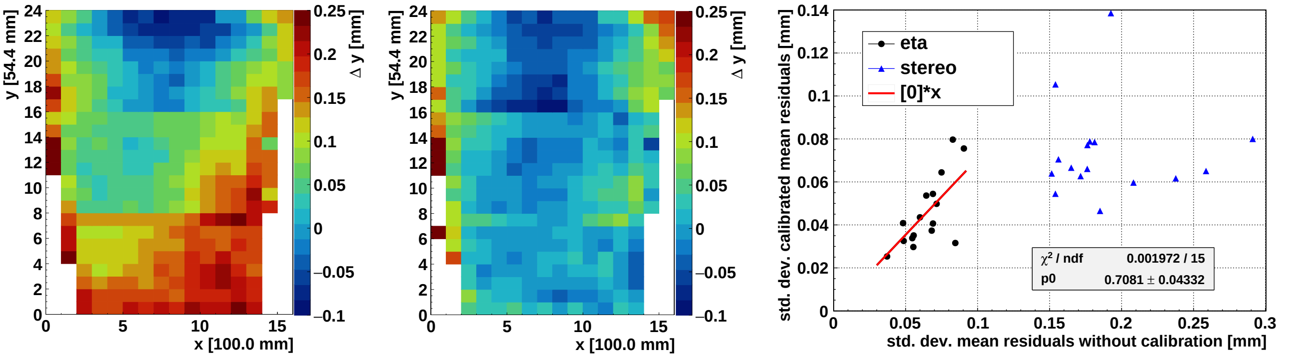

(a) Deviation of the strip pattern to the nominal design. Exemplaric plot for module three eta-out. The active area belongs to the second gluing side of the eta-panel three.

(b) Deviations after the calibration of pitch-deviations and rotations of single boards. Also the shift between the boards is corrected.

(c) Standard deviations of the mean residuals across the surface of the active area. Plotted are the values after calibration as function of the values before calibration.

Figure 6.18.: The homogeneity of the strip-pattern is distorted due to several effects. The calibration improves the homogeneity by reducing the residual-dependence on the position for all tested modules.

caused by systematics, the stereo-layers are excluded from the fit to the standard deviations. The slope of the fit indicates an average improvement of about (29±5)% due to this correction.

6.2.5. Comparison of Alignment Reconstructions

The muon tracks in ATLAS will be reconstructed using the combined information of all layers. Therefore it is important to know the position of each layer with respect to the other. As already seen in chapter 6.2.3 each board shows individual shifts and rotations. This is also reconstructed using the optical inspection from chapter 6.1.4. These two measurements should be comparable.

To investigate systematic effects, the alignment-reconstruction in the CRF is investigated for the eta-panels of three modules. As the stereo-layers show the unexpected systematic rotations they are excluded for this analysis. For eta panels three, eight and nine the alignment can be compared with respect to the Rasfork-measurement. Additionally for the latter two panels also the CMM-scan done in Saclay can be used. Due to the unsatisfactory calibration of the CMM at the LMU no comparison with these data is performed. Only the deviations in precision-direction, so perpendicular to strips, are considered. This is the most important information for the NSW-tracker of the ATLAS experiment. Deviations along the strips are neither reconstructible in the CRF nor of concern for the track reconstruction.

Comparison of the Layer-to-Layer Alignment-Reconstruction by Rasfork and Cosmic-Measurements

Several cosmic-measurement campaigns were performed with eta-panel three. The panel was assembled in module three for the first two periods, during August and September 2018. Afterwards the module was disassembled and the eta-panel was assembled as doublet for further testing. The alignment is reconstructed for measurements in December 2018, January and May 2019. For a first investigation the board rotation and strip-shapes of the three boards are compared in figure 6.19. The overall alignment between the measurements is different, due to slight different positions of the chamber in the CRF. This is noticed by the slightly different slopes and mean values, which are created by the rotation with respect to the MDT wires[9].

Similar features are observed for all measurement periods. For the small board (6) the two layers seem to have almost parallel orientation, with a constant offset between 0.08 mm and 0.12 mm. The central board (7) and the large board (8) show for both layers in all measurements the U-like shape. While for the large board (8) just offsets are observed, the central board (7) shows one side with a small and the other side with a larger difference between the layers. This would correspond to a rotation of the PCBs during alignment at the panel-construction.

Some explanations for the comparison of these reconstructions with the Rasfork-measurements have to be given. First, the exact evaluation-points of the cosmic-measurements can not be defined. This is caused by the coarse resolution of the position along the strips by the scintillator-hodoscope. As can be seen in several plots in figure 6.19 some outer points have to be excluded. This has to be made as the residual is distorted at the edges, due to the tapered-shape of the modules. Second, for the cosmic-measurements the residual is averaged over one whole readout-PCB. As already seen the pitch between the strips varies. Therefore this averaging introduces, combined with the inhomogeneous illumination a systematic error.

Third, the distance-calculation for the cosmic-measurements is performed within the active area. Whereas the Rasmask-measurements is performed at the outer border of the boards. A fourth issue is the overall alignment

---

[9] A common rotation of the whole module is calibrated for each measurement as described in chapter 6.2.1. Despite this small individual rotations remain as the mean rotation is depending also on the illumination and therefore on the positioning in the CRF.

September 2018, in module three. January 2019, as doublet. May 2019, as doublet.

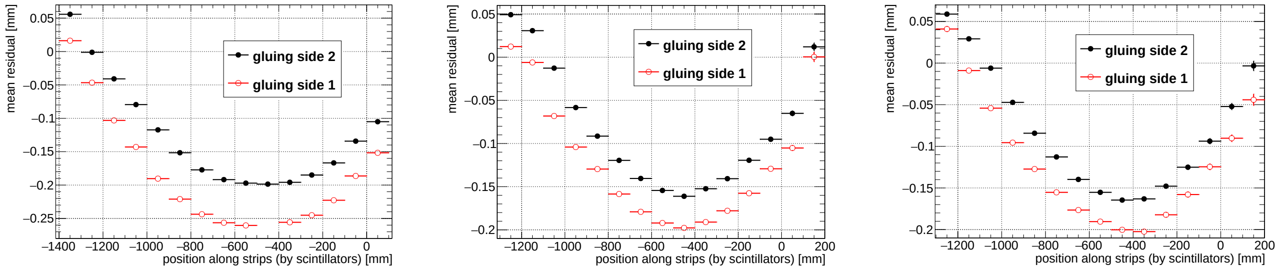

(a) large board (8)

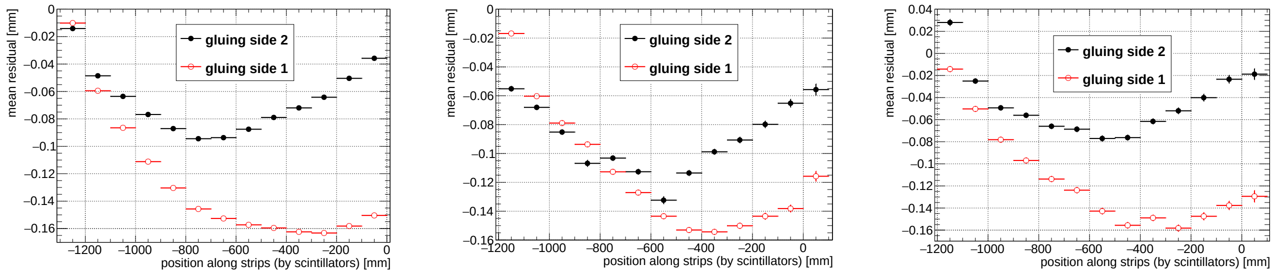

(b) central board (7)

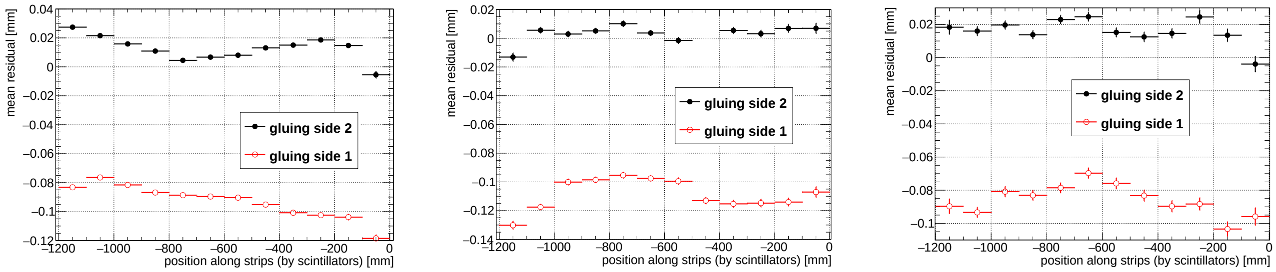

(c) small board (6)

Figure 6.19.: The alignment of the eta three panel was investigated during several measurement campaigns. Between the periods the alignment was alternated and the module was also reassembled into a doublet.

in the CRF. The values reconstructed from the cosmic-measurements are relative to this reference. In order to make them comparable to the Rasmask-measurements the values have to be considered relative to each other. These issues can be tackled using the mean-residual-maps introduced in the last chapter 6.2.4. In figure 6.18a the map is shown for one side of the discussed readout-panel. A similar map is reconstructed for the other side (seen in figure 6.20a).

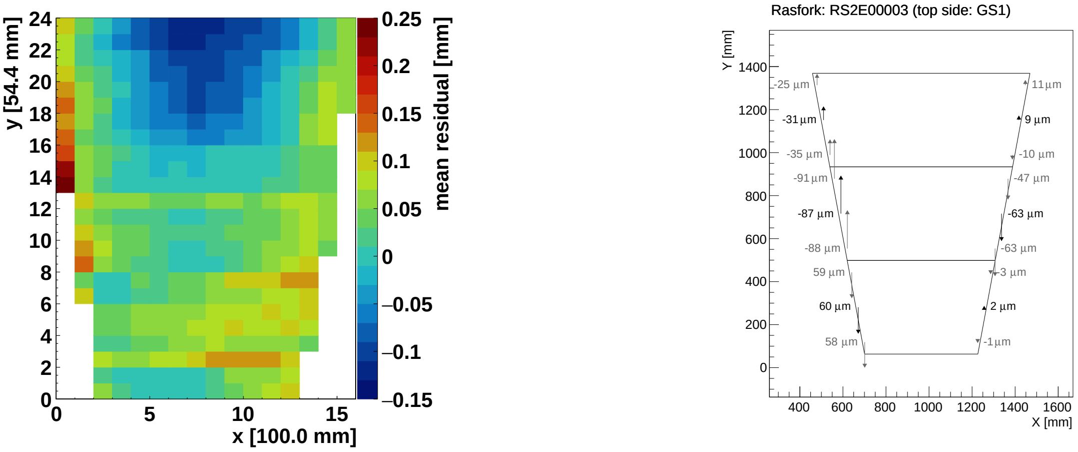

(a) Mean-residual-map for the eta-in layer of module three for measurements during end of September 2018.

(b) Rasfork measurement of the eta-three panel.

Figure 6.20.: The alignment of the panels is measured during assembly and reconstructed during cosmic-measurements in the CRF.

Both are evaluated without the calibration-corrections in order to investigate the initial alignment. They reassemble the already observed strip-shapes averaged over the whole readout-boards, but disentangle the effect of the pitch-deviations. For a first comparison with the Rasfork-measurement (seen in figure 6.20b) slices along the y-axis, so along the precision-direction, are considered. This is done for both layers left and right to the center. The reconstructed mean-residuals along these slices are shown in figure 6.21.

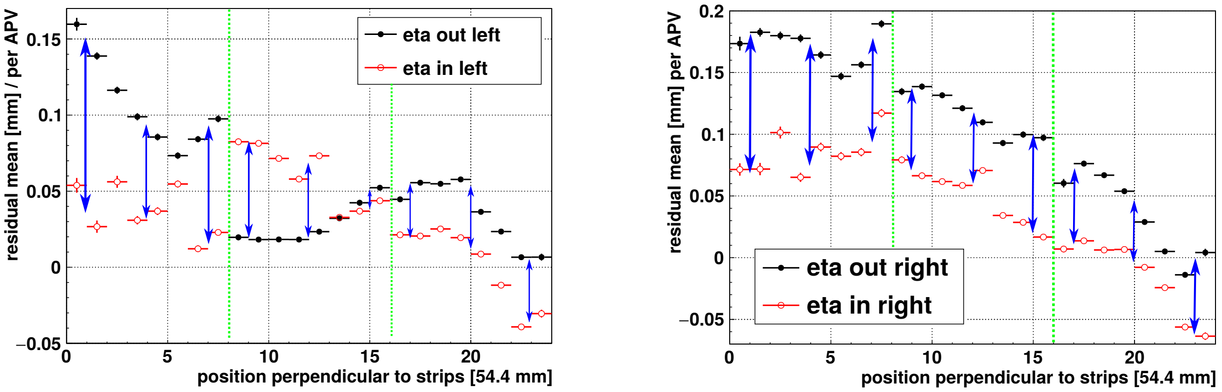

(a) Left band,. **(b)** Right band.

Figure 6.21.: Mean-residual as function of the position perpendicular to the strips, so along the precision-direction. The residuals are considered in a ten centimeter broad range along the strips within the active area. This is done for groups of 128 strips, so about 54.4 mm wide slices perpendicular. Blue arrows indicate the differences at the positions of the Rasmasks. Green lines indicate the junctions of the PCBs.

The green separators indicate the junctions of the readout-PCB. The left side of the plots correspond to the small boards (6), whereas the right side correspond to the large boards (8). The blue arrows indicate the reconstructed shifts between the two layers. The sizes of the arrows have to be compared to the Rasfork-measurements of this panel. The direct comparison is made in table 6.2 (column int.). No clear correlation between the values is observed. For their interpretation it has to be considered that a difference between the left and the right value corresponds to a rotation between the boards.

The Rasfork measurement reconstructs a rotation between the small boards (6). For these boards the cosmic-measurement reconstructs large shifts and distortions of the pitch seen by varying differences along one board. The difference between the left and right values corresponds more to a general shift than a rotation between these boards. An even larger rotation is reconstructed for the central boards (7) by the Rasfork-measurement. The cosmic-measurement reconstructs here a rotation in the other direction. The smallest differences are found for the large boards (8) in both measurements. Due to the observation of different rotation directions at the central boards (7) the systematics have to be checked for further analysis.

board	left				right				difference			
	Ras.	cosmics			Ras.	cosmics			Ras.	cosmics		
		int.	ext.	dir.		int.	ext.	dir.		int.	ext.	dir.
8	3	4	10	n.a.	1	5	10	n.a.	2	-1	0	n.a.
	3	3	-2	0	1	5	-2	1	2	-2	0	-1
	4	3	2	3	-1	6	4	6	5	-3	-1	-3
7	9	1	2	0	-5	7	10	10	14	-6	-8	-10
	9	-4	0	0	-6	6	13	11	15	-12	-13	-11
	9	-6	-10	4	-6	6	10	13	15	-12	-16	-11
6	-6	8	18	15	0	7	14	14	-6	1	4	1
	-6	6	13	11	0	10	10	13	-6	-4	3	-2
	-6	11	15	13	0	11	8	9	-6	0	7	4
error	1	3	6	4	1	3	6	4	2	5	10	8

Table 6.2.: Reconstructed shifts between the readout layer of the eta-panel three for the two tapered sides of the trapezoid. Also the difference between left and right is shown. Values are given in 0.01 mm. No clear correlation between Rasfork (Ras.) and cosmic-measurement can be observed. For the cosmic-measurements three kinds of reconstructions are investigated. A comparison interior (int.) and extrapolated (ext.) of the active area is made. Also the direct (dir.) difference between the reconstructed hits in the layer is considered.

Using the reconstructed deviations to the strip-pattern the cosmic-measurements can be further evaluated. The Rasfork-measurements are done exterior of the active-area. Therefore the strip-shape is extrapolated. Each slice of the mean-residual-map along x, so along the strips, is fitted using a second-degree polynomial. These functions are evaluated at the positions of the Rasmask, so at the outer borders of the PCB. This approach corresponds to an extrapolation of the strip-shape to the border of the PCB. The extrapolated values are shown separately for the left and the right side of the active area of both layers in figure 6.22.

The left side of the plots in figure 6.22 corresponds to the small side of the trapezoid, while the right side corresponds to the large side. The extrapolation is causing large uncertainties. Also some positions are missing

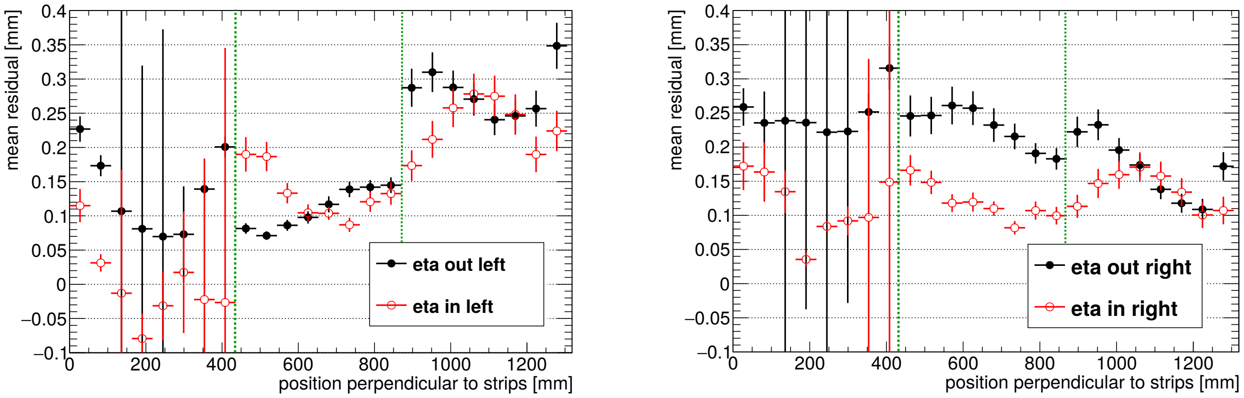

(a) Left extrapolation. **(b)** Right extrapolation.

Figure 6.22.: Reconstructed alignment of the eta-panel three assembled in module three during measurements in September 2018. The reconstruction is achieved by the extrapolation of the strip-shape to the tapered border of the panel.

due to failing fits or problematic regions in the map. This is especially problematic for the small board (6) due to the short strip-length and therefore less fit-points (seen for position between 0 mm and 400 mm).
Comparing these extrapolations with the reconstructed deviations in figure 6.21 one recognizes very different developments. For the large board (8) on the right hand side the difference is most significant, due to the large observed strip-bending (see blue area in the upper part of figures 6.18a and 6.20a). Another interesting observation for this board is that the two layers seem to be closer to each other after extrapolation (seen for values above 900 mm).
All boards show a strong variation of the extrapolated mean residuals perpendicular to the strips in figure 6.22. This could indicate a very inhomogeneous effect of the humidity on the board elongation or shrinkage as discussed in chapter 6.2.2. In order to make this evaluation better comparable to the Rasfork-results the difference between the reconstructed extrapolations of the two layers is calculated. To investigate systematic effects and the stability of this approach the evaluation is done for several measurement-periods. The comparison of their results are shown in figure 6.23.

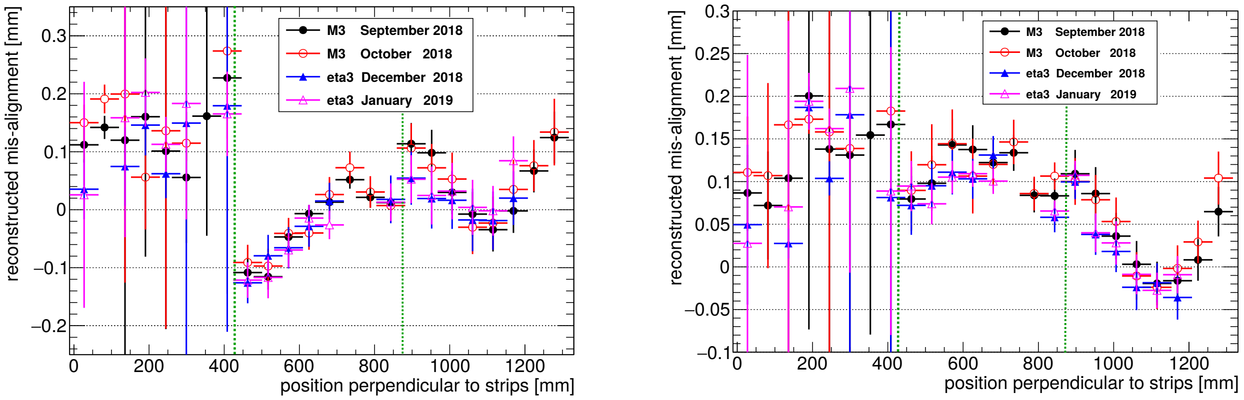

(a) Left extrapolation. **(b)** Right extrapolation.

Figure 6.23.: Reconstructed mis-alignment of the eta-panel three during four measurement periods with cosmic muons. Shown is the difference of the extrapolated strip-shape of the two layers.

The extrapolations of the small board (6) are problematic, reconstructing shifts of about 0.1 mm to 0.2 mm. Similar behavior of the mis-alignment is reconstructed during all measurement-periods for the central board (7) and the large board (8) (seen for positions above 400 mm). For the same assembly situation, either in module three (M3) or as doublet (eta3), the differences between the measurements are not larger than 0.04 mm. Comparing the two assembly situations, larger differences could be caused by deformations during dis- and reassembly. However, also these differences stay below a 0.06 mm level. Therefore the reconstruction is stable up to this magnitude.
In table 6.2 the reconstructed shifts by this method are compared to the values of the Rasfork-measurement (see column ext.). Much larger shifts than for the Rasfork-measurement are reconstructed evaluating the cosmic data with this approach. As this is very unreasonable and the uncertainties are very high another reconstruction technique is also investigated.
Instead of considering the difference to the reference, the direct difference of the position reconstructed in the two layers is calculated. The active surfaces are about 16.5 mm apart for the two layers. This leads to systematic shifts for inclined tracks. Either only normal tracks can be considered, which drastically reduce the statistics, or

the track-slope has to be used as correction for this effect. The second approached yields more homogeneous and stable results, therefore this is chosen for the following investigation. The reconstructed maps of the position-differences are shown in figure 6.24 for three measurement-periods.

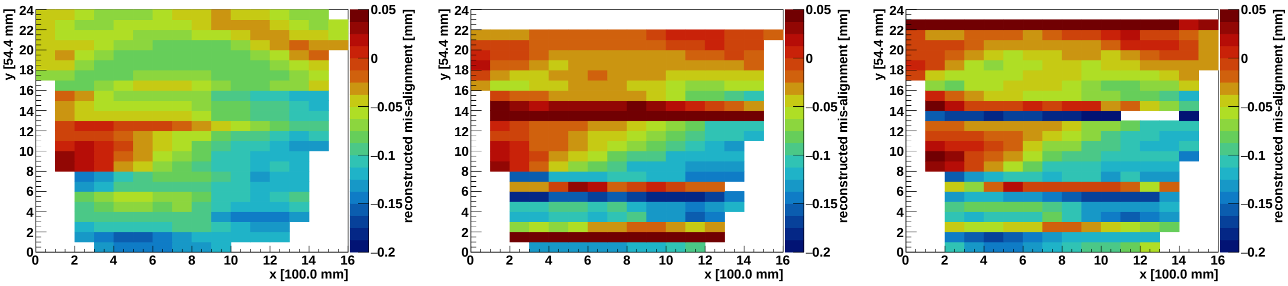

(a) September 2018, in module three. **(b)** January 2019, as doublet. **(c)** May 2019, as doublet.

Figure 6.24.: Maps of the mean difference in reconstructed positions between the two sides of the eta-panel three. The differences had to be corrected for the track-inclination. Several horizontal-lines are mis-reconstructed for the latter two measurements due to problematic electronics.

For the latter measurements several electronic cards lead to problematic reconstructions. This is seen as horizontal lines, which do not fit into the pattern and have very high or low mis-alignment reconstructions. Also unexpected differences between the measurements are observed. Similar structures are found on the central board (7) for all measurements. Also on the large board (8) similarities in U-like shapes are found, but are distorted between the measurements. Therefore this approach shows discrepancies due to systematic effects. For the evaluation of these maps no extrapolation can be performed as the development along the strips in x, is irregular. This arises probably due to the superposition of the strip-shapes from the two layers. To perform the comparison to the Rasfork-measurements as closest as possible the reconstructed differences at the corresponding edges are considered. Here also the values are listed in table 6.2 (see column dir.). The measurement from January 2019 have been considered for this overview.

Despite several outliers, the analyses of cosmic-measurements show all the same tendencies. Rather small deviations on the large boards (8), a rotation of the central boards (7) and a large shift of boards (6). The minor differences between the large boards (8) could be explained by the alignment technique. The large boards (8) are placed closest to the precision pins on the table during construction. Therefore a rotation or deformation of the alignment-frame would have the least effect on these boards. For the small boards (6) the reconstruction can be systematically biased due to the detector position in the CRF. The edge of the detector was for these measurements very close to the border of the measurement region. Therefore the illumination as well as the angular distribution is very inhomogeneous for these boards. No simple explanation for different rotation of the central boards (7) in comparison to the Rasfork-measurements was found.

Several statistical and systematic uncertainties limit this reconstruction comparison. In order to exclude a systematic bias, due to for example faulty Rasfork-measurements, also the two other mentioned eta-panels are investigated using the same approaches. Their results are summarized in tables 6.3 and 6.4.

Eta-Panel Eight has a large rotation between the small boards (6) reconstructed by the Rasfork-measurement. This is seen in table 6.4, column Ras., by the differences of the left to the right values in the range of −0.13 mm to −0.18 mm. For the large boards (8) and the central boards (7) only minor shifts up to −0.06 mm are measured. The evaluation of the cosmic-measurement reconstructs a general shift and an overall rotation between the layers. The shifts are in the range of −0.01 mm to −0.18 mm. The rotations of the large boards (8) and the central board (7) are reconstructed between −0.01 mm and −0.12 mm. For the central board (7) also a minor rotation in opposite direction is reconstructed in the center between 0.01 mm and 0.06 mm.

In figure 6.25a the small boards (6) show an increased left-right-difference, compared the other boards, in the order of −0.05 mm to −0.22 mm. The small boards (6) correspond to positions below 435.2 mm. Also in the map of the mean differences between the layers (see figure 6.25b) the lower part, which corresponds to the small board (6), reconstructs a larger left-right-asymmetry.

The general large shift between the layers could indicate a systematic bias. A slightly wrong assumed distance between the layers would lead, due to the track-slope correction, to such a discrepancy.

Eta-Panel Nine features in the Rasfork-measurement left-right-differences of the two layers in range between −0.10 mm and −0.22 mm (see table 6.4, column Ras.). This corresponds to an overall rotation of the two layers. Similar in the cosmic-evaluation the layers show large left-right-differences. This is seen in figure 6.26. On the right side the layers reconstruct almost the same values, whereas on the left side larger differences are found. In contrast the Rasfork-measurement reconstructs also for the right side larger differences. For the cosmic-measurements the differences are ranging from −0.04 mm to −0.17 mm. The extrapolated values on the left side are very large, showing the strong effect of the strip-shape on this reconstruction.

board	left				right				difference			
	Ras.	cosmics			Ras.	cosmics			Ras.	cosmics		
		int.	ext.	dir.		int.	ext.	dir.		int.	ext.	dir.
8	-4	-20	n.a.	-20	2	-18	n.a.	-13	-6	-2	n.a.	-7
	-5	-16	-5	-15	0	-15	-7	-12	-5	-1	2	-3
	-6	-18	-6	-16	-2	-12	-1	-9	-4	-6	-5	-7
7	-3	n.a.	-9	-14	0	n.a.	-6	-13	-3	n.a.	-3	-1
	-2	-12	-3	-12	2	-13	-9	-13	-4	1	-6	1
	0	-12	-19	-13	1	-7	-7	-9	-1	-5	-12	-4
6	-7	-10	-20	-17	11	-3	-5	-4	-18	-7	-15	-13
	-8	-7	-18	-12	8	-2	-5	-4	-16	-5	-13	-8
	-9	-13	-25	-17	5	-3	-4	-3	-14	-10	-21	-14
error	1	3	10	4	1	3	6	4	2	5	10	8

Table 6.3.: Reconstructed shifts between the readout layer of the eta-panel eight at the two tapered sides of the trapezoid. Also the difference between left and right is shown. Values are given in 0.01 mm. No clear correlation between Rasfork (Ras.) and cosmic-measurement can be observed. For the cosmic-measurements a comparison interior (int.) and extrapolated (ext.) of the active area is made. Also the direct (dir.) difference between the reconstructed hits in the layer is considered.

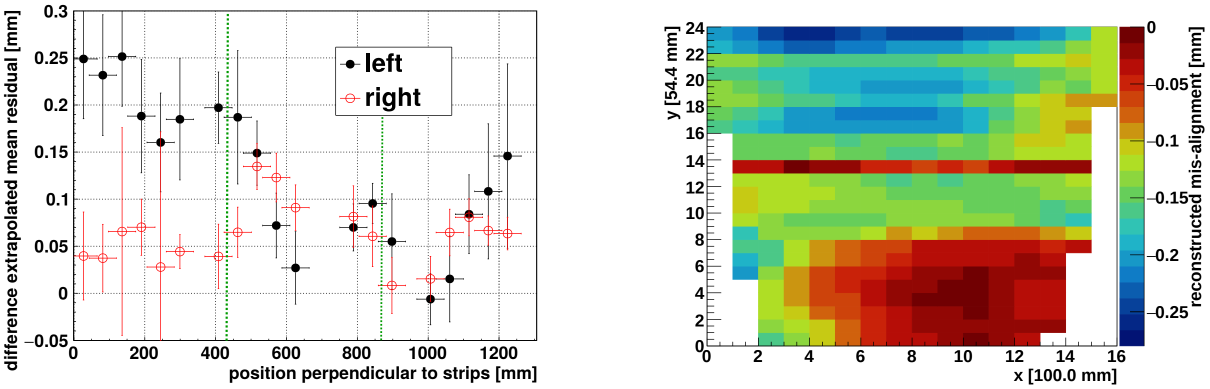

(a) Differences of the extrapolated mean residual as function of the position perpendicular to the strips. The differences are shown for the left and right extrapolation.

(b) Map of the mean difference in reconstructed positions between the two the eta-layers. The differences had to be corrected for the track-inclination.

Figure 6.25.: Reconstructed differences between the layers of eta-panel eight. Horizontal lines in the map and missing points for the extrapolations are due to mis-configured electronics. For table 6.3 the sign of the differences of the extrapolated mean residuals has to be inverted.

The rotations of the boards can be considered individually. The Rasfork-measurement reconstructs the smallest left-right-differences for the central board (7), in the range of −0.10 mm to −0.13 mm. Whereas the cosmic-measurement reconstructs the smallest left-right-differences for the large board (8) between −0.04 mm and −0.13 mm. For the small board (6) and the large board (8) the Rasfork-measurement predicts similar rotations with left-right-differences of about −0.21 mm. Contrary the cosmic-measurement reconstructs larger left-right-differences for the small board (6) between −0.05 mm and −0.30 mm.

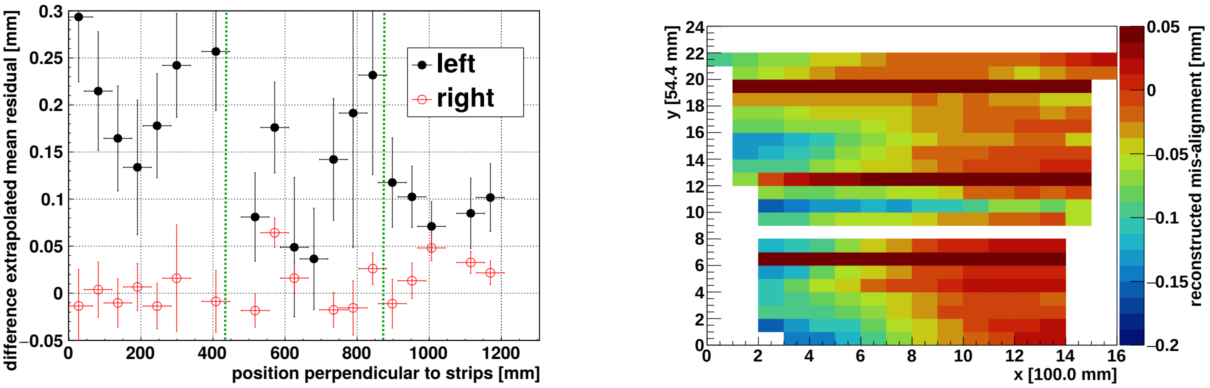

(a) Differences of the extrapolated mean residual as function of the position perpendicular to the strips. The differences are shown for the left and right extrapolation.

(b) Map of the mean difference in reconstructed positions between the two the eta-layers. The differences had to be corrected for the track-inclination.

Figure 6.26.: Reconstructed differences between the two layer of eta-panel nine. Horizontal lines in the map and missing points for the extrapolations are due to mis-configured electronics. For table 6.4 the sign of the differences of the extrapolated mean residuals has to be inverted.

board	left				right				difference			
	Ras.	cosmics			Ras.	cosmics			Ras.	cosmics		
		int.	ext.	dir.		int.	ext.	dir.		int.	ext.	dir.
8	-13	n.a.	n.a.	n.a.	9	n.a.	n.a.	n.a.	-21	n.a.	n.a.	n.a.
	-12	-6	-7	-6	7	-1	-3	-1	-19	-5	-4	-5
	-11	-6	-12	-8	5	0	1	0	-16	-6	-13	-8
7	-3	-14	-23	-14	10	-2	-3	-2	-13	-12	-20	-12
	-5	-5	-4	-8	7	-4	-2	-2	-12	-9	-6	-10
	-5	-8	n.a.	-9	5	1	n.a.	0	-10	-9	n.a.	-9
6	-12	-12	-26	-12	10	1	1	1	-22	-13	-27	-13
	-11	-6	-16	-10	10	1	1	2	-21	-7	-17	-12
	-9	-13	-29	-15	13	-1	1	2	-23	-12	-30	-17
error	1	3	10	4	1	3	6	4	2	5	10	8

Table 6.4.: Reconstructed shifts between the readout layer of the eta-panel nine at the two tapered sides of the trapezoid. Also the difference between left and right is shown. Values are given in 0.01 mm. No clear correlation between Rasfork (Ras.) and cosmic-measurement can be observed. For the cosmic-measurements a comparison interior (int.) and extrapolated (ext.) of the active area is made. Also the direct (dir.) difference between the reconstructed hits in the layer is considered.

Discussion : To summarize this investigation, one can say that the direct comparison between the Rasfork-measurements and cosmic-measurements is very difficult at values below a few 10 µm. This is due to limitations by statistical fluctuations, as well as systematic uncertainties. The largest problem is the difference of the measurement positions. The Rasfork-measurements are performed outside of the active area, whereas the cosmic-results have to be extrapolated or evaluated at the edges. This is aggravated due to the deformed strip-shape, but also limited by the coarse resolution of the scintillator-hodoscope. Also effects due to inhomogeneous illumination and mechanical alignment could not be excluded. Despite the limitations, for the two eta-panels eight and nine features are reconstructed very similar with both measurements. The used reconstruction techniques for the cosmic-measurements differ in their stability, as in their performance. The fit of the strip-shape leads to large fluctuations and errors for the extrapolation. The most stable and best comparable results to the Rasfork-measurements enables the direct difference between the two eta-layers. Also this reconstruction can be biased due to the evaluation at the edges. Therefore a good selection of evaluation-points is required. The investigation showed the need for statistics for this comparison. Therefore a period of about a week for the module validation measurements should be envisaged.

Comparison of the In-Plane Alignment-Reconstruction by CMM and Cosmic-Measurements

The alignment-reconstruction within a single layer is performed using reference systems. This introduces dependencies on the used system, as the deviations are calculated with respect to the reference. The dependencies are caused by the shift and the rotation of the layer with respect ot the reference system. To compare CMM and cosmic-measurements the total shift and rotation of the two measurements have to be equalized.

This is achieved by defining a common axis, which acts as reference between the two measurements. A suitable choice for this axis is the middle line along the strips on the central board (7). The end-positions of this line on the central board (7) define the axis. The deviations of these positions are set to zero and all other deviations are calculated with respect to this axis. For the CMM-Rasmask-measurements these positions correspond to the central Rasmasks on the central board (7). The cosmic-measurements have to be aligned for one layer according to the shift and rotation reconstructed on the central board (7). The deviations are calculated similar to the last sub-chapter either at the edges of the active area or by the extrapolated strip-shapes. Additionally to this two approaches the integrated residuals are considered. This is done according to chapters 6.2.2 and 6.2.3.

The integration over the active area introduces a bias due to the inhomogeneous illumination in the CRF (see figure 4.4a). Also the orientation of the layers has to be kept in mind. The second gluing-side, considered as eta-out during cosmic-measurements, is facing the ground. To account for this, the CMM-reconstruction values are swapped for these layers. The data for the CMM-Rasmask-measurement done at Saclay can be found unrotated in the appendix E. In order to make quantitative reasonable statements, rotations are considered in the following as differences of the left and the right value. Similar, shifts are considered as the common offset of the left and the right value. For the alignment procedure the most important information is the total alignment of the boards with respect to each other. Therefore the discussion is made for whole boards instead of only single positions. In the mean-residual-maps the central board (7) is located from 8 to 16 times 54.4 mm, while the small board (6) is at the bottom and the large board (8) the top of the plot.

Eta-Panel Eight, Gluing Side One shows a rotation of the small board (6) with respect to the central board (7) in the CMM-Rasmask-measurement. This is seen by the left-right-difference of 0.08 mm to 0.11 mm in table 6.5 (column Ras.). A rotation is reconstructed for cosmics as well in figure 6.27a. The small board (6) has a more positive slope, while the central board(7) has a stronger U-like deformation, seen in the mean-residual-map of figure 6.27c. The left-right-difference of the mean residual difference of the small board (6) to the central board (7) for the cosmic-reconstruction from figure 6.27a is about −0.05 mm. The extrapolation reconstructs also a rotation of about −0.06 mm to −0.14 mm. This is hardly recognized in figure 6.27d due to the large errors and the initial rotation of the central board (7). From this plot a non-uniform rotation of the large board (8) is reconstructed in the range of −0.03 mm to 0.10 mm. The behavior of the mean residual as function of the position perpendicular to the strips in figure 6.27b is unexpected from the CMM-Rasmask-measurement. The board edges are clearly distinguishable in this distribution at about −700 mm and −50 mm. The U-like shape for the small board (6) on the left and the large board (8) on the right are not understood yet.

board	left			right			difference		
	Ras.	cosmics		Ras.	cosmics		Ras.	cosmics	
		int.	ext.		int.	ext.		int.	ext.
	-3	6	7	-2	4	-3	-1	2	10
8	-2	3	14	0	5	4	-2	-2	10
	0	0	3	2	4	6	-2	-4	-3
7	-2	3	-4	-1	5	1	-1	-2	-5
	1	-2	-2	2	2	-2	-1	-4	-3
	6	-1	-7	-5	5	-1	11	-6	-6
6	6	1	-8	-2	0	-4	8	1	-12
	8	-9	-10	2	-6	-4	10	-3	-14
error	1	4	6	1	4	6	2	8	10

Table 6.5.: Reconstructed alignment for the first gluing side of eta-panel eight for the two tapered sides of the trapezoid. Also the difference between left and right is shown. Values are given in 0.01 mm. No direct correlation between Rasmask (Ras.) and cosmic-measurement can be observed. A comparison interior (int.) and extrapolated (ext.) of the active area is made.

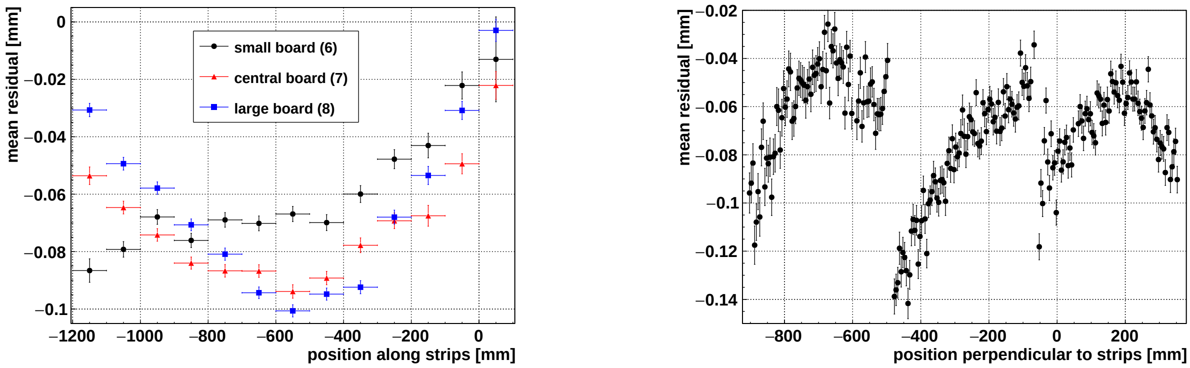

(a) Mean residual as function of the position along the strips. Separately shown for the three readout-boards.

(b) Mean residual as function of the position perpendicular to the strips. Integrated over the full active area.

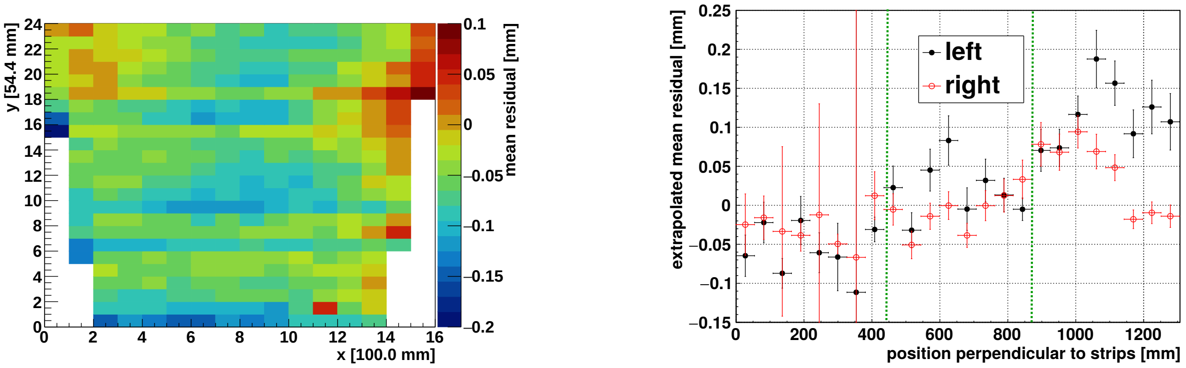

(c) Mean-residual-map.

(d) Mean residuals perpendicular to the strips, left and the right extrapolated to the positions of the Rasmasks.

Figure 6.27.: Reconstructed deviations to the nominal strip-pattern for the first gluing-side of eta-panel eight. This side is considered as eta-in in module eight.

Eta-Panel Eight, Gluing Side Two shows a minor shift of about 0.03 mm for the large board (8) in the CMM-Rasmask-measurement. Also an only slight rotation for the small board (6) between −0.02 mm and −0.07 mm is reconstructed. Rather large rotations and shifts are reconstructed for the cosmic-measurements. This is especially recognized in the mean-residual-map in figure 6.28c. Here the three boards are distinguished by the colors red for the large board (8), green-yellow for the central board (7) and blue for the small board (6). The reconstructed rotations for the small board (6) are ranging from 0.06 mm to 0.20 mm. Also for the large board (8) rotations from 0.01 mm to 0.14 mm are reconstructed. A deformation of the whole panel is suggested by the mean residual as function of the position perpendicular to the strips seen in figure 6.28b. The linear dependence indicates a shrinkage, which is not seen in the CMM-Rasmask-measurement. Also for the other gluing side such a behavior is not reconstructed[10]. The discrepancy between CMM-Rasmask-measurement and cosmic-measurement could be explained by the deformed strip-shape, which aggravates the comparison.

board	left			right			difference		
	Ras.	cosmics		Ras.	cosmics		Ras.	cosmics	
		int.	ext.		int.	ext.		int.	ext.
	-3	13	14	-3	3	0	0	10	14
8	-4	7	15	-3	6	6	-1	1	9
	-4	2	6	-2	0	3	-2	2	3
7	-3	3	4	-3	3	4	0	2	3
	4	3	8	2	-1	-3	2	4	11
	-3	1	7	4	-5	-4	-7	6	11
6	1	1	5	3	-10	-5	-2	12	10
	2	-6	11	4	-14	-5	-2	8	16
error	1	4	6	1	4	6	2	8	10

Table 6.6.: Reconstructed alignment for the second gluing side of eta-panel eight for the two tapered sides of the trapezoid. Also the difference between left and right is shown. Values are given in 0.01 mm. No direct correlation between Rasmask (Ras.) and cosmic-measurement can be observed. A comparison interior (int.) and extrapolated (ext.) of the active area is made.

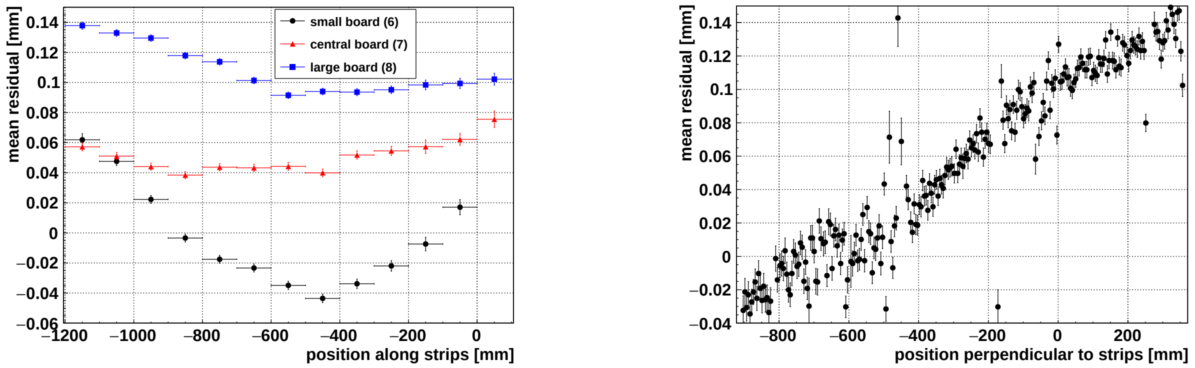

(a) Mean residual as function of the position along the strips. Separately shown for the three readout-boards.

(b) Mean residual as function of the position perpendicular to the strips. Integrated over the full active area.

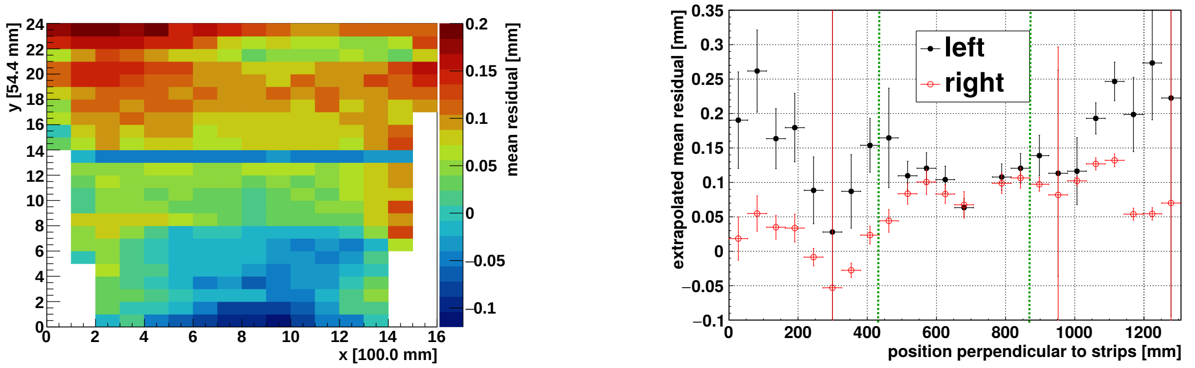

(c) Mean-residual-map.

(d) Mean residuals perpendicular to the strips, left and the right extrapolated to the positions of the Rasmasks.

Figure 6.28.: Reconstructed deviations to the nominal strip-pattern for the second gluing-side of eta-panel eight. This side is considered as eta-out in module eight.

---

[10] A thermal effect on the MDT reference can be excluded. Such an effect would also be seen on the other gluing side and would be in the order of more than 5 °C.

Eta-Panel Nine, Gluing Side One shows a shift of about 0.02 mm and a rotation of about 0.05 mm for the small board (6) in the CMM-Rasmask-measurement. Only minor deviations are reconstructed for the large board (8). For the cosmic-measurement the alignment of this layer has to be redone, due to the initial rotation with respect to the other layer of the panel[11]. The large board (8) and the central board (7) show the U-like shape, while for the small board (6) a major a shift and rotation is seen in figure 6.29a. The reconstructed rotation of the small board (6) from the cosmic-measurement is between 0.00 mm and −0.16 mm in the opposite direction as expected from the CMM-Rasmask-measurement. For this layer similar structures as seen for gluing side one of the eta-panel eight are reconstructed in the mean residual as function of the position perpendicular to the strips.

board	left			right			difference		
	Ras.	cosmics		Ras.	cosmics		Ras.	cosmics	
		int.	ext.		int.	ext.		int.	ext.
8	-3	2	10	-2	10	7	-1	-8	3
	-3	0	6	-1	4	0	-2	-4	6
	-2	-2	8	1	6	7	-3	-8	1
7	-3	-1	-7	-3	4	-1	0	-5	-6
	2	-7	3	2	-1	-4	0	-6	7
6	7	-13	-12	2	-3	-8	5	-10	-4
	7	-7	-5	2	-2	-5	5	-5	0
	7	-16	-12	2	0	-4	5	-16	-8
error	1	4	6	1	4	6	2	8	10

Table 6.7.: Reconstructed alignment for the first gluing side of eta-panel nine for the two tapered sides of the trapezoid. Also the difference between left and right is shown. Values are given in 0.01 mm. No direct correlation between Rasmask (Ras.) and cosmic-measurement can be observed. A comparison interior (int.) and extrapolated (ext.) of the active area is made.

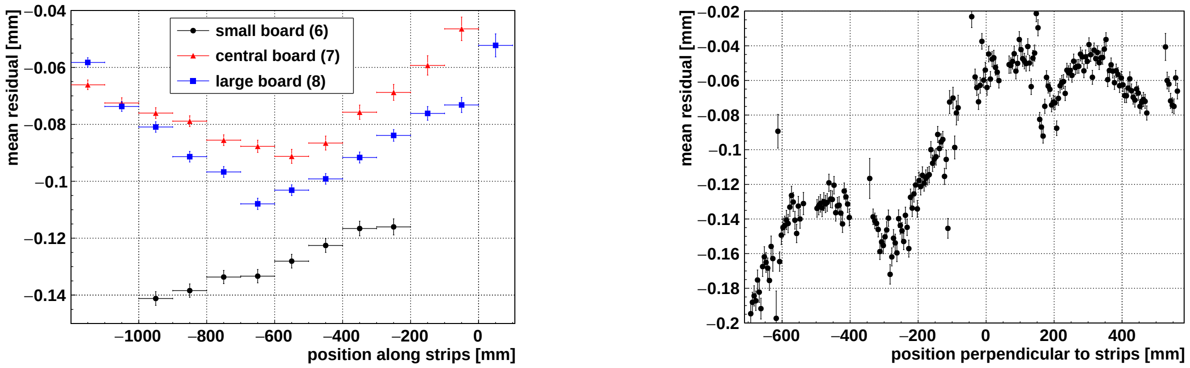

(a) Mean residual as function of the position along the strips. Separately shown for the three readout-boards.

(b) Mean residual as function of the position perpendicular to the strips. Integrated over the full active area.

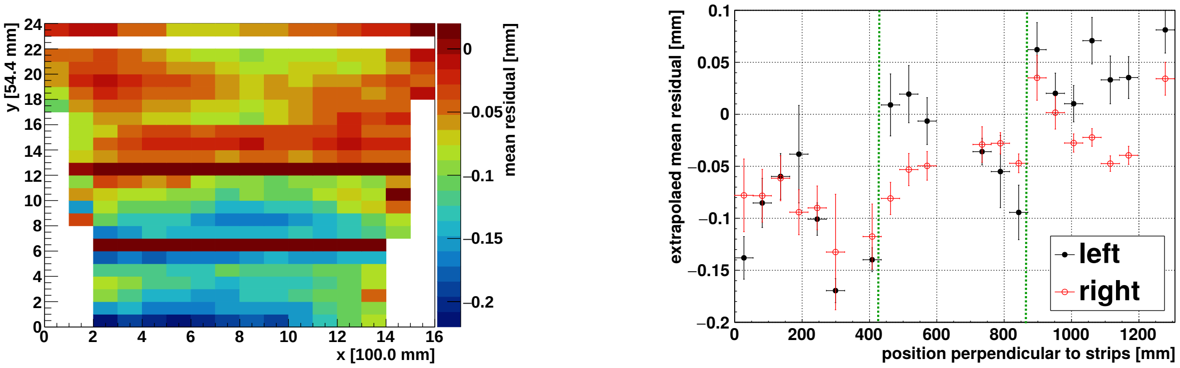

(c) Mean-residual-map.

(d) Mean residuals perpendicular to the strips, left and the right extrapolated to the positions of the Rasmasks.

Figure 6.29.: Reconstructed deviations to the nominal strip-pattern for the first gluing-side of eta-panel nine. This side is considered as eta-in in module nine.

---

[11] The Micromegas alignment for CRF-measurements is performed with respect to the eta-out layer which corresponds to the second gluing side. Due to the initial rotation of the two layers the values for gluing side one showed a large rotation of the whole layer.

Eta-Panel Nine, Gluing Side Two shows rotations of the small board (6) in the range of −0.03 mm to −0.05 mm in the CMM-Rasmask-measurement. Larger rotations between 0.10 mm and 0.13 mm are reconstructed for the large board (8). These two rotations are contrary. A similar behavior is seen in figure 6.30b for the cosmic-measurement. The extrapolated values for the left side of the small board (6), seen for positions below 450 mm, are above the right side values. Vice versa for the large board (8), seen for positions above 850 mm. For the small board (6) the left-right differences are in the range between −0.03 mm and −0.11 mm. The large board (8) shows left-right differences in the range of 0.01 mm to 0.16 mm. Therefore this cosmic-reconstruction is in agreement with the CMM-Rasmask-measurement. The linear dependence seen for the central board (7) in the averaged and in the extrapolated mean residual as function of the position perpendicular to the strips is unexpected from the CMM-Rasmask-measurement. This dependence suggests a shrinkage of the board with respect to the nominal pattern.

board	left			right			difference		
	Ras.	cosmics		Ras.	cosmics		Ras.	cosmics	
		int.	ext.		int.	ext.		int.	ext.
8	10	3	4	-3	3	3	13	0	1
	9	6	5	-3	-1	1	12	7	4
	7	5	10	-3	1	6	10	4	4
7	-1	3	4	-1	5	3	0	-2	-1
	1	5	-3	2	-2	0	-1	7	-3
6	0	-8	-6	5	-3	0	-5	-5	-6
	1	-4	-5	5	-1	-1	-4	-3	-4
	2	-3	-6	5	0	4	-3	-3	-10
error	1	4	6	1	4	6	2	8	10

Table 6.8.: Reconstructed alignment for the second gluing side of eta-panel nine for the two tapered sides of the trapezoid. Also the difference between left and right is shown. Values are given in 0.01 mm. No direct correlation between Rasmask (Ras.) and cosmic-measurement can be observed. A comparison interior (int.) and extrapolated (ext.) of the active area is made.

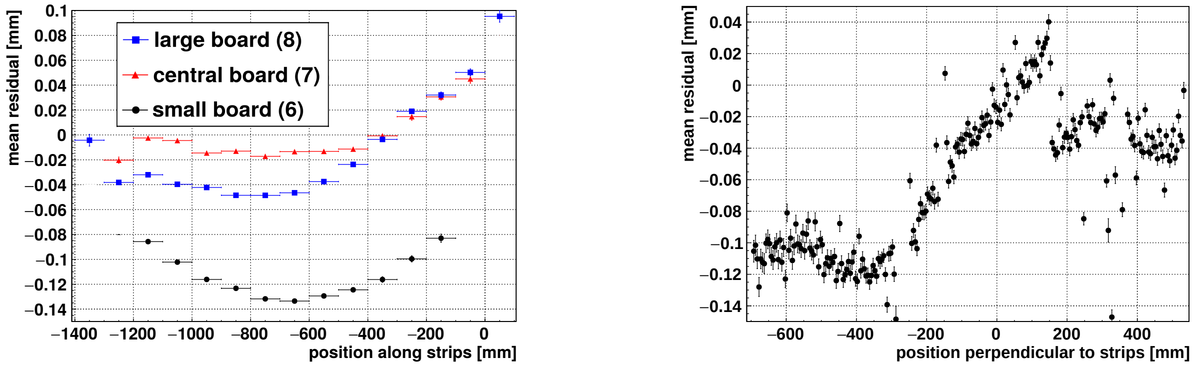

(a) Mean residual as function of the position along the strips. Separately shown for the three readout-boards.

(b) Mean residual as function of the position perpendicular to the strips. Integrated over the full active area.

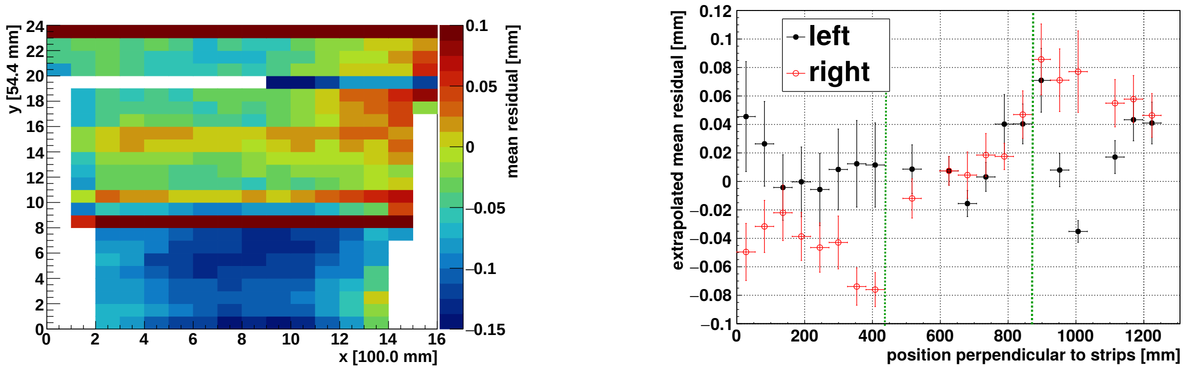

(c) Mean-residual-map.

(d) Mean residuals perpendicular to the strips, left and the right extrapolated to the positions of the Rasmasks.

Figure 6.30.: Reconstructed deviations to the nominal strip-pattern for the second gluing-side of eta-panel nine. This side is considered as eta-out in module nine.

Discussion : No quantitative agreement between the CMM-Rasmask-measurement and the reconstruction using cosmic tracks is found. Despite this agreeable reconstructions for the rotations of two boards on the second gluing side of eta-panel nine are achieved. For the first gluing sides of eta-panels eight and nine contrary rotations are reconstructed by the two measurements for the small boards (6). This suggest a systematic effect, which could be due to a different definition of the residuals at Saclay. The second gluing side of eta-panel eight shows large rotations and shifts in the cosmic-measurement. No such effects are expected from the CMM-Rasmask-measurement.
The largest problem for the comparison of these two measurements originate from the different measurement-positions. The CMM-Rasmask-measurement only considers the deviations at the borders. Contrary the cosmic-measurement is performed inside of the active area. An interpolation if the CMM-reconstruction is disabled due to the deformed strip-shape. But also the extrapolation is complicated due to this observation.
Further obstacles for the cosmic-measurements are the inhomogeneous illumination and the averaging over different inclinations. Also lacking statistics aggravates the stability of the approaches. Another consideration which has to be made is that the actual position-measurement is performed at the center of the drift-gap. Therefore the reconstructed deviations are projections of the track-evaluation 2.5 mm apart from the anode. For these two panels, data-periods of only four days were available, as the ongoing production requires short measurement-times. Therefore the reconstruction could benefit from longer measurement-periods.
The track reconstruction with Micromegas modules in ATLAS will be worsened without a correction for the observed deviations. Therefore the calibration-results should be incorporated for a better single-point-resolution.

6.3. Summary of Alignment Reconstructions

The reconstruction of the deviations from the design strip-pattern over an active area of 2 m^2 showed problematic aspects. The optical surveying is complicated by the imperfections of the CMM movement. Despite this, agreeable reconstructions with variations of about 20 µm were obtained between two separate measurements. The reconstruction using tracks of cosmic muons revealed deformations of the strip-straightness and the parallelism of the readout-PCBs. Therefore methods were developed to compare these two reconstruction techniques. It has been shown that general mis-alignments, like rotations, can be reconstructed similar with both approaches. The lacking quantitative agreement can be pinned down to the aggravation due to the need of an extrapolation. This extrapolation requires the fit of the strip-shape and evaluation of the fit-function with a precision below 10^{-4}. The accuracy of better than 100 µm over distances of more than 1.1 m motivates the precision. Therefore these investigations showed not only the obstacles, which come along such reconstructions, but also the high requirements of the Micromegas production. The most observed deviations stayed between ±100 µm. Larger deformations are mainly caused by the deformed strip-shape. Therefore the production scheme in Munich is under good control.

I must not fear.
Fear is the mind-killer.
Fear is the little-death that brings total obliteration.
I will face my fear.
I will permit it to pass over me and through me.
And when it has gone past I will turn the inner eye to see its path.
Where the fear has gone there will be nothing.
Only I will remain.

- Frank Herbert , 1965 , *Dune*

7. Position and Track Reconstruction

The main purpose of the Micromegas modules in the ATLAS experiment is precision tracking. For this the hit information of several layers will be combined to reconstruct the path of the muons. Each layer should work independently as tracking detector. Therefore in the following the layers will be investigated separately with different kinds of reconstruction techniques. The simplest approach is a charge weighted reconstruction of the position given by the strip-signals. A further enhancement is the fit of the track in the drift-region using the time-information of each signal. By combining the charge and the time-information a very robust reconstruction can be implemented for the NSW. Using this knowledge from a single layer tracks can be reconstructed for a combination of layers. The reconstructed tracks can then be compared to the tracks from the reference system. The layers with strips inclined by ±1.5° enable a reconstruction along the strips.

7.1. Charge Weighted Position

For the so called centroid position-reconstruction the charges and the corresponding channel-numbers of the strips in the cluster are considered. Each channel number gets weighted by the maximum of the charge measured by this channel. These values are summed up and divided by the sum of the charges. By this a charge weighted average strip-number can be assigned to the cluster. To reconstruct a position with this the pitch, the distance of the center of the strips, has to be multiplied. This is a scaling to natural units of millimeter instead of strip-numbers. The last step is the transformation into the global coordinate-system in which the value will be compared to the reference. For this the position in non-precision-direction, along the strips has to be used given by the reference.

7.1.1. Resolution Estimation using Reference Tracks

The resolution of a Micromegas layer can be estimated using the residual, the difference of the reconstructed hit to the track-reference. This value should peak after Micromegas to MDT alignment (see chapter 6.2.1) around zero. The width of the distribution is related to the resolution, if all dependencies are eliminated. To describe this distribution a double-Gaussian-function of

$$c(r) = p_0 \cdot \exp\left[-\frac{1}{2}\left(\frac{r-p_1}{p_2}\right)^2\right] + p_3 \cdot \exp\left[-\frac{1}{2}\left(\frac{r-p_4}{p_5}\right)^2\right] \tag{7.1}$$

is fitted to extract the sigma of the narrow and the broad part of the distribution. The narrow part describes the intrinsic detector resolution, while the broad part takes into account an accumulation of secondary effects. The multiple scattering of the cosmic muons during passage of the detector material is one effect. The muon track is reconstructed in the reference system, but can be distorted in the part between the MDT chambers. This leads to a larger residual than expected, by a wrong interpolation of the muon track. Another effect is the mis-reconstruction due to delta-electrons. These high energy electrons create additional charges or additional tracks in the active volume ands distort the position-reconstruction. They are caused by high energy-transfers of the muon to electrons in the shells of the atoms. Also the not-perfectly aligned detector-geometry can broaden this distribution.

parameter number	variable	unit	description
0	N_{narrow}	counts/mm	$= I_{\text{narrow}}/\sqrt{2\pi}\sigma_{\text{narrow}}$, normalization factor narrow distribution
1	μ_{narrow}	mm	mean narrow distribution
2	σ_{narrow}	mm	width narrow distribution
3	N_{broad}	counts/mm	$= I_{\text{broad}}/\sqrt{2\pi}\sigma_{\text{broad}}$, normalization factor broad distribution
4	μ_{broad}	mm	mean broad distribution
5	σ_{broad}	mm	width broad distribution

Table 7.1.: Overview of the residual-distribution fit-parameters for formula 7.1. The counts $c(r)$ are described at the residual r. The distributions are fitted with a double-Gaussian-function to describe the core-resolution and the broadening due to mis-reconstructions and multiple-scattering. It should be noted that for the fit-stability the parameter p_1 and p_4 can be fixed to the same value with no considerable effect on the results of the other parameter.

As seen exemplarily in figure 7.1a the distribution can be described by the chosen function. The large χ^2/ndf can be explained by the high amount of residuals exactly around zero. For the investigation of the resolution the sigmas have to be considered. In this case $\sigma_{\text{narrow}} = 0.384\,\text{mm}$ and $\sigma_{\text{broad}} = 1.16\,\text{mm}$ are measured. To describe the whole distribution by one number these two values can be combined in a weighted sigma σ_{w}. The weights for the averaging are the integrals of the corresponding Gaussian-functions, according to [Herrmann et al., 2017]. This leads to a value of $\sigma_{\text{w}} = 714\,\mu\text{m}$. The observed widths are therefore not in agreement with the expected resolution of a Micromegas of about $100\,\mu\text{m}$ for normal incident.

This discrepancy can be explained by several effects. The distribution is integrated over all incident angles. Therefore the dependence of different incidents is not considered, which is crucial as contrary to the MDTs the Micromegas are planar detectors. But also for residual-distributions for almost normal tracks the bare-width of the distribution is not comparable to the expected resolution (see figure 7.1b). For this the tracking-accuracy of the reference system, so the MDT-resolution, has to be considered. This can be achieved by comparing the tracks of the MDT-chambers.

To give an estimation of the tracking-accuracy, the tracks have to be evaluated at the position of the Micromegas. The difference between the tracks can then be considered like the Micromegas-residuals. Their distributions can also be investigated with the double-Gaussian-fit. Here the sigmas have to be divided by $\sqrt{2}$ to account for the combined resolution of the two chambers. Doing this evaluation of the residual-distributions for different track slopes separately, the sigmas of Micromegas and MDTs can be compared.

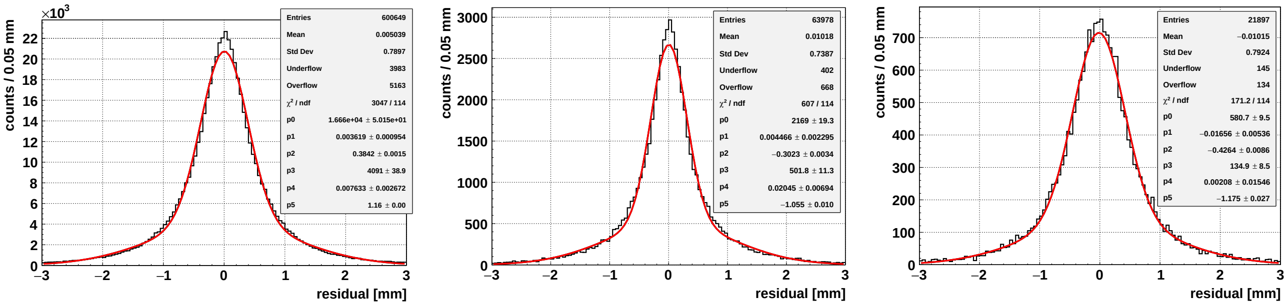

(a) Residual-distribution integrated over all track-inclinations.

(b) Residual for tracks with almost normal incident (inclination between ±0.04).

(c) Residual for tracks with inclinations between 0.28 and 0.32 (about 16°).

Figure 7.1.: The residual-distributions are fitted with double-Gaussian functions to extract their width. The track-inclination influence heavily the width of the distributions. To disentangle this the distributions are considered as function of the track-slope.

Typical behavior of the residual-widths can be seen in figure 7.2b. The widths for the MDTs stay almost constant over all considered track-slopes. A deterioration is expected at track angles of 30°, which corresponds to a track-slope of about 0.58 due to reconstruction ambiguities (see figure 4.3 and 4.5). For the Micromegas (seen for the eta-out layer) the broadening and therefore the increase of the residual-width as function of the track-slope is expected.

The broadening arises from the inhomogeneous-ionization of the cosmic muons along their track. The centroid determines the charge-average of the track projected onto the readout-plane. Therefore the inhomogeneous ionization leads to larger fluctuations of the reconstructed position for inclined tracks. The development of the residual-widths has to be compared to the contributions of the two Gaussians to the distributions. A measure for their contribution is the ratio of their integrals. Figure 7.2c shows the ratios for the MDTs and the Micromegas for the considered track-slopes.

Like the sigmas the ratios for the MDTs stay almost constant for all inclinations. The independence of the residual-behavior on the track-slope for the MDTs can be explained by the circular geometry of their active volume. Whereas for the Micromegas, which are planar detectors, the inclination with respect to the active surface is crucial.

For the reconstruction of the position-resolution the narrow-widths of the Micromegas residual-distributions have to be corrected by the MDT-tracking-accuracy. As suggested by [Lösel, 2017] the MDT-tracking-accuracy can be estimated in the same manner as for the Micromegas by the narrow-width of their residual-distribution. This means the resolution σ_{res} can be determined by $\sigma_{\text{res}} = \sqrt{\sigma^2_{\text{MM,narrow}} - \left(\frac{1}{\sqrt{2}}\sigma_{\text{MDT,narrow}}\right)^2}$, with σ_{narrow} being the fitted sigma of the narrow Gaussian for the Micromegas (MM) or the MDTs respectively.

A ten-days measurement with module 3 gives the calculated resolution as shown in figure 7.3a. Here the resolutions of the two eta-layers are compared. Both show almost the same structure. Resolutions around $100\,\mu\text{m}$ for normal tracks decrease almost linearly to resolutions of about $550\,\mu\text{m}$ at inclinations of ±0.5, which corresponds to angles of about 26°. To investigate this approach a shorter measurement period with the same module was also studied. It shows a similar behavior and similar values as for the long measurement (see 7.3b). But also larger fluctuations and errors are reconstructed, which arise due to the lower statistics. In both distributions the eta-in layer shows a systematically better resolution than the eta-out layer. One possible

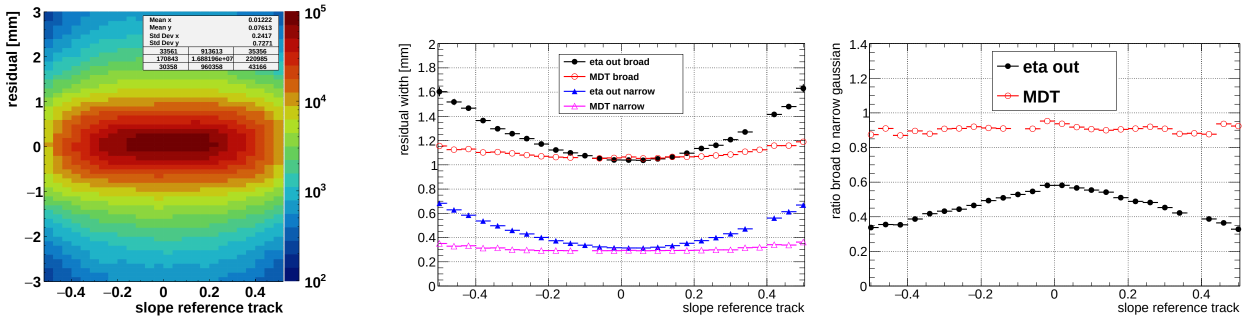

(a) Residual as function of the slope from the reference track. After alignment the residual should be centered around zero for all track-inclinations. For the resolution-estimation the width of the residual-distributions has to be evaluated as function of the slope of the reference track.

(b) Sigmas of the double-Gaussian fits as function of the slope from the reference track. The sigmas are a measure of the width and give therefore an estimation of the resolution. Curves are shown for one layer of the Micromegas, as well as for the MDTs. For the MDTs the sigma is divided by $\sqrt{2}$.

(c) Ratio of integrals for the two Gaussian functions fitted to the residual-distributions as function of the slope of the reference track. The ratio is calculated by dividing the integral of the broader Gaussian by the integral of the more narrow Gaussian.

Figure 7.2.: For the reconstruction of the resolution the residual is considered as function of the track-slope. The residual-distribution is evaluated with a double-Gaussian-fit for small track-slope-intervals. This has to be done for Micromegas, as for the reference MDTs. The widths and the ratios of the two Gaussians enable the resolution-estimation by the comparison of the two detector-systems. The plots are exemplarily taken from module 3 eta-out layer.

explanation could be the method for track averaging between the MDTs and the position of the two layers. As reference track just the average of the track parameters of the two MDTs is used. Therefore the best reconstruction should be exactly between the two chambers. At this height also the eta-in layer is situated. Whereas eta-out is displaced by about 16 mm from the center. Therefore this interpolation can systematically bias the reconstruction. Another reason for the worse resolution of the eta-out layer can be a not as good alignment as for the eta-in layer. The eta-in layer showed a standard deviation of mean residuals of 56 µm over the active area. A standard deviation of 67 µm is calculated for eta-out which could also broaden the distribution.

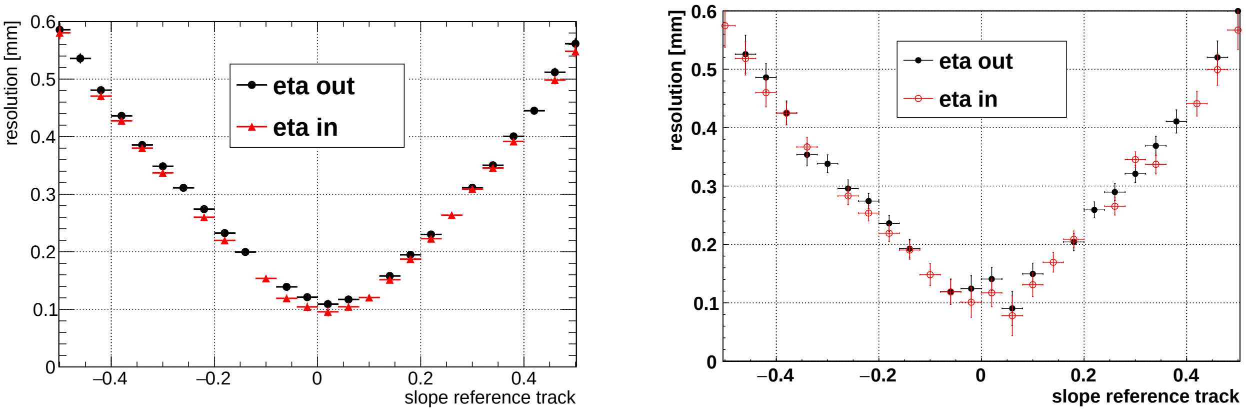

(a) Ten-day-measurement with about 16 million reconstructed events.

(b) One-night-measurement with about 1 million reconstructed events. These data are not included in the long measurement of 7.3a.

Figure 7.3.: Resolution as function of the reference track slope. The resolution reconstruction shows the expected dependence on the track-inclination. The actual values are depending on the quality of the alignment, mechanically and reconstruction-wise. The duration of the measurement, so the number of recorded events, influences the estimation slightly.

The systematics of this approach on the resolution-reconstruction has to be determined. Therefore the dependencies of the sigmas of the narrow-Gaussian are investigated. In figure 7.4a σ_{narrow} is shown as function of the slope from the reference track for the eta-in layer of all yet measured modules. Very similar behaviors as already observed in 7.2b are seen for almost all modules.

Only module zero, six and seven show systematically broader distributions, which indicate worse resolutions. This bad behavior can be understood by their mechanical alignment in the CRF. Most crucial for the comparison of the position-reconstruction is the parallelism of the Micromegas-strips with respect to the MDT-wires.

If a module is rotated around the Z-axis, which corresponds to non parallel strips and wires, this rotation has to be corrected by the scintillator-resolution in non-precision-direction (X). As the scintillators are 10 cm broad only a coarse position-information is given along the wires. This introduces a systematic broadening of the residual-distribution for not-well-aligned modules even after correction of this rotation. The correction only shifts the mean value while the residual-dependence broadens the distribution for the not-resolvable-part of the position along the wires.

The effect can be seen in figure 7.4c. Here σ_{narrow} is shown for all readout-boards of all yet measured modules individually as function of their rotation around the Z-axis. Large rotations of about ±0.028 correspond typically to stereo-boards of modules with well aligned eta-boards in the region between ±0.005. Module zero is indicated by the blue-triangles. For this module all rotations are larger than 0.005. The eta-boards show a rotation of about −0.013, which explains the broad observed residual-width. Also the stereo-boards follow the fitted second-degree-polynomial. The dependence shows the importance of mechanical alignment in the CRF. It can also explain the broad distributions of module six and seven, which are the points with rotations around 0.007. For these two modules another alignment-issue is found causing the increased width of the residual-distribution.

As seen in figure 7.4d σ_{narrow} also depends on the rotations around the other two axis. On the abscissa the Pythagorean-addition of the reconstructed-rotations around the x and y-axis is shown. As function of this σ_{narrow} is plotted for the two eta-layers of each measured module, besides module zero. Here a similar argument as for the rotation around the z axis holds. Despite this a much smaller dependence is observed, which can be understood by the less crucial impact on the residual. The value for the total rotation of module six is around 0.0164. For module seven a total rotation of about 0.0142 is reconstructed. Therefore both modules have a significantly higher mis-alignment than the other modules, which broadens their residual-distribution.

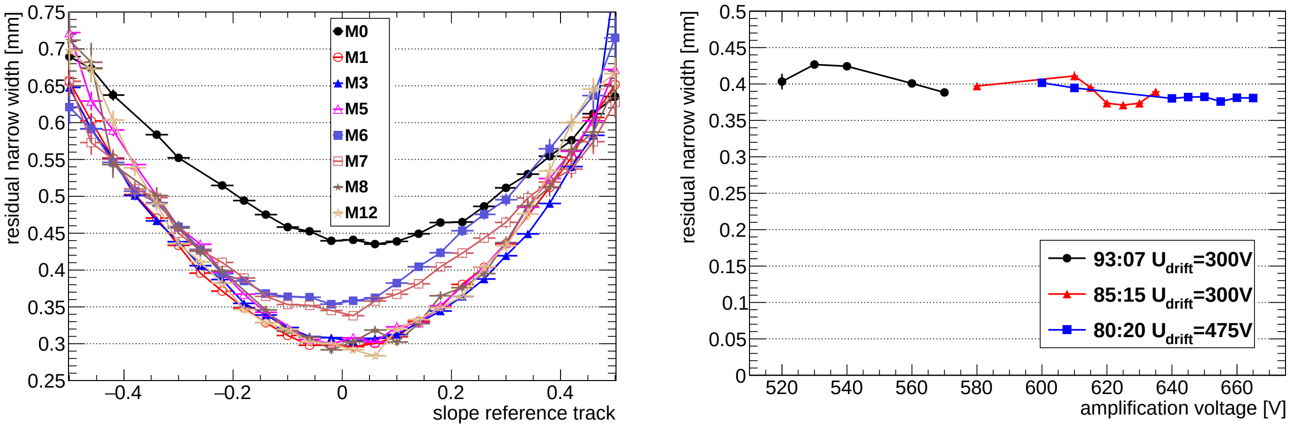

(a) Width of the narrow Gaussian fitted to the residual-distribution as function of the slope from the reference track. The curves are shown for the eta-in layers of all yet measured modules.

(b) Width of the narrow Gaussian fitted to the residual-distribution for module 8 eta-in as function of the amplification-voltage for three different gas-mixtures of Ar:CO_2. The residual-distributions are integrated over all track-slopes.

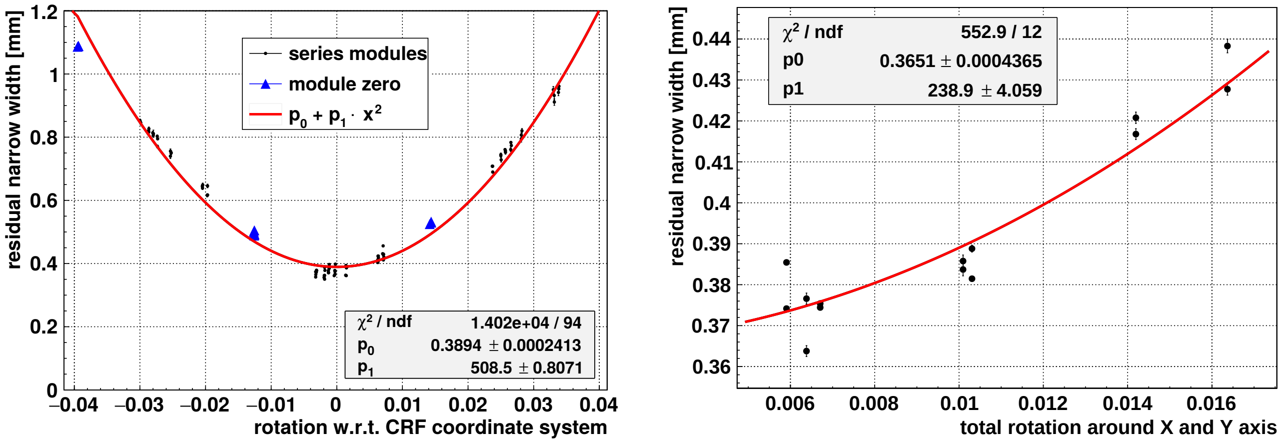

(c) Width of the narrow Gaussian fitted to the residual-distribution for all readout-boards of all yet measured modules as function of the rotation around the Z-axis with respect to the CRF coordinate-system. The residual-distributions are integrated over all track-slopes.

(d) Width of the narrow Gaussian fitted to the residual-distributions as function of the Pythagorean-addition of the rotations around the x and y-axis with respect to the CRF coordinate-system for all eta-layers of all yet measured series-modules. The residual-distributions are integrated over all track-slopes.

Figure 7.4.: The residual-distributions are fitted with double-Gaussian functions to extract their width. The sigma of the narrow Gaussian, which is connected to the resolution, shows several dependencies. The geometrical alignment in the CRF is influencing the resolution estimation. Also the amplification-voltage, which corresponds to the pules-height, has an effect.

Another systematic effect influencing with smaller impact the residual-width for this kind of reconstruction is the gain. As the centroid method uses only the charge-information of the strip-signals the position-reconstruction is also depending on the amplification-process. For low gains the probability increases to lose signals which would be detected on additional strips (see figure 5.9a). Also the charge-resolution decreases, which influences directly the charge weighted-averaging over the strips. The effect of improved resolution as function of amplification-voltage, which determines the gain can be seen in figure 7.4b. Here for three gas-mixtures the width of the residual-distributions gets more narrow for higher voltages.

7.2. Time-Projection-Chamber-like Reconstruction

In a single Micromegas layer the muon track can be reconstructed using the drift-time-measurement of the primary electrons. The time and the knowledge of the drift-velocity enables to assign to each strip-signal a track-point. Therefore the track is reconstructed by combining the neighboring track-points of the layer. This method is referred to as µTPC, which should indicate the similarity to Time-Projection-Chambers (TPC) in much smaller drift-gaps [Ntekas, 2016]. Most crucial for this is a good measurement of the time. Therefore in the following an evaluation of the time-measurement with the APV25 front-end-electronics is performed. With this the reconstructed muon tracks are investigated for angular- and position-reconstruction capabilities.

7.2.1. Signaltime Measurement

The time of the primary ionizations can be reconstructed using the signal-time of each strip. Therefore the charge-signals have to be evaluated. This is achieved as mentioned in chapter 4.3.1 with a fit of an inverse-Fermi-function to the rising-edge of the signals. The fit gives an estimation for the 50%-time of the signal and the slope of the rising-edge.

The 50%-time is called inflection and is investigated as one possible evaluation-time. Combining the two fit-values also the start of the signal at the baseline can be extrapolated, which is the second considered timing [Lösel, 2013]. Another time-point which can be extracted is the maximum of the signal. For this investigation the extrapolation is done symmetrically around the inflection-time. Therefore in the following the maximum corresponds not to the actual time of the highest charge, but to the extrapolated time as seen in figure 7.5a. This approximation is done to save PC-resources as the signal-fits influence heavily the evaluation-duration of the data-samples.

Although both extrapolations are symmetrically around the inflection for a single strip-signal the relative timing of the strips in a cluster depends on which timing is used. The distribution of reconstructed times can be seen exemplarily in figure 7.5b for a single muon-passage. Here the difference between the evaluation-times and their effect on the overall time-distribution can be seen very good. Due to different rise-times of the single-strip-signals the time-distributions for the two extrapolation-times are quite different.

Each timing has a special motivation. The inflection-time should be the most stable one in sense of fit-accuracy as here only one parameter is used. An assumption for the baseline-time is that this timing should be independent of the maximum charge of the signal. The maximum charge influences the slope of the rising-edge as can be seen in figure 7.5b by the distance between red and blue points. Therefore the start of the signal should be independent, while each later timing could be influenced by the height of the signal. As the signals of the strips are preprocessed and shaped by the APV-electronic the distributions of maximum-times are also evaluated.

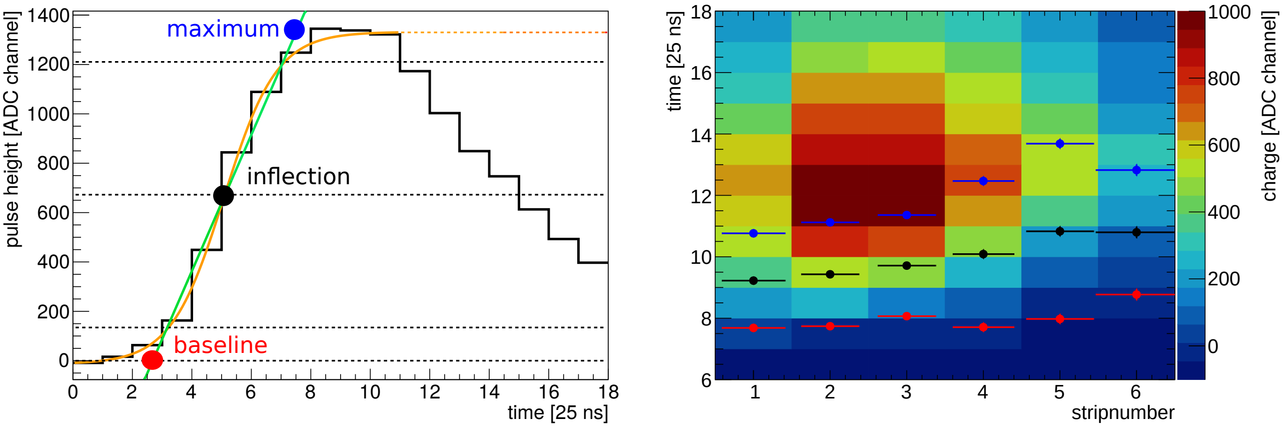

(a) Time-evolution for a single-strip charge-signal . For each 25 ns time sample a charge value is stored. Using a fit of an inverse Fermi function (yellow) a time can be assigned to the signal. Three possible evaluation-points of the fit are indicated.

(b) Time-evolution of the charge-signal for a cluster of strips. The position of the three possible timings are indicated for each strip in the same colors as in figure 7.5a.

Figure 7.5.: The evaluation of the strip-signal requires an inverse-Fermi-fit. With this three suitable time-points can be determined. The muon track should be reconstructible by combining the times of all strips in a cluster. The two plots are taken from measurements with different setups and are just exemplaric.

Drift-Velocity-Reconstruction

To determine which timing is the best to be used for the position and track reconstruction the time-distributions are investigated. The reconstruction of the drift-velocity is used for this investigation. A determination of the drift-velocity is possible by determining the width of the time-distribution. The earliest signals correspond to electrons originating from ionizations near the mesh. Vice versa the latest signals can be associated with ionizations that occurred at the cathode. By determining the difference of their timing and knowing the drift-distance, so the gap-width, the drift-velocity should be calculable.

Most measurements with the SM2 Micromegas are performed with the nominal gas-mixture of Ar:CO_2 of 93:7 volume percent. The drift-voltage is set to 300 V, which leads due to the drift-gap of 5 mm to a simulated drift-velocity of 47 $\frac{\mu m}{ns}$. Therefore a maximum drift-time of about 106 ns is expected, which corresponds to 4.3 time-samples of 25 ns.

The time-determination using the fit of the single-strip charge-signal itself is very problematic. The fit is very sensitive to fluctuations and the height of the signal. So a very noisy environment aggravates a good time-determination. The inhomogeneous ionization produces signals with various heights, which leads to time-measurements with different qualities. Another obstacle is the inhomogeneous timing across the active-area. The readout electronics, so the APV-chips and the FEC-cards, vary in their quality. Also each FEC-card uses its own clock which introduces time differences. These differences have to be corrected.

The trigger of the CRF given by the scintillator-coincidence could introduce also a dependence over the area. As the readout strips are more than one meter long for the SM2 Micromegas also the signal-propagation-time on the strips influences the timing. This was already shown by [Lösel, 2013]. Another effect of the long strips is the capacitive-coupling of signals on neighboring strips. A correction is necessary and was implemented by [Lösel, 2013] and [Flierl, 2018]. The factor for the coupling-correction was determined to be about 30%. The implementation of this correction influences heavily the signal-shape. Therefore the effect of this correction on the signal-timing has to be investigated as well.

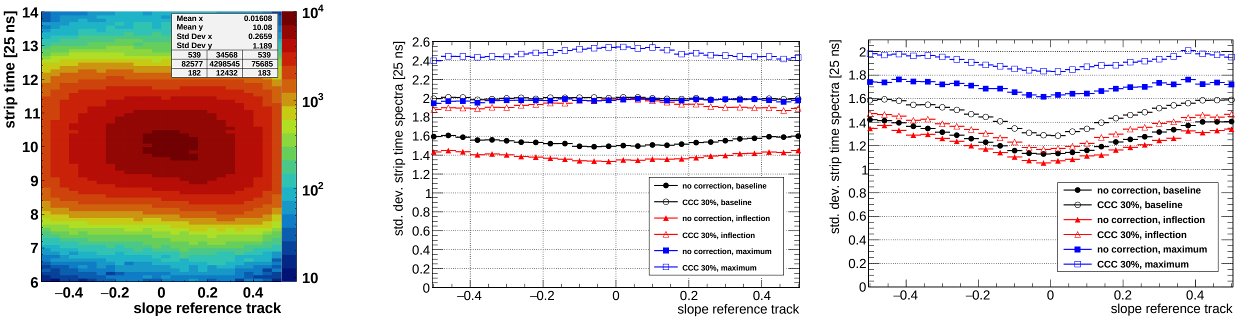

(a) Single-strip time as function of the reference-track-slope. No correction for capacitive-coupling is applied. The signal is evaluated at the inflection-point.

(b) The standard deviation of the strip time-distribution as function of the reference-track-slope. The colors indicate the different evaluation-points of the single-strip-signal.

(c) The standard deviation of the strip time-distribution as function of the reference-track-slope. Here only the highest charged signals in the clusters are taken into account.

Figure 7.6.: To reconstruct the drift-velocity the single-strip time-spectra have to be evaluated. The width of these distributions should correspond to the drift-time between cathode and mesh. Exemplaric plots for module 3 eta-in board 7 at 300 V cathode-voltage with the nominal gas-mixture.

The difference in signal-time between the strips arises due to different drift-lengths of electrons originating in different distances between cathode and mesh. If the muon track is penetrating the active volume very steep, which means with a low slope, the different ionization-processes occur directly above each other. Therefore the electrons drift almost parallel to the track, which leads to an overlap of their signals. This can be seen by the peaking of the drift-time-spectra for low track-slopes in figure 7.6a.

Effects of the signal-evaluation-technique on the width of these distributions can be seen in figures 7.6b and 7.6c. In the left plot the distributions of all strips are evaluated. It shows broader distributions for the extrapolated times (baseline,maximum) and the coupling-correction (CCC) than for the inflection-times.

This could be explained by mis-reconstructions due to bad strip-signal-fits. In these cases the coupling-correction and the extrapolations are expected to worsen the time-information. The extrapolated evaluation-points of the Fermi-signal-fit are more unstable, as they rely on two instead of one fit-parameter. The capacitive-coupling-correction can distort signals further, which increases the width.

To evaluate the techniques in the case of good signals for the right plot only the time-distributions of the highest signal in the strip-cluster are evaluated. Also in figure 7.6c the time-distributions are broader for the extrapolated timings and the coupling correction. Despite this, for all methods the distributions are narrower for the highest charged signals than for all signals. For track-slopes around zero the expected decrease of width, due to overlapping-signals, can be seen for all methods in figure 7.6c.

The widths are determined here just by the standard deviation of the distributions. This is on the one hand very sensitive to fluctuations and on the other hand not suitable for the actual description of these distributions.

The expected width of 4.3 time-samples for this drift-voltage is not observed for any of the methods. To avoid the problems due to overlapping signals, the time-spectra are evaluated for tracks with slopes larger than 0.44, which correspond to angles larger than 23°. An exemplaric distribution can be seen in figure 7.7a.

One would expect a box-like distribution due to the uniform probability for charge-creation in the drift-gap. The broadening and rounding of the edges define the time resolution and can be explained by mis-measurements and the averaging over different angles. Also the large area of one readout-board and differences of the FEC-cards can lead to undefined borders.

For the evaluation of these distributions two Fermi-functions are fitted to the edges. With the inflection-point and the slope of the fit the width of the drift-time-spectra can be defined. Here electrons originating near the mesh are associated with the rising edge or early times. Vice versa electrons created at the cathode correspond to large times at the falling edge.

It is worthwhile noting that in general the slope of the falling edge is lower. The drift-path from the cathode is longer, therefore the probability for recombination is higher. This leads to the loss of signals of electrons coming from the cathode. The loss causes a longer tail of the distribution at the high edge.

The drift-velocity is calculated by dividing the drift-gap-height, in this case 5 mm, by the reconstructed drift-time. For the drift-time the time-position of the low edge of the distribution is subtracted from the time-position of the high edge. A priori it is not determined which position of the distribution-fits should be used to reconstruct the width. Either the inflections or the extrapolation to the baseline of the edge fits could be used. The inflections describe the main part of the distribution, while assuming the falling edges to describe measurement-uncertainties. Whereas the extrapolations take the complete distribution width into account.

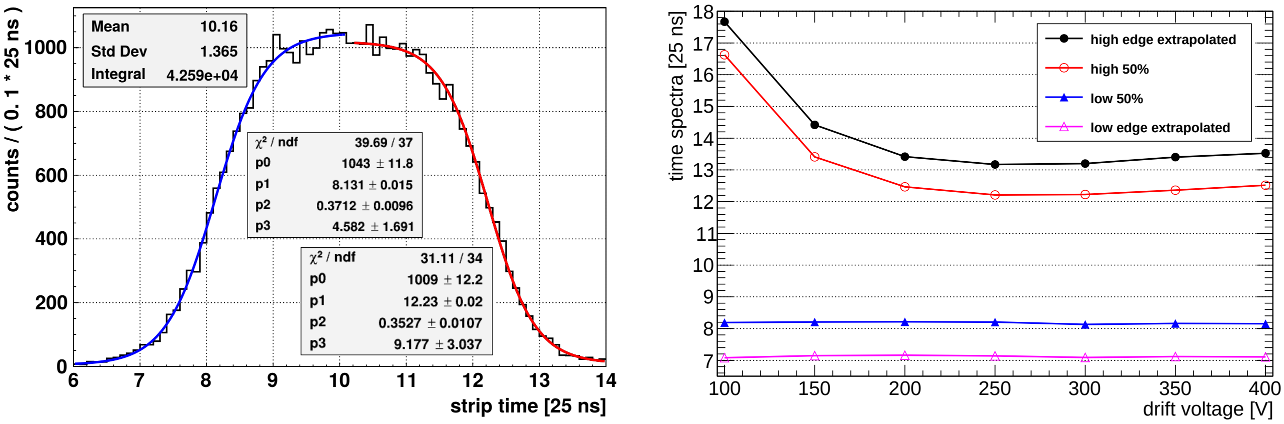

(a) Strip time spectra for the maximum charged signals of strip-cluster reconstructed for track-slopes larger than 0.44. Two Fermi-like functions are fitted to the edges of the distribution to determine the drift-time. Plot is shown for a cathode voltage of 300 V.

(b) For each cathode-voltage the edges of the time-distribution are fitted with Fermi-like functions. The points correspond to either the inflection (50% of maximum) or the extrapolation to the baseline of these fits for the low and the high edges.

Figure 7.7.: The single-strip time-spectra are evaluated at the edges of the distribution using two Fermi-like functions. The width of the distributions and therefore the fit-parameters are depending on the drift-field. Exemplaric plots for module 3 eta-in central board (7). The strip-charge-signal is evaluated at the inflection-point. A capacitive-coupling-correction of 30% is performed.

The evolution of the time-points extracted by the Fermi-fits to the strip time distributions as function of the drift-voltage can be seen in figure 7.7b. It can be noticed that the low edge stays constant over the full drift-voltage range. This is expected as the electrons from ionizations near the mesh have almost no drift-distance. So the time for the lower edge corresponds to the electronics offset for the readout. The high edge shows almost the same evolution for the fifty-percent-point and the extrapolation.

The dependence illustrates the effect of the drift-field on the strip time distribution. For the calculation of the drift-velocity the right choice for the time differences has to be made. This is illustrated in figure 7.8a.

Either the fifty-percent-points, the extrapolations or a combination of them could be used for the drift-velocity calculation. As the difference for the fifty-percent-points is closest to the simulation this is chosen for the following investigation. It should be noted that in other analyses of Micromegas-data the difference between the low edge fifty-percent-point and the extrapolation of the high edge lead also to successful reconstructions of the drift-velocity [Bortfeldt, 2014]. In this approach the assumption is that the electrons from the cathode are frequently lost due to recombination, which leads to longer extension of the high edge. As here the distribution seems rather symmetrical not much losses due to this seems to be observed. Therefore the time-resolution could be estimated using the edge slopes.

The observed differences to the simulation can be explained by a deformation or wrongly assumed drift-gap. The variation of the drift-gap width changes the drift-field and due to this also the expected drift-velocity. Such an analytical variation can be seen in figure 7.8b. The best correspondence is found for a drift-gap of about 4.8 mm. This observation can be interpreted with different approaches. The frames on which the micro-mesh is

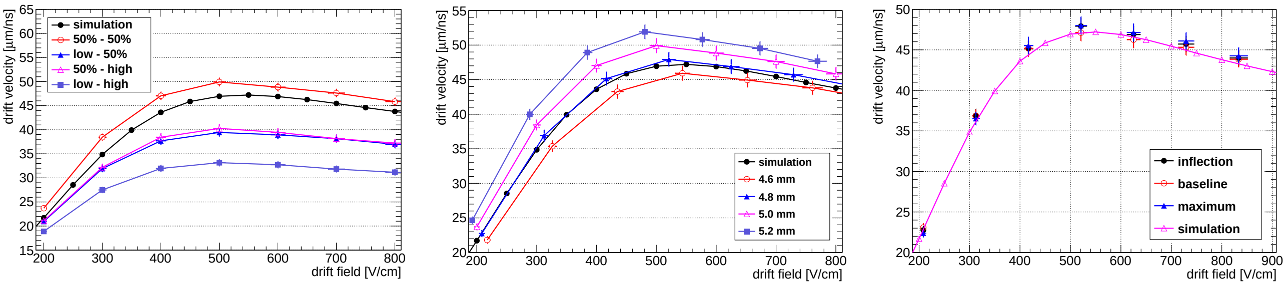

(a) Reconstructed drift-velocity as function of the drift-field. Calculated with the nominal drift-distance of 5 mm. The edge-fit of the strip time distribution for maximum charged signals is evaluated either at the inflection (50%) or the extrapolation to the baseline (low,high).

(b) Reconstructed drift-velocity as function of the drift-field. A variation of the assumed drift-gap width revealed an optimal overlap between measurement and simulation for a drift-gap of 4.8 mm. The maximum charged signal-time-distributions are evaluated at the inflection of the edge-fit. The single-strip-signals are evaluated at their inflection-point.

(c) Reconstructed drift-velocity as function of the drift-field. The time-distributions for the three single-strip-signal evaluation-points are used for the reconstruction. A drift-gap of 4.8 mm is assumed for the calculation. All signals are corrected for capacitive-coupling.

Figure 7.8.: To reconstruct the drift-velocity the single-strip time-spectra have to be evaluated. The width of these distributions is measured at different edge-positions. Using the difference of inflection-points of these distributions a drift-distance of 4.8 mm is reconstructed. For all three single-strip-signal evaluation-points almost the same drift-velocity evolution is reconstructed.

glued are tested in several steps for their height. Therefore is should be sure that their height corresponds to 5 mm.

The discrepancy could be due to the height of the pillars (0.12 mm) and the thickness of the micro-mesh (0.07 mm). If these parts are pressing the micro-mesh with their given thickness into the drift-gap the gap-size is reduced. Against this argument is a dedicated construction around the borders of the active area. This should lead to the mesh sitting flat on the pillars. Another suitable explanation could be the deformation of the cathode surface. Also deviations of the gas-mixture and impurities can not be excluded.

In figure 7.8c the drift-velocity reconstruction is shown for all three signal-evaluation-points. All three show within the error-bars almost the same reconstructed values. Therefore this investigation shows only the possible reconstruction of the drift-velocity, without giving further insights into systematics of the timings.

The evaluation underlies large systematic effects. The impact of the capacitive-coupling-correction is crucial, as it affects the time-distribution-width. Whether this is beneficial or not could not be disentangled. The variation of the drift-gap-width is rather artificial as the construction implies a mechanical correctness. Also systematic effects of the detector-gas could not be excluded. Contamination with air or humidity would result in different drift-velocities. For each measurement-point the measurement-duration was more than a day. Therefore effects due to pressure and temperature change could not be taken into account.

None the less it should be remarked that this investigation is made with the data of a whole readout-board. This implies the usage of two individual FEC-cards each connected to four APVs. The active-area for this is more than half a square-meter.

The drift-velocity-reconstruction for the other connected readout-boards were also evaluated. For these slightly different drift-gap-sizes have to be assumed. These sizes are ranging from 4.5 mm to 4.8 mm. Therefore this implies either larger variations of the drift-gaps as expected or larger systematic discrepancies.

First and Last Signal-Timing in Strip-Cluster

The drift-velocity reconstruction uses solely the edges of the time-distribution. These edges are mainly reconstructed by the first and the last signals in a cluster. Therefore it is advised to investigate the effects of the evaluation-techniques, e.g. the coupling-correction and the signal-point, on these signals.

Electrons are created not at each passage at the borders of the drift-region, due to the inhomogeneous ionization of the muons. Therefore the distribution of earliest and latest timing are broadened. Exemplaric distributions for a drift-voltage of 300 V are shown in figure 7.9a. Here the comparison between the evaluation-points can be made. The baseline-timing increases the width for the first strip and leads to a longer extension for early times. Vice versa the maximum-timing increases the width for the last strip and leads to a longer extension for late times. This can be explained by their respective direction of extrapolation and shows the effect of mis-reconstructions due to a badly fitted signal-slope. As can be seen by the indicated time differences neither the peak-to-peak differences nor the edge-differences at full-width-half-maximum (FWHM) correspond to the expected drift-times of 106 ns.

The event-wise difference of these timings gives a measure for the width of the observed time-distributions in a single event. To disentangle the effects coming from different track-inclinations the time differences are

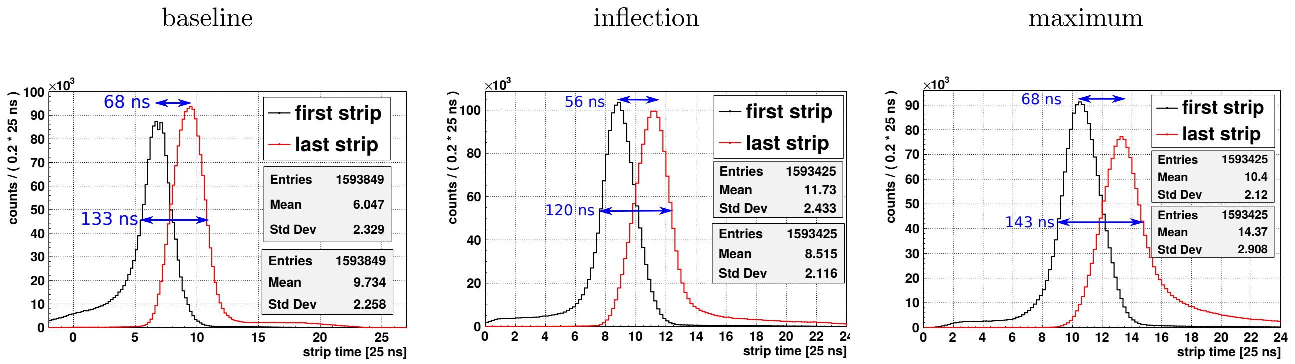

(a) Time-distributions of the first and last signal in a cluster. The expected drift-time from simulation is about 106 ns.

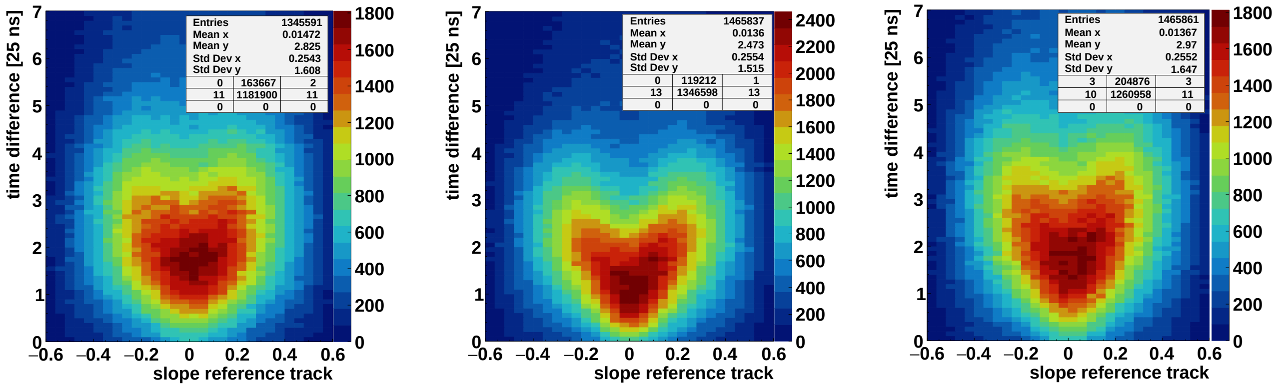

(b) Time difference of the last and the first signal in a cluster as function of the reference track slope.

Figure 7.9.: The first and the last signal in a cluster define the edges of the time-distribution. Their distribution is depending on the track-slope. The difference of these timings is not a good measure for the drift-velocity due to the inhomogeneous ionization and the overlap of signals. Shown are measurements with module one eta-in at an drift-voltage of 300 V. The single-strip-signals are corrected for capacitive-coupling.

investigated as function of the reference-track-slope. The distributions for the three signal-evaluation-points can be seen in figure 7.9b.

A V-like shape is reconstructed, which is due to overlap of signals for normal tracks. As already noted the extrapolated times increase the average time difference, therefore the time-means of these distributions are larger with respect to the inflection. Also the shapes differ, which is probably caused by the distortion of the time-measurement due to the extrapolations.

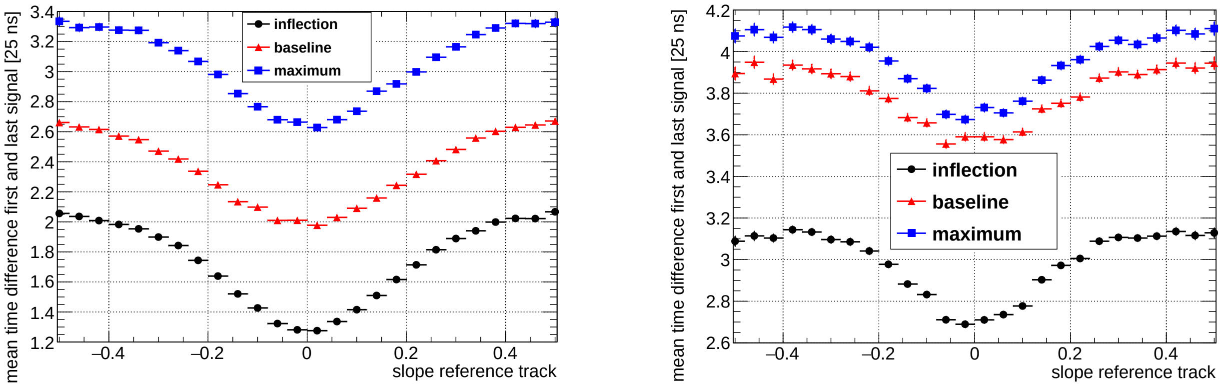

(a) Without capacitive-coupling-correction. **(b)** Capacitive-coupling-correction by 30%.

Figure 7.10.: Mean time difference of the first and the last signal as function of the slope of the reference track. The three curves correspond to the three signal evaluation-points. The time difference increases for both extrapolations with respect to the evaluation at the inflection.

The effect of the different time-evaluation-techniques is studied using the mean of these distributions. This is done as function of the reference-track-slope in figure 7.10. Here also the differences due to the usage of the coupling correction can be seen. Without correction no mean-time difference is in the range expected from the drift-velocity around 4.3·25 ns. For all signal-evaluation-points the expected effect of smaller time differences at low track-slopes is observed. Around a track-slope of about ±0.35, which corresponds to angles of about 20°, a

constant difference is reconstructed.
For larger slopes the projection of the track onto the readout-pattern should lead to more than four hit strips. Therefore the time difference is biased for lower inclination due to the low number of affected strips. Large differences between the three signal-evaluation-points are reconstructed. An explanation for this could be an effect of the charge-coupling on the signal-slope.
Using the coupling-correction the distributions for the two extrapolated-times become much more equal. Also the time differences approach the expected value. For the inflection-time the lowest mean time difference is reconstructed. This could either be due to the unstable extrapolation for the other two time-points, which increase the time-distribution, but could also indicate a systematic bias using the inflection.

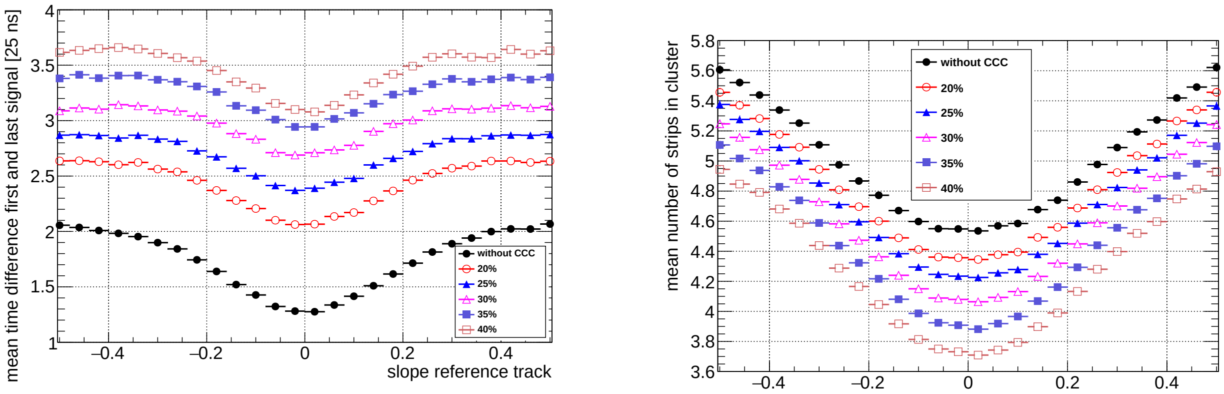

(a) Mean time difference of the first and the last signal as function of the slope of the reference track. The times are determined at the inflection of the signal.

(b) Mean number of strips in the leading cluster as function of the slope of the reference track.

Figure 7.11.: Influence of the capacitive-coupling-correction on cluster-properties. A time difference between the first and the last signal of 106 ns would be expected due to the drift-velocity of 47 µm/ns. The decrease in the mean number of strips is expected to come from removing signals at the borders of the cluster which are only capacitively coupled.

The effects of the coupling-correction are further investigated in figure 7.11. The left plot shows the influence on the inflection-time for various factors of the coupling correction. For higher values the mean time difference increases, but even for a factor of 40% the expected value is not reached. Besides the timing, also the multiplicity, so the number of strips in the cluster is affected by the correction. For increasing correction-factors less strips are reconstructed in the clusters.
This is explained by two facts. First the correction subtracts charges from neighboring strips. This leads to a reduction of charges at the edges of the cluster, which are expected to originate mainly from the signal-coupling. Therefore these strips are removed from the cluster by eliminating all charges on them. Second the correction can also harm the signal-shape, which leads to unstable signal-fits. Hence, more strips are discarded due to bad fits. A correction factor of 30% is expected from simulation [Lösel, 2017] and showed reasonable results in previous analyses [Flierl, 2018].

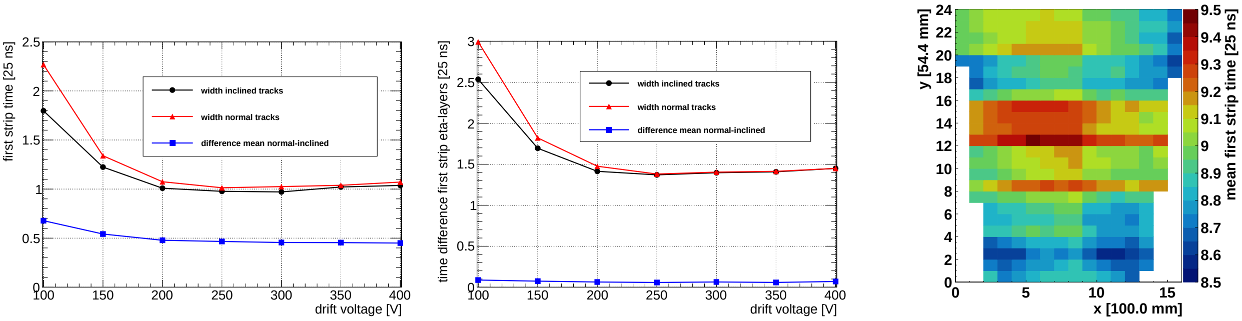

(a) Properties of the time-distributions for the first signal in a cluster. Shown for the large board (8) of eta-in layer.

(b) Properties of the time difference distribution between the first signals in clusters of the two eta-layers. Shown for the large board (8).

(c) Map of the mean first signal timing in clusters of the eta-in layer at a drift-voltage of 300 V.

Figure 7.12.: The time-resolution of a Micromegas detector is determined using the width of the time-distribution for the first signals in a cluster. Due to the large size, the differences of the readout electronic and an inhomogeneous trigger-timing the mean timing is inhomogeneous across the active area. This leads to broad time-distributions and therefore to a bad time-resolution. The differences of the means for inclined and normal tracks (blue triangles) stays almost constant, but show a systematic offset. Exemplaric reconstruction for module three. The signals are evaluated at their inflection without the capacitive-coupling-correction.

The time difference investigations are limited, as only the mean values are considered. Comparing the distributions in figure 7.9b one recognize that the most probable value of the distributions is much lower than the mean. This can be explained by the inhomogeneous ionization, which leads to clusters with no signals from the edges of the drift-region. The actual distributions vary also between the modules and the readout-boards as effects coming from the resistivity or the electronics could not be disentangled yet. Therefore these investigations are only on a qualitative level.

In order to make quantitative statements, the timing-resolution can be estimated using the width of the first signal-times. This is done in figure 7.12a for the drift-scan with module three. Differences between normal and inclined tracks are expected to come from the overlapping of signals for normal tracks. Similar to this approach the difference of the timing for the two eta-layers can be considered, seen in figure 7.12b. [Flierl, 2018] reports for the testbeam with module zero a resolution of about 18.6 ns at a drift voltage of 300 V. For both approaches in figure 7.12 only resolutions of about 25 ns are achieved[1]. This worse resolution can be explained by figure 7.12c. In this map the mean timing of the first strip is shown. Differences between the FEC-cards can be seen by groups of four horizontal lines with similar time-behaviors. Also a step is visible at $x = 9{\times}100\,\mathrm{mm}$, which is probably caused by the trigger-time of the scintillator groups. This inhomogeneous mean timing across the surface leads to the worse resolution.

7.2.2. µTPC Angular Reconstruction

Using the drift-time-measurements the track of the muons can be reconstructed in the drift-gap. For this each single-strip drift-time is translated to a track-point. The position perpendicular to the strips is given by the strip-number and the pitch p. To reconstruct the position in the drift-gap the measured times have to be scaled by the drift-velocity v_{drift}. A global time-offset can be estimated by the mean timing of all strip times. An immediate translation into length units is not necessary for the reconstruction of the incident angle. Instead a track-fit to the signal-time strip-number correlation can also be performed. An exemplaric fit for a drift-voltage of 300 V is shown in figure 7.13a. The slope $m_{\mathrm{\mu TPC}}$ of this fit can reconstruct the incident-angle θ using

$$\theta = \arctan\left(\frac{s}{m_{\mathrm{\mu TPC}} \cdot v_{\mathrm{drift}}}\right). \tag{7.2}$$

Here s denotes a scale-factor. In the implementation of this method it is important to keep track in which units the signal-points are fitted. The signals are recorded using the 40 MHz-sampling, therefore the time is measured for this analysis in ticks of 25 ns. The measurement in precision-direction is performed using the numbering of the strips, without the pitch p. Hence, the scale-factor is given by $s = p/25\,\mathrm{ns}$. For the angular-reconstruction it is necessary to know the drift-velocity. Vice versa the drift-velocity could be reconstructed for a known incident-angle. Normal tracks, which means incident almost perpendicular to the readout-surface, are problematic for this reconstruction. The ionizations in the drift-gap happen above each other and the time-measurements are distorted by the overlap of the signals. Also the tracks have a much smaller projection onto the readout-area. Therefore only a few strips are able to reconstruct the track. To investigate the capabilities of this method using the SM2 Micromegas only tracks with an inclination between 20° and 22° are considered in figure 7.13. Figure 7.13b illustrates the main motivation for the usage of the capacitive-coupling-correction.

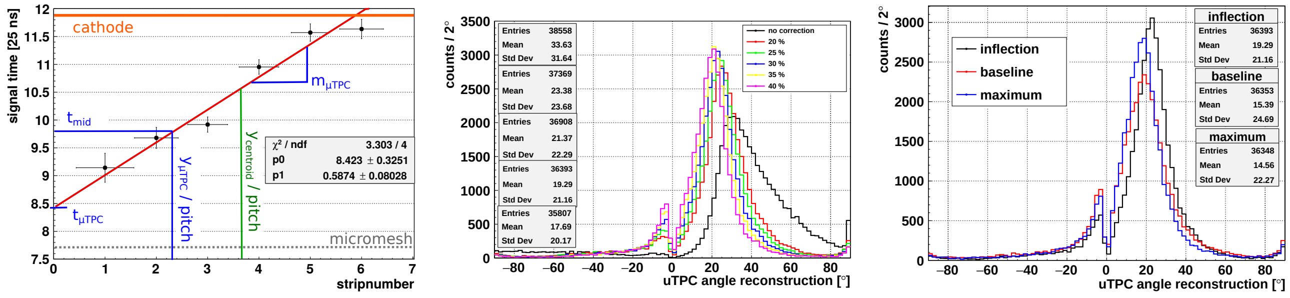

(a) Reconstructed signal-time as function of the strip-number. Using the slope of the fit the incident angle can be reconstructed. Exemplaric plot for an event recorded with the nominal gas-mixture at an drift-voltage of 300 V.

(b) Reconstructed incident angle for reference tracks of 20° to 22° inclination. Shown are the distributions for various factors of the capacitive-coupling-correction. The signal-timing is evaluated at the inflection.

(c) Reconstructed incident angle for reference tracks of 20° to 22° inclination. Shown are the distributions for the evaluation of the single-strip-signals at three time-points. The data is corrected for capacitive-coupling by 30%.

Figure 7.13.: A fit to the signal-time strip-number correlation enables the reconstruction of the incident angle. The reconstruction is sensitive to the evaluation technique of the signals. The capacitive-coupling-correction improves the reconstruction, while leading to the loss of signals. The loss is seen in the entries for the middle plot. The ordering of th statistic boxes are the same as in the legend.

---

[1] The width shown in figure 7.12b has to be divided by $\sqrt{2}$ as the resolutions of both layers are convoluted.

As can be seen for larger correction factors the width of the reconstructed angular-distribution is reduced. Also the mean and the most probable value are approaching the expected value of 21°. An undesired observation is the loss of reconstructed tracks. This is expected due to the reduction of signal-strips seen in figure 7.11b. The evaluation of the signals at different points influences also this distribution. The two extrapolated times reconstruct less good signals as seen by fewer entries and broader distributions. Also the most probable value is shifted to lower angles. The broadening could be explained by mis-reconstructions due to the extrapolation. The shift to lower angles corresponds to steeper fitted slopes. This can be caused by the increase of the time difference between the single-strip time-measurements (see figure 7.10).
For a full investigation of the tracking-capabilities the reconstructed angle for all reference-angles in the CRF is shown in figure 7.14. Here a cut on the inverse µTPC-slope of 0.05 is applied to exclude reconstruction and fit failures. Comparing these three plots one observes about 1.6% less reconstructed events for the two methods using the extrapolated-times. The main differences between the distributions can be seen at reference-angles close to zero. Here the reconstruction is expected to fail due to only a small projected-track-length onto the readout-area. Despite this for the evaluation using the two extrapolated-times also here considerable narrow distributions are reconstructed.

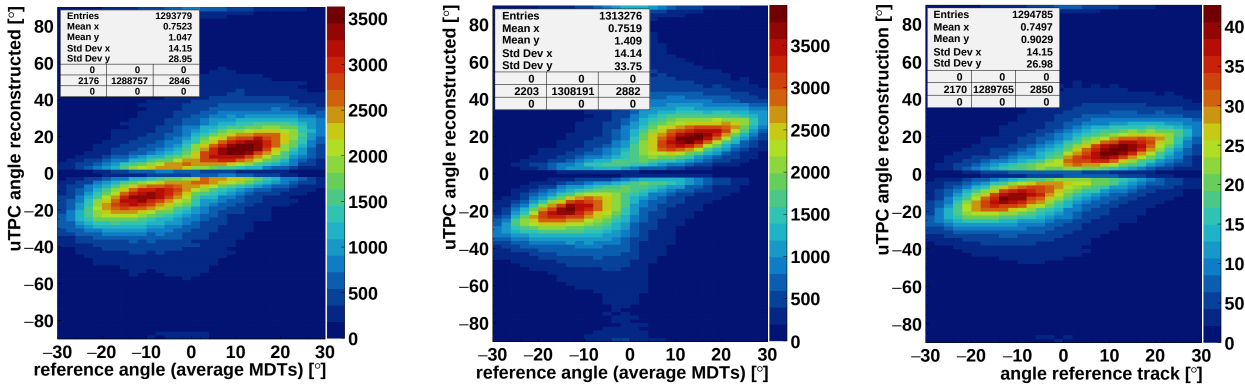

(a) Baseline extrapolation. **(b)** Inflection point. **(c)** Maximum extrapolation.

Figure 7.14.: Reconstructed angle by the µTPC method as function of the reference track angle for different signal-time determinations. Important to note is the different scale of the x and the y axes. The measurements are performed using module one

To evaluate this behavior the reconstructed angular-distributions are fitted using a Gaussian, ±15° around their most probable value (MPV). The behavior of the MPV and the width of the Gaussian is shown in figure 7.15. The expectation would be good reconstructions for large inclination angles due to the large projected track-length onto the readout-pattern. Vice versa worse reconstructions are expected for small inclination angles.
Therefore the reconstruction using the inflection-times is in agreement with this expectation. The width is broader for small angles and narrower for large angles. The MPV follows at large angles the diagonal (in black) and shows for small angles deviations due to the problematic reconstruction. The reconstructions using the two extrapolated-times show a systematic shift of the MPV with respect to the diagonal (in black). This can be explained by the broadening of the event-wise time-distribution using these evaluations (seen in figure 7.10b) resulting in higher reconstructed track-slopes. Therefore systematically too small track angles are reconstructed (expected from formula 7.2).

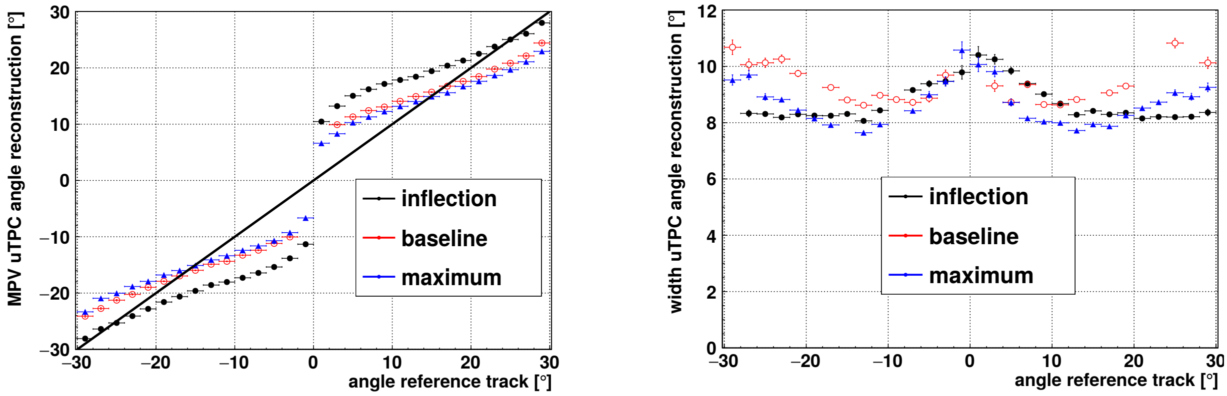

(a) Most probable value of the µTPC angle reconstruction as function of the reference track angle. **(b)** Width of the µTPC angle reconstruction as function of the reference track angle.

Figure 7.15.: Dependencies of the µTPC angle reconstruction on the signal-time evaluation. A slightly better reconstruction for the maximum extrapolation can be assumed.

The width for the baseline-extrapolation is larger, while for the maximum-timing an improvement for small angles is reconstructed. The evaluation of the width is biased for the inflection-method as here the long extensions are not taken into account. Therefore the method using the maximum-time seems to be the optimal for the angular-reconstruction, due to best angular-resolution.

Much better resolutions in the order of 3° to 6° are expected from small chambers [Ntekas, 2016] and reconstructed by [Flierl, 2018] for module zero in the testbeam at H8. The worse resolution in the CRF can be explained by several effects. First the timing during measurements at accelerators is much better defined than in the CRF. This is due to the only small investigated areas of about 10 cm×10 cm. For the presented results the resolution is determined over an active area of about $2\,\mathrm{m}^2$. Effects from resistivity-differences as well as the signal-propagation along the strips worsen the time-resolution and therefore the angular-reconstruction.

Second the ionization of the cosmic muons is much more inhomogeneous due to the much broader energy-distribution. This aggravates the track-fit as commonly low charged signals lead to unstable time-measurements. As third point it should be mentioned that during testbeams only one angle is investigated in a single data-set. Whereas during cosmic-measurements any given angle has to be reconstructed. Therefore much more parameters have to be controlled.

7.2.3. µTPC Position Reconstruction

Using the track-fit in the drift-gap also the intercept-position can be reconstructed. For this the point of time has to be determined at which the fit-function has to be evaluated. This time corresponds to the center of the drift-gap as here the reference track is evaluated. It is therefore called t_{mid}. Using the fit-parameters $t_{\mathrm{\mu TPC}}$ and $m_{\mathrm{\mu TPC}}$ the position can be reconstructed with the pitch p according to

$$x_{\mathrm{\mu TPC}} = \frac{t_{\mathrm{mid}} - t_{\mathrm{\mu TPC}}}{m_{\mathrm{\mu TPC}}} \cdot p \quad . \tag{7.3}$$

A priori t_{mid} is not known. Several ways for the determination exist. A very robust method is described by [Flierl, 2018]. Here the difference to the reference-prediction of the reconstructed position with $t_{\mathrm{mid}} = 0$ is calculated. This difference is evaluated as function of the inverse fit-slope $m_{\mathrm{\mu TPC}}$. The slope of the distribution reconstructs t_{mid}. Instead of the reference-prediction also the centroid-reconstruction can be used.

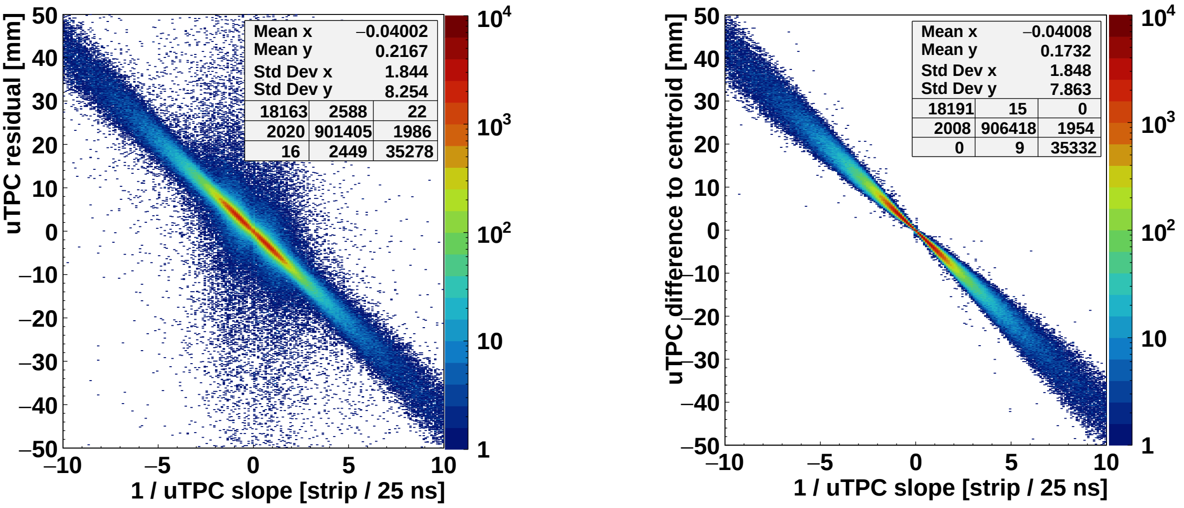

(a) Residual of the position reconstructed using the µTPC-fit without the correct timing t_{mid} as function of the slope from the fit.

(b) Difference of the position reconstructed using the µTPC-fit without the correct timing t_{mid} to the position reconstructed by the centroid as function of the slope from the fit.

Figure 7.16.: The µTPC-fit has to be evaluated at the correct time for position-reconstruction. This right time corresponds to the central position in the drift grap. The time can be reconstructed using the dependence in the shown distributions. The unit of strips indicates the dependence on the pitch, which is for the NSW Micromegas 0.425 mm.

An exemplaric reconstruction is shown in figure 7.16. Due to the angular acceptance of the CRF of ±30° only inverse µTPC-fit-slopes up to ±1.6 are expected. Larger values indicate a priori a wrongly reconstructed incident-angle. Despite this the residual follows also for this mis-reconstructions the observed dependence. An explanation is the limitation of the fit-parameter to the reconstructed-time-distribution. The slope could be biased, but time is none the less reconstructed in the time-window of the drift-gap. The alternative methods for the determination of t_{mid} use the mean timing of the strip time-distributions. These can be evaluated for a large number of events similar to the approaches in the last chapter 7.2.1. Also the event-wise calculated mean strip time can be used. As the method of [Flierl, 2018] showed the best results, this is used in the following.

According to chapter 7.2.1 the single-strip-signals are evaluated using either a correction for capacitive-coupling of 30% or not. Also the differences between the three signal-evaluation-points are considered. For the investigation of the µTPC-position-resolution the same approach as described in chapter 7.1.1 is chosen. The widths of the residual-distributions evaluated using the double-Gaussian-fit and the Gaussian-ratios are shown in figure 7.17.

The narrow width as well as the broad width decrease using the coupling correction. Also the ratio of the two Gaussians gets smaller, which means more reconstructions in the narrow Gaussian. Therefore it can be concluded that the coupling-correction indeed improves the resolution. The next observation is that using the correction almost the same behavior is reconstructed for the three time-evaluation-points. Without correction the inflection point shows the broadest distributions, followed by the baseline and the maximum-extrapolation. This indicates that by using the slope of the inverse-Fermi-fit the time-information can be improved for better position-resolutions.

One would expect a narrowing of the distributions for larger track-slopes due to the increasing projected track-length onto the readout-pattern. This is not observed. Already [Lösel, 2017] sees for cosmic-measurements with large Micromegas no improving µTPC-residual-distribution for larger inclinations.

The problem of these large detectors is the stability of the timing. The timing is affected by many parameters and is generally distorted due to the large active area. A strange observation, which could not be explained yet, is the step of the width-behavior around track-slopes of about -0.3 and 0.2. At these slopes the width of the distribution starts to increase for higher track-slopes. A slope of 0.3 corresponds to an angle of about 17° and could indicate systematic effects due to the time-resolution of the trigger in the CRF.

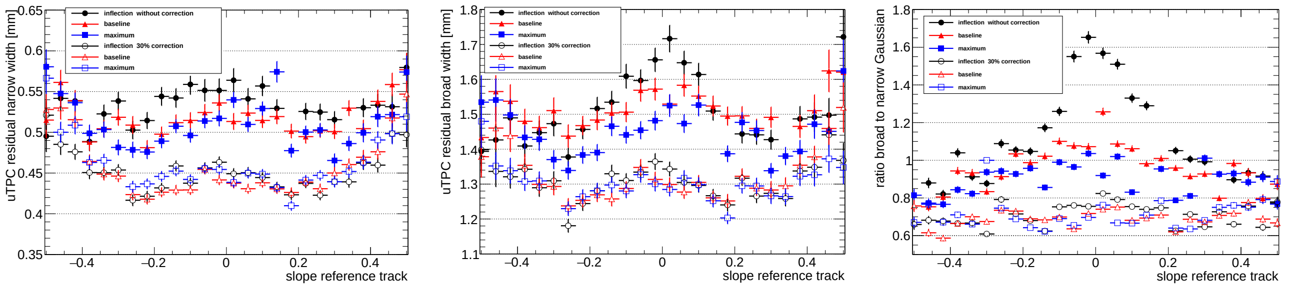

(a) Width of the narrow Gaussian as function of the reference-track-slope.

(b) Width of the broad Gaussian as function of the reference-track-slope.

(c) Ratio of the broad to the narrow fitted Gaussians.

Figure 7.17.: The residual-distributions for the µTPC-position-reconstruction are evaluated using a double-Gaussian-fit. The width of the Gaussians and their ratios are depending on the signal-evaluation-technique.

These evaluations have to be compared to the centroid-reconstruction in figure 7.2. The discussion is made only for the reconstruction using the coupling-correction, as here better resolutions are achieved. One notices a not as good position-reconstruction for the µTPC-method for small track-slopes. Around track slopes of ±0.3 the narrow width becomes smaller than for the centroid-method. For the maximum shown track-slopes of ±0.5 the improvement of the narrow-width for the µTPC-method is about 0.15 mm. This shows the general advantage of this method at large angles. An unfortunate observation is the large contribution of the broad Gaussian to the overall distribution. For the µTPC-method the ratio of the broad to the narrow Gaussian fluctuates around 0.7. For the centroid-method this ratio stays almost always below 0.6 and is decreasing for larger track-slopes.

7.3. Charge weighted Clustertime Reconstruction

Following the approach of [Flierl, 2018] the charge-averaged-clustertime t_c is investigated. Similar to the centroid-method the position in the drift-gap with the largest charge accumulation can be reconstructed. This is achieved by the sum over the measured-drift-times each weighted by the charge of the corresponding strip. Here also the value is normalized using the total sum of all charges in the cluster.

[Flierl, 2018] used the dependence of the centroid-residual on this time to improve the resolution for inclined tracks. The idea is sketched in the simulation seen in figure 7.18a. As the charges are created not equally distributed along the track of the muon, the averages are shifted with respect to the nominal positions. The reconstructed position in precision-direction (in the figure labeled with x) is depending on the incident position and on the charge-clustering. The position in the drift-gap (in the figure labeled with z) is only depending on the current charge-clustering. Therefore knowing the angle of incident, the position in precision-direction can be corrected using the position in the drift-gap. The drift-gap-position scales linearly with the measured time, as the electron-drift is almost constant. An exemplaric correlation of the clustertime with the residual can be seen in figure 7.18b.

For a correction of this effect the track-inclination m and the timing t_{mid} in the drift-gap-center have to be known. Also the correlation-factor c between timing and residual has to be determined in order to correct the position according to

$$x_{\text{nom}} = x_{\text{c}} - c \cdot m \cdot (t_{\text{c}} - t_{\text{mid}})\,. \tag{7.4}$$

Here x_{c} corresponds to the already discussed centroid-position. For t_{mid} the timing reconstructed by the µTPC-reconstruction can be used. As the track-slope is a priori not known, this has to be an input variable for this reconstruction. The actual implementation for the usage in ATLAS could take advantage of the known angle to the interaction point. Also track-predictions from other subsystems could be used, as only a coarse incident-angle-information is required. A preliminary track from uncorrected hits in multiple layers of the wheel could be used in an iterative reconstruction, as well. Therefore the following approach uses the slope of the track-prediction from the MDTs in the CRF. Instead of this also a coarse slope-prediction from the two eta-layers could have been used. This would result in less reconstructed events due to the requirement of simultaneous hits in both layer. For the determination of the correlation factor c the dependence between residual and t_{c} has to be evaluated as function of the track-slope m.

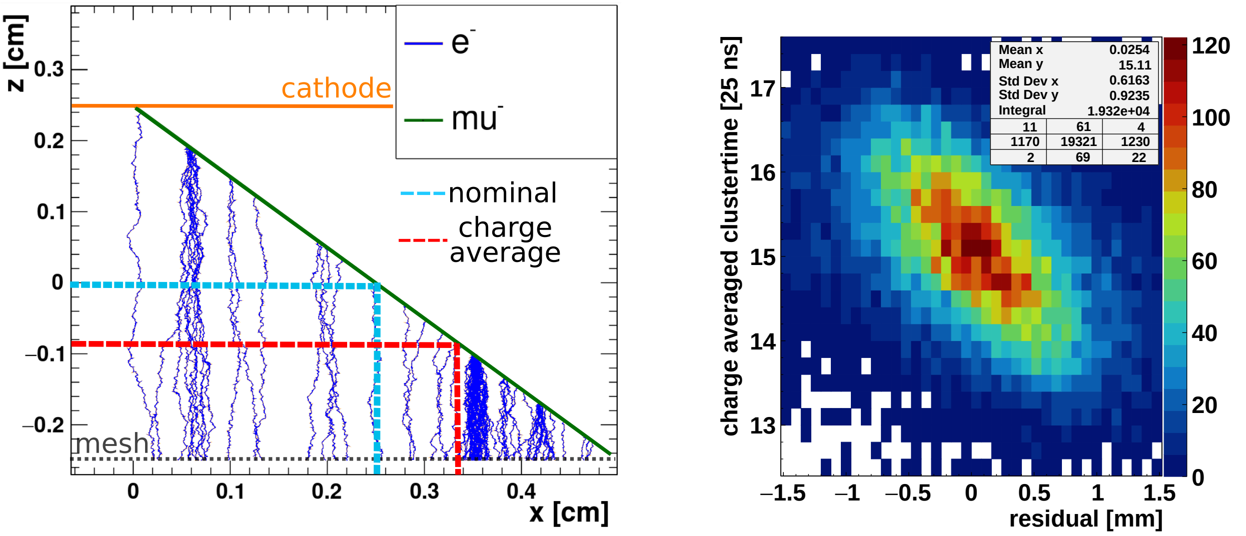

(a) Simulation of the inhomogeneous ionization along the path (green) of a muon between cathode and mesh. Indicated are the average expected position of the charge and the time (blue). Also the simulated distorted charge average is shown (red). Adapted from [Flierl, 2018].

(b) Correlation between the centroid-residual and the charge averaged clustertime for tracks with an inclination between -0.48 and -0.44. Exemplaric plot for module eleven at a drift-voltage of 300 V. In the actual implementation for the correction of this effect the axes of the plot are interchanged.

Figure 7.18.: Due to the inhomogeneous ionization of the muons along their path in the drift-gap the position-reconstruction is distorted. The distortion is correlated linearly to the charge averaged cluster-time due to the constant electron drift.

In the implementation of this reconstruction the residual is plotted as function of t_{c} (see figure 7.18b). Therefore the unit of the slopes is given in mm/25ns. The slopes of these distributions extracted by linear fits are shown for the four layers in figure 7.19a. The differences between the layers arise due to their drift-gap-orientation. Eta-in and stereo-out have the drift-gap above the amplification-gap. For the other two layers the orientation is inversed, which causes a different drift-direction for the electrons. Therefore this dependence can be explained by the drift of the electrons [Flierl, 2018].

The determination of c is achieved by a linear fit of the reconstructed dependencies as function of the track-slope. Typical values for the reconstructed correlation factor c at a drift-voltage of 300 V are in the range from 0.76 mm/25ns to 0.83 mm/25ns, with fit-errors of about 0.02 mm/25ns.

Another information which can be extracted from the linear fits of the residual-clustertime-distributions is the mean-timing at zero residual. The expectation is that this time should be constant over all track-inclinations and it should be equal to t_{mid}. The explanation would be that for all track-slopes this time corresponds to the center of the drift-gap at which the track is evaluated. The reconstructed times are shown in figure 7.19b.

For small track-slopes the linear fit can not reconstruct this time as the distributions are too flat[2]. Despite this for larger inclinations almost constant times are reconstructed. Unexpectedly these times differ for positive and negative track-slopes. Also this difference is not equal for all layers. One possible reason could be a different trigger-time due to the response-behavior of the scintillator.

Correcting for the residual dependence on the charge-averaged-clustertime using formula 7.4 the resolution can be improved as seen in figure 7.20a. Here the resolutions for the three position-reconstruction techniques are compared directly as function of the reference-track-angle. This plot shows that for large track angles the

---

[2] The fit is parametrized by $f(x) = p_1 \cdot (x - p_0)$. Here $f(x)$ reconstructs the mean residual as function of the charge-averaged-clustertime (given by x). Therefore p_0 corresponds directly to the time for a mean-residual of zero.

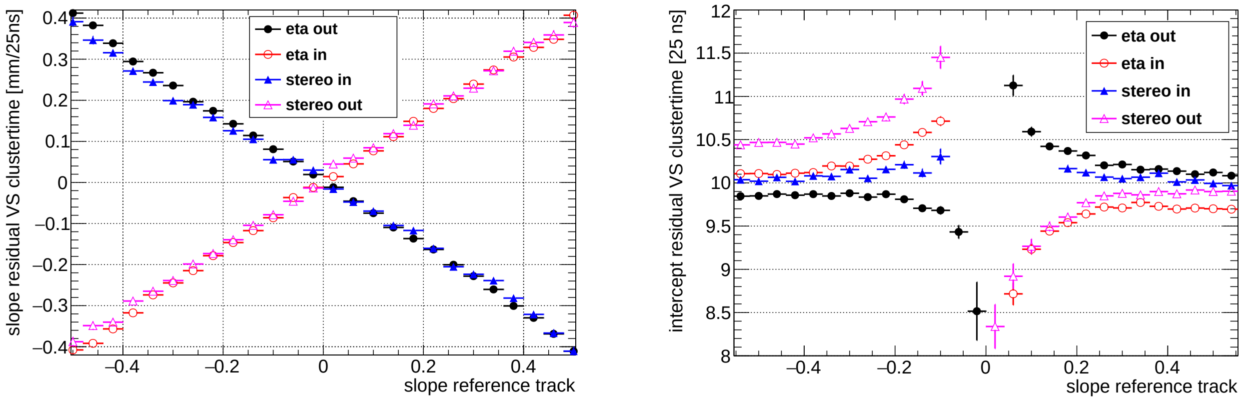

(a) Slope of the residual-clustertime distribution as function of the reference track slope. Exemplaric plot for module eleven at a drift-voltage of 300 V.

(b) Timing of hits with residuals close to zero. Reconstructed by linear fits to the clustertime-residual correlation like in figure 7.18b.

Figure 7.19.: The residual is depending on the charge-averaged-clustertime. The correlation is depending on the track-inclination. Using linear fits the dependence as function of the track-slope can be reconstructed.

clustertime-correction is superior over the µTPC-method. Also the efficiency is not as spoiled as for the µTPC-method, which reconstructs less good events due to bad fits.

Despite this [Flierl, 2018] reports much better resolutions using this method even for larger incident-angles. [Flierl, 2018] evaluated the testbeam-data of module zero at the H8-beamline from august 2017. For the core-resolution at 20° a value of about 0.17 mm is stated, which corresponds to the width of the narrow Gaussian corrected by the tracking-accuracy. The resolution reconstructed using the weighted width of the two Gaussians of 0.26 mm corresponds much better to the here reconstructed resolution-values. Similar values are reported for inclinations at angles of about 30°. Extrapolating the behavior to these angles, such resolutions are not achieved for the cosmic data-samples. Therefore this comparison shows the strong limitation of the resolution-reconstruction-capabilities using cosmic muons.

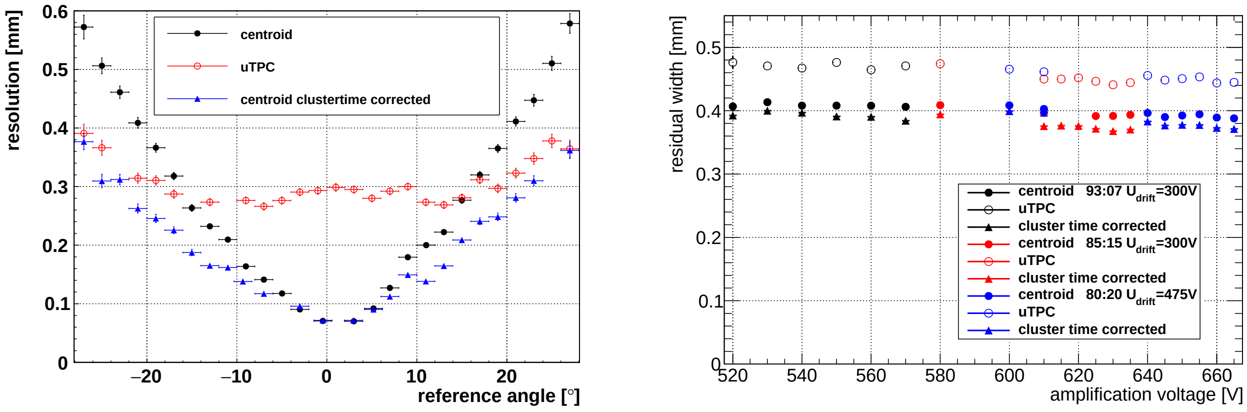

(a) Resolution as function of reference-track-angle determined for the three position-reconstruction approaches. Exemplaric reconstruction for the eta-in layer of module one at an amplification-voltage of 570 V and a drift-voltage of 300 V.

(b) Narrow width of the residual-distributions integrated over all track-inclinations as function of the amplification-voltage. Determined for the three position-reconstruction approaches for different gas-mixtures of argon-CO$_2$. Exemplaric plot for the second gluing side of the eta-three doublet.

Figure 7.20.: Comparison of the three position-reconstruction methods as function of the track-slope and the amplification-voltage. The centroid uses solely the charge-information, while the µTPC-method relies on the timing-reconstruction. Combining charge and time-information the resolution can be improved for all inclinations. For these plots the signals are evaluated at the inflection point and a correction for capacitive-coupling of 30% was applied.

The comparison of the three methods can be made for the gas-study-measurements with module eight and the eta-three-doublet. In figure 7.20b the narrow width of the residual-distributions integrated over all track-slopes is shown as function of the amplification-voltage. The different gas-mixtures are indicated by different colors. For all measurements the µTPC-method shows the broadest distributions. This can be explained by the integration over all angles. Normal tracks contribute the most to the overall distribution, as seen in the slope-distribution in figure 4.4b. Therefore the µTPC-resolution is dominated by the worse resolution for normal tracks compared to inclined tracks. Due to the same reason the clustertime-correction only slightly improves the residual-width compared to the common centroid-method. For all reconstructions the improving effect due

to the higher reachable gain for the two non-nominal gas-mixtures can be seen.
The µTPC-method is expected to have yet better resolutions for larger inclinations as observed for these data. Therefore the dependence of the residual for this reconstruction-method is investigated also for the charge-averaged-clustertime. For individual track-inclination-intervals similar linear dependencies as for the bare centroid-residual are observed. As the µTPC-reconstruction heavily depends on the time-reconstruction the dependencies are investigated for the three-evaluation-points and coupling corrections separately. This is shown in figure 7.21. In contrast to the centroid-dependence no linear correlation is found. Instead an almost constant value for high inclinations is observed, which is mirrored at the center for the opposite track-slopes. Here also large differences between the three evaluation-timings are reconstructed. The largest dependencies on the charge-averaged-clustertime are observed for the inflection-evaluation. This explains the worse resolution for this timing compared to the other two, seen in figure 7.17. Another observation is the decrease of the dependencies using the coupling correction. Therefore this correlation could be explained by charge-sharing which influences the time-reconstruction.

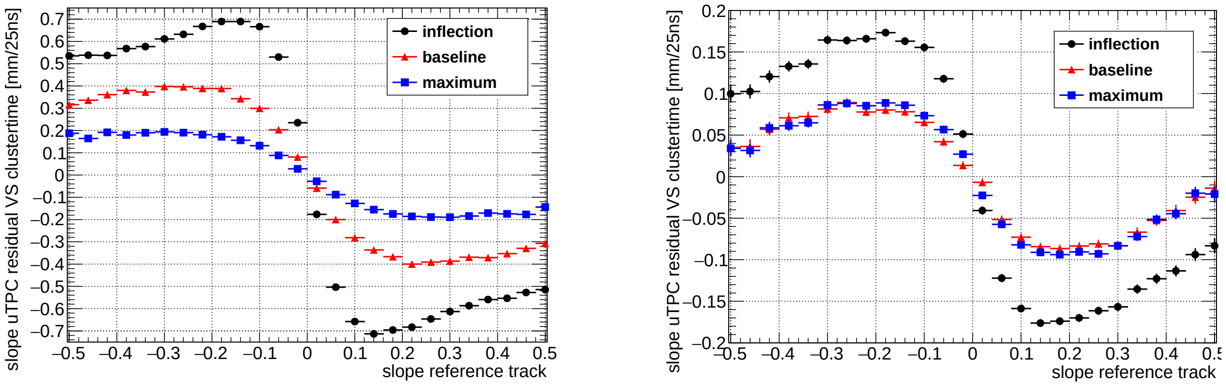

(a) Without capacitive-coupling.

(b) capacitive-coupling factor of 30%.

Figure 7.21.: µTPC residual dependence on the clustertime as function of the reference track-inclination. Shown are the results for the three different signal evaluation-points. For all evaluation-points the capacitive-coupling-correction reduces the dependence.

The linear dependence of the centroid-residual-clustertime-correlation and the track-slope can be explained by the constant drift of the electrons. [Flierl, 2018] reconstructs that the correlation-factor c exactly corresponds to the drift-velocity. Therefore the dependence of this factor on the drift-field is investigated. Exemplaric correlations are shown in figure 7.22a for various drift-fields. Using the different signal-evaluation-techniques the drift-velocity is reconstructed for the drift-scan with module three. As can be seen much too low drift-velocities are reconstructed, compared to the expectation from the simulation in figure 7.22b. This is especially unsatisfactory as the linear-dependencies between the residual-correlation and the track-slope are very stringent. Therefore systematic effects have to be considered. The large differences between the signal-evaluation-techniques suggest a problematic time-reconstruction. As the results for the drift-velocity-reconstruction from the time-distribution-width are successful, this is unexpected. For the dependence on the track-slope a systematic effect can be considered coming from the increasing distribution for small slopes. This could cause for each point in figure 7.22a a lower value than expected.

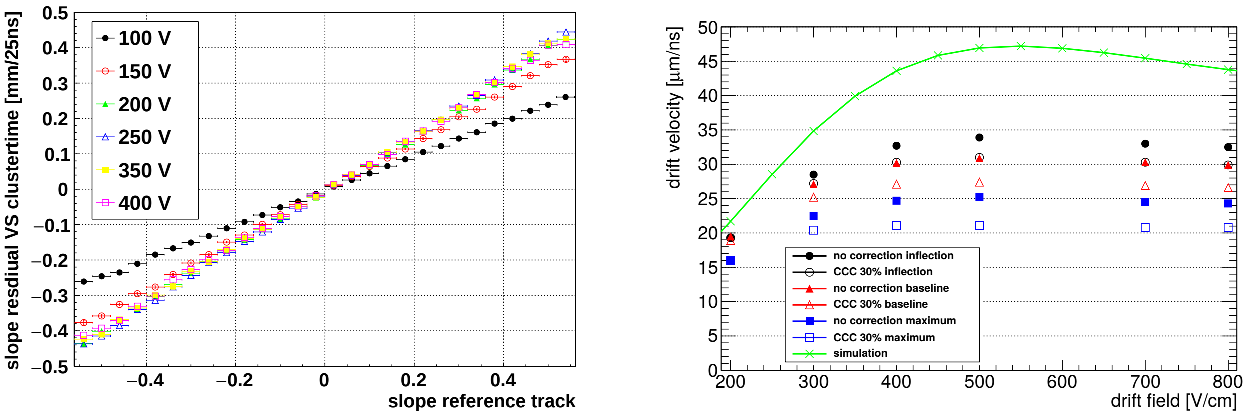

(a) Slope of the residual-clustertime-distribution as function of the reference track slope. Reconstructed for various drift-voltages using the inflection-time for capacitively corrected signals.

(b) Reconstructed drift-velocities for the different signal-evaluation-techniques as function of the drift-field.

Figure 7.22.: Reconstruction of the drift-velocity using the dependence of the centroid residual on the charge-averaged-clustertime.

7.4. Track Reconstruction using Multiple Micromegas Layers

7.4.1. Reconstruction in Non-Precision-Direction with Stereo Strips

The position in non-precision-direction, which means along the eta-strips, can be reconstructed using the combined information of the stereo-layers. The strips in these layers have a slight rotation of ±1.5° in the active plane with respect to the strips in the eta-layers (see figure 7.23a). One stereo-layer is rotated in the opposite direction than the other layer. In the following a short explanation for the reconstruction will be given following [Alexopoulos et al., 2015] and [Flierl, 2018], after which the performance will be discussed. η is the position in precision-direction, perpendicular to the eta-strips, and ϕ is the position in non-precision-direction, so along the eta-strips[3]. The procedure for the reconstruction uses the mean and the difference of the hits in the two stereo-layers. The position reconstructed in one layer is denoted by v and the position given by the other layer with u. Using only one of these layers for the position-reconstruction in precision-direction requires a rotation. The position in these layers can be calculated using the original coordinates by

$$v = \eta \cdot \cos\alpha + \phi \cdot \sin\alpha \quad \text{and} \tag{7.5}$$

$$u = \eta \cdot \cos\alpha - \phi \cdot \sin\alpha \quad , \tag{7.6}$$

where α is the angle between the eta and one-layer of the stereo-strips. Here the assumption is a symmetrical rotation around the center of the boards for the two stereo-layers. Solving these equations for the two required coordinates, one arrives at

$$\eta = \frac{v+u}{2 \cdot \cos\alpha} \quad , \tag{7.7}$$

$$\phi = \frac{v-u}{2 \cdot \sin\alpha} \quad . \tag{7.8}$$

These formulas assume the same plane for the three coordinate-systems (the eta and the two stereos). However, for the spatially separated layers of the Micromegas modules this is not true. Therefore the difference in height of the planes introduces an error for tracks which are not perpendicular to the surfaces. This error can be corrected using the angles of the track-inclinations. At this point [Alexopoulos et al., 2015] and [Flierl, 2018] differ in their approach to correct for this effect. While [Alexopoulos et al., 2015] reconstructs the position in one of the stereo-layers, [Flierl, 2018] determines the position between the two planes. As the second approach treats the layer symmetrically this is chosen for the reconstruction in the following. Correction terms of

$$\triangle\eta = -\frac{\tan\alpha}{2} \cdot \triangle z \cdot \tan\Theta \cdot \cos\Phi \quad , \tag{7.9}$$

$$\triangle\phi = -\frac{1}{2\tan\alpha} \cdot \triangle z \cdot \tan\Theta \cdot \sin\Phi \tag{7.10}$$

were derived. For these formulas $\triangle z$ denotes the difference between the centers of the drift-gaps in the two stereo-layers. This corresponds to the difference in z of the central-areas reconstructed in the CRF coordinate-system. Θ and Φ are the track parameters given in polar-coordinates. These two can be derived from the track-slopes m_x and m_y, given by the CRF using

$$\Theta = \arccos\left(\frac{1}{m_\mathrm{x}^2 + m_\mathrm{y}^2 + 1}\right), \tag{7.11}$$

$$\Phi = \arctan(m_\mathrm{y}/m_\mathrm{x})\,. \tag{7.12}$$

For a first test of this reconstruction the correlations between the difference of the positions given by the stereo-layers and the position given by the scintillator-hodoscopes are investigated. An exemplaric distribution for module one can be seen in figure 7.23c. The slope of this distribution should correspond to the factor given by the numerator of equation 7.8. Therefore a theoretical value of about 0.05235 is expected. The mean value for all yet measured modules calculated for each of the boards individually is 0.05268 with a standard deviation of 0.00086.

A problem which can influence this correlation is the alignment between the readout-boards. If the rotation of the stereo-strips is not as intended the angle α is modified and with this the correlation receives a different slope. Also shifts between the boards influence this reconstruction. This reconstruction is also probably biased due to the scale-error of the hodoscope.

---

[3] The naming-convention follows the physics and the coordinate-system of the ATLAS-experiment. The η-coordinate reminds for the pseudo-rapidity-value, which is reconstructed in precision-direction of the Micromegas. The ϕ-coordinate gives the angle around the beam-tube, which is correlated to the position along the strips.

In the nominal design of the modules the stereo-strips should overlap in such a way that the center of the readout-board corresponds to the position where the strips with equal numbers of the two-layer cross each other. This is sketched in figure 7.23b. Here strips of the two stereo-layers are shown from top around specified strips o and i. The position in non-precision-direction is proportional to the difference of the layer-positions. Therefore if the strips o and i are hit this corresponds to a non-precision-position of $o - i$ times a scale-factor. This position is also reconstructed if strips $o + k$ and $i + k$ are hit, where k is an arbitrary integer number. If o and i are the same number this position is zero.

The design foresees the zero-position in the center of the boards along the eta-strips (indicated as brown dot in figure 7.23a). Therefore the center of the readout-boards can be reconstructed by evaluating the correlation between the position-difference of the stereo-layers as function of the position given by the scintillators. Positions at which the correlation crosses the zero-difference of the two stereo-layers are the center of the boards. This is used during Micromegas alignment, as discussed in chapter 6.2.1, for the shift $\triangle x$ along the non-precision-direction.

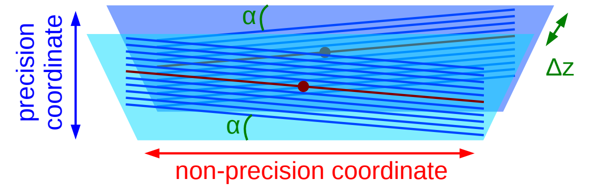

(a) Sketch of the strip inclination of the stereo boards.

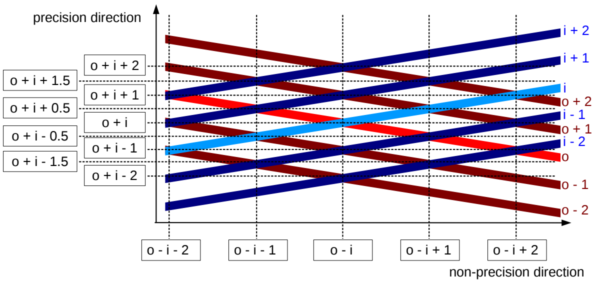

(b) The position-reconstruction with the stereo-layers enables also a coarse resolution along the eta-strips, so in non-precision-direction.

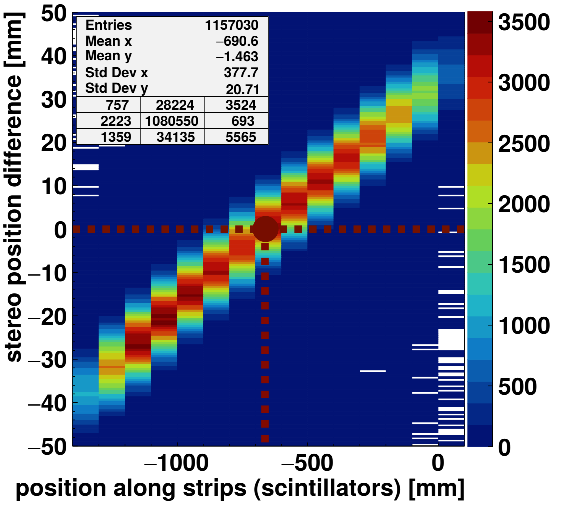

(c) Difference of the centroid position in the two stereo-layers as function of the position along the strips given by the scintillator-hodoscope. The board-center is reconstructed at the crossing of the zero, indicated by the brown dot.

Figure 7.23.: Basic principle for the reconstruction of the position in non-precision-direction.

For a further investigation of this reconstruction the difference to the reference, called residual, is considered. Due to the coarse 10 cm resolution of the scintillator-hodoscope the investigation is limited. Without the correction formula 7.10 the difference between reconstruction and reference should depend on the track parameter Φ and Θ. The measured dependencies without these corrections can be seen in figure 7.24. As expected a sinusoidal dependence on the Φ angle given in radians is observed. The changing width of this residual-distribution along Φ can be explained by the Θ-distribution. As the track-parameters are independent, for one Φ-value all measured Θ-values can be reconstructed. The same is true vice versa.

Therefore the width of the distribution is depending not only on the reference resolution. Also the distribution of the other track parameter have to be considered. For the dependence of the mean residual on one track-parameter, formula 7.10 has to be evaluated with the mean value of the other parameter. As seen in figure 7.24b the Θ mean is about 0.3217 and the standard deviation about 0.1299. Therefore the mean residual $\bar{r}$ should depend on Φ like

$$\begin{aligned}\bar{r} &= -\tfrac{1}{2 \cdot \tan(1.5^\circ)} \cdot 16.9\,\mathrm{mm} \cdot \tan(\tfrac{180^\circ}{\pi} \cdot 0.3217) \cdot \sin(\Phi) \\ &\approx -107.5\,\mathrm{mm} \cdot \sin(\Phi).\end{aligned}$$

A sinusoidal fit to the mean-behavior revealed an amplitude of about (-107.0 ± 0.1) mm. The small discrepancy to the expected value can be explained by several effects. In formula 7.10 enters the distance between the stereo-layers. As seen in chapter 6.2.1 this can differ from the design value. Also the angle between two layers is varying in the CRF-reconstruction from the nominal value.

A third point is the not considered shape of the Θ-distribution. The fit[4] required an additional phase of 0.1340(5), an offset of (4.02 ± 0.04) mm and a not perfect scaling with Φ of 0.9963(2). These unexpected parameters could be explained by systematic errors due to the scaling of scintillator-hodoscope and the not-perfect alignment.

---

[4] The fit is performed using the parameterization $f(x) = p_0 \cdot \sin(p_1 + p_2 x) + p_3$. The phase p_1, the offset p_3 and the scaling p_2 are additional parameters.

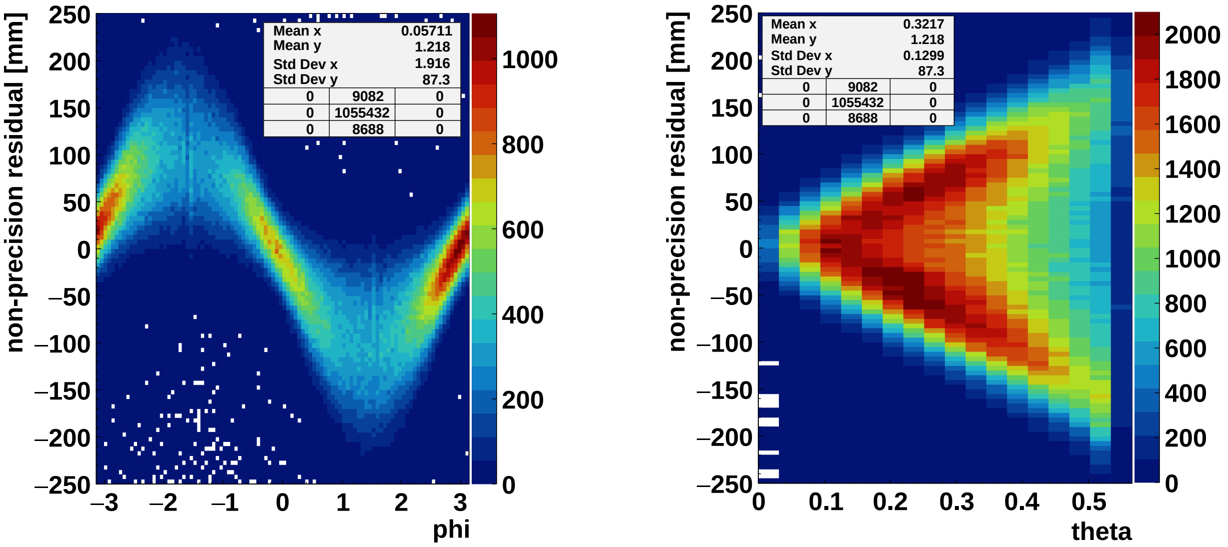

(a) Residual of the stereo reconstruction as function of the angle phi Φ.

(b) Residual of the stereo reconstruction as function of the angle theta Θ.

Figure 7.24.: Dependence of the residual in non-precision-direction on the track-inclinations.

Applying the correction formula 7.10 the dependence on the track-parameters vanishes almost. The resulting distributions can be seen in figure 7.25. For the Θ-distribution no correlation is visible. Still unexpected is a strong dependence of the residual on the Φ-parameter. Contrary to the previous reconstruction the width of this residual-distribution is not depending on the Φ-parameter. Neither [Alexopoulos et al., 2015] nor [Flierl, 2018] account for a dependence only on the Φ-angle. Therefore this has to be either a missing part of the reconstruction-correction or a systematic effect of the CRF.

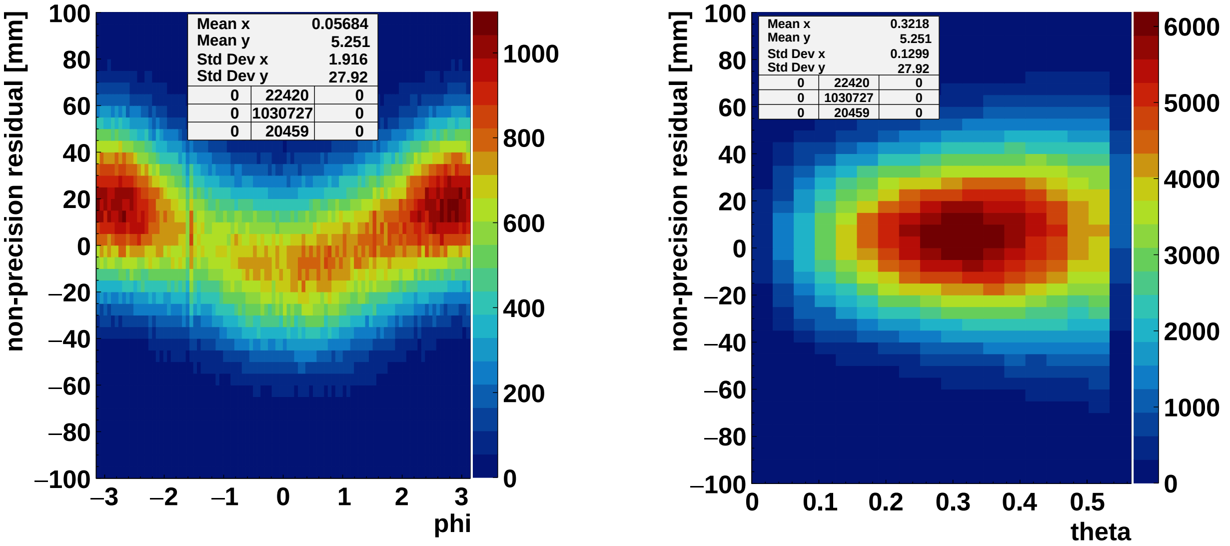

(a) Residual of the stereo reconstruction as function of the angle phi Φ.

(b) Residual of the stereo reconstruction as function of the angle theta Θ.

Figure 7.25.: Dependence of the residual in non-precision-direction on the track-inclinations after correction with formula 7.10.

The dependence seen in figure 7.25a can be interpreted as a dependence on the reference-track-slope in non-precision-direction. This can be seen in figure 7.26a. Similar to the alignment procedure explained in chapter 6.2.1, this suggests a shift in direction perpendicular to the active area. As the module is aligned using the method described in chapter 6.2.1, no shift in this direction is expected.

To probe this reconstruction the same distribution is evaluated for all yet measured series-modules. All of them show almost the same dependence. A linear fit of these distributions revealed a mean slope of $(-55 \pm 2)\,\mathrm{mm}$ with a standard deviation of 3 mm. An explanation of this observation could be wrongly assumed positions of the scintillators. The slope suggests a difference between the z-centers of the MDT track reconstruction in the y-z-plane and the scintillator track reconstruction in the x-z-plane.

Another unexpected dependence of the residual in non-precision-direction is seen in figure 7.26b. Here the residual is plotted as function of the position reconstructed using the stereo-layers along the eta-strips. This dependence is another indication of the scale error of the scintillator-position-reconstruction. The linear dependence is calculated for all yet measured modules to be about 0.016(2) with a standard deviation of 0.003.

Therefore the scale error is about 2%.

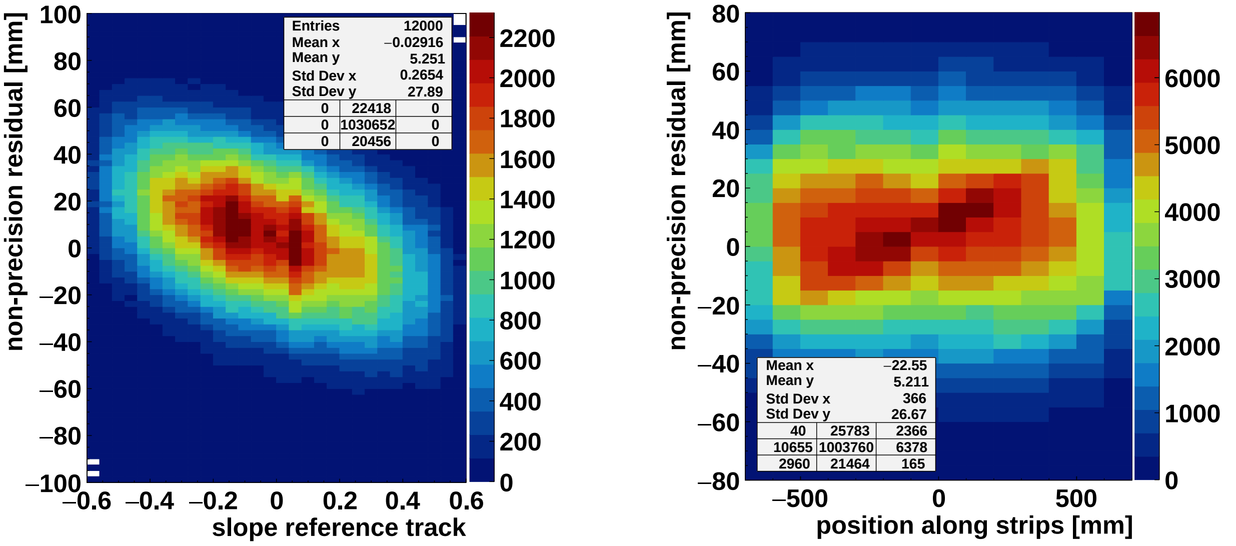

(a) Residual of the stereo reconstruction as function of the track slope in non-precision-direction.

(b) Residual of the stereo reconstruction as function of the position along the strips given by the scintillator-hodoscopes.

Figure 7.26.: Dependence of the residual in non-precision-direction after correction of the track parameters in non-precision-direction given by the scintillator-hodoscopes. The visible dependence indicates a systematic error of the scintillator track reconstruction.

Using the position-information along the eta-strips reconstructed by the stereo-layers the effect of the coarse scintillator-resolution can be investigated further. This is shown in figure 7.27.

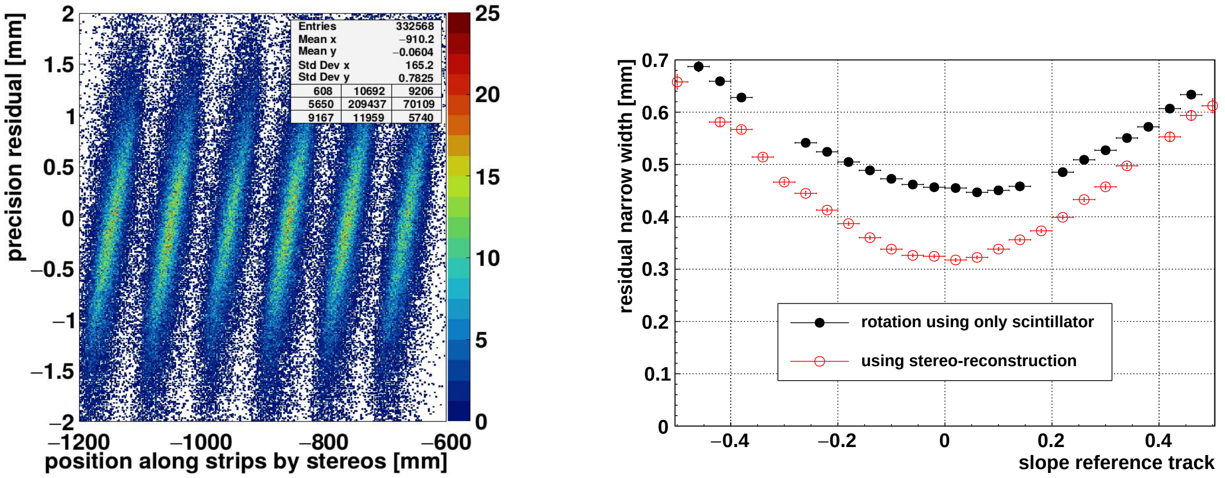

(a) Residual of one stereo-layer in precision-direction as function of the position along the strips (non-precision-direction). The position along the strips is reconstructed using the combination of the two stereo-layers. A cut on the non-precision track-slope of 0.01 is applied.

(b) Narrow width of the residual-distribution as function of the reference track-slope. Plot for the eta-out layer of module zero. Due to not parallel strips and wires the stereo reconstruction is required for a decent position-reconstruction.

Figure 7.27.: The information of the stereo reconstruction can be used to improve the resolution for not well aligned layers.

For bad aligned layers[5] the residual is depending on the position along the strips. The coarse resolution of the scintillator-hodoscope prevents a sufficient correction of this effect. For the stereo-in layer of module one the dependence can be seen in figure 7.27a. Here only the information from the hodoscope is used for the rotation-correction. The position along the strips is reconstructed using the stereo-layers. A cut on the non-precision track-slope is applied to visualize the effect of the scintillator-segmentation. Each 100 mm another scintillator-segment reconstructs the position along the wires for the rotation-correction. Therefore the residual is centered around zero, but is depending on the position along the strips within such a segment.

Using the information given by the stereo-layers this dependence can be reduced. The improvement of the width of the residual-distribution can be seen in figure 7.27b. Here the narrow widths are shown using only the scintillator-information or using the stereo-information. For the reconstruction using the stereo-information the width is in good agreement with the observed widths of well aligned layers as shown exemplarily in figure 7.2b.

---

[5] This means not parallel strips of the Micromegas and wires of the MDT.

7.4.2. Combination of four Layers

Using all four layers of a NSW Micromegas quadruplet the muon tracks in the precision-plane can be reconstructed on a length of about 5 cm. For the investigation of the performance of this reconstruction a bachelor thesis was supervised [Mohl, 2019]. A simple approach for the track reconstruction uses for each layer the charge-centroid. These values reconstruct the track-position in precision-direction perpendicular to the strips. Perpendicular to the readout-plane the positions can be estimated using the reconstructed centers of the drift-gap (see chapter 6.2.1). Using, instead of the centroid, each strip-information individually more track-points are reconstructed. Additionally the drift-time-measurements can be used to improve the position-information perpendicular to the readout-plane. The reconstruction of the position in the drift-gap is performed analogous to chapter 7.2.3. In this case the center of the drift-gap is determined using the mean-time of the strip time distribution.

$$z_{\text{strip}} = z_{\text{layer}} \pm v_{\text{drift}} \cdot (t_{\text{strip}} - \overline{t_{strip}}) \tag{7.13}$$

In formula 7.13 the sign accounts for the orientation of the different drift layers[6]. It was tested which timing reconstructs the points closest to the reference[7]. The inflection point of the timing signal shows the best performance. The most useful reconstructed signals, which are closest to the reference, are reconstructed with this timing. An explanation is the distortion of the drift-time-measurement due to the usage of the second fit-parameter for the other two timings.

In order to investigate the full reconstruction-capabilities of a module, no track-information of the reference should be used. The reconstructed position by the stereo-layers have to be rotated in order to be in the same plane as the eta-layers. This is done using the reconstruction of the position along the eta-strips by combining the informations of the two stereo-layers. As seen in the last chapter 7.4.1 this reconstruction is depending on the track-slope. Therefore the reconstruction has a systematic bias by using only the bare information of the stereo-layers. This is seen in figure 7.28a. Here is shown an exemplaric muon track and the reconstructed track-points by the four layers.

The right two clusters of points belong to the two stereo-layers. The stereo-layers show this kind of shift with respect to the reference for almost all tracks. For one stereo-layer the difference of the reconstructed points to the reference are plotted as function of the reference-track-slope in figure 7.28b. The almost linear dependence comes from the wrong reconstructed position along the eta-strips. This can be explained using the sketch in figure 7.23b. If the track is inclined strips are hit which overlap not at the coordinate at which the track passes through the center of the layers. Therefore the combination of these strips reconstructs a wrong position.

The rotation of the stereo-points into the precision-plane is biased due to this wrong position. The error can be corrected for track-inclinations along the precision-axis. A coarse track-slope can be reconstructed using only the eta-layers. The stereo-positions are corrected using this coarse track-slope.

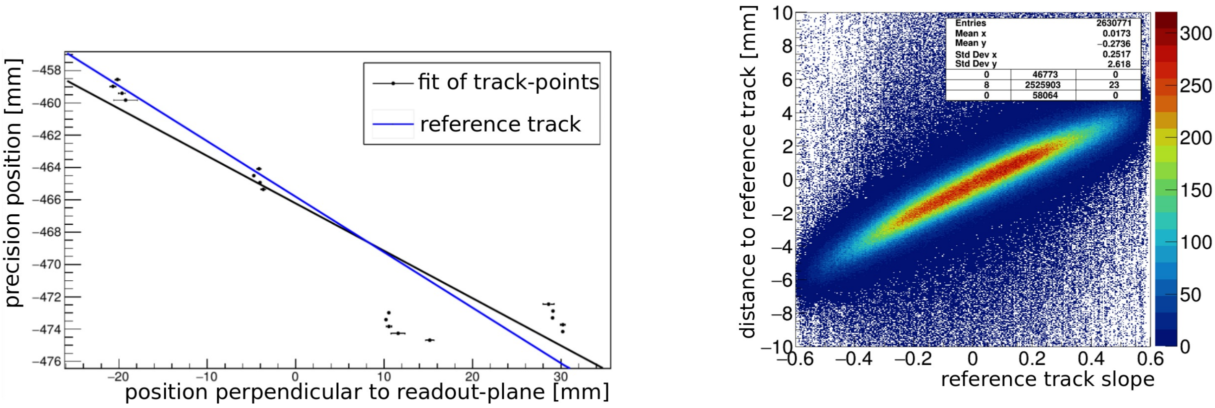

(a) Muon track reconstructed using all four layer of a NSW Micromegas quadruplet (black). The track-points of the stereo-layer (two right clusters) are systematically shifted away from the reference track (blue).

(b) Distance of stereo-track-points to the reference track. The almost linear dependence on the track-slope can be explained by a mis-reconstruction of the position along the eta-strips.

Figure 7.28.: The position-reconstruction in the stereo-layers is biased due to the track-slope. Taken from [Mohl, 2019].

For this investigation the strip-information is not combined into clusters, but taken individually. Therefore it is of utmost importance to discard outliers due to noise or bad signal-fits. Such outliers can be identified using the

---

[6] For the most measurements performed in the CRF the stereo-out layer was on top. Therefore stereo-out and eta-in layers reconstruct using the positive sign, while for stereo-in and eta-out the negative sign is used.

[7] In chapter 7.2.1 the three evaluation-points called baseline, inflection and maximum are discussed.

Hough-transformation [Hough, 1962]. This transformation reconstructs for each given point (y,z) all lines going through this point. The lines are parametrized in polar-coordinates[8] r and θ using

$$r = y \cdot \cos\theta + z \cdot \sin\theta \quad . \tag{7.14}$$

Here z corresponds to the position perpendicular to the readout-plane, whereas y is the position in precision-direction perpendicular to the strips or wires. Therefore the parameters of lines for one point follows a sinusoidal behavior. This method accumulates the found parameters for all points and searches for the most common ones. Outliers can then be identified as points, which are not belonging to the most common line or have a too large distance to this line.

The implementation of the OpenCV C++ framework is used for the Hough-line-reconstruction [Bradski, 2000]. The coordinates of the track-points are scaled by 0.1 mm to integers, which are translated to pixel-coordinates. In a bitmap these pixels are set to one, while all other pixels are kept at zero. The algorithm then reconstruct lines only for the considered pixels.

The accumulation is performed using discrete steps of the line-parametrization. Due to this the step-length has to be determined at which the algorithm works best. Also the number of at least required points for a good reconstruction has to be specified. For this the reconstructed track using the Hough-transformation is compared to the track given by the MDT-reference. Of course the best reconstruction is performed for the smallest step-lengths. Therefore the determination has to account for the losses due to mis-reconstructions or not found tracks due to wrong parametrization.

The step-length for the θ-parameter was investigated in the range of 0.01 to 0.25. A worsening of the slope-resolution of about three percent was determined with a loss below one per-mill of efficiency. Also the intercept-resolution showed only a degrading of about one percent. Hence, no strong improvement with the variation of this step-length is seen. The computing-time difference between the two limits scales almost linearly with the step-length of this parameter. For a decent computing-time a value of 0.1 is chosen in the following.

The step-length for the r-parameter was investigated in the range of 4 to 27. Due to the scale-factor this corresponds to distances of 0.4 mm to 2.7 mm. For the upper limit the slope-resolution was about 60% worse than for the lower one. The intercept-resolution showed even a worsening of more than 100%. The loss-rate for the step-length of this parameter is connected to the number of required points. This can be see in figure 7.29a. In order to stay below one percent of losses only three points are required for the Hough-transformation at the r-step-length of 0.5 mm. The value of 0.5 mm is chosen to stay above the pitch of 0.425 mm.

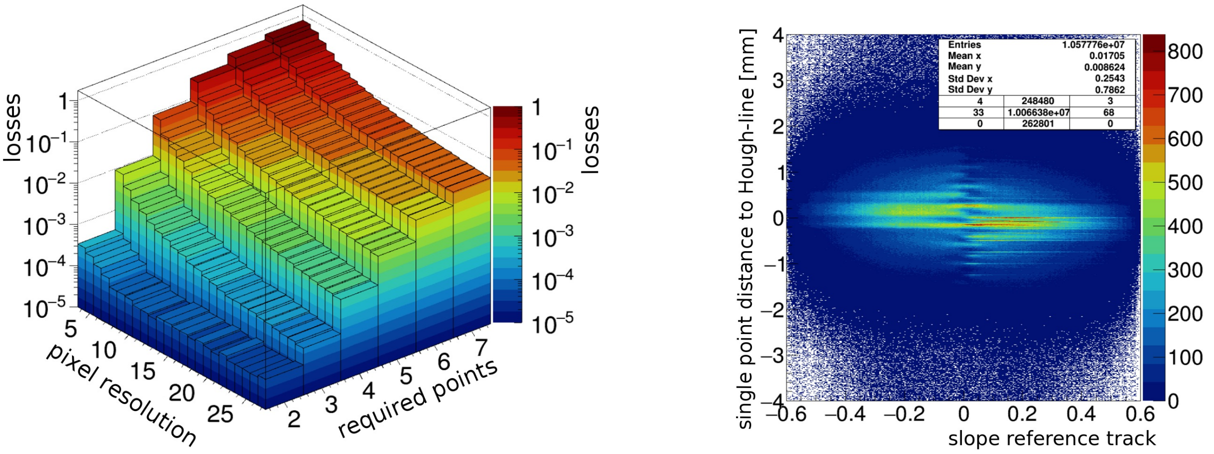

(a) Losses due to mis-reconstructed Hough-lines as function of the required-points and the pixel-resolution. The pixel-resolution determines the allowed point-distance to the Hough-line and is given in 0.1 mm. The required-points determine how many points at least define a line. The losses are considered for not found tracks or mis-reconstructions.

(b) Distance of single-strip track-points to the Hough-line as function of the reference-track-slope. The discrete structures can be explained by the strip-pattern. The strips have a distance of about 0.425 mm. This distance is also reconstructed between the horizontal accumulations.

Figure 7.29.: The Hough-transformation enables an improvement of the track reconstruction by rejecting outliers. For a good performance of this rejection the parameters for the transformation have to be chosen correctly. The reconstruction using the Hough-transformation is limited due to the discrete strip-pattern. Taken from [Mohl, 2019].

The Hough-transformation is performed using for the r-step-length 0.5 mm, for the θ-step-length 0.1 and requiring at least 3 points. The distances of the track-points to the reconstructed Hough-line are shown in figure 7.29b. Due

---

[8] This parametrization can be connected to the tracks given by the CRF. The precision-slope is given by $m_y = -\frac{\cos\theta}{\sin\theta}$. The intersection is given by $t_y = \frac{r}{\sin\theta}$

to the discrete strip-pattern a modulation of the distances to the Hough-line is reconstructed. The modulation is of the same magnitude as the pitch, so a maximum every 0.425 mm is observed. A range of ±4 mm to the Hough-line is chosen as about 95% of the found points are within. Points outside of this range are discarded for the further investigations.

To determine the impact of this selection on the reconstruction, a linear fit to the track-points is performed (see figure 7.28a). The fit-parameters are compared to the reference from the MDTs. This is done with and without the selection of the Hough-transformation. The comparison considered the intercept-differences in the range of ±3 mm and the slope-difference in the range of ±0.1. The standard deviation of the intercept-difference is reduced by about two percent for the selection. For the slope-difference an improvement of the standard deviation of about six percent is reconstructed. Using the selection about four percent more events are reconstructed in the considered ranges.

The optimization of the reconstruction using four layers was performed on a data-sample of module one. In order to investigate the method data-samples of module three and module eight are investigated. For these modules, measurements with different drift-voltages and gas-mixtures were performed.

The comparison of the results for these measurements are shown in figure 7.30. Here the differences between the reconstructed tracks in the Micromegas and the reference tracks by the MDTs are considered. The difference of the slopes and the difference of the intersection-positions within the module are calculated. The evaluation of the distributions is done similar to chapter 7.1.1 as function of the reference-slope. For each track-slope-interval the difference-distribution is fitted using a double-Gaussian. Shown are the sigmas of the narrow Gaussians, which are an estimation for the width of these distributions.

The evaluations for the intercept-differences can be compared to the single-layer centroid-reconstructions in figures 7.2b and 7.4a. The evaluation of the track reconstruction for the gas-study with module eight is problematic due to the position of the module during data-taking. The module was situated above the eta-three doublet and therefore not centered between the two MDT chambers. As seen in figure 4.8b, this introduces a worse track-prediction by the reference. Another problem for the investigation of this module was the usage of wrong alignment-parameters during the bachelor thesis. Therefore first the drift-scan with module three will be discussed.

For normal tracks with slopes around zero, the centroid-tracking-method reconstructs widths of about 300 µm similar to the single layer reconstruction. This is anticipated as for normal tracks the width is mainly determined by the reference-accuracy and the transverse-diffusion. The width for inclined tracks is more narrow than for single layers. The inhomogeneous ionization is compensated by the combination of multiple layers. Using the strip-track-points the intercept is reconstructed for almost all inclinations with same accuracy of about 350 µm. The worse resolution for normal tracks, compared to the centroid-tracking-method, is caused by the distribution of the charge over several strips. The strip-track-points take the charge less into account than the centroid. Therefore the mean shows a larger fluctuation.

For both methods the intercept-difference-width shows no dependence on the drift-voltage. The strip-track-point-reconstruction shows a worse slope-resolution for normal tracks, but a considerably improved resolution for inclined tracks, compared to the centroid-tracking-method. The charges for normal tracks are distributed due to the diffusion over several strips. Therefore the track-points are ill-defined, as they are scattered perpendicular around the track in the four layers. Whereas for inclined tracks the strip-track-points receive distinctive positions in and perpendicular to the active area by the drift-time-measurement.

This is also the reason for the improving resolution for lower drift-voltages. The time-points and so the position in the drift-gap can be reconstructed with higher accuracy, as the time difference increases for lower fields.

Besides the worse resolution, compared to the drift-scan with module three, the gas-study with module eight shows no mayor differences between the three gas-mixtures. The differences between the measurements for the intercept-reconstruction arises due to different alignment-parameters. These are also causing the differences to measurements with module three.

The track reconstruction using the four adjacent layers of Micromegas quadruplet was investigated using two different approaches. The simple, but robust combination of the single-layer centroids yield for normal tracks slightly better resolutions than the strip-track-point reconstruction. The more elaborate strip-track-point method improves the resolution for inclined tracks by using the drift-time-measurement. The combination of the four layers reduced the sensitivity to strongly deviating measurements of single strips compared to the common µTPC-method.

centroid strip-track-points

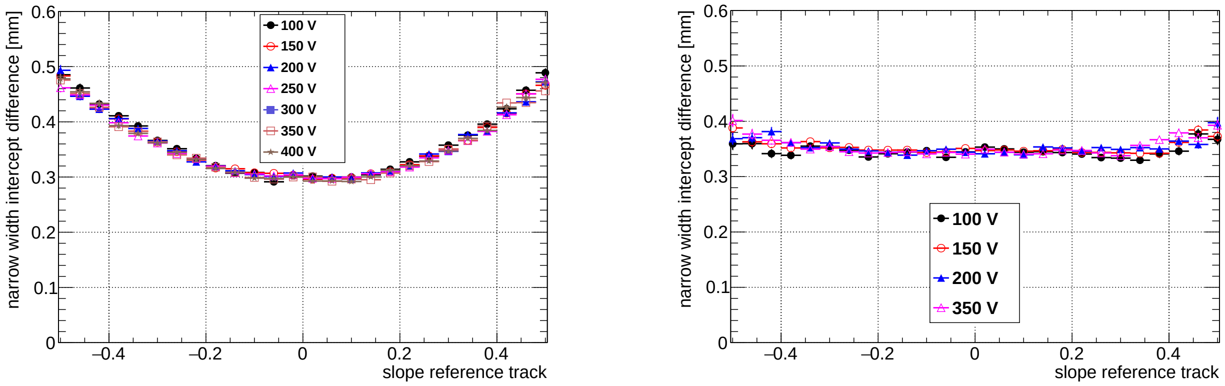

(a) Module three, drift-scan, intercept-resolution.

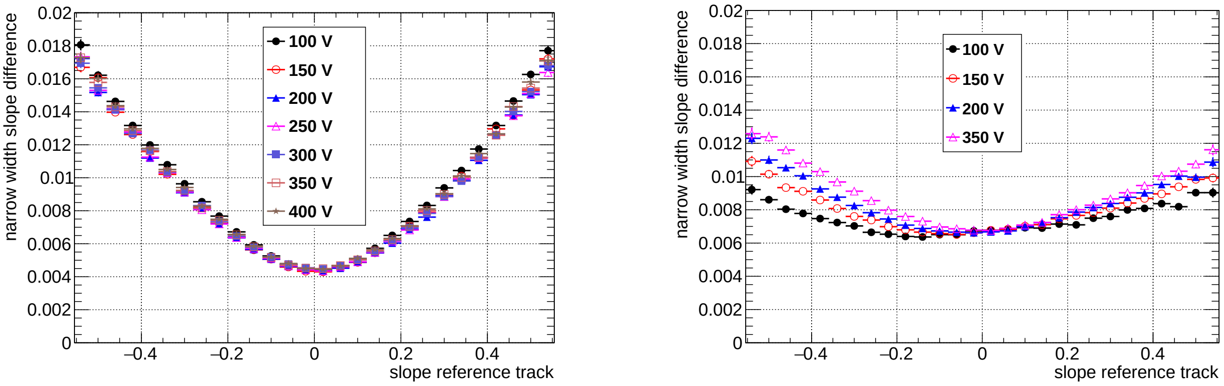

(b) Module three, drift-scan, track-slope-resolution.

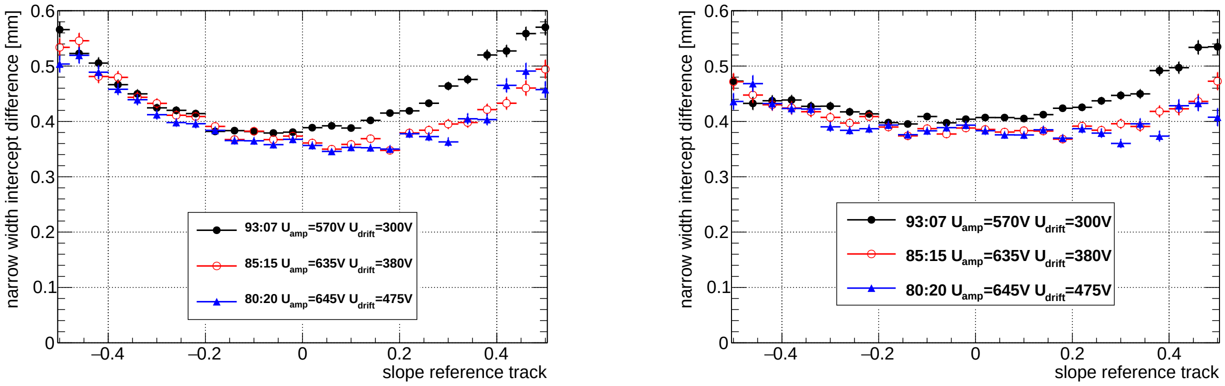

(c) Module eight, gas-study, intercept-resolution.

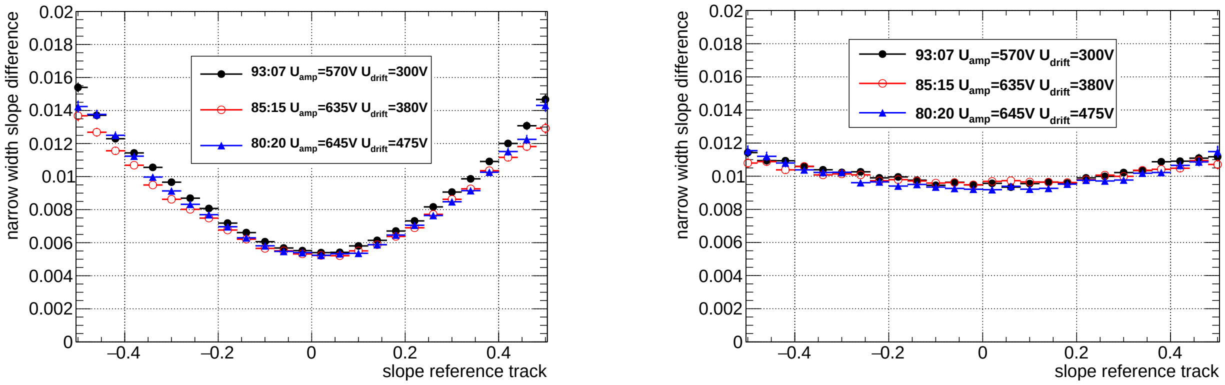

(d) Module eight, gas-study, slope-resolution.

Figure 7.30.: Resolution of the track reconstruction by combination of the four layers. Two approaches are investigated for the drift-scan of module three and the gas-study with module eight. Either the centroids of the clusters are considered as single track-points or the track is reconstructed using each strip-information individually. The intercept difference to the reference-track-prediction is calculated within the module. Also the difference of the reconstructed slope to the reference is shown. For the strip-track-point reconstruction of module eight wrong alignment-parameters were used.

8. Conclusion

The ongoing upgrades of the LHC will increase its luminosity above ten times the design value in the next years. Simultaneously the background hit-rate in the various experiments around the accelerator will be enhanced. This leads to a decrease of efficiency for current detector-systems. In order to cope with the aggravated conditions new detector technologies have to be used. For the inner end-caps of the ATLAS muon-spectrometer a redundant system of in total 16 active layers of sTGC and Micromegas will be installed as New Small Wheels. While the sTGC are foreseen primarily for triggering, the Micromegas will be used as precision tracker. Both detectors are currently under construction as four-layered modules with active areas of $2\,\mathrm{m}^2$ to $3\,\mathrm{m}^2$. This thesis describes the data quality and the calibration of one type of the Micromegas modules using cosmic muons. The considered type, called SM2, is built by a German collaboration. The final assembly and commissioning is performed in Garching, near Munich by a group of the LMU. Due to the large size the active area has a threefold segmentation. This requires the geometrical calibration.

Micromegas are gas detectors with a planar cathode and a planar micro-structured strip-anode. The gas volume is divided by the eponymous micro-mesh into a 5 mm drift-region and 120 µm amplification-region above the anode. The electrons released by MIPs in the drift-region are guided by electric field-lines through the micro-mesh. This is achieved by a moderate field of $0.6\,\frac{\mathrm{kV}}{\mathrm{cm}}$ in the drift-region and a high field of $47.5\,\frac{\mathrm{kV}}{\mathrm{cm}}$ in the amplification-region. The high field leads subsequently to electron avalanches towards the strip-anode. This anode consists of resistive strips at high voltage for field-generation and underneath copper readout strips. The track-position of the through-going particles can be reconstructed by the evaluation of the charge-signals on the readout strips. The reconstruction is achieved perpendicularly to the strips.

For the construction of the Micromegas modules the electrodes are built on flat panel surfaces. To achieve the required planarity, the collaboration developed the construction by a two-step gluing process using flat granite-tables. A dedicated procedure for the alignment of the threefold anode has to be performed also. The alignment between multiple layers is guaranteed by a system of distance pieces assembled into the panels.

The modules built in Garching are investigated using tracks of cosmic muons referenced by the Cosmic Ray Facility. The CRF consists of two MDT chambers for precision tracking within one plane. Triggering and a coarse track-information in the perpendicular plane is achieved by two layers of segmented scintillator-hodoscopes. The Micromegas modules are installed between these systems to interpolate the tracks into the active volumes. The tracks of the CRF are investigated for their systematics. The mean differences of the interpolated tracks between the two chambers show fluctuations of less than 20 µm. A slight inclination of 0.01° is reconstructed between the chambers. The influence of multiple scattering on the track-resolution is used for muon tomography. Using two weeks of data-taking the material distribution of one module in the facility is reconstructed.

The readout-scheme for the more than 12000 channels of a module with APV25 electronics is described. Online preprocessing of the data is implemented to reduce the storage-consumption. This enabled the data-taking at the CRF with a rate up to 100 Hz. After measurements the data have to be merged and further processed. More than a year of data-taking with this setup achieved more than 50 million coincidence events, considered for the central area of two layers. This can be seen in the integrated counts shown in figure 8.1.

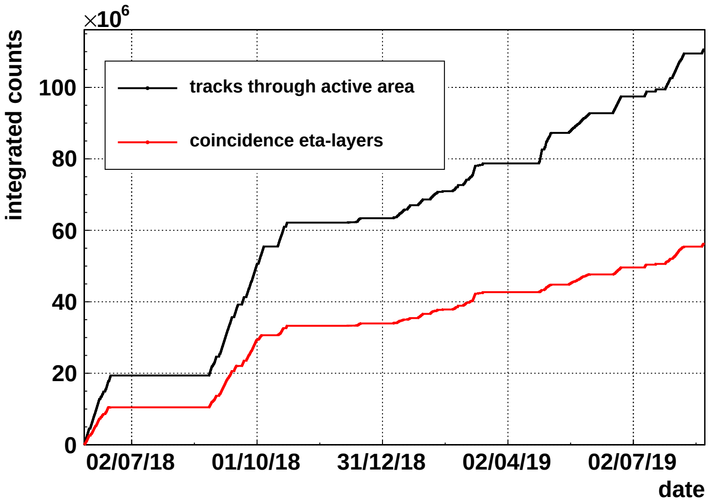

Figure 8.1.: Integrated recorded events with tracks reconstructed going through the active area of the Micromegas modules. As active area only the central part is considered of about 96 cm × 78 cm. This limitation is made to avoid systematic effects at the borders. The efficiency is lowered due to the integration over all measurements with different amplification-voltages.

For the characterization of a Micromegas module the two main aspects are the efficiency and the resolution. The efficiency is strongly influenced by the detector noise and problematic channels. Therefore two approaches for the determination of bad channels are investigated. In a first attempt the charge baseline-variation is used for an estimation. Due to the large overall noise-level this approach fails. Problematic channels can be identified in cosmic data by their response behavior. A scheme to account for the inhomogeneous illumination due to the angular acceptance of the facility is developed. The efficiency is further affected by the signal-height. The increase of signal-height with larger applied voltages is described by the Townsend-avalanches. The variation of the amplification-gap-height due to fluctuations during anode production is seen as different signal-heights across the active areas. For three detector-gas-mixtures of argon and carbon dioxide the effect of the signal-height on the efficiency is investigated. The expected exponential increase of the signal-height as function of the amplification-voltage is observed for all mixtures. Using the nominal mixture of 93:7 volume percent, efficiencies slightly above 90% on areas of about $32\,\mathrm{cm} \times 18\,\mathrm{cm}$ are reconstructed at a voltage of 570 V. Almost the same signal-height and efficiency is reached for 85:15 at 610 V and for 80:20 at 640 V. Despite this the detector-voltage could be increased further only for the two latter mixtures without discharge in the detector. An explanation for this is the capture of UV-photons by the higher fraction of CO_2. More than 96% efficiency is reached for 85:15 at 635 V and for 80:20 at 665 V. A linear dependence of pulse-height with the amplification-gap-height is observed for all three mixtures. The dependence is 6 %/µm for the mean value and about 10 %/µm for the most probable value of the signal-height. The effect of noise on the efficiency is investigated. In order to reach 90% efficiency the baseline-variation has not to exceed 2% of the most probable cluster-charge for this setup.

Before the resolution can be investigated the segment-alignment has to be evaluated. This is done using two techniques. A visual-inspection is done by the combination of a coordinate measuring machine and a camera. The machine inaccuracies are measured using a laser-interferometer. Periodicities of 2 cm and 10 cm are reconstructed due to mechanical imperfections. Also the bending of the support structure is considered for a correction-scheme of the deviations. The images of precision markers at the edges of the readout-structures taken by the camera are evaluated. Therefore template matching and edge detection functions implemented by the OpenCV framework for C++ are used. The combination of CMM and camera enabled the reconstruction of the positions of the markers. In a first iteration an accuracy of about 8 µm is achieved. Due to additional modifications of the CMM, as well as deformation effects due to longer wait-times, in a second iteration the accuracy is degraded to about 18 µm. The mean variations do not correspond to the calibration-values of the CMM, therefore a straight forward correction-scheme cannot be applied.

The second investigated technique for the alignment reconstruction uses the deviations to muon tracks. The track-interpolation is compared to the hit reconstruction in one layer. The reconstruction of deviations to the nominal pattern is achieved by partitioning of the active area. Deviations of the strip-distance are investigated, as well as rotations and shifts between the segments of the active layers. A calibration of these effects enabled the improvement of the Micromegas alignment homogeneity by about 29%. An undesired U-like deformation of the strip-shape is found for multiple segments due to the susceptibility of the support material to humidity. This aggravates the comparison of the two techniques as an extrapolation is required. Still similar deviations are reconstructed in an exemplaric discussion for two modules between and within the active layers. The rotation of two segments are reconstructed in both measurements separately to other parts of the detector. Also the rotation of whole layers with respect to each other could be disentangled on a level of $100\,\frac{\mu\mathrm{m}}{\mathrm{m}}$. Within the active area the deviations reconstructed by the cosmic-measurements are commonly larger than by the visual-inspection. As the cosmic-reconstruction features the investigation of the whole active area this is the preferred technique.

For the investigation of the resolution several reconstruction methods have been used. Also the track-accuracy of the reference has to be considered for this. A simple charge weighted approach enables resolutions of about 100 µm for normal tracks. Due to the inhomogeneous ionization of the muons in the drift-gap this resolution declines to about 520 µm for 25° inclined tracks. The effects on the resolution of bad mechanical alignment with respect to the reference system are investigated.

To account for the worsening of the resolution for inclined tracks the signal-time-reconstruction is used. The time difference between the signals on adjacent strips corresponds to the drift of the electrons after ionization. Therefore the signals of the copper readout strips are evaluated with a Fermi-function-like fit. Two aspects of this evaluation are further investigated. The correction for capacitive-coupling between signals on neighboring strips affects the signal-time-distribution. Also the evaluation-points of the fit are investigated for their track reconstruction capabilities. Using the width of the strip time distribution the drift-velocity is reconstructed. Therefore an artificially smaller drift-gap-size has to be introduced in the analysis.

Using the strip times the muon track can be reconstructed in a single drift-gap in a TPC-like fashion. This enables the reconstruction of the track angle. The correction for capacitive-coupling drastically improves this reconstruction. Angular-resolutions better than 10° are obtained averaged over the whole active area. Using a fixed timing for the evaluation of the track-fit improved the position-resolution for tracks inclined more than 15°. In an alternative approach the charge and the time-information is combined to reconstruct the deviations due to the inhomogeneous ionization. This improved the resolution for 25° inclined tracks to about 340 µm.

Two of the four layers have a foreseen slight, contrary rotation with respect to the other two strip-layer. This enables the reconstruction of the position along the parallel strip-layers. The effects of the three-dimensional track-inclinations on this reconstruction is investigated. A correction-scheme revealed systematic biases of the reference tracks in non-precision-direction. These systematics correspond to a shift of the center of about 5.5 cm and a scale-deviation of about 2%.

The combination of multiple Micromegas layers enables the full track reconstruction along about 5 cm. Therefore each strip-signal reconstructs an individual track-point using the drift-time-measurement and the knowledge of the drift-gap-center-position. A Hough-transformation is used for the rejection of false track-points. The reconstructed tracks are improved compared to a simple approach using only the charge weighted positions.

Several obstacles were found during the investigations of the $2\,\mathrm{m}^2$, four-layered Micromegas modules. The large size leads to inhomogeneities in pulse-height and alignment. Also the overall high noise-level introduces problems concerning reconstructions and reproducibility. Despite this an improving effect of larger fractions of CO_2 in the argon-based gas-mixture is found for the pulse-height and efficiency behavior. Using two very different approaches the alignment is reconstructed for the four layers over the whole active area. Improved track reconstruction techniques are implemented for a better resolution-performance. Therefore the cosmic-measurements of the modules in Garching enables a full calibration.

> *Wonder had gone away, and he had forgotten that all life is only a set of pictures in the brain, among which there is no difference betwixt those born of real things and those born of inward dreaming, and no cause to value the one above the other.*
>
> - Howard Philipps Lovecraft , 1926 , *The Silver Key*

A. Signal Processing and Eventdisplays

Before the signal-fit can be performed the raw APV-data has to be preprocessed. This is seen for an exemplaric event measured at the H8 testbeam in figures A.1 and A.2.

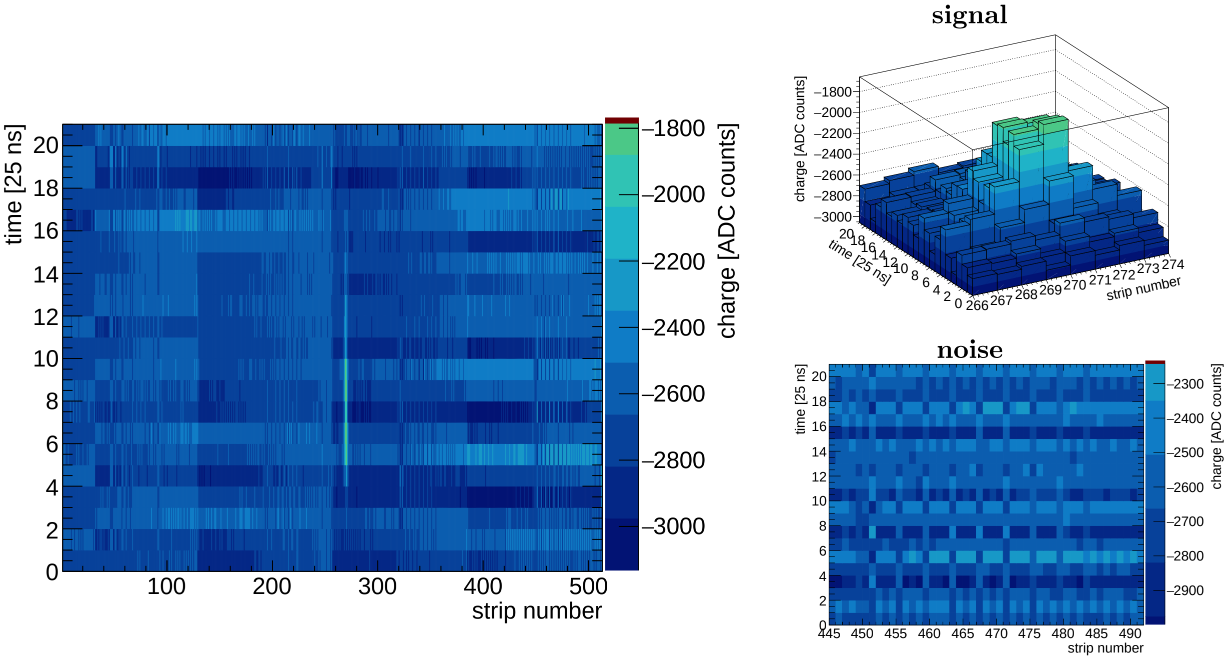

Figure A.1.: Eventdisplay before offset correction and zerosuppression.

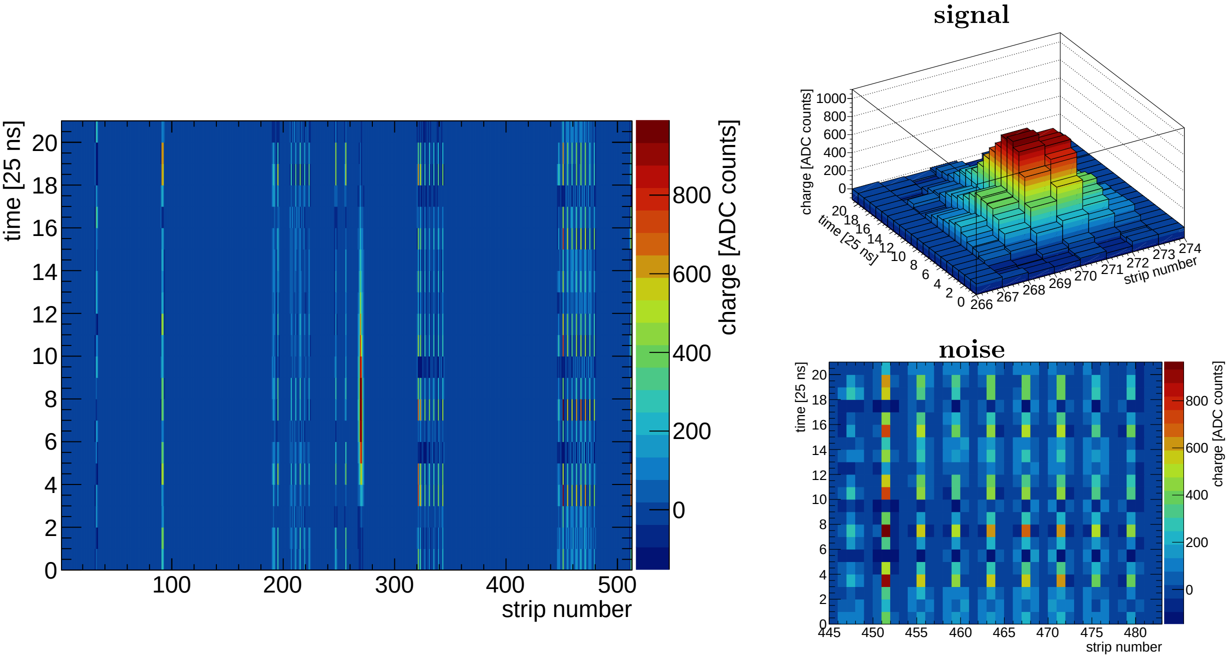

Figure A.2.: Eventdisplay after offset correction and zerosuppression.

B. Measurements Overview

B.1. Investigation Points during the H8 Beamtime of Module Zero

Module zero was investigated at several positions across the active area during the test-beam in August 2017. The spots are marked without scale in figure B.1.

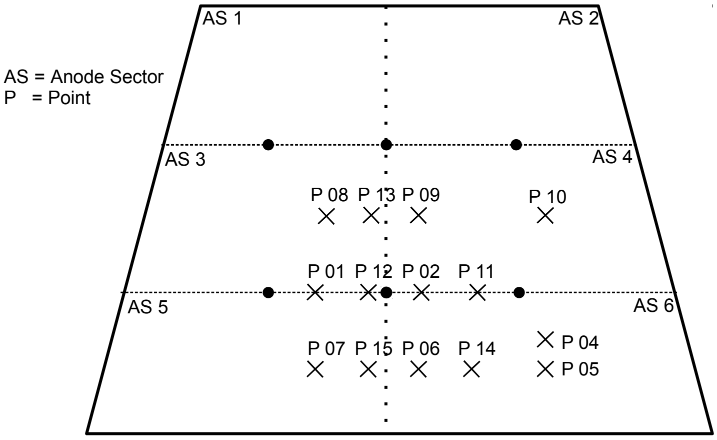

(a) Stereo-panel facing the beam.

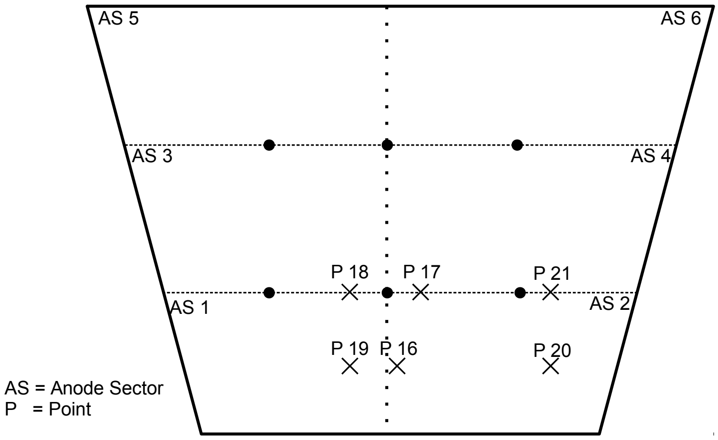

(b) Eta-panel facing the beam.

Figure B.1.: During the H8 beamtime of module zero several positions were investigated. The module was also flipped to investigate parts of the small board (6).

B.2. Module 8 Gas Study

Ar:CO$_2$ 93:7 vol%				Ar:CO$_2$ 85:15 vol%				Ar:CO$_2$ 80:20 vol%			
date	trig.	U_{amp}	U_{drift}	date	trig.	U_{amp}	U_{drift}	date	trig.	U_{amp}	U_{drift}
	10^6	[V]	[V]		10^6	[V]	[V]		10^6	[V]	[V]
28.05.	4.8	570	300	16.05.	4.9	620	300	23.05.	3.2	640	475
29.05.	3.8	560	300	17.05.	3.9	625	300	24.05.	2.8	645	475
30.05.	2.2	570	300	17.05.	3.9	630	300	24.05.	4.0	650	475
30.05.	2.4	550	300	18.05.	4.7	635	300	25.05.	1.9	655	475
30.05.	2.9	540	300	19.05.	5.3	615	300	25.05.	3.7	660	475
31.05.	2.8	530	300	20.05.	1.8	610	300	26.05.	1.9	665	475
31.05.	n.a.	520	300	20.05.	5.4	580	300	26.05.	2.4	600	475
				21.05.	3.4	620	380	27.05.	2.7	610	475
				22.05.	2.5	635	380				
				22.05.	2.8	635	450				

B.3. Pillar-Heights for Module 8 and Eta 3

layer	board	mean [µm]	std. dev. [µm]
M8 eta-out	6	120.3	1.9
(=L1)	7	120.1	1.9
	8	120.3	2.3
M8 eta-in	6	120.6	3.1
(=L2)	7	121.1	1.6
	8	120.6	2.6
M8 stereo-in	6	121.6	3.0
(=L3)	7	122.2	1.6
	8	123.0	2.5
M8 stereo-out	6	121.5	2.5
(=L4)	7	122.2	2.2
	8	122.3	3.8
eta3 top	6	113.9	1.5
(=gs1)	7	117.7	3.3
	8	116.2	2.3
eta3 bot	6	114.7	2.1
(=gs2)	7	116.8	4.0
	8	115.7	2.6

C. Coordinate Transformation

For a Cartesian coordinate transformation a shift $\vec{s}$ and a rotation $\boldsymbol{R}$ has to be applied to the position vector $\vec{p}$. Depending on the definition of the two coordinate-systems one is applied before the other. The evaluation of the Micromegas-data (MM) in the CRF uses the following convention:

$$\vec{p}_{\mathrm{CRF}} = \vec{s} + \boldsymbol{R}\ \vec{p}_{\mathrm{MM}}\ . \tag{C.1}$$

The rotation-matrix is defined using the angles α_{x}, α_{y} and α_{z} as

$$\begin{aligned}
\boldsymbol{R} = &\qquad \boldsymbol{R}_{\mathrm{x}}(\alpha_{\mathrm{x}}) \qquad\cdot\qquad \boldsymbol{R}_{\mathrm{y}}(\alpha_{\mathrm{y}}) \qquad\cdot\qquad \boldsymbol{R}_{\mathrm{z}}(\alpha_{\mathrm{z}}) \\
= &\begin{pmatrix} 1 & 0 & 0 \\ 0 & \cos\alpha_{\mathrm{x}} & \sin\alpha_{\mathrm{x}} \\ 0 & -\sin\alpha_{\mathrm{x}} & \cos\alpha_{\mathrm{x}} \end{pmatrix}
\begin{pmatrix} \cos\alpha_{\mathrm{y}} & 0 & -\sin\alpha_{\mathrm{y}} \\ 0 & 1 & 0 \\ \sin\alpha_{\mathrm{y}} & 0 & \cos\alpha_{\mathrm{y}} \end{pmatrix}
\begin{pmatrix} \cos\alpha_{\mathrm{z}} & \sin\alpha_{\mathrm{z}} & 0 \\ -\sin\alpha_{\mathrm{z}} & \cos\alpha_{\mathrm{z}} & 0 \\ 0 & 0 & 1 \end{pmatrix} \\
= &\begin{pmatrix}
\cos\alpha_{\mathrm{y}}\cos\alpha_{\mathrm{x}} & \cos\alpha_{\mathrm{y}}\sin\alpha_{\mathrm{z}} & -\sin\alpha_{\mathrm{y}} \\
\sin\alpha_{\mathrm{x}}\sin\alpha_{\mathrm{y}}\cos\alpha_{\mathrm{z}} - \cos\alpha_{\mathrm{x}}\sin\alpha_{\mathrm{z}} & \sin\alpha_{\mathrm{x}}\sin\alpha_{\mathrm{y}}\sin\alpha_{\mathrm{z}} + \cos\alpha_{\mathrm{x}}\cos\alpha_{\mathrm{z}} & \sin\alpha_{\mathrm{x}}\cos\alpha_{\mathrm{y}} \\
\cos\alpha_{\mathrm{x}}\sin\alpha_{\mathrm{y}}\cos\alpha_{\mathrm{z}} + \sin\alpha_{\mathrm{x}}\sin\alpha_{\mathrm{z}} & \cos\alpha_{\mathrm{x}}\sin\alpha_{\mathrm{y}}\sin\alpha_{\mathrm{z}} - \sin\alpha_{\mathrm{x}}\cos\alpha_{\mathrm{z}} & \cos\alpha_{\mathrm{x}}\cos\alpha_{\mathrm{y}}
\end{pmatrix} .
\end{aligned} \tag{C.2}$$

The intersection of the CRF-track, defined by the slopes m_x , m_y and the intercepts t_x , t_y, with the Micromegas active-area is calculated using:

$$\boldsymbol{R}_3 \cdot \left(\vec{s} - \vec{l}(z)\right) \overset{!}{=} 0 \tag{C.3}$$

Here $\vec{s}$ is the center position of the Micromegas in the CRF-system, $\boldsymbol{R}_3$ is the third row-vector of the above defined rotation-matrix. The track-intersection-vector $\vec{l}(z)$ is depending on the z-position, which has to be determined, and on the track-parameter:

$$\begin{aligned}
\vec{l}(z) &= \quad \vec{t} \quad + \quad \vec{m} \quad \cdot z \\
&= \begin{pmatrix} t_x \\ t_y \\ 0 \end{pmatrix} + \begin{pmatrix} m_x \\ m_y \\ 1 \end{pmatrix} \cdot z\ .
\end{aligned} \tag{C.4}$$

Equation C.3 corresponds to the line-intersection formula for the x-y-plane of the Micromegas-system, as the third row-vector of the rotation-matrix is perpendicular to this plane. The intersection point is determined by solving this equation for z.

$$z = \sum_{c=1}^{3} k_c \Bigg/ \sum_{c=1}^{3} n_c \tag{C.5}$$

where k_c and n_c are given by:

$$\begin{aligned}
k_c &= \boldsymbol{R}_{3,c} \cdot (\vec{s}_c - \vec{t}_c) \\
n_c &= \boldsymbol{R}_{3,c} \cdot \vec{m}_c
\end{aligned}$$

with $c \in \{1, 2, 3\}$.

D. Dimensions of Readout-Panels

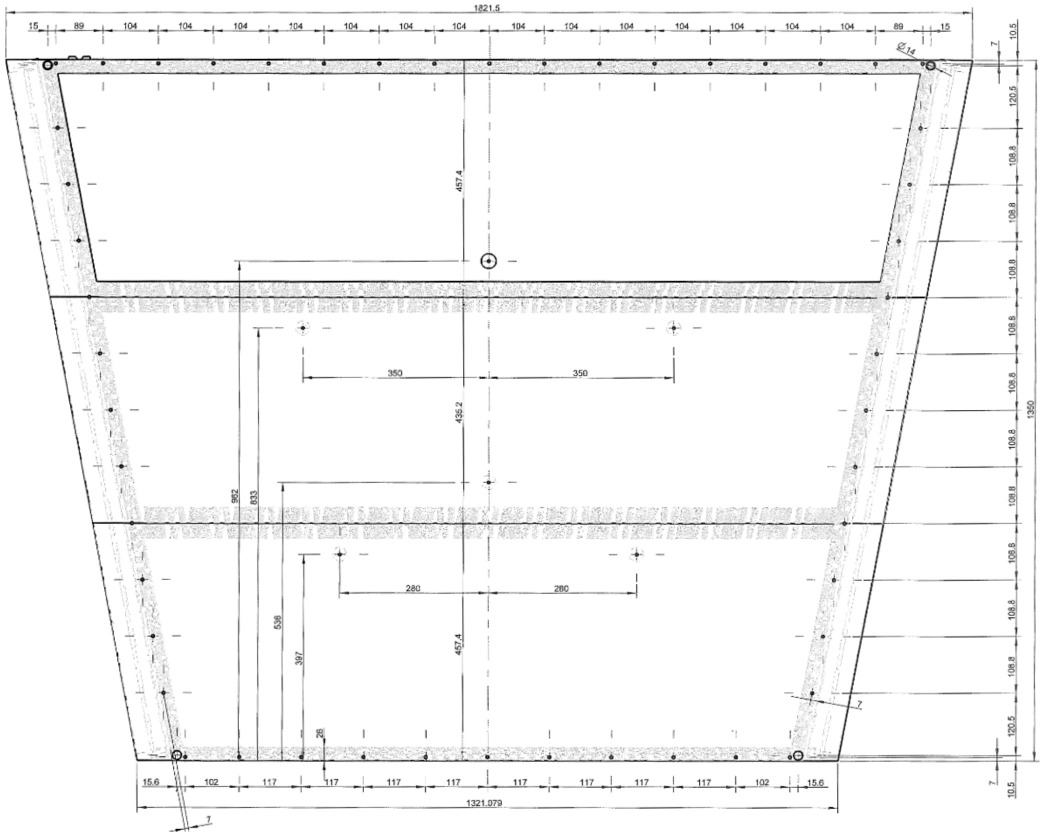

(a) Precision-direction.

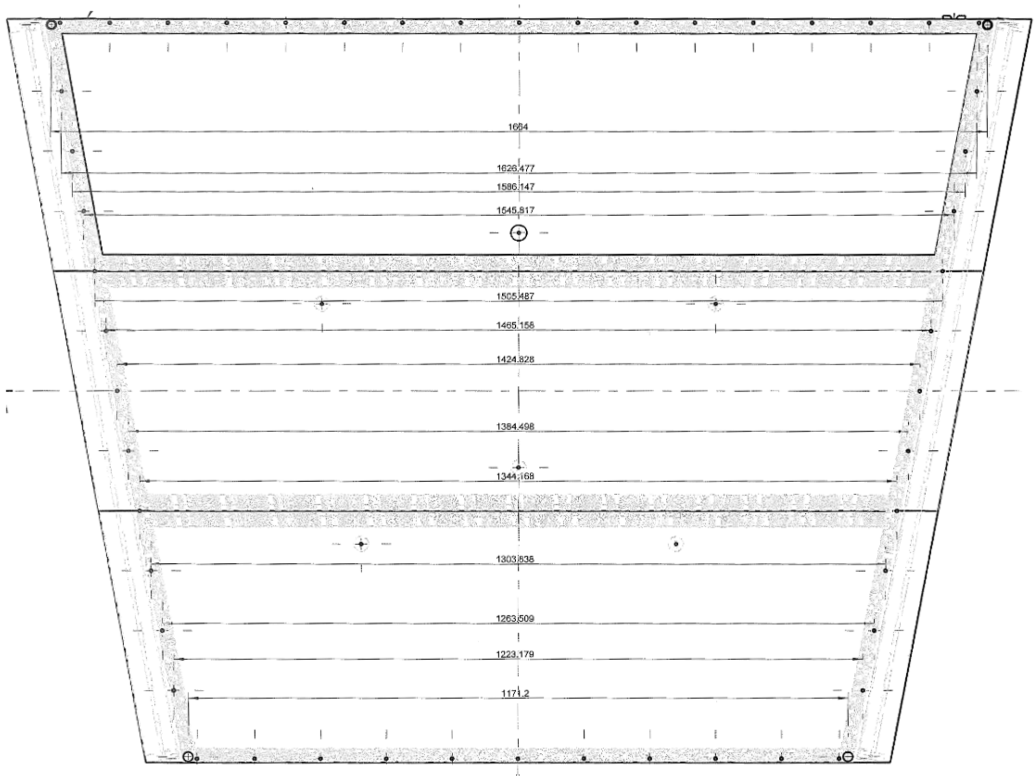

(b) Non-precision-direction.

Figure D.1.: Dimensions of a readout-panel and distances of the precision marker.

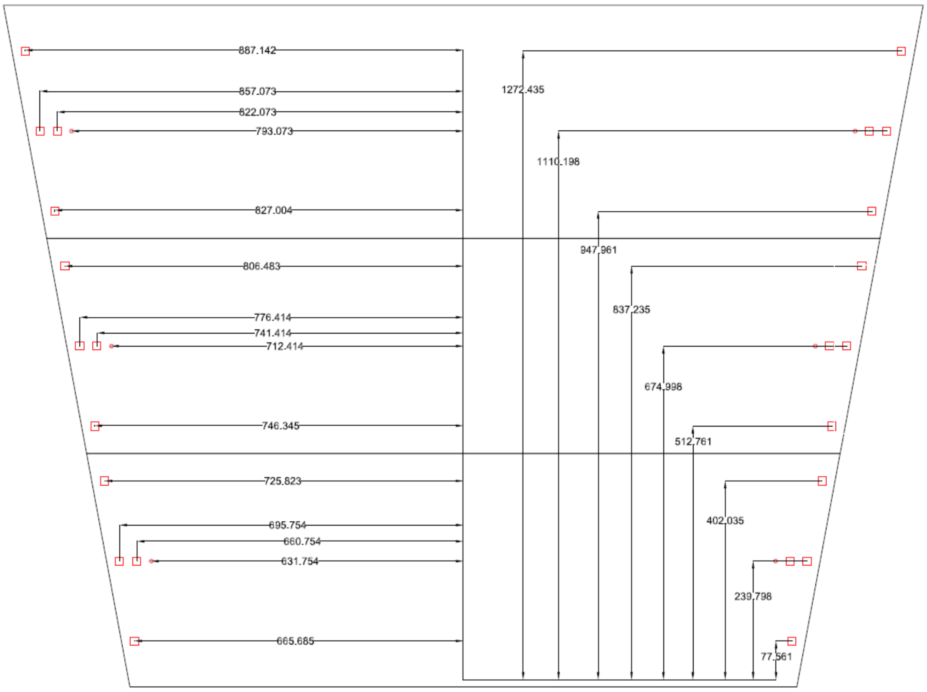

Figure D.2.: Positions of the Rasmasks on the readout-panel.

E. Eta-Panels Alignment Reconstruction

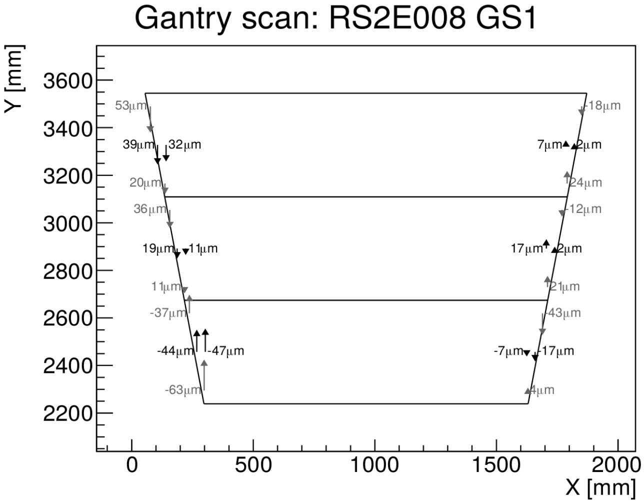

(a) Gantry scan gluing side one.

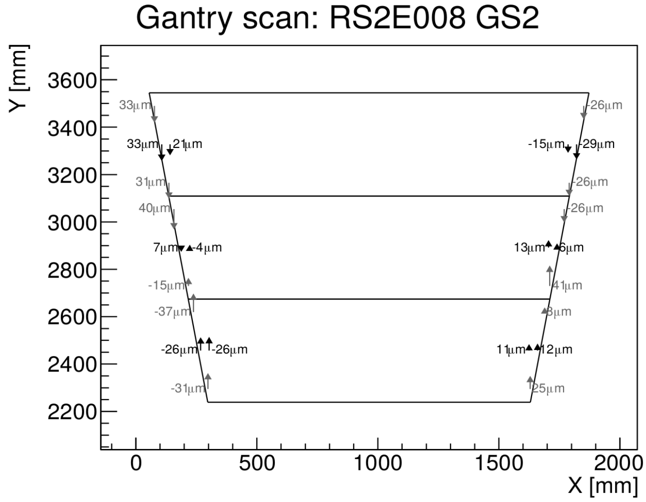

(b) Gantry scan gluing side two.

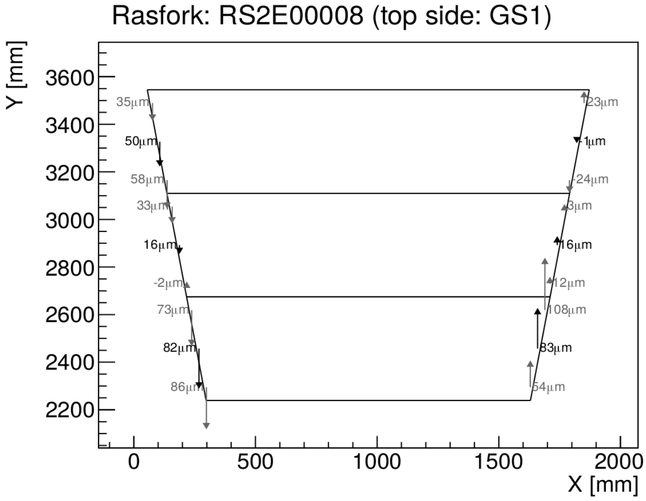

(c) Rasfork measurement gluing side one on top.

Figure E.1.: Reconstructed alignment of the eta-panel eight using measurements of the Rasmasks performed at Saclay.

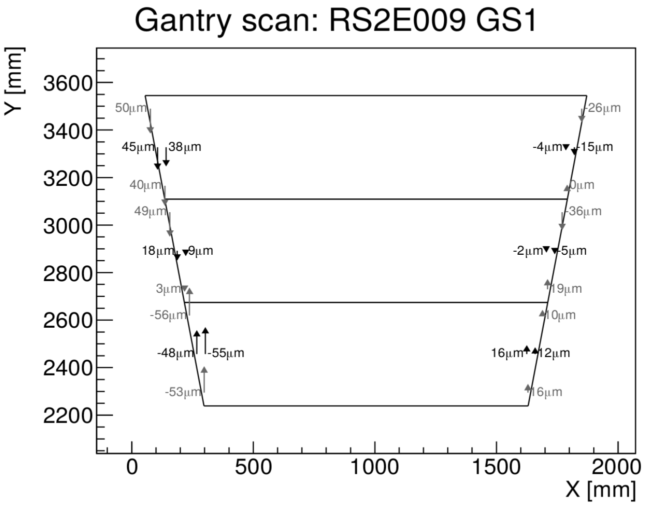

(a) Gantry scan gluing side one.

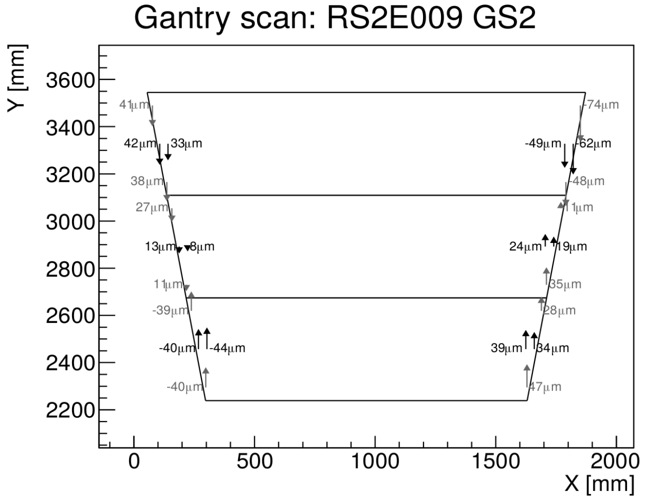

(b) Gantry scan gluing side two.

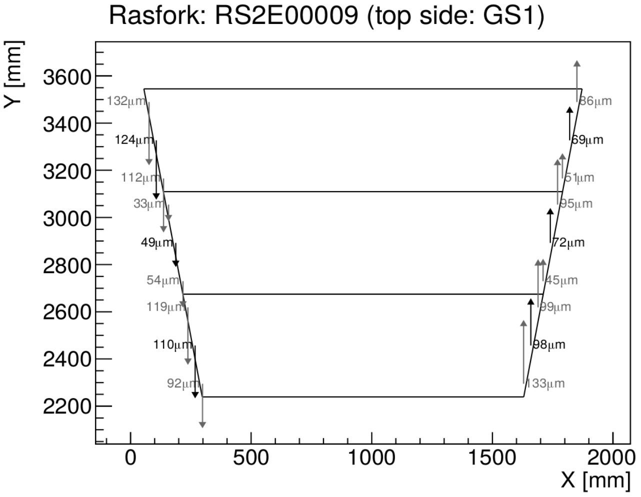

(c) Rasfork measurement gluing side one on top.

Figure E.2.: Reconstructed alignment of the eta-panel nine using measurements of the Rasmasks performed at Saclay.

F. Interpolation of Laser-Interferometer Deviation-Measurements

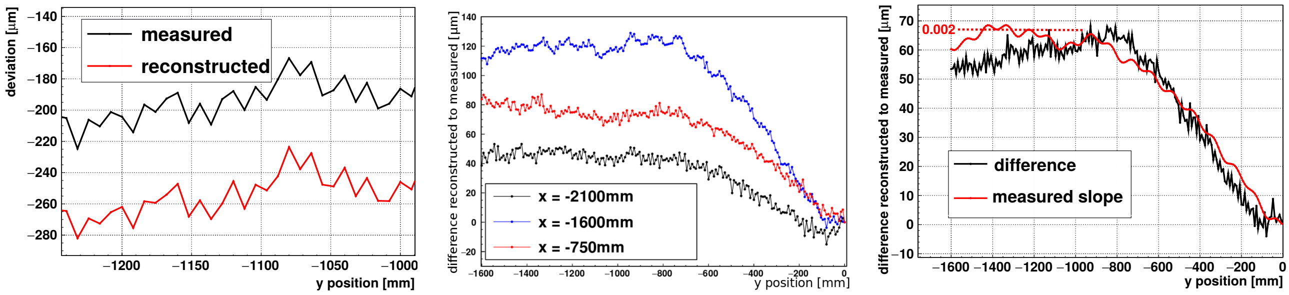

(a) Detail of the measured and reconstructed deviations of the CMM movement along the precision-direction (y). The reconstruction is achieved by the interpolation of two measurements at the legs of the CMM-bridge.

(b) Differences of the reconstructed and measured CMM-movement-deviations. Three positions along the non-precision-direction (x), so along the bridge are investigated.

(c) Differences of the reconstructed and measured CMM-movement-deviations. Overlayed is the reconstructed slope of the measurement-arm, which is caused by tilting.

Figure F.1.: Differences between measurements in precision-direction (y) are seen for different positions in the non-precision-direction (x). This is due to the unequal movement of the CMM-bridge on the two rails at the sides of the granite-table. Measurements at the borders can be interpolated to account for this effect. This enables the reconstruction of the fine-structure of the deviations. Large differences between measured and reconstructed deviations are coming from an additional tilt of the measurement-arm. Taken from [Feil, 2017].

G. Reconstructed Alignment Parameters

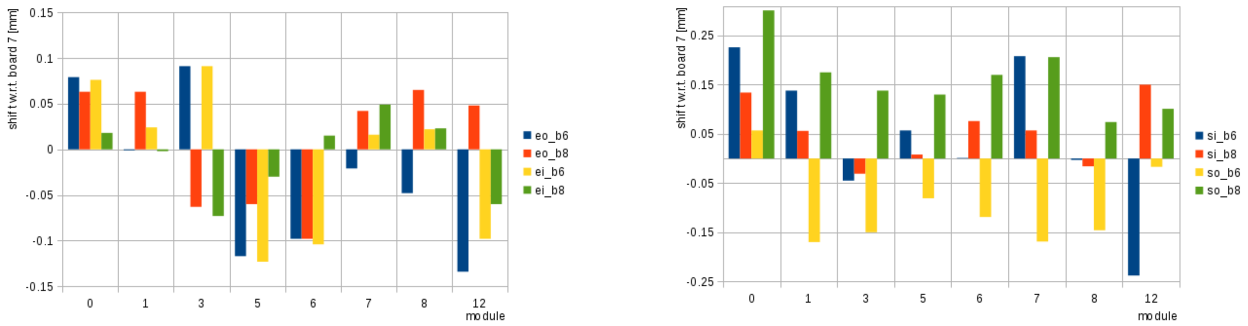

(a) Shifts of the eta-boards (6) and (8) with respect to the central board (7).

(b) Shifts of the stereo-boards (6) and (8) with respect to the central board (7).

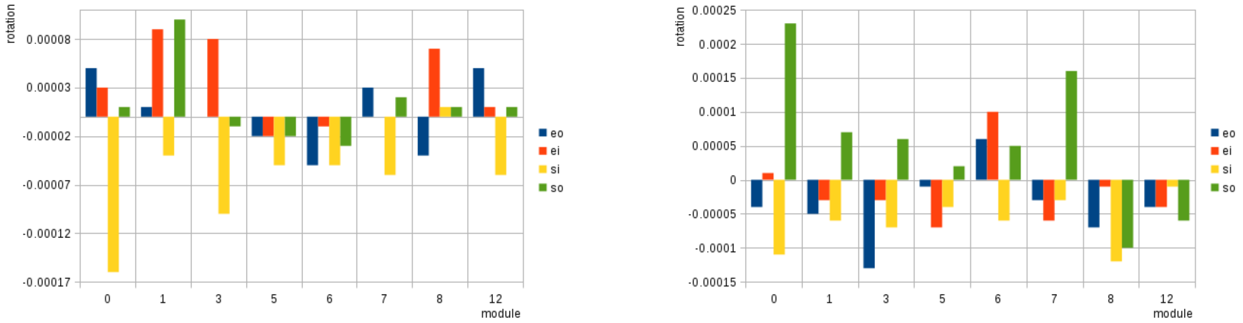

(c) Rotations of the small board (6) with respect to the central board (7).

(d) Rotations of the large board (8) with respect to the central board (7).

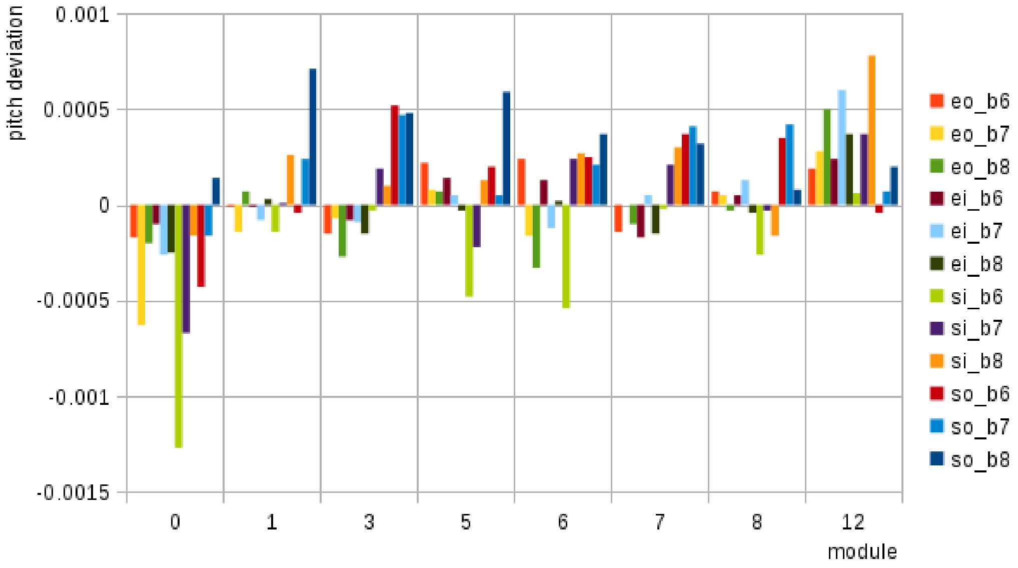

(e) Deviation to the nominal pitch per board.

Figure G.1.: Reconstructed alignment-parameter for the first measured modules. The reconstruction is performed according to chapter 6.2. The colors disentangle the reconstruction for the four layers eta-out [=eo], eta-in [=ei], stereo-in [=si] and stereo-out [=so]. Shifts and rotations of the small boards (6) [=b6] and the large boards (8) [=b8] are considered with respect to the central board (7) [=b7]. The pitch-deviations are considered as fraction to the nominal pitch for eta-layers of 0.425 mm and for the stereo-layers of 0.424 85 mm.

Abbreviations

ADC	Analog-to-Digital Converter
APV25	Analogue Pipeline ASIC, designed for read-out of silicone strip detectors
ASIC	Application-Specific Integrated Circuit
ATLAS	A Toroidal LHC ApparatuS, one of the two multi-purpose experiments at the LHC
CERN	Conseil Européen pour la Recherche Nuclèaire, European Organization for Nuclear Research
CMM	Coordinate Measuring Machine
CRF	Cosmic Ray Facility
FEC	Front-end-Concentrator card
FWHM	Full-Width-Half-Maximum
HDMI	High Definition Multimedia Interface
LHC	Large Hadron Collider, proton accelerator located at CERN
LMU	Ludwig-Maximilians Universität in Munich, Germany
MDT	Monitored Drift Tube, muon tracking system used by ATLAS
Micromegas	Micromesh Gaseous Structure
MIP	Minimum Ionizing Particle
MPV	Most Probable Value
NSW	New Small Wheel, upgrade of the ATLAS muon-spectrometer inner end-caps
PCB	Printed Circuit Board
SM2	Moduletype of Micromegas quadruplets built in Germany for the NSW
SPS	Super Proton Synchroton, proton accelerator located at CERN
sTGC	small-Strip Thin Gap Chamber, detector technology used for the NSW
TDC	Time-to-Digital Converter
TPC	Time-Projection-Chamber
µTPC	TPC-like reconstruction method used for inclined incident

Bibliography

[Adloff et al., 2009] Adloff, C., Attie, D., Blaha, J., Cap, S., Chefdeville, M., Colas, P., Dalmaz, A., C.Drancourt, A., Espargiliere, Gaglione, R., Gallet, R., Geffroy, N., Giomataris, I., J.Jaquemier, Karyotakis, Y., Peltier, F., Prast, J., and Vouters, G. (2009). MICROMEGAS chambers for hadronic calorimetry at a future linear collider, 2009.

[Alexopoulos et al., 2015] Alexopoulos, T., Amelung, C., Iakovidis, G., Leontsinis, S., Ntekasa, K., Palestini, S., Polychronakos, V., and Vlachos, S. (2015). Stereo information in micromegas detectors. *CERN*. `https://cds.cern.ch/record/2052206/files/ATL-MUON-PUB-2015-001.pdf` [accessed 04-July-2019].

[ANSYS, Inc., 2013] ANSYS, Inc. (2013). ANSYS Mechanical APDL Element Reference. `http://148.204.81.206/Ansys/150/ANSYS%20Mechanical%20APDL%20Element%20Reference.pdf` [accessed 05-July-2016].

[ATLAS Collaboration, 2008] ATLAS Collaboration (2008). The ATLAS Experiment at the CERN Large Hadron Collider. *JINST*, 3. `https://iopscience.iop.org/article/10.1088/1748-0221/3/08/S08003/pdf` [accessed 04-July-2019].

[ATLAS Collaboration, 2013] ATLAS Collaboration (2013). New Small Wheel Technical Design Report. Technical Report CERN-LHCC-2013-006. ATLAS-TDR-020, CERN. `http://cds.cern.ch/record/1552862/files/ATLAS-TDR-020.pdf` [accessed 04-July-2019].

[Bethe, 1930] Bethe, H. (1930). Zur Theorie des Durchgangs schneller Korpuskularstrahlen durch Materie. *Annalen der Physik*, 397(3):325–400. `https://onlinelibrary.wiley.com/doi/abs/10.1002/andp.19303970303` [accessed 04-July-2019].

[Beyerer et al., 2016] Beyerer, J., León, F. P., and Frese, C. (2016). *Automatische Sichtprüfung: Grundlagen, Methoden und Praxis der Bildgewinnung und Bildauswertung*. Springer-Verlag.

[Biagi, 1995] Biagi, S. (1995). Magboltz - transport of electrons in gas mixtures. `http://magboltz.web.cern.ch/magboltz/` [accessed 26-July-2019].

[Biebel et al., 2003] Biebel, O., Binder, M., Boutemeur, M., Brandt, A., Dubbert, J., Duckeck, G., Elmsheuser, J., Fiedler, F., Hertenberger, R., Kortner, O., et al. (2003). A Cosmic Ray Measurement Facility for ATLAS Muon Chambers. *arXiv preprint physics/0307147*. `https://arxiv.org/pdf/physics/0307147.pdf` [accessed 04-July-2019].

[Bini et al., 2014] Bini, C., Giraud, J., Giraud, P.-F., Hertenberger, R., Iengo, P., .Iodice, M., Jeanneau, F., Lacava, F., Ponsot, P., Schune, P., and Vlachos, S. (2014). Micromegas Mechanical Tolerances. Technical report, CERN. `https://edms.cern.ch/ui/file/1400235/1/MM_Panel_Module_Mechanical_Requirements_v4_20140725.pdf` [accessed 17-September-2019].

[Bortfeldt, 2014] Bortfeldt, J. (2014). *Development of Floating Strip Micromegas Detectors*. PhD thesis, Ludwig-Maximilians Universität, München.

[Bortfeldt et al., 2016] Bortfeldt, J., Dubinin, F., Iengo, P., and Samarati, J. (2016). Expansion of Micromegas Readout PCBs. (Presentation for the NSW upgrade at CERN) `https://indico.cern.ch/event/585834/contributions/2359881/attachments/1373799/2086003/bortfeldt_ROPCBexpansion.pdf` [accessed 25-June-2019].

[Bradski, 2000] Bradski, G. (2000). The OpenCV Library. *Dr. Dobb's Journal of Software Tools*.

[Brun and Rademakers, 1997] Brun, R. and Rademakers, F. (1997). ROOT - An Object Oriented Data Analysis Framework. In *Proceedings AIHENP'96 Workshop*, pages 81–86, Lausanne. `https://root.cern.ch/` [accessed 23-July-2019].

[Brüning et al., 2004] Brüning, O. S., Collier, P., Lebrun, P., Myers, S., Ostojic, R., Poole, J., and Proudlock, P. (2004). *LHC Design Report*. CERN Yellow Reports: Monographs. CERN, Geneva. `http://cds.cern.ch/record/782076/files/CERN-2004-003-V1-ft.pdf`.

[Burnens et al., 2011] Burnens, J., de Oliveira1, R., Glonti, G., Pizzirusso1, O., Polychronakos, V., Sekhniaidze, G., and Wotschack, J. (2011). A spark-resistant bulk-Micromegas chamber for high-rate applications. *Nucl. Instrum. Meth.* `https://arxiv.org/pdf/1011.5370.pdf` [accessed 04-July-2019].

[CAEN, 2019] CAEN (2019). *SY4527 Universal Multichannel Power Supply*. `https://www.caen.it/products/sy4527/` [accessed 27-August-2019].

[Canny, 1986] Canny, J. (1986). A computational approach to edge detection. *IEEE Transactions on Pattern Analysis and Machine Intelligence*, PAMI-8(6):679–698.

[Caron, 1998] Caron, J.-L. (1998). Overall view of LHC experiments. Vue d'ensemble des experiences du LHC. AC Collection. Legacy of AC. Pictures from 1992 to 2002.

[De Geronimo et al., 2012] De Geronimo, G., Fried, J., Li, S., Metcalfe, J., Nambiar, N., Vernon, E., and Polychronakos, V. (2012). VMM1 - An ASIC for micropattern detectors. In *2012 IEEE Nuclear Science Symposium and Medical Imaging Conference Record (NSS/MIC)*, pages 633–639.

[Dekker et al., 1993] Dekker, H., Graaf, H. v. d., Groenstege, H., Linde, F., Sman, S., Steensma, R., Jongkind, B., and Smeulders, A. (1993). The RASNIK/CCD 3-Dimensional Alignment System. In *Proceedings, 3rd International Workshop on Accelerator Alignment (IWAA 93): Annecy, France, September 28-October 1, 1993*, volume C930928, page 017. `http://www.slac.stanford.edu/econf/C930928/papers/017.pdf` [accessed 23-July-2019].

[Feil, 2017] Feil, M. (2017). Calibration of a coordinate measuring machine for optical computer-aided surveying of microstructured anode surfaces. Bachelor thesis.

[Flierl, 2018] Flierl, B. (2018). *Particle Tracking with Micro-Pattern Gaseous Detectors.* PhD thesis, Ludwig-Maximilians Universität, München.

[Giomataris et al., 1996] Giomataris, Y., Rebourgeard, P., Robert, J. P., and Charpak, G. (1996). MICROMEGAS: a high-granularity position-sensitive gaseous detector for high particle-flux environments. *Nuclear Instruments and Methods in Physics Research, Section A*, 376:29–35.

[Giraud, 2016] Giraud, P.-F. (2016). The RASFORK tool for checking MM alignment quality. (Presentation for the NSW upgrade at CERN) `https://indico.cern.ch/event/638149/contributions/2585748/attachments/1456602/2248033/rasfork.pdf` [accessed 23-July-2019].

[Giraud, 2018] Giraud, P.-F. (2018). LM1 metrology. (Presentation for the NSW upgrade at CERN) `https://indico.cern.ch/event/737118/contributions/3041087/attachments/1671530/2681651/LM1.pdf` [accessed 20-August-2019].

[Groom et al., 2001] Groom, D. E., Mokhov, N. V., and Striganov, S. I. (2001). Muon Stopping Power and Range Tables 10 MeV - 100TeV. *Atomic Data and Nuclear Data Tables*, 78(2).

[Herrmann, 2019] Herrmann, M. (2019). Performance and Calibration of $2m^2$-sized 4-layered Micromegas Detectors for the ATLAS Upgrade. *PoS*, ICHEP2018:088. `http://inspirehep.net/record/1748403/files/PoS(ICHEP2018)088.pdf` [accessed 05-September-2019].

[Herrmann et al., 2017] Herrmann, M., Biebel, O., Flierl, B., Hertenberger, R., Klitzner, F., Lösel, P., Müller, R., Valderanis, C., and Zibell, A. (2017). Calibration of large area micromegas detectors using cosmic rays. *Journal of Instrumentation*, 12(06):C06013–C06013. `https://doi.org/10.1088%2F1748-0221%2F12%2F06%2Fc06013` [accessed 09-September-2019].

[Hertenberger, 2016] Hertenberger, R. (2016). Micromegas: Gaseous Micropattern Detectors. (Presentation during the Interdisciplinary Cluster Workshop: "Detectors and Instrumentation" in Garching) `https://indico.ph.tum.de/event/3598/attachments/2078/2212/Hertenberger.pdf` [accessed 11-September-2019].

[Hough, 1962] Hough, P. (1962). METHOD AND MEANS FOR RECOGNIZING COMPLEX PATTERNS. US Patent 3,069,654. `http://www.freepatentsonline.com/3069654.pdf` [accessed 28-July-2019].

[Jones, 2001] Jones, L. (2001). *APV25-S1 User Guide.* `http://cds.cern.ch/record/1069892/files/cer-002725643.pdf` [accessed 04-July-2019].

[Klitzner, 2019] Klitzner, F. (2019). *Development of Novel Two-Dimensional Floating Strip Micromegas Detectors with an In-depth Insight into the Strip Signal Formation* . PhD thesis, Ludwig-Maximilians Universität, München.

[Kortner, 2002] Kortner, O. (2002). *Schauerproduktion durch hochenergetische Myonen und Aufbau eines Höhenstrahlungsprüfstandes für hochauflösende ATLAS-Myonkammern.* PhD thesis, Ludwig-Maximilians Universität.

[Kotelnikov, 1933] Kotelnikov, V. A. (1933). On the transmission capacity of the ether and of cables in electrical communications. *Proceedings of the first All-Union Conference on the technological reconstruction of the communications sector and the development of low-current engineering.* `http://ict.open.ac.uk/classics/1.pdf` [accessed 21-July-2019].

[Kuger, 2017] Kuger, F. (2017). *Signal Formation Processes in Micromegas Detectors and Quality Control for large size Detector Construction for the ATLAS New Small Wheel.* PhD thesis, Julius-Maximilians-Universität, Würzburg.

[Lasertex, 2015] Lasertex (2015). *Laser Measurement System HPI-3D.*

[Lippert, 2012] Lippert, B. (2012). Studien zur Signalentstehung und Parametrisierung der Gasverstärkung in einem Micromegas-Detektor. Bachelor thesis.

[Lösel, 2013] Lösel, P. (2013). Performance Studies of Large Size Micromegas Detectors. Master's thesis, Ludwig-Maximilians Universität, München.

[Lösel, 2017] Lösel, P. (2017). *Precision Calibration of Large Area Micro Pattern Gaseous Detectors.* PhD thesis, Ludwig-Maximilians Universität, München.

[Lösel and Müller, 2015] Lösel, P. and Müller, R. (2015). Design and Construction of Large Size Micromegas Chambers for the Upgrade of the ATLAS Muon Spectrometer. *arXiv preprint arXiv:1508.02541.* `http://arxiv.org/pdf/1508.02541v1.pdf` [accessed 04-July-2019].

[Lynch and Dahl, 1991] Lynch, G. R. and Dahl, O. I. (1991). Approximations to multiple Coulomb scattering. *Nucl. Instrum. Meth.*, B58:6–10.

[Martoiu et al., 2013] Martoiu, S., Muller, H., Tarazona, A., and Toledo, J. (2013). Development of the scalable readout system for micro-pattern gas detectors and other applications. *Journal of Instrumentation*, 8(03):C03015–C03015. `https://doi.org/10.1088%2F1748-0221%2F8%2F03%2Fc03015` [accessed 05-September-2019].

[Mohl, 2019] Mohl, C. (2019). Reconstruction of Muon Tracks using four-layered Micromegas Modules. Bachelor thesis.

[Müller, 2017] Müller, R. (2017). *Quality Control of Micromegas Detectors for the ATLAS New Small Wheel Upgrade Project and Opimization of the Spatial Resolution of PoSSuMuS Detectors in two Dimensions.* PhD thesis, Ludwig-Maximilians Universität, München.

[Neubert, 2018] Neubert, P. (2018). Reconstruction of the position deviation on a coordinate measuring machine by using a laser interferometer and an image analysis on precision markers. Bachelor thesis.

[Ntekas, 2016] Ntekas, K. A. (2016). *Performance characterization of the Micromegas detector for the New Small Wheel upgrade and Development and improvement of the Muon Spectrometer Detector Control System in the ATLAS experiment.* PhD thesis, National Technical University of Athens.

[Olive et al., 2014] Olive et al. (2014). Review of particle physics. *Chinese Physics C*, 38(9).

[Opto Engineering, 2019] Opto Engineering (2019). Telecentric lenses tutorial. Opto Engineering Copyright ©2015 - 2019 `https://www.opto-e.com/resources/telecentric-lenses-tutorial` [accessed 28-August-2019].

[Pequenao, 2008] Pequenao, J. (2008). Computer generated image of the whole ATLAS detector. `https://cds.cern.ch/record/1095924` [accessed 06-August-2019].

[Raether, 1964] Raether, H. (1964). *Electron Avalanches and Breakdown in Gases.* Butterworths advanced physics series. Butterworths, London.

[Rauscher, 2005] Rauscher, F. (2005). *Untersuchung des Verhaltens von Driftrohren bei starker Gamma-Bestrahlung sowie Vermessung von Driftrohrkammern mit Hilfe von Myonen der kosmischen Höhenstrahlung.* PhD thesis, Ludwig-Maximilians Universität, München.

[Rose and Korff, 1941] Rose, M. E. and Korff, S. A. (1941). An investigation of the properties of proportional counters. i. *Phys. Rev.*, 59:850–859. `https://link.aps.org/doi/10.1103/PhysRev.59.850` [accessed 26-July-2019].

[Sidiropoulou, 2018] Sidiropoulou, O. (2018). *Characterization of the ATLAS-type Micromegas Detectors.* PhD thesis, Julius-Maximilians-Universität, Würzburg.

[Suzuki and Abe, 1985] Suzuki, S. and Abe, K. (1985). Topological structural analysis of digitized binary images by border following. *Computer Vision, Graphics, and Image Processing*, 30(1):32 – 46. `http://www.sciencedirect.com/science/article/pii/0734189X85900167` [accessed 04-July-2019].

[Townsend, 1910] Townsend, J. (1910). *The theory of ionization of gases by collision.* Van Nostrand. `https://archive.org/details/theoryofionizati00townuoft` [accessed 04-July-2019].

Danksagung

Viele Menschen begleiteten und unterstützten mich während dieser Arbeit. Hier möchte ich diesen Menschen danken. Denjenigen, die nicht explizit genannt sind, gilt ebenso mein Dank und meine Verbundenheit.

- Frau Prof. Dr. Dorothee Schaile leitet den Lehrstuhl an dem diese Arbeit geschrieben wurde. Für die gute Organisation und das familiäre Klima danke ich.
- Herr Prof. Dr. Otmar Biebel ist der Leiter der Top-Quark und Detektor-Entwicklungs-Abteilung. Für seine Hingabe, die jedes Projekt, ob Bachelor, Master oder Doktor-Arbeit, zu einem positiven Ende trotz bürokratischen Hindernissen geführt hat, danke ich Ihm.
- Herrn Prof. Dr. Thomas Kuhr möchte ich für das Erstellen des Zweitgutachtens danken.
- Herr Dr. Ralf Hertenberger ist die unermüdliche Kraft die das Micromegas-Projekt in München vorantreibt. Für die gute Betreuung und die Vermittlung von Begeisterung an den Herausforderungen danke ich Ihm.
- Dr. Bernhard Flierl ist seit 2015 mein Bürokollege. Für all die Diskussionen und Hilfestellungen in dieser Zeit möchte ich mich herzlich bedanken.
- Dr. Philipp Lösel hat die Vorarbeit zu dieser These geleistet und die Strukturen zur Messung mitaufgebaut. Auch für die gute Zeit außerhalb des universitären Betriebs danke ich Ihm.
- Dr. Ralph Müller hat mich während meiner ersten Zeit am Lehrstuhl betreut und mich mit der CMM eingearbeitet. Für seine stets positive und ehrliche Haltung danke ich Ihm.
- Dr. Felix Klitzner hat fast parallel zu mir seine Arbeit geschrieben. Für die Diskussionen rund um die Signal-Entstehung, als auch sein positives Wesen, danke ich Ihm.
- Die Hardware-Gruppe umfasste, während der Zeit in der ich gearbeitet habe noch einige Menschen:

  Dr. Jonathan Bortfeldt, Christoph Jagfeld, Maximilian Paul Rinnagel, Dr. Chrysostomos Valderanis, Dr. Andre Zibell.

  Ihnen sei für die schöne Zeit, als auch das produktive Arbeiten gedankt.
- Mit allen Menschen am Lehrstuhl-Schaile verbinde ich positve Erinnerungen. Für diese guten Erfahrungen danke ich.
- Die Bachelor-Arbeiten, welche während dieser These betreut wurden, haben zu guten Ergebnissen geführt. Für den Elan und den Wissensdurst von

  Maximilian Feil, Philipp Neubert und Christian Mohl

  möchte ich mich bedanken.
- Der Lehrstuhl besteht nicht nur aus Physikern, sondern auch aus Menschen die auf andere Art das Projekt und die Arbeiten zum Erfolg führen. Dafür danke ich

  Frau Elke Grimm-Zeidler, Herrn Attila Varga und Herrn Reinhardt Satzkowski.
- The NSW collaboration consists of many people from different countries. I want to thank for the prospering cooperation in a friendly atmosphere.
- Während meines Werdegangs haben mich auch im privaten Menschen begleitet. Dafür danke ich meinen Freunden.
- Für die Ermöglichung des Studiums, der konstanten Unterstützung und das Erinnern an das Positive in dunklen Zeiten, danke ich meiner Familie. Ich danke meiner Mutter Heike Herrmann, meinem Vater Karl Friedrich Herrmann und meiner Schwester Leonie Herrmann. Insbesondere danke ich meiner Schwester Laura Herrmann für das Korrekturlesen der Arbeit. Auch der Familie meines Onkels Jürgen Smola gebührt Dank, für die Erinnerung an das was mich am Studium begeistert hat.
- Zuletzt möchte ich meinen Großeltern, Renate Smola und Peter Smola, für das danken, was sie aus mir gemacht haben.

> *There is no devil in hell, Mr. Holmes, and there is no man upon earth who can prevent me from going to the home of my own people*
>
> - Arthur Conan Doyle , 1901 , *The Hound of the Baskervilles*